Weak Gravitational Lensing and Intrinsic Galaxy Alignments

Catherine Heymans

St Catherine's College, Oxford

August 2003
Thesis submitted for the degree of Doctor of Philosophy

Declaration

I declare that no part of this thesis has been accepted, or is currently being submitted, for any degree or diploma or certificate or any other qualification in this University or elsewhere.

This thesis is the result of my own work unless otherwise stated. Chapter 3 was carried out in collaboration with Lance Miller (University of Oxford), with section 3.3 carried out also in collaboration with the COMBO-17 team, in particular Michael Brown (Institute for Astronomy, University of Edinburgh). Chapter 4 was carried out in collaboration with the Oxford Dartmouth Thirty team, in particular Paul Allen, Lance Miller and Gavin Dalton (University of Oxford). Chapters 5, 6 and 7, and appendix A, were carried out in collaboration with Alan Heavens (Institute for Astronomy, University of Edinburgh) with chapter 7 also carried out in collaboration with Michael Brown (Institute for Astronomy, University of Edinburgh).

Parts of this thesis have been published in the following conference proceedings and refereed journals:

- Heavens, Refregier & Heymans 2000, MNRAS, 319, 649: Section 5.3
- Heymans & Heavens 2003a, MNRAS, 339, 711: Chapter 6 & Appendix A
- Heymans & Heavens 2003b, "Gravitational Lensing : A unique Tool for Cosmology", Aussois, France: Chapter 6 & section 7.1
- Heymans et al. 2004, MNRAS, 347, 895: Section 5.4 & Chapter 7

Weak Gravitational Lensing and Intrinsic Galaxy Alignments

Catherine Heymans
St Catherine's College, Oxford

Submitted for the Degree of Doctor of Philosophy
Trinity Term 2003

Abstract

This thesis describes an investigation into weak gravitational lensing, a unique and powerful astronomical tool for the study of dark matter on large scales. Lensing distorts background images, inducing correlations in the observed ellipticities of galaxies, and these correlations can be used to estimate many characteristics of the Universe. Key to all weak lensing studies is a reliable and unbiased method to detect weak lensing distortions from observed galaxy images that are contaminated by Earth and telescope-based shearing and smearing distortions. A new galaxy model-fitting technique is presented that has been developed in order to satisfy this requirement, which will also permit future signal-to-noise optimised measurements of weak lensing shear. Model-fitting provides a good alternative to the standard Kaiser, Squires & Broadhurst (1995) method (KSB), and comparisons between the two techniques are drawn from an analysis of deep R band imaging from the COMBO-17 survey, revealing strong evidence for the presence of bias in KSB galaxy shape measurement. With the galaxy model-fitting technique, an investigation into the effectiveness of the Oxford Dartmouth Thirty degree survey (ODT) for gravitational lensing studies is presented, resulting in the detection of weak gravitational lensing by large scale structure, or 'cosmic shear', in 0.7 square degrees of the best seeing ODT images.

One concern for all cosmic shear studies is that the weak lensing signal, manifest in the weakly correlated ellipticities of distant galaxies, is contaminated by the intrinsic alignment of close galaxy pairs, potentially induced during galaxy formation by physical interactions such as tidal forces. This contamination is investigated theoretically, through numerical simulations, and observationally, with an analysis of the COMBO-17 survey and the study of published results from the Red-sequence Cluster survey and the VIRMOS-DESCART survey, concluding that the intrinsic alignment effect is at the lower end of the range of theoretical predictions. The impact of intrinsic galaxy alignments on cosmological parameter estimation is investigated, with an analysis of the weak lensing results from the COMBO-17 survey. When marginalising over the observationally constrained intrinsic alignment signal, the amplitude of the matter power spectrum σ_8 is reduced by ~ 0.03 to $\sigma_8(\Omega_m/0.27)^{0.6} = 0.71 \pm 0.11$, where Ω_m is the matter density parameter.

With distance information from either spectroscopy or photometric redshifts, the downweighting of nearby galaxy pairs in weak lensing analysis can be optimised to virtually eliminate the systematic errors in the shear signal arising from intrinsic galaxy alignments, leaving a much smaller, largely statistical error. This method is applied to the photometric redshift sample of the COMBO-17 survey. Weak lensing measurements from the forthcoming SuperNova/Acceleration Probe weak lensing survey (SNAP), and the Canada-France-Hawaii Telescope Legacy survey, are expected to be contaminated on scales > 1 arcminute by intrinsic alignments at the level of $\sim 1\%$ and $\sim 2\%$ respectively. Division of the SNAP survey for lensing tomography significantly increases the contamination in the lowest redshift bin to $\sim 7\%$ and possibly higher. Removal of the intrinsic alignment effect by the downweighting of nearby galaxy pairs will therefore be vital for the lensing tomography studies of SNAP.

Acknowledgements

First and foremost I would like to thank Alan Heavens who introduced me to the wonderful world of weak gravitational lensing five years ago and has been an unfailing source of support and incredibly bright ideas ever since. I would also like to thank Lance Miller for his patience, encouragement and determination often in the face of adversity. I am indebted to Michael Brown who very generously gave me access to his weak lensing data, making a large chunk of this thesis possible. The Oxford Dartmouth Thirty degree survey would not exist without the incredibly hard work of Paul Allen who not only taught me everything I know about observing but has also been one of my most favourite astrophysics companions, along with the most lovely Kate Brand.

Many people have advised and guided me over the course of this thesis and I would especially like to thank David Bacon, Meghan Gray, Andy Taylor, Alex Refregier, Gavin Dalton, Chris Wolf, Klaus Meisenheimer, Bill Ballinger, Jasper Wall, Andi Burkett, Henk Hoekstra, Priya Natarajan and Rob Crittenden. I would also like to thank my thesis examiners; Ludo Van Waerbeke and Pedro Ferreira, for a very fruitful discussion during my viva with extra special thanks to Ludo for taking the time to spot all my typos! This DPhil was funded by the Particle Physics and Astronomy Research Council. The simulations analysed in chapter 5 were carried out using data made available by the Virgo Supercomputing Consortium using computers based at the Computing centre of the Max-Planck Society in Garching at the at Edinburgh Parallel Computing Centre. I'm very grateful to Rob Smith for providing me with halos from the simulations and his non-linear power spectrum fitting formula and code.

Thanks go to Ed, Ewan, James, Margaret, Dr Beer, Lee, Reba, James T, Jenny, Ranty, Jo, Esther and Susan for providing plenty of light alcoholic relief over the years and to my long suffering office chums Ana and Filipe. Extra special thanks goes to the wonderful Emily MacDonald, without you the last 2 years would have been incredibly dull! I thank the original Dr Heymans, who has been a source of great inspiration and sisterly guidance; Elvis, Aretha, and Dolly, for providing an excellent soundtrack; and finally I thank Rory, who truely is the boy wonder, for his love and friendship.

Contents

1

Introduction

This thesis for the most part concerns the study of the large scale properties of the Universe, its nature, content, and evolution. We will assume the standard frame work of the Hot Big Bang model which became popular in the 1960's and is now the generally accepted paradigm. From Big Bang to structure formation is a complex route that is far from fully understood and in this chapter we will very briefly chart what is currently thought to be the best description, introducing cosmological parameters and models that will be referred to throughout this thesis, concluding with an introduction to gravitational lensing.

1.1 The Cosmological Model

The deduction by Edwin Hubble in the 1920's that galaxies were moving away from us with a recession speed proportional to their distance, lead to one of the most important cosmological discoveries of this century as it provided key evidence for an expanding Universe as described by a hot Big Bang model (Hubble 1929). The similarity of the now famous deep observations by the Hubble space telescope of a patch of the northern sky and a patch of the southern sky[1] is an example however of a fundamental problem that exists with the standard Big Bang model. These images are so similar that on presentation of either image it would be a challenge to say which image was which. On large scales the Universe appears to be isotropic, i.e. the same in every direction we look. Invoking the cosmological principle which states that 'we're not at the centre of the Universe', if it's isotropic here it must be isotropic everywhere, and hence we must live in a homogeneous, isotropic Universe. This conclusion presents a problem

[1] *www.stsci.edu/ftp/science/hdf/hdf.html*

as regions which could never have been in causal contact[2] in the standard Big Bang model are observed to be remarkably similar, particularly if we consider the isotropic temperature of the cosmic microwave background (see below).

The solution to this 'Horizon' problem and several other problems with the standard Big Bang model came with the idea of Inflation, whereby a period of exponential expansion occurred around $t \sim 10^{-34}$ seconds after the Big Bang, greatly inflating the causally connected regions giving rise to isotropy on very large scales. With this theory quantum fluctuations are also inflated producing large scale density fluctuations which become the seeds of structure formation, see section 1.2. Another consequence of this theory is that inflation drives the Universe to a flat geometry which is what we observe today, see section 1.1.3. Post inflation, after a period of re-heating, light nuclei are formed through nucleosynthesis, the predictions of which are very close to what is now observed, matter soon becomes dominant at **equality**, and we come to the era of **recombination** where the ions and electrons combine to form neutral atoms. These decouple from the photons at which point in time the Universe becomes transparent. Photons from this last scattering surface are seen today as isotropic 2.73K black-body spectrum radiation, termed the cosmic microwave background (CMB).

1.1.1 Big Bang Cosmology

An expanding Universe which is homogeneous and isotropic can be described by the Robertson-Walker space-time metric,

$$ds^2 = c^2 dt^2 - a^2(t) \left[dw^2 + f_K(w)^2 (d\theta^2 + \sin^2\theta d\phi^2) \right], \tag{1.1}$$

where ds is the invariant space-time interval between two events which can be agreed upon by fundamental observers. These observers are at rest with respect to the matter in their vicinity and are therefore receding from each other with the general Hubble expansion, described by the scale factor $a(t)$ measured at cosmic time t. $a(t_0) = 1$ at the present day. The spherical polar co-ordinates are w, θ and ϕ, where w is the comoving radial distance, and $f_K(w)$ is the effective distance, also known as the comoving angular diameter distance, that is dependent

[2]Causally connected regions are defined by the horizon scale or Hubble radius $d'_H(t) = c/H(t)$, which is the distance that information can travel in time t.

on the geometry or curvature of the Universe K, such that

$$f_K(w) = \begin{cases} K^{-1/2}\sin(K^{1/2}w) & (K > 0) \quad \text{closed} \\ w & (K = 0) \quad \text{flat} \\ (-K)^{-1/2}\sinh[(-K)^{1/2}w] & (K < 0) \quad \text{open.} \end{cases} \tag{1.2}$$

The evolution of the scale factor $a(t)$, which describes the expansion of the Universe, can be derived from Einstein's gravitational field equations, and is given by the Friedmann equations,

$$\begin{aligned} \frac{\ddot{a}}{a} &= -\frac{4\pi G}{3}\left(\rho + \frac{3p}{c^2}\right), \\ \left(\frac{\dot{a}}{a}\right)^2 + \frac{Kc^2}{a^2} &= \frac{8\pi G}{3}\rho, \end{aligned} \tag{1.3}$$

where p is the pressure and ρ is the total density,

$$\rho = \rho_m + \rho_r + \rho_v, \tag{1.4}$$

which has contributions from the matter, radiation and vacuum energy. The vacuum source term represents the energy density of empty space and has recently been called **dark energy** or the **cosmological constant** Λ, which can alternatively be included as a constant of integration in the solution of the field equations, see for example Peacock (1999).

The first law of thermodynamics for an adiabatic system with no heat flowing in or out is given by

$$dU = -pdV, \tag{1.5}$$

where U is the energy of the system of volume V under pressure p. For a homogeneous Universe, noting that $U = \rho c^2 V$ and that $V \propto a^3$, we find

$$c^2\frac{d\rho}{da} + 3\left(\frac{p + \rho c^2}{a}\right) = 0. \tag{1.6}$$

Defining the relationship between pressure and density for each component, through the **equation of state parameter** w, such that[3]

$$p = \mathrm{w}\rho c^2, \tag{1.7}$$

where

$$\begin{aligned} &\mathrm{w}_m \approx 0 && \text{(matter)}, \\ &\mathrm{w}_r = \tfrac{1}{3} && \text{(radiation)}, \\ &\mathrm{w}_\Lambda = -1 && \text{(cosmological constant)}, \end{aligned} \tag{1.8}$$

[3]For ρ as the energy density, the equation of state can be written simply as $p = \mathrm{w}\rho$.

we find that

$$\begin{aligned}\rho_m &\propto a^{-3}\\ \rho_r &\propto a^{-4}\\ \rho_\Lambda &= \text{constant.}\end{aligned} \tag{1.9}$$

After inflation the Universe was therefore **radiation dominated** until a time when $\rho_m = \rho_r$. As a increases with time the **matter dominated** Universe[4] with a constant vacuum energy density will eventually become dominated by dark energy, (see the review by Peebles & Ratra (2003)). Note that there are many alternative 'quintessence' models for the equation of state of the vacuum energy which can also include some time dependence $w(t)$, (Caldwell, Dave & Steinhardt 1998; Wang et al. 2000).

Hubble's constant is the time-dependent constant of proportionality between a galaxy's recession speed v and its distance in the local Universe. From the Robertson-Walker metric equation 1.1, a small radial distance δl is given by

$$\delta l = a(t)\delta w. \tag{1.10}$$

As w is the time independent comoving distance, the recession velocity at distance δl is then given by

$$v = \frac{\delta l}{dt} = \dot{a}(t)\delta w, \tag{1.11}$$

and hence Hubble's constant can be written in terms of the scale factor such that

$$H = \frac{\dot{a}}{a}. \tag{1.12}$$

The Friedmann equation 1.3 can then be re-written as

$$\frac{8\pi G\rho}{3H^2} - \frac{Kc^2}{a^2} = 1, \tag{1.13}$$

such that for a flat Universe, (K=0), the critical matter density of the Universe is given by

$$\rho_c = \frac{3H^2}{8\pi G}. \tag{1.14}$$

The ratio of the density ρ to this critical density ρ_c is the **density parameter** Ω,

$$\Omega \equiv \frac{\rho}{\rho_c}. \tag{1.15}$$

[4]For large Ω_Λ the Universe could move straight from a radiation dominated phase to a Λ dominated phase. With current estimates of Ω_Λ this is however unlikely.

$$\Omega \equiv \Omega_m + \Omega_r + \Omega_v \equiv \frac{1}{\rho_c}(\rho_m + \rho_r + \rho_v) \ . \tag{1.16}$$

Ω is one of the fundamental parameters of cosmology as it determines the fate of the Universe. A Universe with $\Omega < 1$ is spatially infinite (open), and will increase in size forever. For $\Omega > 1$, we have a spatially finite Universe (closed), which in the absence of a cosmological constant will eventually recollapse. For the critical case with a flat geometry $\Omega = 1$, we are exactly balanced between the open and closed cases. The inclusion of a cosmological constant or vacuum energy term complicates this scenario somewhat. From equation 1.3, we can see for a flat Universe with $\rho = \rho_\Lambda$, $\dot{a} \propto a$, and hence we would see exponential expansion and an accelerating Universe.

1.1.2 Cosmological redshift

The expansion of the Universe can be detected by measuring the shift towards the red of emission lines in the spectra of distance galaxies. Redshifting occurs because the wavelength of light propagating between the source and observer will grow with the expanding Universe. This can be shown from the Robertson-Walker metric, equation 1.1, if we consider the crests of light waves emitted from a source at constant $w_{\rm source}$, with the first crest emitted radially at time t_e and observed at time t_o, and the second following at time $t_e + \Delta t_e$, and observed at time $t_o + \Delta t_o$. From the metric,

$$\int_0^{w_{\rm source}} dw = c\int_{t_e}^{t_o} \frac{dt}{a(t)} = c\int_{t_e+\Delta t_e}^{t_o+\Delta t_o} \frac{dt}{a(t)} \ . \tag{1.17}$$

Assuming that the expansion rate is slow compared to the frequency of the light $a(t) \approx a(t + \Delta t)$, then it follows that,

$$\frac{\lambda_e}{\lambda_o} = \frac{a(t_e)}{a(t_o)} \, , \tag{1.18}$$

where $\lambda = c\Delta t$ and λ_e is the wavelength of the emitted light, and λ_o is the observed wavelength. The redshift is defined as

$$z = \frac{\lambda_o - \lambda_e}{\lambda_e} \, , \tag{1.19}$$

and as $a(t_o) = 1$ for a present day observer,

$$a(t) = \frac{1}{1+z} \ . \tag{1.20}$$

The redshift is therefore a measure of the scale factor at the time of the emission. Note that the highest redshift objects discovered so far have $z \sim 6$ (Fan et al. 2003).

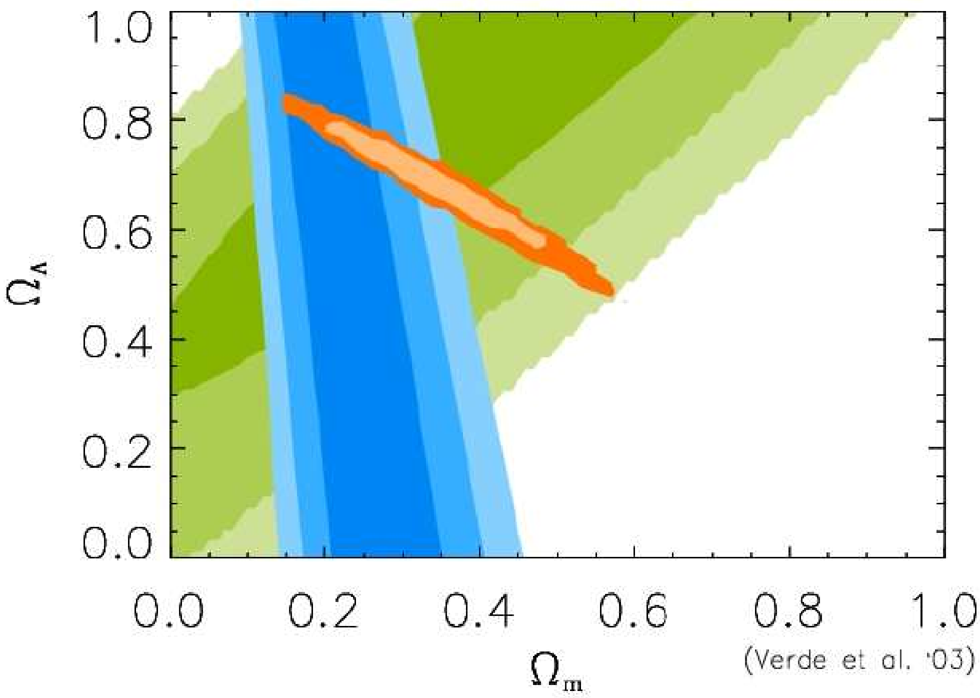

Figure 1.1: Constraints on the geometry of the Universe: $\Omega_m - \Omega_\Lambda$ plane. In green are the likelihood contours from the Supernova Ia Cosmology Project (Perlmutter et al. 1999), in blue, 2dF data from the bispectrum analysis of Verde et al. 2001, and in orange the likelihood contours from the best fit ΛCDM model to the WMAP power spectrum, (Spergel et al. 2003). Picture from L. Verde (Penn).

1.1.3 The Concordance Model

The CMB contains a wealth of cosmological information and has been the subject of intense study since it was first discovered by Penzias & Wilson (1965), recently producing some exquisite results from the the Wilkinson Microwave Anisotropy Probe (WMAP) (Spergel et al. 2003). Before recombination, oscillations smaller than the Jeans' length $M_J \sim ct/\sqrt{3}$ during radiation domination, are set up in the bound plasma of photons and baryons, as gravity compresses the fluid which the pressure counteracts. These oscillations which cease at recombination when the radiation decouples, cause temperature fluctuations. Oscillation modes caught at their extrema represent characteristic scales related to the distance sound can travel by recombination. Reducing a map of the fluctuating temperature of the CMB into its angular power spectrum reveals peaks corresponding to these extrema (Hinshaw et al. 2003). Measurement of the position of the peaks in the CMB power spectrum tells us the characteristic angular scale of the fluctuations which can be directly related to the geometry of the universe. WMAP, like many other CMB experiments, finds that we live in a flat Universe which agrees with the prediction from inflationary models that $\Sigma\,\Omega_i = 1$. The ratio between the amplitude of the peaks of different oscillation modes tells us about the baryon fraction. With more baryons there will be stronger gravitational compressions leading to a larger temperature difference between a compression mode and a rarefied mode. WMAP finds that with todays Hubble parameter set to $H_0 = 72\mathrm{km\,s^{-1}\,Mpc^{-1}}$ (Freedman et al. 2001), the density parameter of baryons is $\Omega_b \sim 0.04$, implying only 4% of our Universe is comprised of baryonic material.

The results from the CMB experiments are well complemented by studies of Supernova type Ia. Type Ia spectra and light curves, their rising and falling brightness over time, are all nearly alike provided a decay correction is made. They are also bright enough to be seen at very great distances and therefore act as excellent standard candles which can be used to to measure cosmological parameters. Taking the information from CMB experiments that the Universe is flat, it has been found that today the matter density parameter $\Omega_m \sim 0.3$, leaving a vacuum energy component $\Omega_\Lambda \sim 0.7$. This concordance model is consistent with several independent experiments such as the two degree field survey (2dF), (Verde et al. 2002), leading some people to claim that we are reaching an era of high precision cosmology where the important cosmological parameters will be established within the cosmological model to one significant figure or better.

The concordance model tells us the Universe is composed of $\sim$ 30% matter and $\sim$ 70% of an unknown dark energy component. With knowledge of the baryon fraction from CMB and nucleosynthesis calculations we find that 26% of the matter in the Universe must be non-baryonic, hence dark and unknown. Understanding the nature of dark matter and dark energy is therefore one of the most important challenges facing modern day cosmology.

1.1.4 Evidence for Dark Matter: Dark Matter candidates

The first evidence for the existence of dark matter came from studies of the dynamics of the Coma cluster by Zwicky (1933), which implied that the cluster would simply disperse if there was not an additional gravitational pull from some invisible dark matter. This has since been confirmed by both X-ray measurements of the mass of hot intra-cluster gas and strong gravitational lensing measurements of the dark matter distribution (section 1.3.2). Galaxies themselves also show evidence for dark matter, as the measured rotational speed of stars in spiral galaxies are found to be approximately constant as a function of radial distance from the galaxy core. The density of light-emitting matter decreases towards what is seen to be the edge of the galaxy, but the rotational velocities do not to appear to decrease accordingly. We conclude from this that there is a dense outer halo of dark matter that extends far beyond the visible edges of the galaxy, which is typically found to be five to ten times the mass of the visible galaxy.

The search for a dark matter candidate has been a hot topic of research since its existence was first proposed. Early favourite baryonic candidates featured compact objects such as brown dwarfs and white dwarfs. These have now been definitively ruled out as a significant component of the dark matter through searches for microlensing events in our own halo and the halo of M31, see section 1.3.1. This result is consistent with the concordance model which forces us to the conclusion that most of the dark matter, which comprises about a quarter of the Universe, is made up of non-baryonic matter that cannot consist of ordinary atoms. The favoured view is that these exotic particles have no charge, as they pass through ordinary material with an undetectable interaction, and from theories of structure formation, as discussed in the next section, they must also be non-relativistic or 'cold'. These weakly interacting massive particles, WIMP, could potentially be the supersymmetric cousins of particles in the Standard Model of particle physics. These particles may be detectable, if they exist, when the large hadron collider at CERN begins operation in 2005.

1.2 Structure formation

This thesis focuses on probing the large scale structure of the Universe, using a technique called weak gravitational lensing. Our assumption will be that structure in the Universe can be fully described by the **matter power spectrum** which can be modelled, as shown in the next section, from the following theory for structure formation.

As discussed in section 1.1 it is believed that a period of exponential expansion in the very early Universe inflated quantum fluctuations outwith the horizon scale, 'sowing the seeds for structure formation'. This scenario for the origin of structure in the Universe predicts adiabatic Gaussian fluctuations[5] which is consistent with the WMAP CMB data (Komatsu et al. 2003). A fluctuation at position $\mathbf{x}$ produces a matter density contrast such that

$$\delta(\mathbf{x}) = \frac{\rho(\mathbf{x}) - \bar{\rho}}{\bar{\rho}}. \tag{1.21}$$

Provided that $\delta \ll 1$ then relativistic perturbation theory, (see for example Bardeen (1980)), shows that adiabatic matter density fluctuations will grow according to

$$\begin{array}{lclll} \delta(a) & \propto & a^2, & a < a_{\rm eq} & \text{before equality} \\ \delta(a) & \propto & a, & a > a_{\rm eq} & \text{after equality,} \end{array} \tag{1.22}$$

for an Einstein-de Sitter model which is valid at early times, with $K = 0$ and $\Omega_\Lambda = 0$. For later times where $a \gg a_{\rm eq}$ the density perturbations change according to a growth function $g(a)$, such that

$$\delta(a) = \delta_0\, a\, \frac{g(a)}{g(a_0)}, \tag{1.23}$$

where the growth function $g(a)$ has a fitting formula (Carroll, Press & Turner 1992), given by

$$g(a, \Omega_m, \Omega_\Lambda) = \frac{5}{2}\Omega_m(a)\left[\Omega_m^{4/7}(a) - \Omega_\Lambda(a) + \left(1 + \frac{\Omega_m(a)}{2}\right)\left(1 + \frac{\Omega_\Lambda(a)}{70}\right)\right]^{-1}. \tag{1.24}$$

Figure 1.2 shows a sketch of perturbation growth. Until matter domination the expansion time-scale, determined by the radiation density, is shorter than the collapse time-scale of the dark matter. Hence the fast radiation driven expansion will prevent the growth of dark matter perturbations. This however will only affect the perturbations which are smaller than the regions over which light or radiation can travel. These causally connected regions are determined by the horizon size d_H, and larger scale perturbations with wavelength $\lambda > d_H$ will remain unaffected, growing in amplitude as given by equation 1.22. As the horizon scale grows with time, more perturbations enter the horizon and their growth is stalled until matter equality. This results in the overall suppression of the amplitude of fluctuations which enter the horizon before matter radiation equality. At the time when matter becomes dominant the collisionless cold dark matter collapses under gravity whilst the ionic baryonic matter is prevented, still bound and oscillating with the photons. At recombination, baryonic matter

[5] An alternative to adiabatic perturbations are isocurvature perturbations which behave differently from their adiabatic counterparts and can arise from stresses in the matter which causally push matter around. CMB results strongly favour primordial adiabatic perturbations and upcoming CMB polarisation results are likely to provide even tighter constraints (Hu, Spergel & White 1997). If it is found that the density fluctuations are not adiabatic then we will have to rethink our standard ideas about the origin of structure.

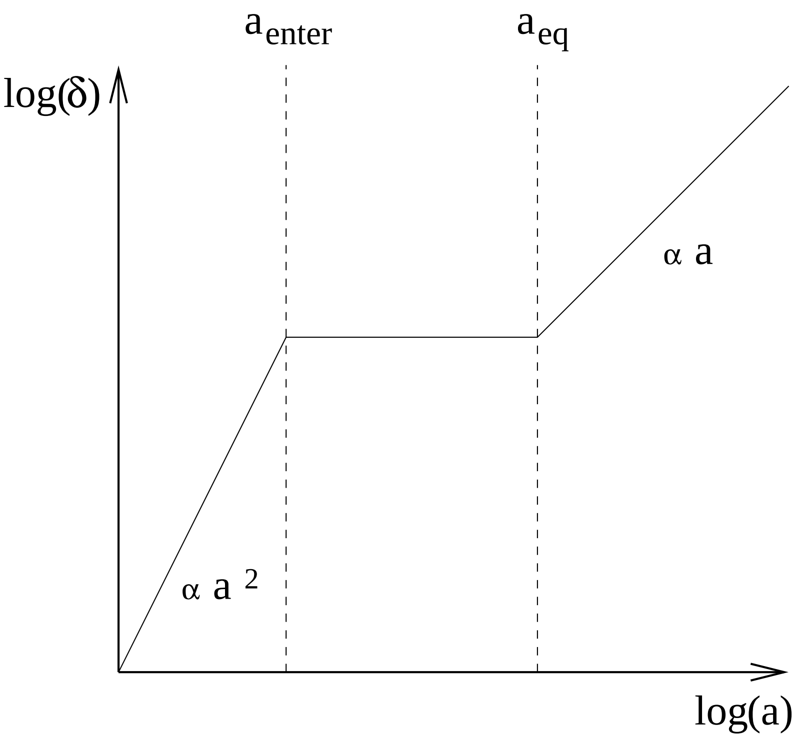

Figure 1.2: Schematic of the suppression of fluctuation growth during the radiation dominated phase when the density perturbation enters the horizon at $a_{\rm enter} < a_{\rm eq}$. The rapid radiation driven expansion prevents the perturbation from growing until matter radiation equality.

falls into the awaiting potential wells that have been created by the cold dark matter giving rise to a simple picture of galaxy formation where we see large dark matter haloes each with a baryonic galaxy at the core. As the horizon size grows, larger scale fluctuations become causally connected, forming some of the superstructures we see today (Brand et al. 2003). This is known as the 'bottom-up' model of structure formation. Note that if the dark matter was relativistic or 'hot', the small scale fluctuations would be completely erased by diffusion, leaving only the largest scale fluctuations and a 'top-down' model of structure formation, which is difficult to reconcile with observations, see for example White, Davis & Frenk (1984).

1.2.1 The matter power spectrum

A random isotropic Gaussian density field, such as the density field produced by primordial adiabatic fluctuations, can be described completely by its ensemble averaged power spectrum $P_\delta(k)$, see section 2.4.1, such that

$$(2\pi)^3 P_\delta(k)\delta_D(\mathbf{k}-\mathbf{k}') = \langle|\delta(\mathbf{k})\delta^*(\mathbf{k}')|\rangle\,, \tag{1.25}$$

where δ_D is the Dirac delta function and $\delta(\mathbf{k})$ is the Fourier transform of $\delta(\mathbf{x})$, equation 1.21 such that

$$\delta(\mathbf{k}) = \int d^3\mathbf{x}\delta(\mathbf{x})e^{-i\mathbf{x}\cdot\mathbf{k}} . \tag{1.26}$$

The wavenumber k is related to the wavelength of a fluctuation λ by $k = 2\pi/\lambda$. Large k scales imply small wavelength fluctuations and small k scales imply large wavelength fluctuations. A density fluctuation of comoving wavelength λ enters the horizon at time t_{enter} when

$$\lambda = d_H(a_{\mathrm{enter}}) = \frac{c}{a_{\mathrm{enter}}H(a_{\mathrm{enter}})}, \tag{1.27}$$

where H is the Hubble parameter defined in equation 1.12, $H^{-1} \propto t$, and the additional factor of a converts to comoving distances. The Hubble parameter can be written in terms of present day cosmological parameters, denoted by $_0$, such that

$$H^2(t) = H_0^2\left[a^{-4}(t)\,\Omega_{r,0} + a^{-3}(t)\,\Omega_{m,0} - a^{-2}(t)\frac{Kc^2}{H_0^2} + \Omega_\Lambda\right] \tag{1.28}$$

where we have used equations 1.3, 1.4 and 1.9. For an Einstein-de Sitter model, ($K = 0, \Omega_\Lambda = 0$), noting that at matter radiation equality, $\rho_r = \rho_m$ and hence $a_{\mathrm{eq}}^{-4}\,\Omega_{r,0} = a_{\mathrm{eq}}^{-3}\,\Omega_{m,0}$, we find from equation 1.27 that a fluctuation which enters the horizon at time $t_{\mathrm{enter}} < t_{\mathrm{eq}}$ will have a wavelength λ that is proportional to the scale factor at that time.

$$\begin{aligned} \lambda &\propto a_{\mathrm{enter}} \quad (t_{\mathrm{enter}} \ll t_{\mathrm{eq}}) \\ \lambda &\propto \sqrt{a_{\mathrm{enter}}} \quad (t_{\mathrm{eq}} \ll t_{\mathrm{enter}} \ll t_0)\,. \end{aligned} \tag{1.29}$$

We can use this relationship to understand the shape and growth of the power spectrum. At t_{enter} the power spectrum has changed from the primordial perturbation spectrum $P_i(k)$ according to the growth equation 1.22 and equation 1.25 such that

$$\begin{aligned} P_{\mathrm{enter}}(k) &\propto a_{\mathrm{enter}}^4 P_i(k) \propto k^{-4}P_i(k) \quad (t_{\mathrm{enter}} \ll t_{\mathrm{eq}}) \\ P_{\mathrm{enter}}(k) &\propto a_{\mathrm{enter}}^2 P_i(k) \propto k^{-4}P_i(k) \quad (t_{\mathrm{eq}} \ll t_{\mathrm{enter}} \ll 1)\,. \end{aligned} \tag{1.30}$$

The total power of the density fluctuations at t_{enter} is assumed to be scale-invariant such that $k^3P_{\mathrm{enter}}(k)$ = constant, implying that the primordial spectrum scales as $P_i(k) \propto k^{n_s}$ with $n_s = 1$. This is called the Harrison-Zeldovich spectrum, sketched in figure 1.3 (Harrison 1970; Zeldovich 1972), which is consistent with CMB results finding $n_s = 0.99 \pm 0.04$ (Spergel et al. 2003).

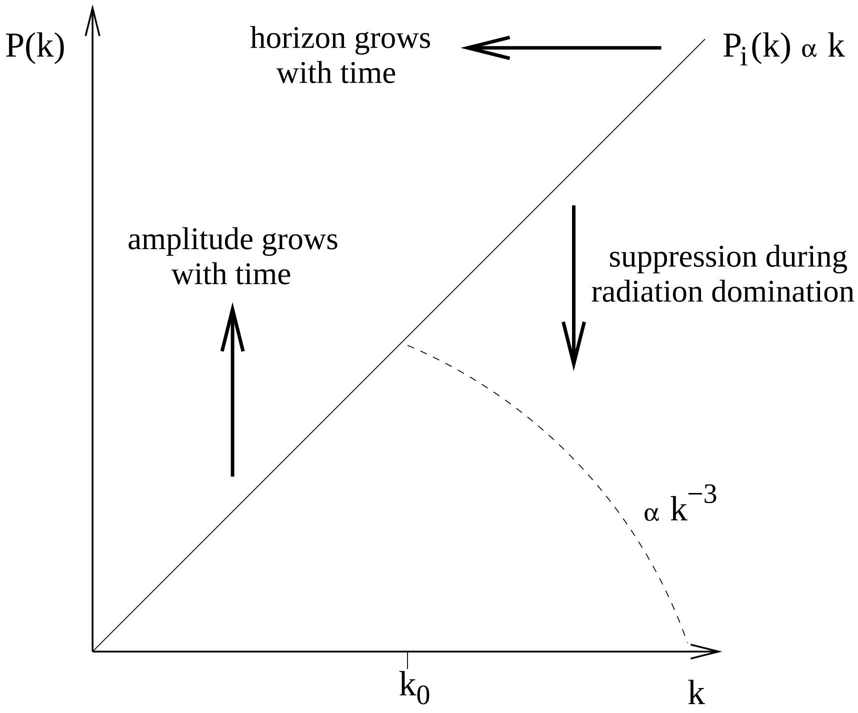

Figure 1.3: Schematic of the modification to the initial scale invariant power spectrum, (note log scale).

As discussed in section 1.2 and sketched in figure 1.2, if a fluctuation has wavelength $\lambda < d_H(a_{\rm eq})$, then its growth will be suppressed by the factor

$$f_{\rm sup} = \left(\frac{a_{\rm enter}}{a_{\rm eq}}\right)^2 . \tag{1.31}$$

This affects the largest k scales first and hence we see a turnover in the power spectrum as the small k scales continue to grow unimpeded, see figure 1.3. Defining k_0 as the wavenumber corresponding to the horizon size at $a_{\rm eq}$ and noting that $P_\delta(k \gg k_0) = f_{\rm sup}^2 P_i(k)$, the power spectrum at matter radiation equality can be written as

$$\begin{array}{lcll} P_\delta(k) & \propto & k & k \ll k_0 \\ P_\delta(k) & \propto & k^{-3} & k \gg k_0, \end{array} \tag{1.32}$$

where we have used equation 1.29 such that $f_{\rm sup} \propto k^{-2}$. After equality the shape of the power spectrum is slightly modified by non-linear effects, see section 1.2.2, and grows in amplitude according to the growth factor, equation 1.24.

The modification to the initial power spectrum during radiation domination, that has just been described, is formally contained in the transfer function T such that

$$P_\delta(k, z) = T(k, z)^2 P_i(k), \tag{1.33}$$

where T is dependent on the constituents of the Universe, see section 15.6 Peacock (1999), and is typically is parameterised by the shape parameter Γ where

$$\Gamma \sim \Omega_m h \sim 0.21, \tag{1.34}$$

and h is the dimensionless Hubble parameter $h = H_0/100\mathrm{km\,s^{-1}\,Mpc^{-1}}$. For a cold dark matter model there are several fitting formulae for T (Bond & Efstathiou 1984; Bardeen et al. 1986; Eisenstein & Hu 1999), and in this work we will use the Bond & Efstathiou (1984) formula for cold dark matter only, such that

$$T(k) = A\left[1 + (6.4q + 5.2q^{1.5} + 2.9q^2)^{1.13}\right]^{-\frac{1}{1.13}}, \tag{1.35}$$

where $A(z)$ is a normalisation factor, and

$$q = \frac{k\,/\,h\,\mathrm{Mpc}^{-1}}{\Gamma}. \tag{1.36}$$

The redshift dependence of the transfer function is given by equation 1.23 such that

$$T(k,z) = a(z)\,\frac{g(z)}{g(z=0)}\,T(k)\,, \tag{1.37}$$

where the growth function $g(z)$ is given by equation 1.24.

1.2.2 The non-linear matter power spectrum

The transfer function $T(k,z)$ considers the linear collapse of structures which applies only at small k. At large k non-linearity corrections should be applied to the power spectrum to take into account the fact that collapsing structures do stabilise, effectively increasing the amplitude of the linear power spectrum at large k, see figure 1.4. This effect has been estimated from numerical simulations resulting in fitting formulae such as the Peacock & Dodds (1996) formula from an 80^3 particle N-body simulation where,

$$\Delta^2_{nl}(k_{nl}) = f_{nl}\left[\Delta^2_l(k_l)\right]. \tag{1.38}$$

f_{nl} is the non-linear fitting function, equation 21 in Peacock & Dodds (1996) and $\Delta(k)$ is the dimensionless power spectrum defined as,

$$\Delta(k) = \frac{k^3 P_\delta(k)}{2\pi^2}. \tag{1.39}$$

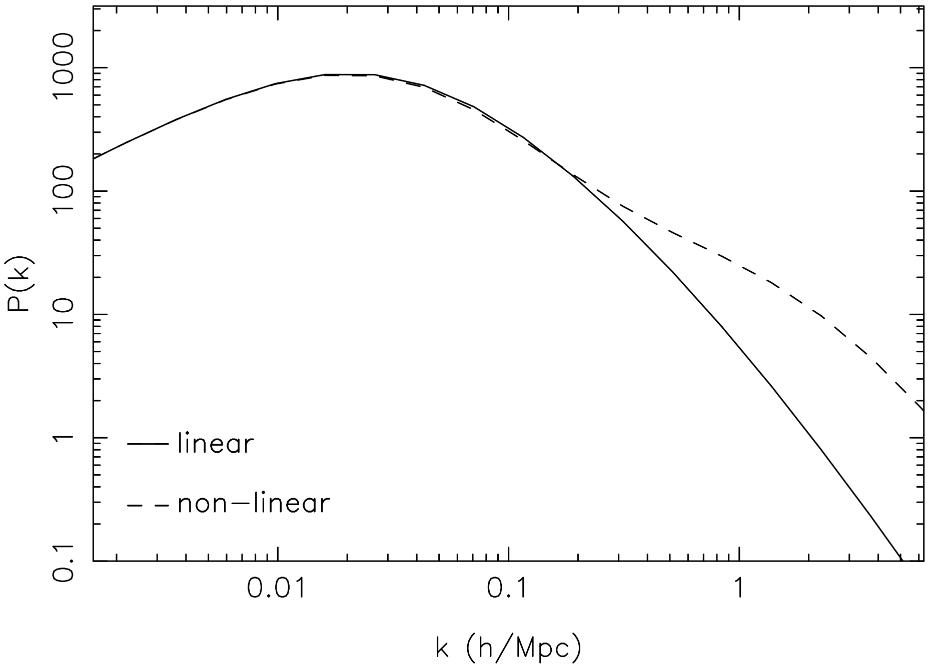

Figure 1.4: ΛCDM power spectrum, normalised by $\sigma_8 = 0.9$. The linear power spectrum is shown solid, and the non-linear power spectrum is shown dashed. Non-linearities increase the power in the large k scales.

The linear wavenumber k_l is related to the non-linear wavenumber k_{nl} through

$$k_l = \left[1 + \Delta^2_{nl}(k_{nl})\right]^{-\frac{1}{3}} k_{nl}. \tag{1.40}$$

More recently Smith et al. (2003) produced the 'halofit' formula which has been shown in general to be a better fit to the Virgo simulations (Jenkins et al. 1998) compared to the Peacock & Dodds (1996) formula. It is defined such that

$$\Delta^2_{nl}(k) = \Delta^2_Q(k) + \Delta^2_H(k) \tag{1.41}$$

where Q denotes a quasi-linear term which represents the power generated by the large scale placement of dark matter haloes and H denotes the power that results from the self-correlation of dark matter haloes. Fitting formulae for both these terms are given in the appendix of Smith et al. (2003) with code made available[6] to evaluate the non-linear power spectra with this method. Figure 1.4 compares the linear power spectrum (solid) and the non-linear power spectrum (dashed) for a ΛCDM model calculated with the 'halofit' formula equation 1.41.

[6] from *www.as1.chem.nottingham.ac.uk/~res/software.html*

1.3 Gravitational lensing

One of the key results from Einstein's theory of general relativity is that a ray of light will experience a curvature of its path when passing through a gravitational field, succinctly expressed as 'mass bends light'. This was first tested in 1919 by Arthur Eddington who lead a solar eclipse expedition to the island of Principe, in the Gulf of Guinea, with a second expedition heading to Sobral, Brazil. During this particular solar eclipse the Sun was directly in front of the Hyades star cluster. Comparison of the observed stellar positions during totality with reference positions taken previously revealed that the gravitational field of the sun had indeed bent the path of the light rays, altering the apparent positions of the Hyades stars. Subsequent solar eclipse expeditions and radio observations have confirmed this result to higher and higher precision finding that the observed angular shift in stellar positions is exactly that predicted by general relativity, knowing the mass of the sun. This result forms the basis for a unique astronomical tool termed gravitational lensing due to similarities with optical lenses, see section 2.1. The more massive the lens, the stronger the lensing distortions, which are described completely through general relativity. Observations of gravitational lensing can therefore provide us with a direct way to measure mass in the Universe.

The concordance model relies on the belief that dark matter exists, but because it is 'dark' it is impossible to detect by searching through the electromagnetic radiation spectrum. This is where gravitational lensing comes into its element as it is the only astronomical tool that can detect mass independently of its state or nature. A detailed mathematical description of gravitational lens theory can be found in chapter 2, here we will simply review three different applications for gravitational lensing, the later of which forms the basis of this thesis.

1.3.1 Microlensing

When a massive dark object, for example a brown dwarf, passes in front of a background star, the light from the star is gravitationally lensed and the star light is significantly magnified, see section 2.2. This amplification produces a sharp peak in the intensity of light from the background star and has been the subject of an extensive study by several dedicated groups, for example the MACHO collaboration, EROs and OGLE, who have monitored millions of stars in the large and small magallenic clouds in order to determine the number of MAssive Compact

Figure 1.5: Hubble space telescope image of strong gravitational lensing by the galaxy cluster 0024+1654 (NASA HST archive).

Halo Objects, MACHO, in our galaxy. Both groups find that the number of microlensing events can only account for $\leq 10\%$ of the missing galactic dark matter, (Alcock et al. 2000; Lasserre & The EROS collaboration 2000; Zebrun et al. 2001). This microlensing technique has been used in searches for planetary objects, (see for example Sackett (2000)), and a new microlensing search is now being directed towards the Andromeda galaxy (Calchi Novati et al. 2002).

1.3.2 Strong Lensing

Strong gravitational lensing is the study of massive lenses, such as the galaxy cluster shown in figure 1.5. The mass of the galaxy cluster is producing multiple sheared and magnified arc-like images of very distant background galaxies, which can be used to determine the surface mass density of the lens, see for example Tyson, Wenk & Valdes (1990) and the review Blandford & Narayan (1992). This strong lensing effect is also observed with multiply imaged quasars which can produce estimates of H_0 (Courbin 2003).

1.3.3 Weak Lensing

Weak gravitational lensing introduces a coherent distortion or shear in faint galaxy images. It is distinct from strong gravitational lensing as in the weak lensing régime we do not observe multiply imaged objects. Detection of the weak tangential distortions of the order of a few percent around lensing galaxies and of the order 10% around galaxy clusters, enables constraints to be set on the masses and sizes of the lensing galaxy halos and in some cases it is possible to produce a full surface mass reconstruction of a cluster lens (Brainerd, Blandford & Smail 1996; Seitz et al. 1996; Hoekstra et al. 1998; Hoekstra, Franx & Kuijken 2000; Lombardi et al. 2000; Athreya et al. 2002; Clowe & Schneider 2002; Gray et al. 2002). This thesis will focus on an even weaker effect called **cosmic shear**, which is caused by the weak lensing distortions of order 1%, from the distribution of large scale structure in the Universe.

1.4 Cosmic shear

The detection of cosmic shear is a direct way to measure the total matter distribution in the Universe, which unlike other large scale structure experiments, demands no assumptions for how luminous matter traces the dominant, largely unknown, dark matter component. Figure 1.6 shows an exaggerated ray tracing simulation of the cosmic shear effect where the light from distant galaxies propagates through the intervening large scale structure. In an empty flat Universe a light ray would travel in a straight line, but in the presence of matter the light ray's path is deflected by gravitational fields. Individual light rays experience a series of small deflections such that in the 2D projection, images of nearby galaxies are coherently distorted in directions determined by the distribution of dark matter along that particular line of sight. Unlike figure 1.6 suggests, this is a very weak effect and to detect it requires careful statistical treatment over many patches of the sky. A detailed mathematical description of cosmic shear can be found in chapter 2.

Several groups have successfully detected weak gravitational lensing. Now a well established technique, it has been used to set joint constraints on the matter density parameter Ω_m and the amplitude of the matter power spectrum σ_8, (see section 1.4.1), (R.Maoli et al. 2001; Rhodes, Refregier & Groth 2001; Van Waerbeke et al. 2001; Hoekstra, Yee & Gladders 2002; Bacon et al. 2003; Jarvis et al. 2003; Brown et al. 2003; Hamana et al. 2003), to measure the

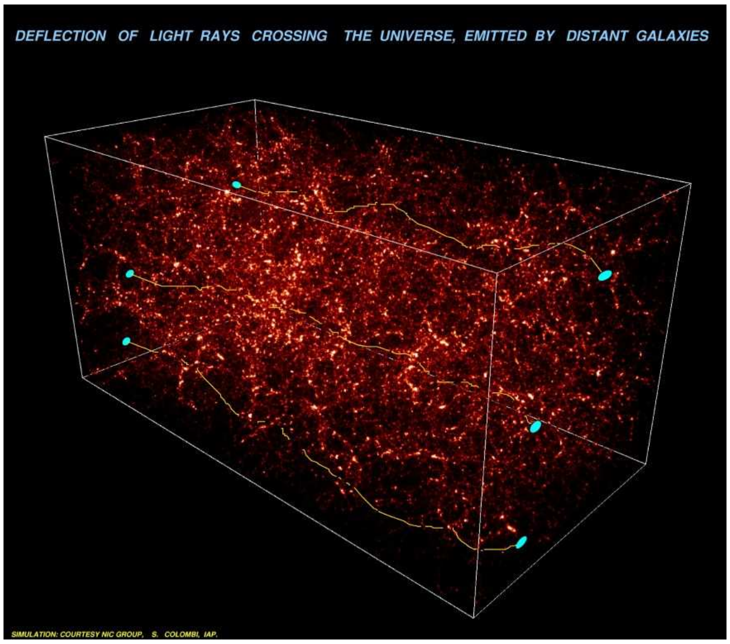

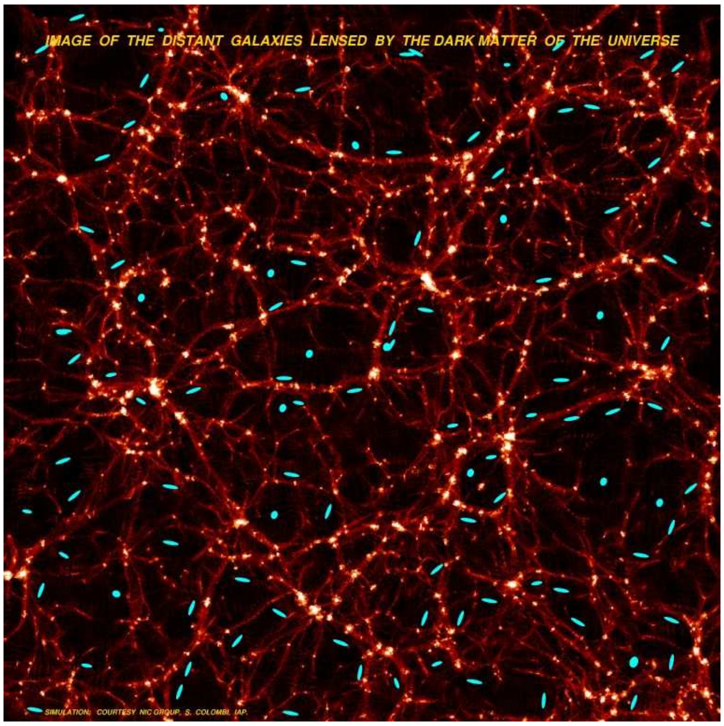

Figure 1.6: Numerical simulation showing the distribution of dark matter in a large volume of the Universe. The structures are displayed so that the brighter regions have a higher density than the darker regions. The ray tracing of light from distant galaxies, coloured blue, has been greatly exaggerated to show the principle of the weak lensing effect, resulting with the observed 2D projection (lower) showing a preferential elongation of the lensed galaxy images along the direction parallel to the filaments of dark matter. Images from S. Colombi (IAP).

bias parameter b (Hoekstra, Yee & Gladders 2001; Pen et al. 2003), and has recently been used to directly extract the 3D non-linear matter power spectrum $P_\delta(k)$ (Tegmark & Zaldarriaga 2002; Pen et al. 2003). Combined with CMB observations, weak lensing provides strong constraints on σ_8 and Ω_m, as the degeneracies in each measurement are almost orthogonal in the $\sigma_8 - \Omega_m$ plane (Brown et al. 2003; Contaldi, Hoekstra & Lewis 2003), resulting in the direct evidence for a low value of the matter density Ω_m, indicating a high non-zero value for the cosmological constant that is independent of the Supernova type Ia results.

Unlike many other tests of cosmology, cosmic shear surveys with photometric redshift information, discussed in section 4.1, can constrain cosmological quintessence models and the equation of state parameter w, equation 1.7, which will be key to our understanding of dark energy (Heavens 2003; Refregier et al. 2003; Benabed & Van Waerbeke 2003; Jain & Taylor 2003). With the increased image resolution available from multi-colour space-based lensing surveys it will also be possible to construct high-resolution projected dark matter maps, and 3D dark matter maps of mass concentrations with mass $M > 1 \times 10^{13} M_\odot$ (Taylor 2001; Hu & Keeton 2002; Bacon & Taylor 2003; Massey et al. 2003a). With future deeper and wider multi-colour surveys, for example the Canada-France-Hawaii Telescope Legacy Survey[7] (CFHTLS), and the space-based SuperNova/Acceleration Probe[8] (SNAP), weak gravitational lensing will soon reach its 'era of high precision cosmology', provided it can get a good handle on the many causes of systematic errors that arise when trying to detect this minute weak lensing signal.

1.4.1 Normalisation of the matter power spectrum: σ_8

Measurements of weak gravitational lensing can be directly related to the amplitude of the matter power spectrum σ_8 and the matter density parameter Ω_m. The shape of the matter power spectrum to first order, is fairly well agreed upon, but its normalisation, A in equation 1.35, quantified by σ_8, is one of the few cosmological parameters that is not yet 'concordant'. σ_8 is defined to be the root mean square matter density variation averaged over $8h^{-1}$ Mpc spheres such that

$$\sigma_8{}^2 = \int_0^\infty \frac{3}{k(kR)^3} \left[\sin(kR) + kR\cos(kR)\right] \Delta^2(k)\, dk\,, \tag{1.42}$$

[7] *www.cfht.hawaii.edu/Science/CFHTLS*
[8] *snap.lbl.gov*

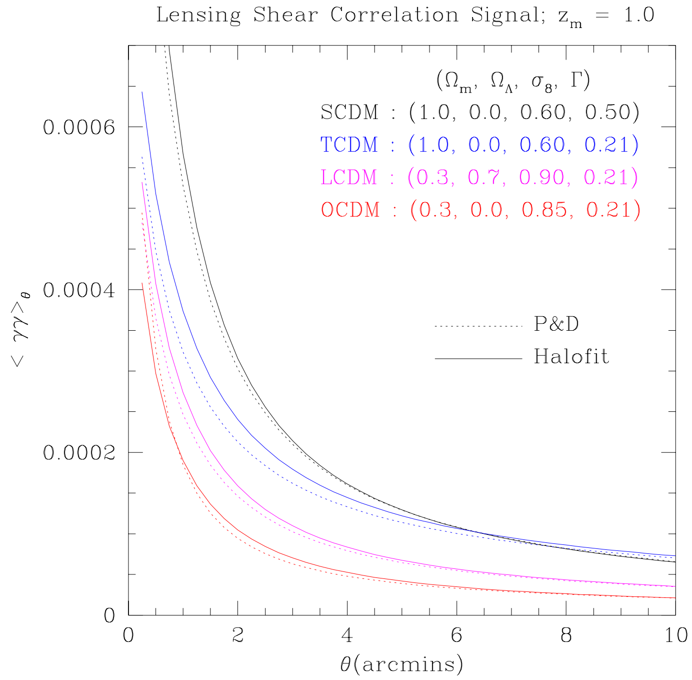

Figure 1.7: The shear correlation function $\langle\gamma\gamma^*\rangle$ for different cosmological models, using the Peacock & Dodds (1996) (dashed) and 'halofit' (Smith et al. 2003), (solid) non-linearity corrections.

where $R = 8h^{-1}$ Mpc. For cold dark matter power spectra, σ_8 measures the power at an effective wavenumber $k_{\rm eff}$,

$$\sigma_8^2 = \Delta^2(k_{\rm eff}), \tag{1.43}$$

which is well approximated by (Peacock 1999),

$$k_{\rm eff}/\,h\mathrm{Mpc}^{-1} = 0.172 + 0.011\,[\ln(\Gamma/0.34)]^2\,. \tag{1.44}$$

Attempts to measure σ_8 from the matter power spectrum result in a degeneracy with the matter density parameter Ω_m. With more matter from a higher Ω_m, the amplitude of the power spectrum at large k increases, which would also result from a higher σ_8 normalisation. Taking $\Omega_m = 0.3$, measurements of cluster abundance find $\sigma_8 = 0.6$ (Seljak 2002), WMAP combined with 2dF measurements find $\sigma_8 = 0.84$ (Spergel et al. 2003), and measurements of cosmic shear find σ_8 varying from $0.7-1.0$ (see table 4.1 and Van Waerbeke & Mellier (2003) for review). The discrepancy between different weak lensing results could be caused by the many sources of systematic error in weak lensing measurement which will be discussed at length throughout this thesis. One cause that could be more fundamental than measurement

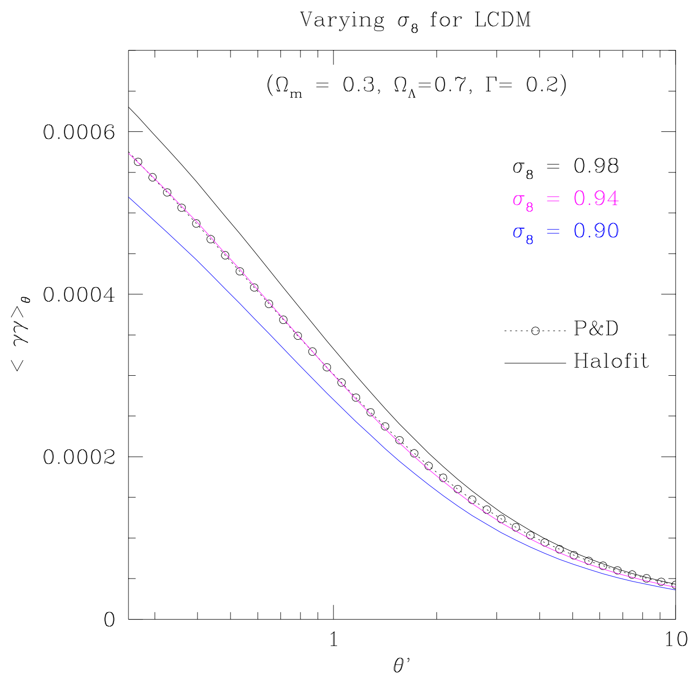

Figure 1.8: The shear correlation function for ΛCDM model with different values of σ_8. A $\sigma_8 = 0.98$ Peacock & Dodds (1996) ΛCDM model (dashed) matches a $\sigma_8 = 0.94$ 'halofit' ΛCDM model (Smith et al. 2003) (pink).

errors however is the use of differing non-linearity corrections, section 1.2.2, and transfer functions, equation 1.33. Figure 1.7 shows the weak lensing shear correlation function statistic $\langle\gamma\gamma^*\rangle$ detailed in section 2.5.1, for four different cosmologies using the Peacock & Dodds (1996) fitting formula equation 1.38 (dotted), and the Smith et al. (2003) fitting formula equation 1.41 (solid). For a ΛCDM cosmology, figure 1.8 shows that if measured weak lensing data points were the circles, using the Peacock & Dodds (1996) formula would yield parameter estimates of $\sigma_8 = 0.98$ whereas using the Smith et al. (2003) formula would yield $\sigma_8 = 0.94$. As weak lensing is one of the few probes of the non-linear end of the power spectrum, this sort of fundamental problem will limit the fine accuracy that weak lensing measurements can achieve. It can be thought of conversely however. With the CMB, SuperNova Ia, and other large scale structure experiments pinning down cosmological parameters to a high degree of accuracy, the role of weak lensing is changing, using parameters essentially known from other experiments to explore the non-linear end of the matter power spectrum.

This thesis is organised as follows. In the next chapter we will review gravitational lens theory and its application to weak lensing by large scale structure or cosmic shear, detailing the two-point statistics which can be used to relate cosmic shear to cosmological parameters. We will then, in chapter 3, review methods used to measure cosmic shear and present our new model fitting technique, which we apply to observations of the Chandra deep field from the COMBO-17 survey. In chapter 4 the results of a feasibility study of the Oxford Dartmouth Thirty degree survey for use as a cosmic shear survey are presented. Chapter 5 discusses the potential contamination to all weak lensing studies from the intrinsic alignment of nearby galaxies, reviewing different theoretical estimates to the severity of this contaminating effect and presenting a new theoretical estimate from numerical simulations. In chapter 6 a new technique to remove the systematic errors in weak lensing measurements caused by intrinsic galaxy alignments is presented. This technique is applied to the COMBO-17 survey in chapter 7, producing new observational constraints for models of intrinsic galaxy alignments, which we use to update the COMBO-17 constraints in the $\Omega_m - \sigma_8$ plane. Future prospects for weak lensing studies and the main conclusions of this thesis are discussed in chapter 8.

2

Gravitational lens theory

Gravitational lensing is the phenomenon whereby a ray of light experiences a curvature of its path, when passing through a gravitational field from nearby mass concentrations. This can be rigorously described from Einstein's theory of relativity, whereby the light propagates along null geodesics, as described by the perturbed space time Robertson-Walker metric. In most astrophysical situations however a more simple approximate description, called gravitational lens theory, is permitted. In this chapter we will derive some of the basics of gravitational lens theory, which we will then build upon in the weak lensing regime.

2.1 The Lens equation

Figure 2.1 sketches a typical gravitational lensing system where the thin lens at distance $\mathrm{D_d}$ from the observer, perturbs the path of a light ray from a luminous source at distance $\mathrm{D_s}$ from the observer, where the distance between the lens plane and source plane is $\mathrm{D_{ds}}$, and all distances are angular diameter distances. In the absence of the lens, the observer would see the source at position $\boldsymbol{\beta}$. Instead, the lens deflection by angle $\hat{\boldsymbol{\alpha}}$, causes the observer to see the source image at position $\boldsymbol{\theta}$, where all angles, in typical lensing situations, are very small. From figure 2.1 we see

$$\boldsymbol{\theta}\mathrm{D_s} = \boldsymbol{\beta}\mathrm{D_s} + \hat{\boldsymbol{\alpha}}\mathrm{D_{ds}}. \tag{2.1}$$

Defining the reduced deflection angle $\boldsymbol{\alpha} = \hat{\boldsymbol{\alpha}}\,\mathrm{D_{ds}}/\mathrm{D_s}$, the lens equation is given by

$$\boldsymbol{\beta} = \boldsymbol{\theta} - \boldsymbol{\alpha}. \tag{2.2}$$

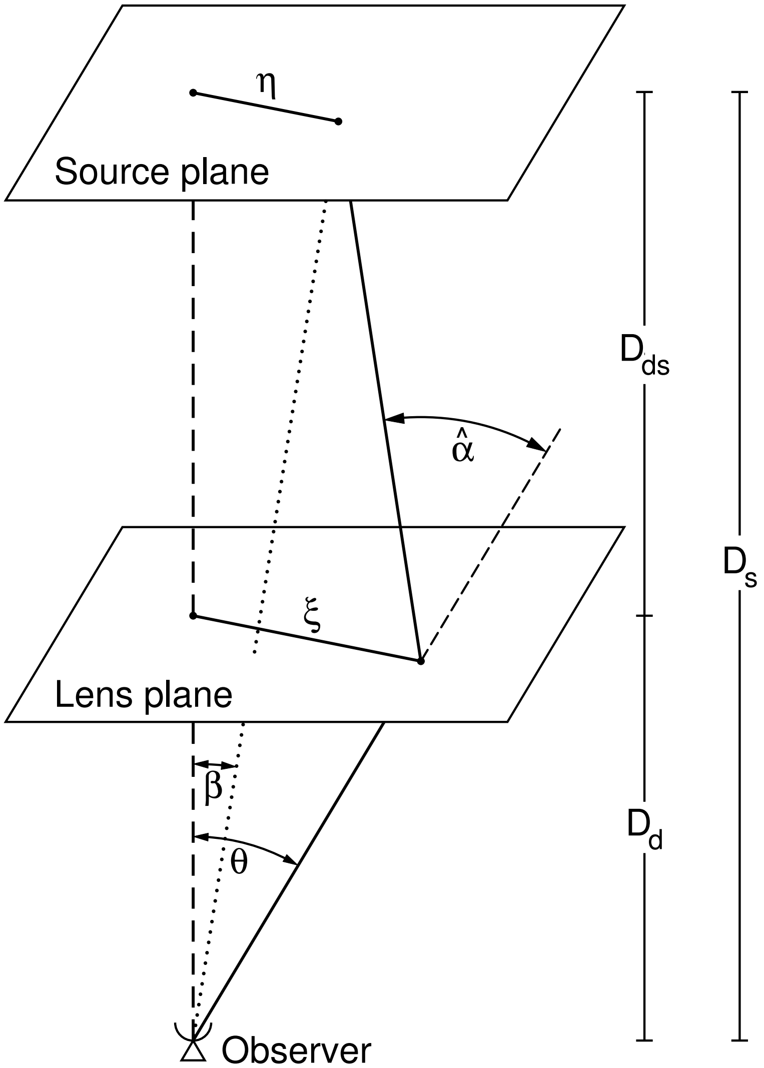

Figure 2.1: Sketch of a typical gravitational lensing system, taken from Bartelmann & Schneider 2001.

2.1.1 The deflection angle α

From Einstein's theory of General Relativity, it can be shown that a light ray passing within distance ξ of a point mass gravitational lens of mass M, is deflected by an angle $\hat{\alpha}$ given by

$$\hat{\alpha} = \frac{4GM}{c^2\,\xi}, \tag{2.3}$$

for impact parameters $\xi \gg R_{\rm S} \equiv 2GM\,c^{-2}$. For a mass distribution $\rho(\mathbf{r})$, if the gravitational field is weak, then we can approximate the deflection angle produced by the total mass distribution, as the sum of deflection angles produced by a series of point masses. We can divide our mass distribution in cells of volume dV, with each cell acting as a point mass lens, with mass $dm = \rho(\mathbf{r})dV$. A light ray propagating along the z axis with position $(\boldsymbol{\xi}, z)$ where $\boldsymbol{\xi}$ is a two dimensional vector in the lens plane, is allowed to pass through the mass distribution. At the mass element dm with position $(\boldsymbol{\xi}', z')$, the light ray has impact parameter $\boldsymbol{\xi} - \boldsymbol{\xi}'$, if we assume that the deflected light ray can be approximated as a straight line in the neighbourhood of the deflecting mass. This assumption corresponds to the Born approximation in atomic and nuclear physics and is valid as long as the deviation of the actual light ray from a straight line within the mass distribution is small compared to the scale on which the mass distribution changes significantly[1]. The total deflection angle is the sum of each small deflection

$$\begin{aligned} \hat{\boldsymbol{\alpha}}(\boldsymbol{\xi}) &= \frac{4G}{c^2} \sum dm(\xi_1', \xi_2', z')\, \frac{\boldsymbol{\xi} - \boldsymbol{\xi}'}{|\boldsymbol{\xi} - \boldsymbol{\xi}'|^2} \\ &= \frac{4G}{c^2} \int d^2\xi' \int dz'\, \rho(\xi_1', \xi_2', z')\, \frac{\boldsymbol{\xi} - \boldsymbol{\xi}'}{|\boldsymbol{\xi} - \boldsymbol{\xi}'|^2}. \end{aligned} \tag{2.4}$$

Defining the surface mass density of the lens plane

$$\Sigma(\boldsymbol{\xi}) \equiv \int dz\, \rho(\xi_1, \xi_2, z), \tag{2.5}$$

we find the two dimensional vector of the deflection angle

$$\hat{\boldsymbol{\alpha}}(\boldsymbol{\xi}) = \frac{4G}{c^2} \int d^2\xi' \Sigma(\boldsymbol{\xi}') \frac{\boldsymbol{\xi} - \boldsymbol{\xi}'}{|\boldsymbol{\xi} - \boldsymbol{\xi}'|^2}. \tag{2.6}$$

[1]For weak gravitational lensing by large scale structure, the Born approximation has been shown to give quite accurate results in ray-tracing simulations (Bernardeau, Van Waerbeke & Mellier 1997; Schneider et al. 1998; Van Waerbeke et al. 2002). The effect of using this approximation is however expected to become important in any high order statistics. Note that in this thesis we will only consider second order statistics.

In the special case of a circularly symmetric lens with constant surface mass density Σ, the deflection angle at impact radius r is given by

$$\hat{\alpha}(r) = \frac{4G}{c^2 r}(\Sigma \pi r^2). \tag{2.7}$$

Rewriting in terms of the reduced deflection angle and the lens parameters defined in section 2.1, $r = \mathrm{D_d}\,\theta$ and

$$\alpha(\theta) = \frac{\Sigma}{\Sigma_{\mathrm{cr}}}\,\theta, \tag{2.8}$$

where Σ_{cr} is the critical surface mass density of the lens defined to be

$$\Sigma_{\mathrm{cr}} = \frac{c^2}{4\pi G}\frac{\mathrm{D_s}}{\mathrm{D_d}\,\mathrm{D_{ds}}}. \tag{2.9}$$

For $\Sigma = \Sigma_{\mathrm{cr}}$, $\alpha = \theta$, and we see an Einstein ring.

For a more general case we now define the dimensionless surface mass density, or convergence κ,

$$\kappa(\boldsymbol{\theta}) = \frac{\Sigma(\mathrm{D_d}\,\boldsymbol{\theta})}{\Sigma_{\mathrm{cr}}}. \tag{2.10}$$

A mass distribution which has $\kappa \geq 1$ at some $\boldsymbol{\theta}$, will produce multiple images for some source positions, as we observe in cases of strong gravitational lensing. κ therefore distinguishes between the strong lensing regime ($\kappa \geq 1$) and weak lensing regime ($\kappa \ll 1$). The scaled deflection angle in terms of the convergence κ is given by

$$\boldsymbol{\alpha}(\boldsymbol{\theta}) = \frac{1}{\pi}\int d^2\theta'\,\kappa(\boldsymbol{\theta'})\,\frac{\boldsymbol{\theta}-\boldsymbol{\theta'}}{|\boldsymbol{\theta}-\boldsymbol{\theta'}|^2}. \tag{2.11}$$

Noting the identity $\nabla \ln \boldsymbol{x} = \boldsymbol{x}/|\boldsymbol{x}^2|$, we can define the deflection angle $\boldsymbol{\alpha}$ as the gradient of a deflection potential or lensing potential ψ, which will simply be the two-dimensional analogue of the projected Newtonian potential Φ of the lens.

$$\psi(\boldsymbol{\theta}) = \frac{1}{\pi}\int d^2\theta'\,\kappa(\boldsymbol{\theta'})\,\ln|\boldsymbol{\theta}-\boldsymbol{\theta'}|. \tag{2.12}$$

such that

$$\boldsymbol{\alpha}(\boldsymbol{\theta}) = \nabla_\theta \psi(\boldsymbol{\theta}). \tag{2.13}$$

The inverse 2D Laplacian operator δ^{-2}, is defined by

$$\delta^{-2} = \int d^2\theta'\,\ln|\boldsymbol{\theta}-\boldsymbol{\theta'}|. \tag{2.14}$$

Hence

$$\begin{aligned}\boldsymbol{\kappa}(\boldsymbol{\theta}) &= \frac{1}{2}\nabla_\theta^2\psi(\boldsymbol{\theta}) \\ &= \frac{1}{2}(\psi_{,11} + \psi_{,22}),\end{aligned} \tag{2.15}$$

and therefore the convergence is related to the deflection angle by

$$\kappa(\boldsymbol{\theta}) = \frac{1}{2}\,\nabla_\theta \cdot \alpha(\boldsymbol{\theta}). \tag{2.16}$$

2.1.2 The effective lensing potential

The deflection angle can also be determined by considering the line integral of the gravitational acceleration perpendicular to the light path $a_\perp$.

$$\hat{\boldsymbol{\alpha}} = \frac{2}{c^2}\int a_\perp dz, \tag{2.17}$$

where acceleration is caused by the gravitational potential of the lens Φ such that $a_\perp = \nabla_\perp \Phi$, and hence

$$\hat{\boldsymbol{\alpha}} = \frac{2}{c^2}\int \nabla_\perp \Phi dz. \tag{2.18}$$

The lensing potential has been defined such that

$$\boldsymbol{\alpha}(\boldsymbol{\theta}) = \nabla_\theta \psi(\boldsymbol{\theta}) = \mathrm{D_d}\nabla_\xi \psi, \tag{2.19}$$

where as before $\boldsymbol{\xi} = D_d\boldsymbol{\theta}$. Therefore the effective lensing potential is given by

$$\psi = \frac{\mathrm{D_{ds}}}{\mathrm{D_d D_s}}\frac{2}{c^2}\int \Phi(\boldsymbol{\xi}, z)dz. \tag{2.20}$$

The Laplacian of the lensing potential is directly related to the convergence of the lens, equation 2.15, which can be shown again, using Poisson's equation $\nabla_\xi^2\Phi = 4\pi G\rho(\boldsymbol{\xi}, z)$ such that

$$\begin{aligned}\nabla_\theta^2\psi &= \frac{\mathrm{D_d D_{ds}}}{\mathrm{D_s}}\frac{2}{c^2}\int \nabla_\xi^2\Phi \\ &= 2\frac{\Sigma(\mathrm{D_d}\,\boldsymbol{\theta})}{\Sigma_{\mathrm{cr}}} = 2\boldsymbol{\kappa}(\boldsymbol{\theta}).\end{aligned} \tag{2.21}$$

2.2 Magnification and distortion

The absence of any photon emission or absorption process in gravitational lensing, combined with Liouville's theorem, implies that lensing conserves surface brightness (Kristian & Sachs

1966). Therefore if gravitational lensing increases the area of an image we will see magnification μ where

$$\mu = \frac{\text{image area}}{\text{source area}} = \frac{\delta\theta^2}{\delta\beta^2}, \tag{2.22}$$

for an element of source $\delta\beta^2$ mapped onto an area of image $\delta\theta^2$. Note that lensing effectively focuses the light from a source. For a lensed source we receive photons that we would have detected in the absence of the lens, plus additional photons on previously nearby trajectories that are now bent into the detector by the lens.

If the source is much smaller than the angular scale on which the lens properties change, then the lens mapping is described by the lensing Jacobian

$$\begin{aligned} A_{ij} &= \frac{\delta\beta_i}{\delta\theta_j} = \frac{\delta}{\delta\theta_j}[\theta_i - \alpha_i(\boldsymbol{\theta})] \\ &= \delta_{ij} - \frac{\delta\alpha_i(\boldsymbol{\theta})}{\delta\theta_j} \\ &= \delta_{ij} - \frac{\delta^2\psi(\boldsymbol{\theta})}{\delta\theta_i\,\delta\theta_j} \end{aligned} \tag{2.23}$$

$$A = \begin{pmatrix} 1-\kappa-\gamma_1 & -\gamma_2 \\ -\gamma_2 & 1-\kappa+\gamma_1 \end{pmatrix}, \tag{2.24}$$

where we have used equations 2.13 and 2.15 and introduced the complex shear of magnitude γ and orientation ϕ, as given by

$$\gamma = \gamma_1 + i\gamma_2 = e^{2i\phi}, \tag{2.25}$$

where

$$\begin{aligned} \gamma_1 = \frac{1}{2}(\psi_{,11} - \psi_{,22}) &= \gamma\cos(2\phi), \\ \gamma_2 = \psi_{,12} = \psi_{,21} &= \gamma\sin(2\phi). \end{aligned} \tag{2.26}$$

The magnification is given by the determinant of the inverse of A $= 1/\det[A]$,

$$\mu = \frac{1}{(1-\kappa)^2 - \gamma^2}. \tag{2.27}$$

For a flux limited galaxy sample, magnification from the effect of weak gravitational lensing by large scale structure, will increase the number density of galaxy images, as tentatively detected by Gaztanaga (2003). This magnification aspect of weak lensing by large scale structure is still however in its infancy, in terms of intensive observations.

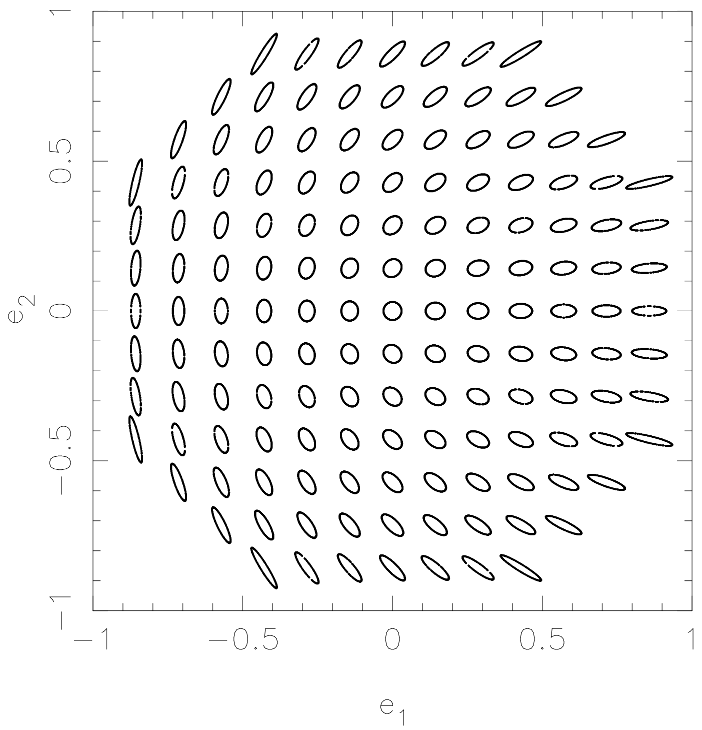

Figure 2.2: Ellipticity parameters for a series of ellipses.

We will now define the reduced shear

$$g(\boldsymbol{\theta}) = \frac{\gamma(\boldsymbol{\theta})}{1-\kappa(\boldsymbol{\theta})}, \tag{2.28}$$

such that

$$A = (1-\kappa)\begin{pmatrix} 1-g_1 & -g_2 \\ -g_2 & 1+g_1 \end{pmatrix}, \tag{2.29}$$

showing the convergence κ only effects the size of the image and hence its magnification, whereas the shear is responsible for image distortions effecting the shape or ellipticity of the image.

2.3 Observables

We have now formally derived the relationships between convergence, κ, shear, γ and the lensing potential ψ and will now relate these quantities to something we can determine observationally: the shape or ellipticity of lensed galaxies. As shown by equation 2.29, from this information we will only be able to extract information about the reduced shear g.

Consider an isolated galaxy with surface brightness $I(\boldsymbol{\theta})$ which we have centred at the origin such that $I(\boldsymbol{\theta}=0) = I_0$. We can measure the quadrupole moment Q_{ij} of this galaxy such that

$$Q_{ij} = \frac{\int d^2\theta \, w[I(\boldsymbol{\theta})] \, I(\boldsymbol{\theta}) \, \theta_i \theta_j}{\int d^2\theta \, w[I(\boldsymbol{\theta})] \, I(\boldsymbol{\theta})}, \tag{2.30}$$

where $w[I(\boldsymbol{\theta})]$ is a weighting function such as a Heaviside step function. We define the complex ellipticity $e = e_1 + ie_2$ where

$$\begin{pmatrix} e_1 \\ e_2 \end{pmatrix} = \frac{1}{Q_{11} + Q_{22}} \begin{pmatrix} Q_{11} - Q_{22} \\ 2Q_{12} \end{pmatrix}. \tag{2.31}$$

For a perfect ellipse, the ellipticity parameters are related to the axial ratio β at position angle ϕ, measured counter-clockwise from the x axis such that

$$\begin{pmatrix} e_1 \\ e_2 \end{pmatrix} = \frac{\beta^2 - 1}{\beta^2 + 1} \begin{pmatrix} \cos 2\phi \\ \sin 2\phi \end{pmatrix}, \tag{2.32}$$

as shown in figure 2.2. Relating the ellipticity of the image to the ellipticity of the source, in order to measure the distortion induced by lensing, we transform the image quadrupole moment using the lensing Jacobian such that

$$Q^s_{ij} = A_{il} Q_{lm} A_{mj}. \tag{2.33}$$

The complex ellipticity of the source e^s is then given by

$$e^s = \frac{e - 2g + g^2 e^*}{1 + |g|^2 - 2\Re(ge^*)}, \tag{2.34}$$

(Schneider & Seitz 1995), where e^* is the complex conjugate of e. In the weak lensing regime, $\kappa \ll 1$ and $|\gamma| \ll 1$. The reduced shear is therefore approximately equivalent to the shear, $|g| \sim |\gamma|$, and $g^2 \approx 0$. Equation 2.34 in the weak lensing regime therefore reduces to a linear relationship[2]

$$e_i = e^s_i + 2(\delta_{ij} - e^s_i e_j)\gamma_j. \tag{2.35}$$

If the intrinsic ellipticity distribution of the sources is random, which is a fairly good assumption, then with many galaxy images $\langle e^s \rangle = 0$. Hence, averaging over many sources where the shear is constant, noting that for parity reasons[3] $\langle e_1 e_2 \rangle = 0$, we find

$$\langle e_i \rangle = 2(1 - \langle e^s_i e_i \rangle)\gamma_i. \tag{2.36}$$

[2]This linear approximation has been shown by Barber (2002) to cause negligible effects for sources at redshift $z < 1$, and for angular scales in weak lensing analysis $\theta > 5'$. For smaller scales, effects at the level of a few percent could be detected. Use of the full non-linear lensing equation should not present any theoretical or technical difficulties, and should be used for future high precision surveys.

[3]In a left handed co-ordinate system (i.e $x \to -x$, $y \to y$), e_1 remains unchanged but e_2 changes sign. Hence any correlation between e_1 and e_2 must yield a zero result.

For weak lensing distortions $\langle e_i^s e_i \rangle \approx \langle e_i^2 \rangle$ which can be estimated from the ellipticity dispersion in large data sets as $\langle e_1^2 \rangle \approx \langle e_2^2 \rangle = \sigma_e^2$.

In the special case where all the undistorted sources are circular $e^s = 0$, $\langle e_i e_i^s \rangle = 0$ and we arrive at the most often quoted relationship between ellipticity and shear,

$$\gamma \simeq \frac{1}{2}\langle e \rangle \equiv \frac{1}{2}\langle e_1 + ie_2 \rangle \, , \tag{2.37}$$

which we will use for simplicity in later chapters on intrinsic galaxy alignments.

2.4 Application to weak gravitational lensing by large scale structure

This section is an easy-every-step-guide to the theory behind weak lensing gravitational lensing by large scale structure following in part the prescription of Bartelmann & Schneider (2001). It will use some of the key results from gravitational lens theory detailed in previous sections, but will differ somewhat, as we can no longer assume that the deflection of light rays by gravitational lensing is small compared to the scale on which the lens mass distribution changes. For weak lensing by large scale structure, the mass extends all the way from the source to the observer.

2.4.1 The Correlation Function and Power Spectrum

We will start simply by defining two statistics that will be used throughout this thesis: the correlation function $C(r)$ and power spectrum $P(k)$ of a homogeneous and isotropic random field $g(\mathbf{x})$, such as the matter density field predicted from theories of structure formation, discussed in section 1.2. We will also derive the relationship between them.

Statistically $g(\mathbf{x})$ cannot, by definition, depend on orientation or position in the field. The two-point correlation function of such a field, $\langle g(\mathbf{x}) g^*(\mathbf{x}') \rangle$ can therefore only depend on $r = |\mathbf{x} - \mathbf{x}'|$, the absolute separation between any two points in the field such that

$$\langle g(\mathbf{x}) g^*(\mathbf{x}') \rangle = C(r). \tag{2.38}$$

We define the Fourier transform pair of g in n dimensions,

$$\hat{g}(\mathbf{k}) = \int d^n x g(\mathbf{x}) \mathrm{e}^{i\mathbf{x}\cdot\mathbf{k}} \quad g(\mathbf{x}) = \tfrac{1}{(2\pi)^n} \int d^n k \hat{g}(\mathbf{k}) \mathrm{e}^{-i\mathbf{x}\cdot\mathbf{k}}. \tag{2.39}$$

and the correlation function in Fourier space,

$$\langle \hat{g}(\mathbf{k})\hat{g}^*(\mathbf{k}')\rangle = \int d^n x\, \mathrm{e}^{i\mathbf{x}\cdot\mathbf{k}} \int d^n x'\, \mathrm{e}^{-i\mathbf{x}'\cdot\mathbf{k}'} \langle g(\mathbf{x})\, g^*(\mathbf{x}')\rangle. \tag{2.40}$$

As $\mathbf{x}'$ is independent of $\mathbf{x}$, $d^n x' = d^n r$ and the above becomes:

$$\langle \hat{g}(\mathbf{k})\hat{g}^*(\mathbf{k}')\rangle = \int d^n x\, \mathrm{e}^{i\mathbf{x}\cdot(\mathbf{k}-\mathbf{k}')} \int d^n r\, \mathrm{e}^{-i\mathbf{r}\cdot\mathbf{k}'} C(r). \tag{2.41}$$

Let $f(\mathbf{k}) = \delta_D(\mathbf{k}-\mathbf{k}')$, where δ_D is the Dirac delta function which has the inverse Fourier transform

$$f(\mathbf{x}) = \frac{1}{(2\pi)^n} \int d^n k \delta(\mathbf{k}-\mathbf{k}')\mathrm{e}^{-i\mathbf{x}\cdot\mathbf{k}} = \frac{1}{(2\pi)^n}\mathrm{e}^{-i\mathbf{x}\cdot\mathbf{k}'}. \tag{2.42}$$

To simplify equation 2.41 we can therefore write

$$\delta_D(\mathbf{k}-\mathbf{k}') = \frac{1}{(2\pi)^n} \int d^n x \mathrm{e}^{i\mathbf{x}\cdot(\mathbf{k}-\mathbf{k}')}, \tag{2.43}$$

and hence

$$\begin{aligned} \langle \hat{g}(\mathbf{k})\hat{g}^*(\mathbf{k}')\rangle &= (2\pi)^n \delta_D(\mathbf{k}-\mathbf{k}') \int d^n r\, \mathrm{e}^{-i\mathbf{r}\cdot\mathbf{k}'} C(|\mathbf{r}|) && (2.44)\\ &= (2\pi)^n \delta_D(\mathbf{k}-\mathbf{k}') P(|\mathbf{k}'|), && (2.45) \end{aligned}$$

where we have defined the power spectrum of the homogeneous isotropic random field g, $P(|\mathbf{k}|)$, to be the Fourier transform of the two-point correlation function $C(|\mathbf{r}|)$.

$$P(|\mathbf{k}|) = \int d^n r\ \mathrm{e}^{-i\mathbf{r}\cdot\mathbf{k}}\ C(|\mathbf{r}|). \tag{2.46}$$

2.4.2 Light deflection, α

In unperturbed Minkowski space the propagation equation for a pair of light rays can be written:

$$\frac{d^2\mathbf{x}}{dw^2} + K\,\mathbf{x} = 0, \tag{2.47}$$

where $\mathbf{x}$ is the comoving separation vector between a fiducial light ray and a closely neighbouring light ray, w is the radial distance from the observer and K is the space-time curvature of the universe. According to the boundary conditions that the fiducial ray starting at the observer $w = 0$, has zero separation from its neighbour $\mathbf{x} = 0$, which propagates at an angle $\boldsymbol{\theta}$ such that $\frac{d\mathbf{x}}{dw} = \boldsymbol{\theta}$, the solution for the comoving separation vector between unperturbed light rays is given by

$$\mathbf{x}(\boldsymbol{\theta}, w) = f_K(w)\,\boldsymbol{\theta}, \tag{2.48}$$

where $f_K(w)$ is the comoving angular diameter distance out to radial distance w defined by the curvature K and given in equation 1.2.

The presence of density perturbations, i.e. mass, causes the deflection of light rays according to

$$\frac{d^2\mathbf{x}}{dw^2} = -\frac{2}{c^2}\nabla_\perp\Phi, \tag{2.49}$$

where Φ is the Newtonian potential of a localised density perturbation, (cf. equation 2.18). The solution to the combined perturbed propagation equation, the comoving separation between two light rays travelling through weakly perturbed Minkowski space, is given by

$$\mathbf{x}(\boldsymbol{\theta}, w) = f_K(w)\boldsymbol{\theta} - \frac{2}{c^2}\int_0^w dw'\, f_K(w-w')\,\nabla_\perp\Phi[\mathbf{x}(\boldsymbol{\theta}, w'), w']. \tag{2.50}$$

To calculate the net deflection we simply subtract the perturbed solution from the unperturbed solution, such that

$$f_K(w)\alpha(\boldsymbol{\theta}, w) = f_K(w)\boldsymbol{\theta} - \mathbf{x}(\boldsymbol{\theta}, w), \tag{2.51}$$

and

$$\alpha(\boldsymbol{\theta}, w) = \frac{2}{c^2}\int_0^w dw'\, \frac{f_K(w-w')}{f_K(w)}\,\nabla_\perp\Phi[f_K(w')\boldsymbol{\theta}, w']. \tag{2.52}$$

2.4.3 Convergence, κ

In section 2.1.2 we used a thin lens model to relate the convergence κ, which is the dimensionless surface mass density of the lens, to the angle of deflection α, experienced by light ray. For cosmological weak lensing, we will use the same relationship to define an effective convergence κ_{eff} such that

$$\begin{aligned} \kappa_{\text{eff}}(\boldsymbol{\theta}, w) &= \frac{1}{2}\nabla_\theta \cdot \alpha(\boldsymbol{\theta}, w) \\ &= \frac{1}{c^2}\int_0^w dw'\, \frac{f_K(w-w')f_K(w')}{f_K(w)}\,\frac{\partial^2}{\partial x_i \partial x_i}\Phi[f_K(w')\boldsymbol{\theta}, w'], \end{aligned} \tag{2.53}$$

where the additional $f_K(w')$ comes from $x(w') = f_k(w')\theta$, $\partial/\partial\theta = f_k(w')\partial/\partial x$.

Poisson's equation relates the total Newtonian potential Φ' to the total matter density $\rho = (1+\delta)\bar{\rho}$ where δ is the density fluctuation field.

$$\nabla_\xi^2\Phi' = 4\pi G\rho. \tag{2.54}$$

As this equation is linear we can subtract off the smooth background $\nabla_\xi^2\bar{\Phi} = 4\pi G\bar{\rho}$ leaving the potential of the perturbations. Introducing the gradient with respect to comoving co-ordinates $\nabla_x = a\nabla_\xi$, where a is the scale factor equation 1.20, we can write

$$\nabla_x^2\Phi = 4\pi G a^2 \bar{\rho}\delta. \tag{2.55}$$

In the matter dominated epoch, from equation 1.9, $\bar{\rho} = a^{-3}\bar{\rho}_0$, and hence

$$\nabla_x^2\Phi = \frac{3H_0^2\Omega_m}{2a}\,\delta, \tag{2.56}$$

where we have included the matter density parameter Ω_m from equation 1.15. Using this form of Poisson's equation we find that the effective convergence is just a weighted integral over the density fluctuations along the unperturbed light path.

$$\kappa_{\text{eff}}(\boldsymbol{\theta}, w) = \frac{3H_0^2\Omega_m}{2c^2}\int_0^w dw'\,\frac{f_K(w-w')f_K(w')}{f_K(w)}\,\frac{\delta[f_K(w')\boldsymbol{\theta}, w']}{a(w')}. \tag{2.57}$$

The 2D convergence $\bar{\kappa}_{\text{eff}}$, projected along the line of sight, is simply the averaged 3D convergence integrated over a normalised source redshift distribution $\phi(w)$ out to the horizon distance, w_H.

$$\begin{aligned}
\bar{\kappa}_{\text{eff}}(\boldsymbol{\theta}) &= \int_0^{w_H} dw'\,\phi(w')\kappa_{\text{eff}}(\boldsymbol{\theta}, w') \\
&= \frac{3H_0^2\Omega_m}{2c^2}\int_0^{w_H} dw'\,\phi(w')\int_0^{w'} dw\,\frac{f_K(w'-w)f_K(w)}{f_K(w')}\,\frac{\delta[f_K(w)\boldsymbol{\theta}, w]}{a(w)} \\
&= \frac{3H_0^2\Omega_m}{2c^2}\int_0^{w_H} dw\,g(w)f_K(w)\,\frac{\delta[f_K(w)\boldsymbol{\theta}, w]}{a(w)},
\end{aligned} \tag{2.58}$$

where the weighting function $g(w)$

$$g(w) = \int_w^{w_H} dw'\,\phi(w')\frac{f_K(w'-w)}{f_K(w')}. \tag{2.59}$$

2.4.4 The Effective Convergence Power Spectrum, P_κ

All two point statistics of weak gravitational lensing can be expressed in terms of the effective convergence power spectrum P_κ, which we will now prove is directly related to the power spectrum of the mass fluctuations, P_δ. From equation 2.46, P_κ is the Fourier transform of the 2D effective convergence two-point correlation function, $C_{12} = \langle\bar{\kappa}_{\text{eff}\,1}(\boldsymbol{\theta})\bar{\kappa}_{\text{eff}\,2}(\boldsymbol{\theta}')\rangle$, where $\bar{\kappa}_{\text{eff}}$ is the projection of the density fluctuations δ along the line of sight, equation 2.58, weighted by say $q(w)$,

$$\bar{\kappa}_{\text{eff}}(\boldsymbol{\theta}) = \int_0^{w_H} q(w)\delta[f_K(w)\boldsymbol{\theta}, w], \tag{2.60}$$

where $q(w) = \frac{3H_0^2\Omega_m}{2c^2}\, g(w) f_K(w)/a(w)$.

$$C_{12}(\theta) = \int dw\, q_1(w) \int dw'\, q_2(w')\, \langle \delta[f_K(w)\boldsymbol{\theta}, w]\, \delta[f_K(w')\boldsymbol{\theta}', w']\rangle. \tag{2.61}$$

The density fluctuation field $\delta[f_K(w)\boldsymbol{\theta}, w]$ is a 3D random homogeneous isotropic field, where we will assume negligible evolution of the fluctuations over the light-crossing time of the correlation scale. Therefore we can use equation 2.45 to define the power spectrum of the mass fluctuations P_δ as a function of the mass fluctuations δ.

$$\langle \hat{\delta}(\mathbf{k}, w)\hat{\delta}^*(\mathbf{k}', w')\rangle = (2\pi)^3 \delta_D(\mathbf{k} - \mathbf{k}') P_\delta(|\mathbf{k}|, w), \tag{2.62}$$

C_{12} can be written in terms of $\langle \hat{\delta}(\mathbf{k}, w)\hat{\delta}^*(\mathbf{k}', w')\rangle$.

$$\begin{aligned} C_{12}(\theta) &= \int dw\, q_1(w) \int dw'\, q_2(w') \int \frac{d^3k}{(2\pi)^3} \int \frac{d^3k'}{(2\pi)^3} \\ &\quad \langle \delta[\mathbf{k}, w]\, \delta^*[\mathbf{k}', w']\rangle\, \mathrm{e}^{-if_K(w)\mathbf{k}_\perp\cdot\boldsymbol{\theta}}\, \mathrm{e}^{if_K(w')\mathbf{k}'_\perp\cdot\boldsymbol{\theta}'}\, \mathrm{e}^{-ik_3w}\, \mathrm{e}^{ik'_3w'} \\ &= \int dw\, q_1(w) \int dw'\, q_2(w') \int \frac{d^3k}{(2\pi)^3} \int d^3k'\, \delta_D(\mathbf{k} - \mathbf{k}') \\ &\quad P_\delta(|\mathbf{k}|, w)\, \mathrm{e}^{-if_K(w)\mathbf{k}_\perp\cdot\boldsymbol{\theta}}\, \mathrm{e}^{if_K(w')\mathbf{k}'_\perp\cdot\boldsymbol{\theta}'}\, \mathrm{e}^{-ik_3w}\mathrm{e}^{ik'_3w'}. \end{aligned} \tag{2.63}$$

We now assume that there is only small scale power in the density fluctuations, producing correlations when $w \approx w'$. We can therefore replace $q(w')$ by $q(w)$ and $f_K(w')$ by $f_K(w)$.

$$C_{12}(\theta) = \int dw\, q_1(w) q_2(w) \int \frac{d^3k}{(2\pi)^3} P_\delta(|\mathbf{k}|, w)\, \mathrm{e}^{-if_K(w)\mathbf{k}_\perp\cdot(\boldsymbol{\theta}-\boldsymbol{\theta}')}\mathrm{e}^{-ik_3w} \int dw'\, \mathrm{e}^{ik_3w'} \tag{2.64}$$

From equation 2.43, $\int dw'\, \mathrm{e}^{ik_3w'} = 2\pi\delta_D(k_3)$. Integrating over k_3, and setting $\boldsymbol{\phi} = \boldsymbol{\theta}' - \boldsymbol{\theta}$ gives us

$$C_{12}(\phi) = \int dw\, q_1(w) q_2(w) \int \frac{d^2k_\perp}{(2\pi)^2} P_\delta(|\mathbf{k}|, w)\, \mathrm{e}^{if_K(w)\,\mathbf{k}_\perp\cdot\boldsymbol{\phi}}. \tag{2.65}$$

Equation 2.46 tells us that the correlation function of the convergence is related to its power spectrum through

$$\begin{aligned} P_\kappa(l) &= \int d^2\phi\, \mathrm{e}^{-i\mathbf{l}\cdot\boldsymbol{\phi}} C_{12}(\phi) \\ &= \int dw\, q_1(w) q_2(w) \int \frac{d^2k_\perp}{(2\pi)^2} P_\delta(|\mathbf{k}|, w) \int d^2\phi\, \mathrm{e}^{if_K(w)\,(\mathbf{k}_\perp - \mathbf{l})\cdot\boldsymbol{\phi}} \\ &= \int dw\, q_1(w) q_2(w) \int \frac{d^2k_\perp}{(2\pi)^2} P_\delta(|\mathbf{k}|, w) (2\pi)^2 \delta_D(f_K(w)\mathbf{k}_\perp - \mathbf{l}) \\ &= \int dw\, \frac{q_1(w)\, q_2(w)}{f_K(w)^2} P_\delta\left(\frac{l}{f_K(w)}, w\right). \end{aligned} \tag{2.66}$$

Putting back in the values for $q(w)$, the effective convergence power spectrum P_κ is hence related to the power spectrum of the mass fluctuations P_δ by

$$P_\kappa(l) = \frac{9H_0^4\Omega_m^2}{4c^4}\int_0^{w_H} dw\, \frac{g^2(w)}{a^2(w)}\, P_\delta\left(\frac{l}{f_K(w)}, w\right) . \tag{2.67}$$

2.5 Weak Lensing Estimators

This section defines the two point weak lensing statistics that can be estimated from weak lensing surveys, using the key result from section 2.3 that in the weak lensing limit, the shear and ellipticity divided by $g = 2(1-\sigma_e^2)$ are interchangeable. Using the tools we have derived in section 2.4, we will show that the two point statistics are functions of the effective convergence power spectrum P_κ, which is directly related to the mass density power spectrum P_δ. From these estimators is is therefore possible to constrain σ_8 and Ω_m for different forms of P_δ.

2.5.1 Shear Correlation: $\langle\gamma\gamma\rangle_\theta$

The shear correlation function can be estimated by correlating measured ellipticities of galaxy pairs at angular separations $\theta \to \theta \pm \Delta\theta$. Ellipticities can be defined in the frame of the observations, e_1 and e_2. Due to the isotropy of the universe, or alternatively the arbitrary choice of CCD orientation we would expect to find $\langle e_1(\mathbf{x})e_1(\mathbf{x}+\boldsymbol{\theta})\rangle = \langle e_2(\mathbf{x})e_2(\mathbf{x}+\boldsymbol{\theta})\rangle$.

$$E[\gamma\gamma(\theta)] = \sum_{\alpha=1}^{2} \frac{\sum_{\text{pairs}} w_{\text{pair}}\, \mathrm{e}_\alpha(\mathbf{x})\, \mathrm{e}_\alpha(\mathbf{x}+\boldsymbol{\theta})}{g^2\, \sum_{\text{pairs}} w_{\text{pair}}}\,, \tag{2.68}$$

where w_{pair} is either the assigned weight for the galaxy pair or the product of the two individual galaxy weights, dependent on the signal to noise of each galaxy detection, and $g = 2(1-\sigma_e^2)$. For parity reasons we expect the cross correlation $\langle e_1(\mathbf{x})e_2(\mathbf{x}+\boldsymbol{\theta})\rangle$ to vanish. With a large number of galaxies we can find a good estimate of the shear correlation function. Typically $E[\gamma\gamma(\theta)]$ is calculated for N_f independent fields and the shear correlation is then given by the average over all fields,

$$C(\theta) = \frac{1}{N_f}\,\Sigma_{f=1}^{N_f} E_f[\gamma\gamma(\theta)]\,, \tag{2.69}$$

where the uncertainty on the estimate is simply the error on the mean given by

$$\sigma^2\left[C(\theta)\right] = \frac{1}{N_f^2}\,\Sigma_{f=1}^{N_f}\left\{E_f[\gamma\gamma(\theta)] - C(\theta)\right\}^2 . \tag{2.70}$$

To relate our estimate of the shear correlation function to the matter power spectrum, P_δ, we will require $\langle\gamma\gamma\rangle_\theta$ in terms of the effective convergence power spectrum P_κ, as given in equation 2.67. Shear γ and convergence κ can be related by their dependence on the second derivatives of the projected gravitational potential as derived in sections 2.1.2 and 2.2,

$$\kappa(\boldsymbol{\theta}) = \frac{1}{2}(\psi_{,11} + \psi_{,22}) \quad \gamma_1(\boldsymbol{\theta}) = \tfrac{1}{2}(\psi_{,11} - \psi_{,22}) \quad \gamma_2(\boldsymbol{\theta}) = \psi_{,12}. \tag{2.71}$$

The Fourier pairs are

$$\hat{\kappa}(\mathbf{k}) = -\frac{1}{2}(k_1^2 + k_2^2)\hat{\psi}(\mathbf{k}) \quad \hat{\gamma}_1(\mathbf{k}) = -\tfrac{1}{2}(k_1^2 - k_2^2)\hat{\psi}(\mathbf{k}) \quad \hat{\gamma}_2(\mathbf{k}) = -k_1 k_2 \hat{\psi}(\mathbf{k}), \tag{2.72}$$

where $\hat{\psi}(\mathbf{k})$ is the Fourier pair of $\psi(\boldsymbol{\theta})$. Hence $\hat{\gamma}(\mathbf{k}) = \lambda(\mathbf{k})\hat{\kappa}(\mathbf{k})$, where, $\lambda(\mathbf{k}) = \lambda_1 + i\lambda_2$, and

$$\lambda_1 = \frac{k_1^2 - k_2^2}{k_1^2 + k_2^2} \qquad \lambda_2 = \frac{2k_1 k_2}{k_1^2 + k_2^2}. \tag{2.73}$$

From the inverse of equation 2.40,

$$\langle \gamma(\mathbf{x})\gamma^*(\mathbf{x}+\boldsymbol{\theta})\rangle = \frac{1}{(2\pi)^4}\int d^2k\hat{\gamma}(\mathbf{k})e^{-i\mathbf{x}\cdot\mathbf{k}} \int d^2k'\hat{\gamma}^*(\mathbf{k}')e^{i(\mathbf{x}-\boldsymbol{\theta})\cdot\mathbf{k}'}. \tag{2.74}$$

Replacing $\gamma(\mathbf{k})$ by $\lambda(\mathbf{k})\hat{\kappa}(\mathbf{k})$ and noting that equation 2.45 tells us

$$\langle \hat{\kappa}(\mathbf{k})\hat{\kappa}^*(\mathbf{k}')\rangle = (2\pi)^2\delta_D(\mathbf{k}-\mathbf{k}')P_\kappa(k), \tag{2.75}$$

integration over $\mathbf{k}'$ then gives

$$\langle \gamma(\mathbf{x})\gamma^*(\mathbf{x}+\boldsymbol{\theta})\rangle = \frac{1}{(2\pi)^2}\int d^2k\lambda(\mathbf{k})\lambda^*(\mathbf{k})P_\kappa(k)e^{i\boldsymbol{\theta}\cdot\mathbf{k}}. \tag{2.76}$$

Let α be the angle such that $\tan\alpha = k_2/k_1$. λ is then given by $\lambda = e^{2i\alpha}$ as $\lambda_1 = \cos 2\alpha$ and $\lambda_2 = \sin 2\alpha$. In the reference frame where $\boldsymbol{\theta} = (\theta, 0)$, α is the angle between $\boldsymbol{\theta}$ and $\mathbf{k}$ and we can write $d^2k = k\,dk\,d\alpha$, where $k^2 = k_1^2 + k_2^2$,

$$\langle \gamma\gamma^*\rangle_\theta = \frac{1}{(2\pi)^2}\int k\,dk\,P_\kappa(k)\int d\alpha e^{i\theta\,k\cos\alpha}. \tag{2.77}$$

Noting Bessel functions of the first kind can be defined as

$$J_n(x) = \frac{1}{2\pi i^n}\int_0^{2\pi} d\alpha\,\mathrm{e}^{i\,x\cos\alpha}\,\mathrm{e}^{i\,n\alpha}, \tag{2.78}$$

we find

$$\langle \gamma\gamma^*\rangle_\theta = \frac{1}{2\pi}\int dk\,k\,P_\kappa(k)\,J_0(k\theta), \tag{2.79}$$

where $J_0(k\theta)$ is the zeroth order Bessel function of the first kind. Comparing to the correlation function of κ we note that the Fourier pair of equation 2.46 gives us

$$\langle \kappa\kappa^*\rangle_\theta = \frac{1}{(2\pi)^2}\int d^2k\,P_\kappa(|\boldsymbol{k}|)\,\mathrm{e}^{i\boldsymbol{k}\cdot\boldsymbol{\theta}}. \tag{2.80}$$

Letting α be the angle between $\boldsymbol{k}$ and $\boldsymbol{\theta}$. $d^2k = k\,dkd\alpha$ and performing the angular integral,

$$\langle\kappa\kappa^*\rangle_\theta = \frac{1}{2\pi}\int dk\,k\,P_\kappa(k)\,J_0(k\theta), \tag{2.81}$$

we find that shear and convergence have the same statistical properties

$$\langle\gamma\gamma^*\rangle_\theta = \langle\kappa\kappa^*\rangle_\theta. \tag{2.82}$$

2.5.2 Tangential and radial shear correlation: $\langle\gamma_{\substack{t\\r}}\gamma_{\substack{t\\r}}\rangle_\theta$

Ellipticities can be determined in a rotated co-ordinate frame, defined by the line connecting the centroids of the two galaxies in question, such that the tangential and radial ellipticity parameters e_t and e_r are given by

$$\begin{pmatrix} e_t \\ e_r \end{pmatrix} = \begin{pmatrix} \cos 2\phi & \sin 2\phi \\ -\sin 2\phi & \cos 2\phi \end{pmatrix}\begin{pmatrix} e_1 \\ e_2 \end{pmatrix}, \tag{2.83}$$

where ϕ is the angle between the original and rotated co-ordinate frames. Performing this rotation in weak lensing analysis produces results that will be independent of the initial frame of reference. The correlation function can be estimated from the data by

$$E[\gamma_t\gamma_t] = \frac{\sum_{\rm pairs} w_{\rm pair}\,\mathrm{e}_t(\mathbf{x})\,\mathrm{e}_t(\mathbf{x}+\boldsymbol{\theta})}{g^2\,\sum_{\rm pairs} w_{\rm pair}}, \tag{2.84}$$

with a similar equation for $E[\gamma_r\gamma_r]$. Again, for parity reasons we expect the cross correlation $\langle e_t(\mathbf{x})e_r(\mathbf{x}+\boldsymbol{\theta})\rangle$ to vanish.

Equation 2.83 can be re-written in terms of the tangential shear γ_t and radial shear γ_r such that

$$(\gamma_1 + i\gamma_2)(\cos(2\phi) - i\sin(2\phi)) = \gamma_t + i\gamma_r. \tag{2.85}$$

The complex shear γ is then given by

$$\gamma e^{-2i\phi} = (\gamma_t + i\gamma_r), \tag{2.86}$$

and the shear correlation functions are

$$\langle\gamma\gamma^*\rangle_{\boldsymbol{\theta}} = \langle\gamma_t\gamma_t\rangle_{\boldsymbol{\theta}} + \langle\gamma_t\gamma_t\rangle_{\boldsymbol{\theta}}, \tag{2.87}$$

$$\langle\gamma\gamma e^{-4i\phi}\rangle_{\boldsymbol{\theta}} = \langle\gamma_t\gamma_t\rangle_{\boldsymbol{\theta}} - \langle\gamma_r\gamma_r\rangle_{\boldsymbol{\theta}}, \tag{2.88}$$

where now the shear correlations are averaged over $\boldsymbol{\theta}$ where $\boldsymbol{\theta} = (\theta\cos\phi, \theta\sin\phi)$ and $\phi = 0 \rightarrow \pi$. From equation 2.76, for real convergence κ,

$$\langle\gamma(\mathbf{x})\gamma(\mathbf{x}+\boldsymbol{\theta})e^{-4i\phi}\rangle = \frac{1}{(2\pi)^2}\int d^2k P_\kappa(k) e^{i\boldsymbol{\theta}\cdot\mathbf{k}}\, e^{4i\alpha}\, e^{-4i\phi}. \tag{2.89}$$

Noting that in this rotated frame $\boldsymbol{\theta}.\boldsymbol{k} = \theta k\cos\beta$, where $\beta = \alpha - \phi$ we find

$$\langle\gamma(\mathbf{x})\gamma(\mathbf{x}+\boldsymbol{\theta})e^{-4i\phi}\rangle = \frac{1}{(2\pi)^2}\int kdkd\beta\, P_\kappa(k) e^{i\theta k\cos\beta}\, e^{4i\beta}. \tag{2.90}$$

Using equations 2.78 and 2.79, noting that

$$\langle\gamma_{\underset{r}{t}}\gamma_{\underset{r}{t}}\rangle_{\boldsymbol{\theta}} = \frac{1}{2}\left(\langle\gamma\gamma^*\rangle_{\boldsymbol{\theta}} \pm \langle\gamma\gamma e^{-4i\phi}\rangle_{\boldsymbol{\theta}}\right), \tag{2.91}$$

we find

$$\langle\gamma_{\underset{r}{t}}\gamma_{\underset{r}{t}}\rangle_\theta = \frac{1}{4\pi}\int dk\, k\, P_\kappa(k)\,[J_0(k\theta) \pm J_4(k\theta)], \tag{2.92}$$

where $J_4(k\theta)$ is the fourth Bessel function of the first kind.

2.5.3 Shear Variance: $\langle\gamma^2\rangle_\theta$

The shear variance can be estimated by averaging the weighted product of paired galaxy ellipticities for all pairs in a radial cell with radius θ.

$$E[\gamma^2(\theta)] = \frac{\sum_{\alpha=1}^{2}\sum_{\text{pairs}}^{N_{\text{pair}}} w_{\text{pair}}\, \mathrm{e}_\alpha(\mathbf{x})\, \mathrm{e}_\alpha(\mathbf{x}')}{g^2\sum_{\text{pairs}}^{N_{\text{pair}}} w_{\text{pair}}}. \tag{2.93}$$

The main observational problem with this estimator is the presence of masking. Some cells will contain bright stars and bad pixels which mask out galaxies. These cells will produce a very noisy estimate of the shear variance. We can therefore average over all the cells in the survey with a weighting dependent on the number of galaxies detected within each cell and the quality of the shape measurements for that galaxy set. Typically the cell weighting is taken to be the squared sum of the individual galaxy weights.

For a cell aperture of radius R the average shear is given by

$$\gamma_{\text{av}}(R) = \frac{1}{\pi R^2}\int_0^R d^2r\,\gamma(\mathbf{r}), \tag{2.94}$$

$$\begin{aligned}\langle\gamma^2\rangle_R &= \frac{1}{(\pi R^2)^2}\int_0^R d^2r\int_0^R d^2r'\langle\gamma(\mathbf{r})\gamma(\mathbf{r}')\rangle \\ &= \frac{1}{(\pi R^2)^2}\int_0^R d^2r\int_0^R d^2r'\langle\kappa(\mathbf{r})\kappa(\mathbf{r}')\rangle \end{aligned} \tag{2.95}$$

where we have used equation 2.82. Using the Fourier pair of equation 2.46

$$\langle\kappa(\mathbf{r})\kappa(\mathbf{r}')\rangle \;=\; C_{\kappa\kappa}(\mathbf{r}'-\mathbf{r}) \;=\; \frac{1}{(2\pi)^2}\int d^2k\, P_\kappa(|\mathbf{k}|)\, \mathrm{e}^{i\mathbf{k}\cdot(\mathbf{r}'-\mathbf{r})}\,, \tag{2.96}$$

and hence

$$\begin{aligned}\langle\gamma^2\rangle_R &= \frac{1}{(\pi R^2)^2}\frac{1}{(2\pi)^2}\int d^2k\, P_\kappa(|\mathbf{k}|)\int_0^R d^2r \mathrm{e}^{-i\mathbf{k}\cdot\mathbf{r}}\int_0^R d^2r'\mathrm{e}^{i\mathbf{k}\cdot\mathbf{r}'}\\ &= \frac{1}{(\pi R^2)^2}\int d^2k\, P_\kappa(|\mathbf{k}|)\int_0^R r dr\, J_0(kr)\int_0^R r' dr'\, J_0(kr')\,,\end{aligned} \tag{2.97}$$

where we have used the zeroth order Bessel function integral representation from equation 2.78. The zeroth order and first order Bessel function are related by

$$\int_0^X x\, J_0(x) dx = X J_1(X)\,, \tag{2.98}$$

hence

$$\langle\gamma^2\rangle_R = \int d^2k\, P_\kappa(|\mathbf{k}|)\left(\frac{J_1(kR)}{\pi kR}\right)^2 . \tag{2.99}$$

Performing the final angular integral $d^2k = kdkd\phi$ and reverting to using the traditional notation of θ as the angular radius of the shear variance aperture we find

$$\langle\gamma^2\rangle_\theta = \frac{2}{\pi\theta^2}\int_0^\infty \frac{dk}{k} P_\kappa(|\mathbf{k}|)[J_1(k\theta)]^2 . \tag{2.100}$$

2.5.4 Aperture Mass: $M_{\rm ap}$

The aperture mass statistic was defined by Kaiser et al. (1994) to be the aperture weighted dimensionless surface mass density of a lens, κ. It was applied to cosmic shear measurements by Schneider et al. (1998),

$$M_{\rm ap}(\theta) = \int_0^\theta d^2\phi\, U(\phi)\, \bar{\kappa}_{\rm eff}(\boldsymbol{\phi})\;, \tag{2.101}$$

where the weight function $U(\phi)$ is defined to be constant on concentric curves, satisfying the criterion

$$\int_0^\theta \phi\, d\phi\, U(\phi) = 0\;. \tag{2.102}$$

With this choice of function, the variations in the lens surface mass density which introduce shear are detected, whilst the underlying constant sheet mass of the lens is ignored. Note that the mass of a sheet of constant surface mass density can only be determined with the inclusion of magnification information, see equation 2.29. The variance of $M_{\rm ap}$ is given by

$$\begin{aligned}\langle M_{\rm ap}^2\rangle(\theta) &= \frac{1}{2\pi}\int_0^\theta d^2\phi\, U(\phi)\int_0^\theta d^2\phi'\, U(\phi')\int d^2k\, e^{i(\boldsymbol{\phi}-\boldsymbol{\phi'}).\boldsymbol{k}} \\ &= 2\pi\int_0^\infty kdk\, P_\kappa(k)\left[\int_0^\theta \phi d\phi\, U(\phi)\, J_0(k\phi)\right]^2 . \end{aligned} \tag{2.103}$$

Schneider et al. (1998) suggested a family of radial filter functions $U(\phi)$, the simplest of which is

$$U(\phi) = \frac{9}{\pi\theta^2}\left(1-x^2\right)\left(\frac{1}{3}-x^2\right), \tag{2.104}$$

where $x\theta = \phi$. With this choice, the variance $\langle M_{\rm ap}^2\rangle(\theta)$ becomes

$$\langle M_{\rm ap}^2\rangle(\theta) = \frac{576}{2\pi\theta^4},\int_0^\infty \frac{dk}{k^3}\, P_\kappa(k)\left[J_4(k\theta)\right]^2 , \tag{2.105}$$

where $\mathrm{J}_4(l\theta)$ is the fourth-order Bessel function of the first kind.

It can be shown that the aperture mass statistic can be expressed in terms of the tangential shear, using a different but related filter function Q where

$$Q(\phi) = \frac{2}{\phi^2}\int_0^\phi d\phi'\,\phi' U(\phi') - U(\phi) \tag{2.106}$$

such that

$$M_{\rm ap}(\theta) = \int_0^\theta d^2\phi\, Q(\phi)\,\gamma_t(\boldsymbol{\phi}) . \tag{2.107}$$

The variance $\langle M_{\rm ap}^2\rangle(\theta)$ can then be estimated in cells such that

$$E[M_{\rm ap}^2(\theta)] = \frac{\sum_{\rm pairs}^{N_{\rm pair}} w_{\rm pair}\, \mathrm{e}_t(\mathbf{x})\, \mathrm{e}_t(\mathbf{x}')\, Q(\mathbf{x})Q(\mathbf{x}')}{g^2\,\sum_{\rm pairs}^{N_{\rm pair}} w_{\rm pair}} . \tag{2.108}$$

This however turns out not to be so useful, as it assumes a contiguous data field, which is not the case for a masked survey. It is therefore more helpful to express the aperture mass statistic in terms of correlation functions. Consider the sum and difference of the tangential and radial correlation functions,

$$\xi_\pm(\theta) = \langle\gamma_t\gamma_t\rangle_\theta \pm \langle\gamma_r\gamma_r\rangle_\theta . \tag{2.109}$$

$$\begin{aligned}\int \theta\, d\theta\, \xi_+(\theta) J_0(l\theta) &= \frac{1}{2\pi}\int kd\, dkP_\kappa(k)\int \theta\, d\theta\, J_0(k\theta)J_0(l\theta) \\ &= \frac{1}{2\pi}P_\kappa(l), \end{aligned} \tag{2.110}$$

where we have used the orthogonality of Bessel functions

$$\int_0^\infty \theta \, d\theta \, J_\nu(k\theta) J_\nu(l\theta) = \frac{\delta_D(k-l)}{l}. \tag{2.111}$$

Applying the same technique to ξ_- we find that the convergence power spectra $P_\kappa(l)$ can be written in terms of $\xi_\pm$ such that

$$P_\kappa(l) = \pi \int_0^\infty \theta[\xi_+(\theta) J_0(l\theta) + \xi_-(\theta) J_4(l\theta)]. \tag{2.112}$$

Hence

$$\langle M_{\rm ap}^2 \rangle = \int_0^\infty \frac{d\vartheta\, \vartheta}{2\theta^2} \left[\xi_+(\vartheta) T_+ \left(\frac{\vartheta}{\theta}\right) + \xi_-(\vartheta) T_- \left(\frac{\vartheta}{\theta}\right) \right], \tag{2.113}$$

where

$$\begin{aligned} T_+ &= 576 \int_0^\infty \frac{dt}{t^3} J_0(xt) [J_4(t)]^2, \\ T_- &= 576 \int_0^\infty \frac{dt}{t^3} J_4(xt) [J_4(t)]^2. \end{aligned} \tag{2.114}$$

$T_\pm(x)$ vanishes for $x > 2$ so the integration range is $0 \leq \vartheta \leq 2\theta$. The aperture mass statistic $\langle M_{\rm ap}^2 \rangle(\theta)$ can therefore be estimated from simply integrating over measured correlation functions. Note that the following analytic expressions for $T_\pm(x)$ have been derived by Schneider, Van Waerbeke & Mellier (2002):

$$\begin{aligned} T_+(x) &= \frac{6(12-15x^2)}{5}\left[1 - \frac{2}{\pi}\arcsin\frac{x}{2}\right] + \frac{x\sqrt{4-x^2}}{100\pi} \\ &\quad \times \left(110 + 2320x^2 - 754x^4 + 132x^6 - 9x^2\right), \end{aligned} \tag{2.115}$$

$$T_-(x) = \frac{192}{35\pi} x^3 \left(1 - \frac{x^2}{4}\right) H(2-x), \tag{2.116}$$

where H is the Heaviside step function.

2.5.5 E and B modes: Curl-Gradient Decomposition

The observable shear field γ can be related to the projected surface mass density or convergence κ, through the second order differential of the lensing potential, equations 2.15 and 2.26. In principle the gradient of κ can be obtained from observations from the the spatial derivatives of the shear such that

$$\nabla\kappa = \begin{pmatrix} \gamma_{1,1} + \gamma_{2,2} \\ \gamma_{2,1} - \gamma_{1,2} \end{pmatrix} \equiv \boldsymbol{u}\,. \tag{2.117}$$

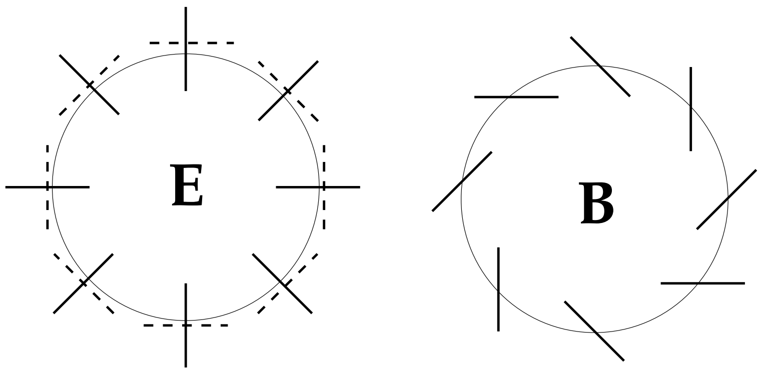

Figure 2.3: E and B mode representation. E modes are either tangential or radial depending on their sign. B modes can be oriented clockwise or counterclockwise.

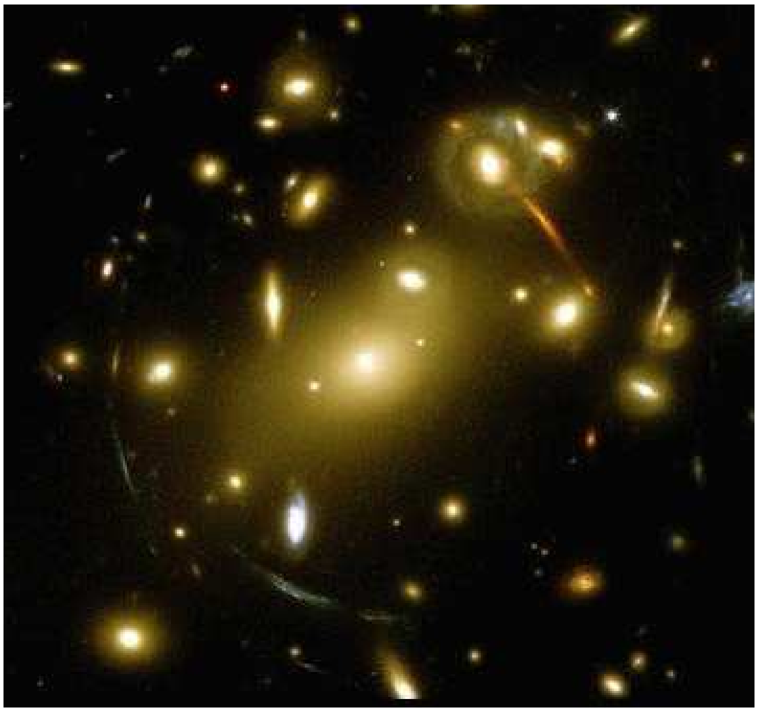

Figure 2.4: Pure **E** mode signal from a strong gravitational lens, galaxy cluster Abell 2218.

where $\boldsymbol{u}$ is a vector gradient field. Projecting out the gradient and curl part of $\boldsymbol{u}$ we define

$$\begin{aligned} \nabla^2 \kappa^E &= \nabla . \boldsymbol{u} \\ \nabla^2 \kappa^B &= \nabla \times \boldsymbol{u} \equiv 0 \end{aligned} \tag{2.118}$$

showing that shear distortions produced by weak gravitational lensing are curl-free, such that $\kappa^E = \kappa$ and $\kappa^B = 0$. Figure 2.3 shows representations of E and B mode distortions which can be compared to figure 2.4 showing the gravitationally lensed arcs of Abell 2218, which are distorted tangentially to the cluster core and are E-mode distortions.

Observationally, measurements of $\nabla \times \boldsymbol{u}$ always reveal a non-negligible B-mode, $\kappa^B \neq 0$, resulting in a readily identifiable noise component, or systematic error component in the shear field, for example from the presence of intrinsic galaxy alignments. Note that Schneider, Van Waerbeke & Mellier (2002) have shown that weak gravitational lensing can produce very small B-type distortions at small angular scales $\theta < 1'$, due to source redshift clustering.

The E/B mode decomposition of the shear field is easiest to carry out using the aperture mass statistic. Defining the complex convergence

$$\kappa = \kappa^E + i\kappa^B \,, \tag{2.119}$$

we have the following Fourier correlation functions

$$\langle \hat{\kappa}(k)\hat{\kappa}^*(k')\rangle = (2\pi)^2 \delta_D(\boldsymbol{k} - \boldsymbol{k'})[P_E(k) + P_B(k)]\,, \tag{2.120}$$

$$\langle \hat{\kappa}(k)\hat{\kappa}(k')\rangle = (2\pi)^2 \delta_D(\boldsymbol{k} - \boldsymbol{k'})[P_E(k) - P_B(k) + 2iP_{EB}(k)]\,, \tag{2.121}$$

where $P_E(k) = P_\kappa(k)$, the convergence E-mode power spectrum from weak gravitational lensing, $P_B(k)$ is the B mode power spectrum and $P_{EB}(k)$ is the cross power spectrum. Using this definition of complex convergence instead of pure E mode convergence, following through equations 2.89 to 2.92 and equations 2.109 to 2.112 we find the B mode power spectrum is given by

$$P_B(l) = \pi \int_0^\infty \theta[\xi_+(\theta)J_0(l\theta) - \xi_-(\theta)J_4(l\theta)]. \tag{2.122}$$

Hence defining the aperture mass B mode statistic $\langle M_\perp^2\rangle$ where

$$\langle M_\perp^2\rangle(\theta) = \frac{576}{2\pi\theta^4}, \int_0^\infty \frac{dk}{k^3}\, P_B(k)\,[J_4(k\theta)]^2 \,, \tag{2.123}$$

we find

$$\langle M_\perp^2\rangle(\theta) = \int_0^\infty \frac{d\vartheta\,\vartheta}{2\theta^2}\left[\xi_+(\vartheta)T_+\left(\frac{\vartheta}{\theta}\right) - \xi_-(\vartheta)T_-\left(\frac{\vartheta}{\theta}\right)\right], \tag{2.124}$$

where $T_\pm$ is given in equation 2.114. In the absence of contaminating non-lensing sources we expect $M_\perp \approx 0$.

3

Measuring cosmic shear

On the path from galaxy to detection the propagation of light is subject to many different effects that distort the final image. The first distortion is the cosmic shear that we wish to detect. On reaching the Earth, galaxy images are blurred by atmospheric refractive index variations arising from turbulence, commonly known as seeing. Atmospheric turbulence is caused by random fluctuations in the wind flow, with additional convection turbulence, arising from air-glass temperature differences at the telescope mirror. On passing through the telescope the galaxy images are smeared anisotropically by the point spread function (PSF) of the telescope optics, and then sheared by optical astrometric distortions. With excellent seeing observing conditions, or diffraction limited space-based data, combined with instruments and detectors that are designed with weak lensing detection in mind, these effects can be minimised (Rhodes et al. 2003), but will still dominate over the minute initial cosmic shear distortion that we wish to detect. Therefore, the aim of cosmic shear detection is to derive a method that will effectively correct for the Earth and telescope-based observational distortions, converting observed galaxy shapes into a measure of the weak lensing shear distortion.

In this chapter, a fast new model-fitting technique is presented that has been developed to produce unbiased estimates of galaxy ellipticities, with a robust method to correct for PSF and seeing distortions. A welcome by-product of the model-fitting analysis is an error estimate on each measured galaxy ellipticity parameter, which will permit future signal-to-noise optimised measurements of weak lensing shear. This new method is compared to the traditional Kaiser, Squires & Broadhurst (1995) method, where comparisons between the two techniques are drawn from an analysis of deep R band imaging from the COMBO-17 survey.

3.1 Shape measurement: KSB+

Kaiser, Squires & Broadhurst (1995) (KSB) prescribed a method to invert the effects of the PSF smearing, recovering a relationship between the measured weighted ellipticity ε of a galaxy image and its associated shear γ. This work was followed by improvements from Luppino & Kaiser (1997) (LK97), who introduced a seeing correction, and Hoekstra et al. (1998) (HFKS), who corrected some of the derivations in KSB and introduced an astrometric distortion correction. In this section we will review the KSB method including the improvements by LK97 and HFKS, (KSB+), thereby detailing the traditional technique, currently used by most weak lensing studies, to extract a measurement of weak lensing shear from a wide field survey. Note that the KSB+ technique is readily implemented with the *imcat* software made publicly available by Nick Kaiser[1].

3.1.1 Weighted ellipticities and shear

To quantify the shear distortions introduced by weak gravitational lensing, the weighted ellipticity ε for each object is calculated from its weighted quadrupole moments Q_{ij},

$$Q_{ij} = \frac{\int d^2\theta \, W(\boldsymbol{\theta}) \, I(\boldsymbol{\theta}) \, \theta_i \theta_j}{\int d^2\theta \, W(\boldsymbol{\theta}) \, I(\boldsymbol{\theta})}, \tag{3.1}$$

where the centre of the object is assumed to be at $(\theta_1, \theta_2) = (0, 0)$. For a perfect ellipse, the weighted quadrupole moments are related to the weighted ellipticity parameters ε_i by

$$\begin{pmatrix} \varepsilon_1 \\ \varepsilon_2 \end{pmatrix} = \frac{1}{Q_{11} + Q_{22}} \begin{pmatrix} Q_{11} - Q_{22} \\ 2Q_{12} \end{pmatrix}. \tag{3.2}$$

The weight W is chosen to suppress divergent sky noise contributions in measurements of the quadrupole moments, minimising the effects of noisy pixels which skew unweighted ellipticities to higher values. KSB propose a circular Gaussian weight function such that

$$W(\boldsymbol{\theta}) = e^{\frac{1}{2}\left(\frac{\theta}{\theta_g}\right)^2}, \tag{3.3}$$

where θ_g is some measurement of galaxy size. KSB propose setting $\theta_g = r_g$, the filter radius as defined by the *imcat* object finding routine *hfindpeaks* which convolves the image with a series of compensated Mexican hat functions of varying size. Significant peaks in the convolved image are extracted as objects with an assigned filter radius set equal to the radius of the

[1] www.ifa.hawaii.edu/~kaiser/imcat

Mexican hat function for which the object's significance is a maximum. Van Waerbeke et al. (2000) propose setting $\theta_g = r_h$, the half light radius measured by the source extraction code *SExtractor*[2] (Bertin & Arnouts 1996). There are merits to both proposals: the signal to noise of the shape measurements are slightly higher when using the filter radius, but *SExtractor* typically locates more sources than *hfindpeaks*.

By introducing weighted quadrupole moments the relationship between ellipticity e and shear γ, equation 2.36, no longer applies and hence KSB re-derive the relationship by replacing the image $I(\boldsymbol{\theta})$ in equation 3.1 with a weakly sheared image $I'(\theta_i) = I(A_{ij}\theta_j)$, where the lensing Jacobian A_{ij} is given by equation 2.24. In the absence of PSF distortions in the limit where seeing can be neglected, KSB find that

$$\varepsilon_\alpha = \varepsilon^s_\alpha + P^{\rm sh}_{\alpha\beta}\gamma_\beta, \tag{3.4}$$

where the shear polarizability tensor $P^{\rm sh}$ is a function of weighted moments, up to fourth order, given by

$$P^{\rm sh}_{\alpha\beta} = X^{\rm sh}_{\alpha\beta} - \varepsilon_\alpha\varepsilon^{\rm sh}_\beta\,, \tag{3.5}$$

where $X^{\rm sh}_{\alpha\beta}$ and $\varepsilon^{\rm sh}_\alpha$ are defined as

$$X^{\rm sh}_{\alpha\beta} = \frac{1}{Q_{11}+Q_{22}}\int d^2\theta \begin{bmatrix} 2W\theta^2 + 2W'(\theta_1^2-\theta_2^2)^2 & 4W'(\theta_1^2-\theta_2^2)\theta_1\theta_2 \\ 4W'(\theta_1^2-\theta_2^2)\theta_1\theta_2 & 2W\theta^2 + 8W'\theta_1^2\theta_2^2 \end{bmatrix} I(\boldsymbol{\theta}) \tag{3.6}$$

and

$$\varepsilon^{\rm sh}_\alpha = 2\varepsilon_\alpha + \frac{2}{Q_{11}+Q_{22}}\int d^2\theta \begin{pmatrix} \theta_1^2-\theta_2^2 \\ 2\theta_1\theta_2 \end{pmatrix} W'\theta^2 I(\boldsymbol{\theta}), \tag{3.7}$$

where W' denotes the derivative of W (equation 3.3) with respect to θ^2. $P^{\rm sh}$ can be measured directly from each galaxy image.

Note that this method assumes that the centre of the galaxy is known, which in the presence of non isotropic centroid errors can lead to **centroid bias** (Kaiser 2000; Bernstein & Jarvis 2002). If, for example, the errors in the x direction exceed those in the y direction there is a tendency to bias towards positive ε_1, whereas if the centroid errors are the same in both directions the net effect is zero.

[2] ftp://geveor.iap.fr/pub/sextractor

3.1.2 PSF correction

KSB calculate the effects of PSF anisotropic smearing by replacing the image $I(\boldsymbol{\theta})$ in equation 3.1 with a PSF convolved image $I_{\rm obs}(\boldsymbol{\theta})$,

$$I_{\rm obs}(\boldsymbol{\theta}) = \int d^2\,\theta' g(\boldsymbol{\theta}') I(\boldsymbol{\theta} - \boldsymbol{\theta}'), \tag{3.8}$$

where $g(\boldsymbol{\theta})$ is the PSF kernel. Using the notation $\odot$ for a convolution, $I_{\rm obs} = I \odot g$. KSB show that if the PSF distortion can be described as a small but highly anisotropic distortion convolved with a large circularly symmetric Gaussian, then the ellipticity of a PSF corrected galaxy is given by

$$\varepsilon_\alpha^{\rm cor} = \varepsilon_\alpha^{\rm obs} - P_{\alpha\beta}^{\rm sm} p_\beta, \tag{3.9}$$

where p_α is a measure of the PSF anisotropy given by the unweighted quadrupole moments of stellar images Q_{ij}^*, $p_\alpha \equiv (Q_{11}^* - Q_{22}^*, 2Q_{12}^*)$, and the smear polarizability tensor $P^{\rm sm}$ is a function of weighted moments up to fourth order, defined as

$$P_{\alpha\beta}^{\rm sm} = X_{\alpha\beta}^{\rm sm} - \varepsilon_\alpha^{\rm obs} \varepsilon_\beta^{\rm sm}, \tag{3.10}$$

where $X_{\alpha\beta}^{\rm sm}$ and $\varepsilon_\alpha^{\rm sm}$ are given by

$$X_{\alpha\beta}^{\rm sm} = \frac{1}{Q_{11} + Q_{22}} \int d^2\theta \begin{bmatrix} W + 2W'\theta^2 + W''(\theta_1^2 - \theta_2^2)^2 & 2W''(\theta_1^2 - \theta_2^2)\theta_1\theta_2 \\ 2W''(\theta_1^2 - \theta_2^2)\theta_1\theta_2 & W + 2W'\theta^2 + 4W''\theta_1^2\theta_2^2 \end{bmatrix} I(\boldsymbol{\theta}) \tag{3.11}$$

and

$$\varepsilon_\alpha^{\rm sm} = \frac{1}{Q_{11} + Q_{22}} \int d^2\theta \begin{pmatrix} \theta_1^2 - \theta_2^2 \\ 2\theta_1\theta_2 \end{pmatrix} (2W' + W''\theta^2) I(\boldsymbol{\theta}), \tag{3.12}$$

where prime denotes differentiation with respect to θ^2.

$p_\alpha(\boldsymbol{\theta})$ can be estimated from images of stellar objects at position $\boldsymbol{\theta}$, by noting that a star, which will be denoted throughout this chapter with *, imaged in the absence of PSF distortions, has zero ellipticity: $\varepsilon_\alpha^{*\,\rm cor} = 0$. Hence,

$$p_\mu = (P^{\rm sm*})^{-1}_{\mu\alpha}\, \varepsilon_\alpha^{*\rm obs}. \tag{3.13}$$

As $P_{\alpha\beta}^{\rm sm} \approx 0$ for $\alpha \neq \beta$,

$$p_\alpha \approx \frac{\varepsilon_\alpha^{*\rm obs}}{P_{\alpha\alpha}^{\rm sm*}}. \tag{3.14}$$

In principle to correct a galaxy image of size θ_g for PSF distortions, $p_\alpha(\boldsymbol{\theta})$ should be calculated using weights with the same value for θ_g. In practice however $p_\alpha(\boldsymbol{\theta})$ is determined across the image for a single weighting where θ_g is approximately equal to the seeing size.

3.1.3 Seeing correction

The effect of seeing is to convolve galaxy images with a seeing kernel q, erasing shear information for galaxies smaller than the kernel or seeing size. Letting $I_{\rm cor}$ be the PSF corrected image

$$I_{\rm cor} = [S_\gamma I_{\rm true}] \odot q, \tag{3.15}$$

where $I_{\rm true}$ is the true image of the galaxy which has been sheared through gravitational lensing as defined by an operator S_γ. LK97 show that, assuming q is a circular Gaussian, the process of shear followed by a seeing convolution, is equivalent to a convolution with an anisotropic anti-sheared kernel $q' = S_\gamma^{-1} q$ followed by a shear,

$$I_{\rm cor} = S_\gamma \left[I_{\rm true} \odot q' \right]. \tag{3.16}$$

Combining the results from sections 3.1.1 and 3.1.2, treating the anti-sheared kernel q' as the equivalent of the PSF kernel g, the PSF corrected weighted ellipticity is related to the source ellipticity ε^s and the weak lensing shear γ by

$$\varepsilon_\alpha^{\rm cor} = \varepsilon_\alpha^s + P^{\rm sh}_{\alpha\beta}\gamma_\beta + P^{\rm sm}_{\alpha\beta} p'_\beta. \tag{3.17}$$

where the additional seeing term $p'_\alpha(\boldsymbol{\theta})$, can be estimated from the stars at position $\boldsymbol{\theta}$ in the image, such that

$$p'_\mu = -\left(P^{\rm sm*}\right)^{-1}_{\mu\delta} P^{\rm sh*}_{\delta\beta}\gamma_\beta\,. \tag{3.18}$$

Defining the pre-seeing shear polarizability tensor P^γ such that,

$$P^\gamma_{\alpha\beta} = P^{\rm sh}_{\alpha\beta} - P^{\rm sm}_{\alpha\mu}\left(P^{\rm sm*}\right)^{-1}_{\mu\delta} P^{\rm sh*}_{\delta\beta}, \tag{3.19}$$

we arrive at a simple relationship between the PSF corrected weighted galaxy ellipticity and its pre-seeing shear γ.

$$\varepsilon_\alpha^{\rm cor} = \varepsilon_\alpha^s + P^\gamma_{\alpha\beta}\gamma_\beta. \tag{3.20}$$

As $P^{\rm sh}_{\alpha\beta} \approx 0$ for $\alpha \neq \beta$,

$$P^\gamma_{\alpha\alpha} \approx P^{\rm sh}_{\alpha\alpha} - P^{\rm sm}_{\alpha\alpha}\frac{P^{\rm sh*}_{\alpha\alpha}}{P^{\rm sm*}_{\alpha\alpha}}, \tag{3.21}$$

and $P^\gamma_{\alpha\beta} \approx 0$ for $\alpha \neq \beta$.

In principle P^γ should be calculated for each galaxy from the PSF corrected image $I_{\rm cor}$, but in practice P^γ is calculated from observed PSF distorted images, producing some very noisy measurements. The P^γ seeing correction is therefore often implemented with a seeing correction equal to the average trace of P^γ estimated as a function of image size where $\langle P^\gamma(\theta_g)\rangle = \langle \frac{1}{2}\left[P^\gamma_{11}(\theta_g) + P^\gamma_{22}(\theta_g)\right]\rangle$. It has been shown, however, that a full tensor correction can give slightly better results (Erben et al. 2001).

3.1.4 Astrometric distortions

Astrometric distortions introduce artificial shear into images, which can arise from, for example, 'pin-cushion' distortion, resulting from curved focal planes meeting flat CCD detectors. This typically introduces a radial displacement for point sources, and hence an overall radial shearing of extended sources. Additional shear distortion would certainly arise in the case where the plane of the detector was not level, a result of small vertical angular offsets between CCD chips.

Following equation 3.4, we can write

$$\varepsilon^*_{\rm obs} = \varepsilon^* + P^{\rm sh*}\delta, \tag{3.22}$$

where $\varepsilon^*_{\rm obs}$ is the observed weighted stellar ellipticity and ε^* is the weighted stellar ellipticity including PSF and seeing distortions, but determined in the absence of astrometric distortions, which introduce a shear δ. Combining equations 3.9 and 3.20, including an astrometric distortion term, we find

$$\varepsilon_{\rm obs} = \varepsilon^s + P^\gamma\gamma + P^{\rm sm}\frac{\varepsilon^*}{P^{\rm sm*}} + P^{\rm sh}\delta. \tag{3.23}$$

Including equation 3.22,

$$\varepsilon_{\rm obs} = \varepsilon^s + P^\gamma(\gamma+\delta) + P^{\rm sm}p\,, \tag{3.24}$$

and averaging over many sources such that $\langle\varepsilon^s\rangle = 0$, the shear is given by

$$\gamma = \langle\frac{\varepsilon_{\rm obs} - P^{\rm sm}p}{P^\gamma}\rangle - \delta\,. \tag{3.25}$$

Hence, to correct for astrometric distortions one can simply subtract δ from the observed shear field.

The shear introduced from astrometric distortions at telescopes chosen by weak lensing surveys is typically small ($\delta < 0.1\%$) and often treated as negligible. This is not the case however for the Oxford Dartmouth Thirty degree survey (ODT), which will be analysed in

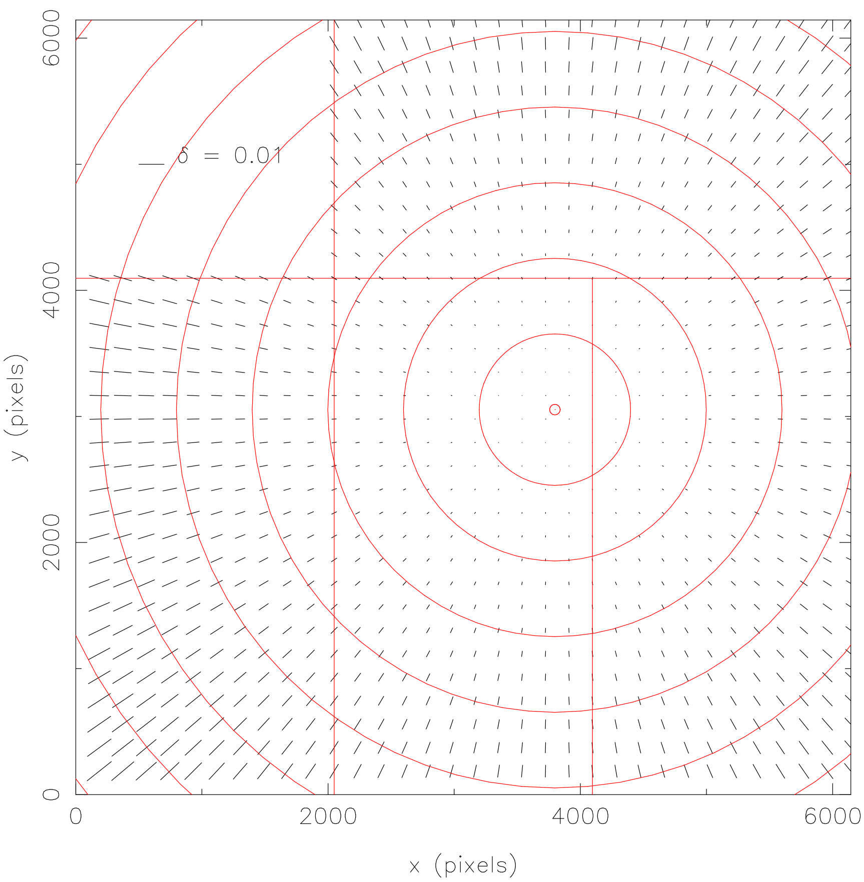

Figure 3.1: The expected instrumental shear pattern of the INT wide field camera as derived from the distortion model given in the ING observer handbook (Carter & Clegg 1994), where the optic axis is positioned at pixel (1751.7, 3059.0) in the central CCD chip.

chapter 4, that has been observed with the INT wide-field camera. Considering only the pin-cushion distortion, INT wide-field camera point sources are expected to be displaced radially by $\Delta \boldsymbol{x} = ar^2 \boldsymbol{r}$, where r is the distance from the optic axis and $a \simeq 5.746 \times 10^{-10}\text{pixels}^{-2}$ (Carter & Clegg 1994). The resulting astrometric shear δ, shown in figure 3.1, is given by $\delta_i = ar^2 q_i$ where $q_i \equiv \{r_1^2 - r_2^2, 2r_1 r_2\}/(r_1^2 + r_2^2)$ (Bacon, Refregier & Ellis 2000). Hence for INT wide-field camera images there is an additional radial shear from pin-cushion distortions reaching $\delta \sim 0.01$ at the edges of the image. Note that the CCDs in the INT wide-field camera have been placed with non-negligible vertical angular offsets, compared to CCD1, and that this will contribute to additional sources of astrometric shear, that are not included in the model distortions shown in figure 3.1.

3.1.5 Alternatives to KSB+

With upcoming high precision weak lensing surveys we will require a shape measurement technique which provides the following:

1. Accurate shape measurements of individual galaxies that are determined without bias in the presence of noise, with an associated error estimate.
2. A correction for PSF distortions, to arbitrary precision, that is not limited by any assumption about the PSF shape, where the PSF can vary continuously across the image and can be different in every exposure.
3. A robust correction for seeing that does not resort to calibration with image simulations.
4. Fast computer processing time.

Although KSB+ is currently the most commonly used shape measurement technique, in part a result of the publicly available software, it is far from being optimal, failing requirements 1-3. Bacon et al. (2001) show from sheared image simulations that KSB+ underestimates shear measurements for γ_1 by$\sim 10\%$ and for γ_2 by $\sim 25\%$, which could be caused by a bias to more circular shapes introduced by the choice of circular Gaussian weighting. Erben et al. (2001) have also tested KSB+ with sheared image simulations, investigating different PSF distortions, finding a systematic error of 10-15% in the recovery of the shear amplitude. In the case of scalar PSF corrections, KSB+ is found to underestimate shear measurements, but when using tensor PSF corrections Erben et al. (2001) find that the shear recovered can be an over or underestimate, depending on the PSF distortion. Note that this result does not lend support to the simple empirical correction to KSB+ shear estimates employed by Bacon, Refregier & Ellis (2000); Bacon et al. (2003); Brown et al. (2003) in light of the results from Bacon et al. (2001). Mathematically the KSB PSF correction is poorly defined for typical PSFs, particularly in very good seeing conditions or space-based observations (Kaiser 2000). An example would be mirror aberrations or coma, which cannot be described as Gaussian with small anisotropic perturbations. Kuijken (1999) consider the co-addition of multiple exposures where the resulting co-added PSF is the sum of elliptical Gaussians. If the ellipticity of the co-added PSF varies with radius, which is fairly likely for a PSF which varies on time-scales the length of individual exposures, Kuijken (1999) find that the compact circular weight function of KSB enhances only the central ellipticity of the co-added PSF, resulting in residual PSF systematic errors of the order of a few percent. The success of the KSB pertubative treatment of the PSF is however testable and has worked surprisingly well, removing PSF induced systematic correlations in some cases to negligible levels (Brown et al. 2003). The success of the seeing correction is, however, significantly harder to test, as it results in a potential calibration error which can only be detected through simulations. Erben et al. (2001) have shown from sheared image simulations that the LK97 seeing correction in the presence of anisotropic PSF distortions is very problematic. P^{γ} should be measured from PSF corrected galaxy profiles, which is impossible without some deconvolution of the image, and hence the best estimate of P^{γ} from PSF distorted images are found to be too high or too low depending on the PSF pattern (Erben et al. 2001). Even with measurements of P^{γ} from a PSF corrected image, the LK97 seeing correction relies on the assumption of a circular Gaussian seeing kernel, which fails for space-based diffraction rings and ground based $r^{-11/13}$ tails from atmospheric Kolmogorov turbulence. In conclusion, although fast, efficient and easy to implement, it has been shown that the KSB+ technique has the potential to seriously bias measurements of cosmic shear, where the level of bias can only be determined using image simulations. For these reasons several groups have been prompted to produce alternatives to the KSB+ technique.

Bernstein & Jarvis (2002) (BJ02) have proposed first convolving the image such that the resulting convolved anisotropic PSF is isotropic and circular (see section 3.4 for discussion). They then follow with the decomposition of the convolved galaxy images into a family of orthogonal 2D Gaussian based functions. Using adaptive elliptical weights to determine coefficients for each function, there is no bias towards particular shapes. For the seeing correction, the measured galaxy ellipticity is divided by a dilution factor $R_g \approx 1 - (< r^2 >_{\rm PSF} \, / < r^2 >_g)$ where $< r^2 >$ is the unweighted second radial moment of the measured image, for the galaxy g, and the PSF. As Hirata & Seljak (2003) point out, however, this method will rely on the Gaussianity of the PSF and galaxy. They show that for non-Gaussian distortions the BJ02 method could underestimate measurements of σ_8 by $\sim 10\%$. Hirata & Seljak (2003) also note that a recent application of the BJ02 method to the Cerro Tololo Inter-American observatory weak lensing survey (Jarvis et al. 2003) finds a lower value of σ_8 compared to the majority of other weak lensing surveys.

Refregier & Bacon (2003) propose an alternative, decomposing galaxy images and PSFs into Gauss-Hermite polynomials. This allows for the shape determination of quite intricate galaxy profiles and is therefore well suited to high resolution space-based imaging. Initial testing with simulations have shown promising results, but this method has not yet been tested with real galaxy images. A formally exact but rather complicated PSF and seeing correction scheme has been put forward as another alternative by Kaiser (2000), which takes into account ground based Kolomogrov turbulence limited seeing or space-based diffraction limited seeing. An entirely different approach of direct model fitting to galaxy images has been proposed by Kuijken (1999) where sheared circular sources convolved with model PSFs are directly fit to stacked galaxy images, which in the absence of any distortions should average to zero ellipticity. The model PSFs and stacked images were introduced primarily in order to decrease the computer processing time, seriously limiting the accuracy of this method owing to the high shot noise produced by the small numbers of co-added galaxy images.

A model fitting method that can be applied to every galaxy image, using typical galaxy profiles convolved with actual stellar images taken from the data, has the advantage that it can correct for any PSF anisotropy and seeing smearing in one step, relying only, in principle, on a galaxy model profile. It should therefore satisfy our first three requirements for a shape measurement technique, permitting a signal to noise optimised unbiased measurement of cosmic shear, in the absence of any initial object selection bias, discussed in section 3.4. The problem then lies solely with the requirement for fast computer processing time.

3.2 Galaxy model fitting

From a deep image of the sky, we wish to determine the position of every resolved galaxy, its size r_c, ellipticity, and orientation, defined through the ellipticity parameters (e_1, e_2). Additional information, concerning the PSF and seeing distortions, is required from images of stellar objects. Given approximate galaxy positions from source extraction algorithms such as *SExtractor*, we will require, for each galaxy, the probability

$$p(r_c, e_1, e_2 | \text{pixel values, stellar images}) \,. \tag{3.26}$$

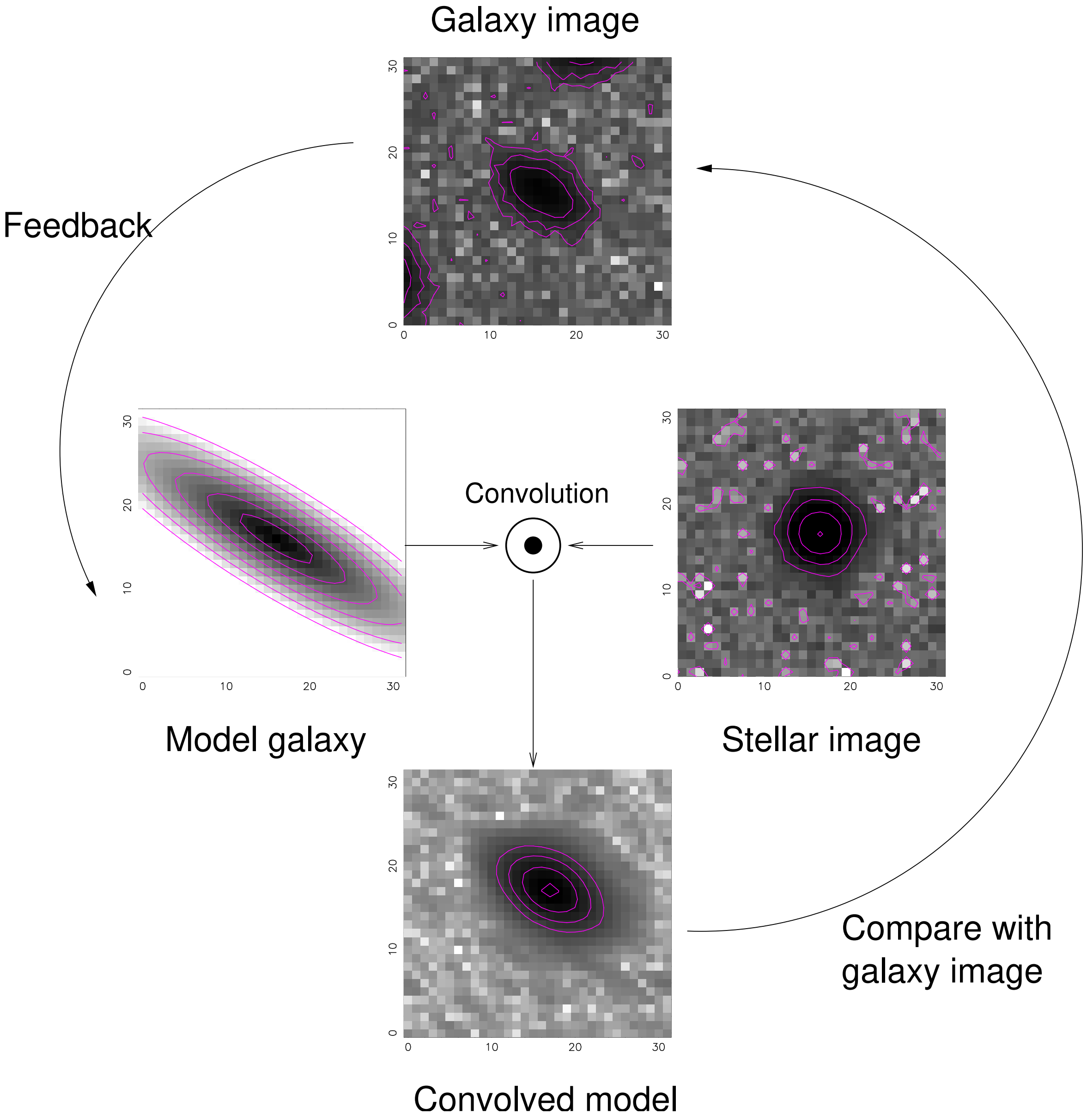

Figure 3.2: Schematic of the model fitting technique. Galaxy images are compared to convolved model galaxies, where model galaxies have been convolved with stellar images taken from the same area of the image. Note that the greyscales are logarithmic.

This is a standard parameter estimation problem, shown schematically in figure 3.2, whereby model galaxies, convolved with stellar images taken from the correct area of the image, are compared with the observed PSF distorted galaxy image. The best fit convolved model in principle yields the true galaxy shape. This method has not previously been attempted due to the lengthy computational processing requirements, where the predominant source of computer processing time comes from the convolution of the galaxy model with the PSF. For a square PSF image $\mathrm{PSF}(i,j)$ and model galaxy $\mathrm{gal}(i,j)$, where i and $j = (0, 1, ..., N-1)$ the convolution $\mathrm{gal}' = \mathrm{PSF} \odot \mathrm{gal}$ is given in real space by

$$\mathrm{gal}'(s,t) = \Sigma_{i=0}^{N-1} \Sigma_{j=0}^{N-1} \mathrm{gal}(i,j)\, \mathrm{PSF}(s-i, t-j) \ . \tag{3.27}$$

For images where $N > 9$ it is typically faster to use Fourier techniques, as $\mathcal{F}(\mathrm{gal}') = \mathcal{F}(\mathrm{PSF})\mathcal{F}(\mathrm{gal})$ where $\mathcal{F}(\mathrm{g})$ is the discrete Fourier transform of a function $g(i,j)$ such that,

$$\mathcal{F}(g) = G(k,l) = \frac{1}{N^2} \Sigma_{i=0}^{N-1} \Sigma_{j=0}^{N-1} g(i,j) \exp\left[\imath 2\pi \left(\frac{ki}{N} + \frac{lj}{N}\right)\right] \ , \tag{3.28}$$

where to save confusion with pixel position i we use the notation $\imath = \sqrt{-1}$. Discrete Fourier transforms can be implemented with fast Fourier transform routines, but initial testing with standard routines[3] produced, at best, model fitting times of the order of one minute. With a 30 square degree survey with a galaxy density of 30 galaxies per square arcminute, which corresponds to a ground based survey with a median redshift of approximately $z_m \sim 1$, this speed of model fitting would take approximately 6 years of computer processing time. To make model fitting feasible, in order to improve on KSB+, object by object fitting time needs to be reduced to the order of seconds.

In this section we will first review some results from Bayesian statistics which lend themselves well to parameter estimation problems. These results will then be used to derive an optimal and fast, of the order of one second, galaxy model-fitting likelihood analysis technique, that requires only one Fourier transform operation per galaxy model.

[3] *www.nag.co.uk/numeric/fl/manual19/html/C06_fl19.html*

3.2.1 Bayes' Theorem and marginalisation

Bayes' Theorem states that the probability of a hypothesis H being true given some results R and any prior information I, $p(H|RI)$, is given by

$$p(H|RI) = \frac{p(H|I)\, p(R|HI)}{p(R|I)} \;, \tag{3.29}$$

which can be derived from the sum and product rules of probability theory, see for example Sivia (1996). If for a particular set of results we wish to choose the best hypothesis between several hypotheses H_i, noting that the factor $p(R|I)$ remains constant, we can simply choose the highest value of $p(H_i|I)\, p(R|H_iI)$, where the first term is known as the **prior** and the second term is known as the **likelihood** $\mathcal{L}$. The prior contains our degree of belief in a hypothesis. For a uniform prior the maximum likelihood informs us of the best hypothesis or best fit model.

Marginalisation allows us to reduce the number of parameters in our model if we are uninterested in their value, for example if our hypothesis depends on two parameters (x, y) and we are only interested in the value of x,

$$p(H(x)|RI) = \int_{-\infty}^{\infty} p(H(x,y)|RI)\, dy \;. \tag{3.30}$$

With some prior information about the parameter y, the marginalised likelihood is given by

$$p(H(x)|I)\, p(R|H(x)I) = \int_{-\infty}^{\infty} p(H(x,y)|I)\, p(R|H(x,y)I)\, dy \;. \tag{3.31}$$

Single-object galaxy profile model-fitting allows us to find the best fit ellipticity parameters (e_1, e_2), whilst marginalising over parameters which are unimportant for cosmic shear studies, such as galaxy brightness, position and size.

3.2.2 χ^2, likelihood $\mathcal{L}$ and errors

We will start by considering the standard χ^2 approach to model-fitting. χ^2 is defined as the sum of the squares of the normalised residuals between some data $y\,(\mathbf{x}_i)$ and a model $m(\mathbf{x}_i)$. For an independent data set with associated errors σ_i, χ^2 is therefore given by

$$\chi^2 = \sum_{i=1}^{N} \left(\frac{y\,(\mathbf{x}_i) - m(\mathbf{x}_i)}{\sigma_i} \right)^2 \;. \tag{3.32}$$

The minimum χ^2 value informs us of the best fit model. For Gaussian errors σ_i, χ^2 has a known distribution. A useful rule of thumb, that we will use in later chapters, is that χ^2 for a moderately good fit is $\chi^2 = \nu \pm \sqrt{2\nu}$, where ν is the number of degrees of freedom. $\nu = N - n$, where N is the number of data points and n is the number of model parameters.

In the limit of a large number of observations where the central limit theorem[4] applies, the likelihood $\mathcal{L} = p(R|HI)$, which is the joint probability distribution of N measured values drawn from a model distribution with q free parameters, is related to a χ^2 distribution with $\nu = q$ through

$$\ln\left(\mathcal{L}\right) = -\frac{1}{2}\chi^2. \tag{3.33}$$

The best fit model is given by the maximum likelihood $\mathcal{L}_{\text{max}}$ and an estimate of the errors on the best fitting parameters can be based on the χ^2 criterion for confidence levels. The 68.3% confidence level which corresponds to 1σ errors, is given for $\nu = 1$ by $\Delta\chi^2 = -2\ln(\mathcal{L}/\mathcal{L}_{\text{max}}) = 1$, and for $\nu = 2$ by $\Delta\chi^2 = 2.3$ (Sivia 1996).

Assuming the model $m(\mathbf{x})$ can be written as a model $y^m\left(\mathbf{x}_i\right)$ with amplitude a, χ^2 is given by

$$\begin{aligned}
\chi^2 &= \sum_i \left(\frac{y\left(\mathbf{x}_i\right) - a y^m\left(\mathbf{x}_i\right)}{\sigma_i}\right)^2 \\
&= \sum_i \frac{y\left(\mathbf{x}_i\right)^2}{\sigma_i^2} - 2a\sum_i \frac{y\left(\mathbf{x}_i\right) y^m\left(\mathbf{x}_i\right)}{\sigma_i^2} + a^2 \sum_i \frac{y^m\left(\mathbf{x}_i\right)^2}{\sigma_i^2} \\
&= \sum_i \frac{y\left(\mathbf{x}_i\right)^2}{\sigma_i^2} + A\left(a - B\right)^2 - AB^2\,,
\end{aligned} \tag{3.34}$$

where

$$\begin{aligned}
A &= \sum_i \frac{y^m\left(\mathbf{x}_i\right)^2}{\sigma_i^2}\,, \\
B &= \sum_i \frac{y\left(\mathbf{x}_i\right) y^m\left(\mathbf{x}_i\right)}{\sigma_i^2} \Big/ \sum_i \frac{y^m\left(\mathbf{x}_i\right)^2}{\sigma_i}\,.
\end{aligned} \tag{3.35}$$

The likelihood can then be written as,

$$\mathcal{L} = \mathrm{e}^{-\sum y(\mathbf{x}_i)^2/2\sigma_i^2}\mathrm{e}^{AB^2/2}\mathrm{e}^{-A(a-B)^2/2}. \tag{3.36}$$

Using a Bayesian approach, discussed in section 3.2.1, we can now marginalise this likelihood function over model parameters which are uninteresting to the problem at hand, resulting in a

[4] The central limit theorem states that the mean of N independent measurements of a random variable from a probability distribution function of finite variance σ^2 tends to be Gaussian distributed about the expectation value for the mean with variance σ^2/N.

final likelihood function that is dependent only on the few model parameters that we require, namely the galaxy ellipticity parameters (e_1, e_2).

3.2.3 Marginalising over the model amplitude

If we are interested only in the shape of the fitted model as defined by the function $y^m(\mathbf{x}_i)$ and not in its amplitude a, we can marginalise over a equation 3.31, adopting a prior p(a)

$$\mathcal{L} = \mathrm{e}^{-\sum y(\mathbf{x}_i)^2/2\sigma_i^2} \mathrm{e}^{AB^2/2} \int_{-\infty}^{\infty} \mathrm{e}^{-A(a-B)^2/2} p(a) da\,. \tag{3.37}$$

We shall adopt a uniform prior $p(a) = 1/\left(a_{\max} - a_{\min}\right)$ for $a_{\min} < a < a_{\max}$. For statistically-significant detections of a galaxy the Gaussian part of the likelihood causes the form of the prior at both large and small a to be unimportant and we can allow $a_{\min} \to -\infty$ and $a_{\max} \to \infty$, in which case the likelihood becomes

$$\mathcal{L} \propto \sqrt{2\pi/A}\, \mathrm{e}^{-\sum y(\mathbf{x}_i)^2/2\sigma_i^2} \mathrm{e}^{AB^2/2}\,. \tag{3.38}$$

As it stands this is rather unsatisfactory, as the $\sqrt{2\pi/A}$ term means that the likelihood depends both on the scaling of the model, $y^m(\mathbf{x}_i)$, and also on the second moment of the model, $\sum y^m(\mathbf{x}_i)^2/\sigma_i^2$, irrespective of any comparison with the data. To remedy this we shall calculate the likelihood subject to the condition $\sum y^m(\mathbf{x}_i)^2/\sigma_i^2 = \text{constant}$. Since for a given dataset $\sum y(\mathbf{x}_i)^2/\sigma_i^2$ is also fixed, we can now write

$$\begin{aligned} \mathcal{L} &\propto \mathrm{e}^{AB^2/2} \\ &\propto \exp\left[\frac{1}{2}\left(\sum_i \frac{y(\mathbf{x}_i)\, y^m(\mathbf{x}_i)}{\sigma_i^2}\right)^2 \Big/ \sum_i \frac{y^m(\mathbf{x}_i)^2}{\sigma_i^2}\right]. \end{aligned} \tag{3.39}$$

3.2.4 Marginalising over the position uncertainty

If we are interested in the shape of a galaxy, and not in its absolute position, then we should also allow some position uncertainty in the model and marginalise over that position uncertainty. To do this, we will first express the data and the model in terms of their Fourier components

$$\begin{aligned} y(\mathbf{x}_i) &= \sum_{\mathbf{k}} y_{\mathbf{k}} \mathrm{e}^{-\imath \mathbf{k}.\mathbf{x}_i} \\ y^m(\mathbf{x}_i) &= \sum_{\mathbf{k}} y^m_{\mathbf{k}} \mathrm{e}^{-\imath \mathbf{k}.\mathbf{x}_i}. \end{aligned} \tag{3.40}$$

If the noise in the data, σ_i, is independent of position, which will be valid for faint galaxies, then

$$\sum_i \frac{y(\mathbf{x}_i)\, y^m(\mathbf{x}_i)}{\sigma_i^2} = \frac{1}{\sigma^2}\sum_i y(\mathbf{x}_i)\, y^m(\mathbf{x}_i) \ . \tag{3.41}$$

Since the model is real, $y^m(\mathbf{x}_i) = y^{m*}(\mathbf{x}_i)$, so

$$\begin{aligned}\sum_i y(\mathbf{x}_i)\, y^m(\mathbf{x}_i) &= \sum_{\mathbf{k}}\sum_{\mathbf{k}'}\sum_i y_{\mathbf{k}} y^{m*}_{\mathbf{k}'} \mathrm{e}^{-\imath(\mathbf{k}-\mathbf{k}').\mathbf{x}_i} \\ &= \sum_{\mathbf{k}} y_{\mathbf{k}} y^{m*}_{\mathbf{k}} \ . \end{aligned}\tag{3.42}$$

If we wish to introduce a position shift $\mathbf{X}$ into the model without changing its shape, we can write the shifted model as

$$y^m(\mathbf{x}_i)' = \sum_{\mathbf{k}} y^m_{\mathbf{k}} \mathrm{e}^{-\imath\mathbf{k}.\mathbf{x}_i} \mathrm{e}^{-\imath\mathbf{k}.\mathbf{X}} \ , \tag{3.43}$$

and

$$\begin{aligned}\sum_i y(\mathbf{x}_i)\, y^m(\mathbf{x}_i)' &= \sum_{\mathbf{k}} y_{\mathbf{k}} y^{m*}_{\mathbf{k}} \mathrm{e}^{\imath\mathbf{k}.\mathbf{X}} \\ &= g(\mathbf{X}) \ . \end{aligned}\tag{3.44}$$

We can recognise $g(\mathbf{X})$ as the cross-correlation of the data $y(\mathbf{x}_i)$ with the model $y^m(\mathbf{x}_i)$, and the likelihood becomes

$$\mathcal{L} \propto \exp\left[\frac{|g(\mathbf{X})|^2}{2\sigma^2 \sum y^m(\mathbf{x}_i)^2}\right] \ . \tag{3.45}$$

To marginalise over $\mathbf{X}$ we will need to adopt a prior $\mathrm{p}(\mathbf{X})$. The prior in this case cannot be uniform, as $\mathcal{L} \rightarrow$constant as $|\mathbf{X}| \rightarrow \infty$ and the marginalised likelihood would not be finite. This arises because a group of pixels with values rather higher than the typical noise σ nonetheless still have a finite chance of being random fluctuations in the noise. Adopting a prior which is centred on some position and which tends to zero at large distances is equivalent to calculating $\mathcal{L}$ given that it is known that a galaxy exists close to the location of the data being fitted. Henceforth we shall assume that we are fitting two dimensional galaxy models, and it is convenient to assume a prior which is symmetric and centred on the origin of the coordinate system,

$$p(\mathbf{X})d\mathbf{X} = p(r)\, 2\pi r\, dr = \frac{1}{2\pi b^2}\mathrm{e}^{-r^2/2b^2} 2\pi r\, dr.$$

The galaxies being fitted are smooth, centrally concentrated distributions which are then convolved with near-Gaussian point spread functions to produce the observed data. Cross-correlation with a model which is itself a model galaxy convolved with the point-spread function will result in a cross-correlation function which is extremely close to being Gaussian, and hence we can write

$$g(\mathbf{X}) = g_0 \mathrm{e}^{\left[-(\mathbf{X}-\mathbf{X}_0)C^{-1}(\mathbf{X}-\mathbf{X}_0)^T\right]}, \tag{3.46}$$

where we allow the cross-correlation function not to be centred on the coordinate origin. In what follows we shall assume circular symmetry for simplicity, although this assumption may be removed without affecting the final result. Then, if the cross-correlation Gaussian function has width s,

$$\mathcal{L} \propto \frac{1}{2\pi b^2} \int_0^\infty \exp\left[g_0^2 \mathrm{e}^{-(r-r_0)^2/s^2} / 2\sigma^2 \sum y^m (\mathbf{x}_i)^2\right] \exp\left[-r^2/2b^2\right] 2\pi r dr. \tag{3.47}$$

We can expand the first exponential as a Taylor series

$$\mathcal{L} \propto \frac{1}{b^2} \int_0^\infty \sum_n \frac{1}{n!} \left(\frac{g_0^2}{2\sigma^2 \sum y^m (\mathbf{x}_i)^2}\right)^n \exp - \left[\frac{n\,(r-r_0)^2}{s^2} + \frac{r^2}{2b^2}\right] r dr\,, \tag{3.48}$$

and hence obtain a series solution for the marginalised likelihood. However, this is computationally expensive, and an alternative is to estimate the likelihood by approximating $\mathcal{L}$ itself as a Gaussian. Suppose we write

$$\begin{aligned} \mathcal{L} &= \mathcal{L}_0 \exp\left[C \mathrm{e}^{-(r-r_0)^2/s^2}\right] \\ &\simeq \mathcal{L}_0 \mathrm{e}^C \mathrm{e}^{-(r-r_0)^2/2w^2} \end{aligned} \tag{3.49}$$

where

$$C = \frac{g_0^2}{2\sigma^2 \sum y^m (\mathbf{x}_i)^2}, \tag{3.50}$$

then equating these two expressions at $r = w$, we expect

$$w^2 \simeq s^2/2C \tag{3.51}$$

for $C >> 1$. Hence the marginalisation becomes

$$\mathcal{L} \simeq \frac{1}{b^2} \int_0^\infty \mathcal{L}_0 \mathrm{e}^C \mathrm{e}^{-C(r-r_0)^2/s^2} \mathrm{e}^{-r^2/2b^2} r dr\,. \tag{3.52}$$

By expanding in Cartesian coordinates and completing the square, we find

$$\mathcal{L} \simeq \mathcal{L}_0 \mathrm{e}^C \frac{\pi s^2}{2Cb^2 + s^2} \exp\left[\frac{-Cr_0^2}{2Cb^2 + s^2}\right], \tag{3.53}$$

For $C >> 1$, and in particular for $2Cb^2 >> s^2$,

$$\mathcal{L} \simeq \mathcal{L}_0 \frac{\pi s^2}{2b^2} \frac{\mathrm{e}^C}{C} \mathrm{e}^{-r_0^2/2b^2}. \tag{3.54}$$

If the width s, centroid r_0 and amplitude g_0 of the cross-correlation function can be measured, the marginalised likelihood may be directly estimated from equation 3.54. Note that in this expression it may seem that the prior on position may be removed by allowing $b \to \infty$, but this is an artifact of approximating the likelihood by a Gaussian, which tends to zero at large distances. There is no clear way of identifying a value for b, the width of the prior for the position uncertainty, but it should not be so large that there is a significant probability of other neighbouring galaxies within a radius $\sim 3b$ of the galaxy being fitted. In the analysis which follows, b is set equal to one pixel.

3.2.5 Implementation

The surface brightness profiles of disk galaxies have been shown to be well fitted by a Freeman disc law (Freeman 1970) such that

$$\mu(r) = I_0 e^{-\frac{r}{r_c}}, \tag{3.55}$$

where $\mu(r)$ is the surface brightness at a radius r from the galaxy centre and r_c is a characteristic scale length at which $\mu(r_c) = I_0$ and is related to the half light radius by $r_h = r_c \ln 2$. Currently we choose to use this simple profile for our model galaxies but future work will test the impact of using alternative models such as the de Vaucoleurs $r^{1/4}$ law (de Vaucouleurs & Capaccioli 1979). For faint noisy galaxies the Freeman disc and de Vaucoleurs profiles are indistinguishable, so it is unlikely that this type of change in galaxy model profile will make significant differences to the final result. For an elliptical profile, the radius r is defined in terms of axial ratio β and orientation ϕ, where ϕ is measured anti-clockwise from the x axis, such that for pixel (i, j) which lies on an ellipse with centroid $(0, 0)$,

$$\begin{aligned} \Delta x &= i\cos\phi + j\sin\phi \\ \Delta y &= -i\sin\phi + j\cos\phi, \end{aligned} \tag{3.56}$$

$$r = \sqrt{\beta \Delta x^2 + \beta^{-1} \Delta y^2}. \tag{3.57}$$

Our two dimensional model galaxy, $M(\mathbf{x})$ is therefore defined by three parameters $M(\beta, \phi, r_c)$ if we marginalise over the amplitude I_0 as discussed in section 3.2.3. The relationship between (β, ϕ) and ellipticity parameters (e_1, e_2) is given in equation 2.32. Knowledge of the best fit scale length parameter is not important for weak lensing studies, and in principle can be marginalised over in the likelihood analysis.

Fourier transforms of the PSFs $\mathcal{F}(\mathrm{PSF})$, and galaxy models $\mathcal{F}(\mathrm{model})$, are stored, such that for every galaxy image only one forward Fourier transform is performed, $\mathcal{F}(\mathrm{galaxy})$. One inverse Fourier transform is performed for every galaxy model, to calculate $g(\mathbf{X})$, equation 3.46 where $g(\mathbf{X}) = \mathcal{F}^{-1}[\mathcal{F}(\mathrm{model})\mathcal{F}(\mathrm{PSF})\mathcal{F}(\mathrm{galaxy})]$. This minimal use of FFTs allows for a model-fit analysis in less than a second per galaxy, made possible from the use of recently available optimal Fast Fourier Transform software (FFT), where the most efficient routine for the problem at hand can be chosen by FFTW[5].

Currently, the likelihood equation 3.54 is calculated with Freeman disc profile model galaxies (equation 3.55). Parameters for the galaxy model are taken from a three-dimensional grid of values for (e_1, e_2, r_c) where $r_c = 0.05i, (i = 0, 100)$ and $e_j = \pm i\Delta e, (i = 0, 11)$ with $\Delta e = 0.025$, $e_j = \pm i\Delta e, (i = 3, 10)$ with $\Delta e = 0.1$, where the variable grid scale has been introduced because of the high proportion of galaxies with low ellipticities. Galaxy images are extracted in a 48×48 pixel sized square[6], centred on the galaxy centroid.

This current implementation of the technique does require some future refinement. The size of the extracted galaxy image should reflect the size of the galaxy, avoiding contamination from nearby neighbours for small galaxies and preventing artificial cuts in large galaxy images. A better method would therefore be to use an adaptive galaxy image size which is taken to be a multiple of the *SExtractor* semi-major axis or *hfindpeaks* filter size as proposed by Refregier & Bacon (2003). The grid method to find the maximum likelihood can also be refined by introducing direction set or simplex methods (Press et al. 1986) to find the best fit model thus removing any sampling scale in parameter space. It should be noted that whilst these refinements are preferable they are certainly not vital to the success of the model fitting method.

3.2.6 Shape measurement errors

There are three types of error on our estimate of galaxy ellipticity parameters. First the measurement error σ_M, which can be calculated from the χ^2 constraints as described in

[5]'Fastest Fourier Transform in the West' *www.fftw.org*

[6]This corresponds to $11.5'' \times 11.5''$ extracted regions for the COMBO-17 images section 3.3, and $15.8'' \times 15.8''$ extracted regions for the ODT images described in chapter 4.

section 3.2.2. As we are interested in joint errors in (e_1, e_2) and marginalising or projecting over r_c, the likelihood is described by a χ^2 distribution with 2 degrees of freedom and hence σ_M is given by the model $M(e_1, e_2)$ where $\ln(\mathcal{L}/\mathcal{L}_{\max}) = 1.25$. The second error is a sampling error $\sigma_s = \Delta e$ resulting from the grid of models used in the likelihood measurement as discussed above. The final error σ_U is an unknown error which could arise from say the choice of galaxy model profile, any residual PSF distortions, and the effects of galaxy isophotes overlapping with those of nearby neighbours. The errors can be combined in quadrature such that the final error on each ellipticity parameter is given by

$$\sigma^2 = \sigma_M^2 + \sigma_s^2 + \sigma_U^2 \tag{3.58}$$

3.2.7 Shape priors

Faint and noisy galaxy images poorly resemble smooth galaxy profiles, which can be seen in figure 3.3. There is a tendency with very noisy galaxy images for the maximum likelihood model to be very small in size $r_c < 0.25$ pixels, with very high ellipticity $|e| > 0.8$ and large associated nominal errors σ_M. Contamination by neighbouring sources, shown in figure 3.4, also leads to close galaxy pairs to be fit with a large highly elliptical model and the nominal fitting error σ_M does not account for this mistake. To rectify these two issues we can include a non-uniform prior on ellipticity $e = \sqrt{e_1^2 + e_2^2}$, in the final likelihood analysis equation 3.29, which favours lower ellipticity parameters where

$$p(e|I) \propto \exp\left[-\frac{1}{2}\left(\frac{e}{e_p}\right)^2\right], \tag{3.59}$$

such that $\chi^2(e) = -2(\ln[\mathcal{L}(e)] + \ln[p(e)])$ increases by 1 for $e = e_p$. The introduction of such a prior is rather unsatisfying as the choice of e_p requires some fine-tuning, but its inclusion is found to be necessary. Note that all methods inherently make some assumptions about shape, but with this Bayesian approach our assumptions become explicit.

A complementary measure places a prior on the scale length of the model r_c. We have tested first fitting galaxy images with PSF convolved circular galaxy models with $e = 0$, setting r_c from the best fit circular model and then fitting galaxy models with varying ellipticity but a constant r_c. This provides a significant speed up in the computer processing time but could potentially bias measurements towards lower ellipticities in a similar fashion to the potential

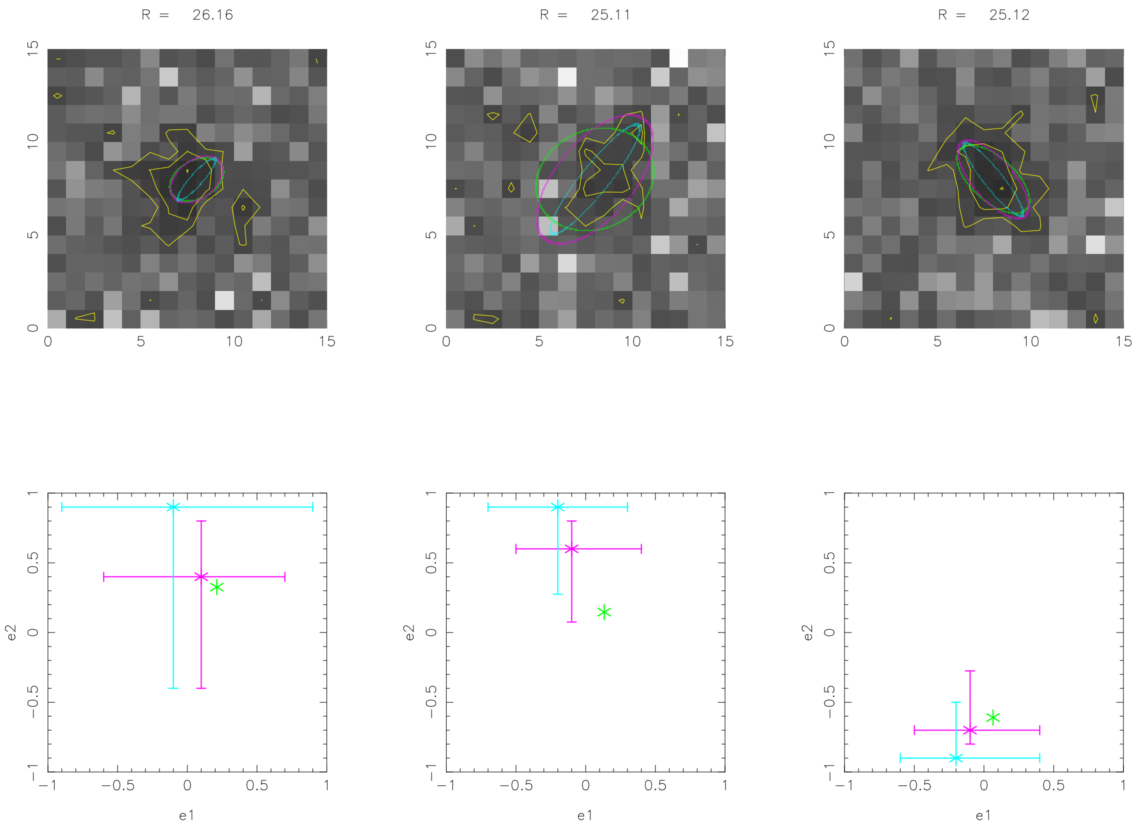

Figure 3.3: $4'' \times 4''$ faint contoured log greyscale galaxy images of magnitude R with KSB+ (green) and model fitted ellipses over-plotted at the half light radius $r_c \ln 2$. The model fitting analysis has included no prior on shape (blue) and a weak shape prior with $e_p = 1.0$ (pink). The errors σ_M on the model fitted ellipticity parameters are shown in the lower panels. The use of shape priors in the model fitting method are shown to be important in order to prevent the erroneous fitting of highly elliptical models in the presence of noise.

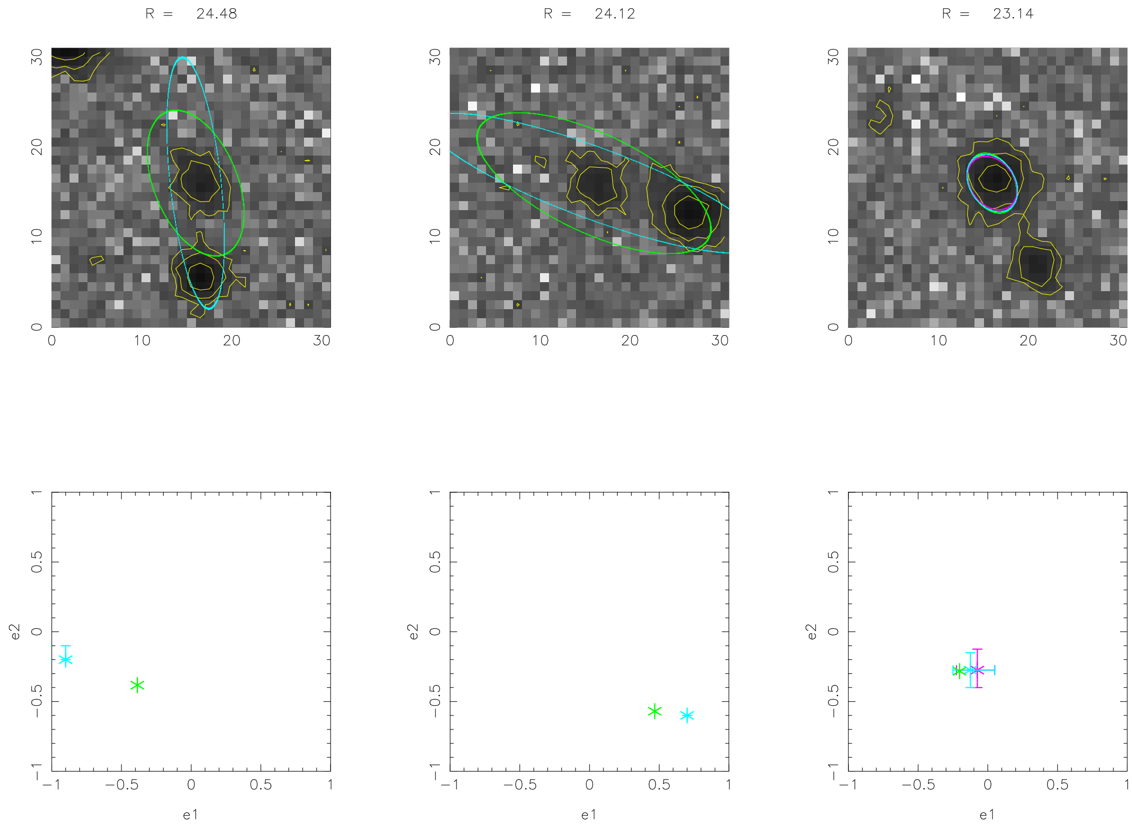

Figure 3.4: $7.6'' \times 7.6''$ contoured log greyscale images of close neighbours showing how the model fitting, including no priors on shape (blue), and the KSB+ method (green), responds to overlapping isophotes, failing in the cases where faint objects are a few pixels from a bright neighbour. The nominal fitting errors σ_M, shown in the lower panels, do not account for the true error on the model fitted ellipticity parameters. For the first two images, when we include a weak shape prior with $e_p = 1.0$ setting r_c equal to the best fitting circular galaxy, the model fitting correctly rejects the object. In the third galaxy images, where the neighbouring galaxy is faint, all three methods are successful, where the best fitting model including a weak shape prior, with $e_p = 1.0$, is shown in pink.

KSB bias from the circular weighted ellipticity measurements (equation 3.3). The preferable alternative would be to include a Gaussian prior on the scale factor with mean $\mu = r_c$, derived from the initial circular model fitting, and width σ_r, the value of which would also require some fine-tuning.

One final measure to further prevent contamination by close galaxy pairs, introduces an object rejection criteria, setting $\mathcal{L} = 0$ if the centroid r_0 of the cross-correlation function (equation 3.46) is found to be more than three pixels from the coordinate origin, i.e the centroid of the object as given by *hfindpeaks* or *SExtractor*.

Note that in the case of known nearby galaxy pairs the model fitting technique can in principle be extended to fit multiple galaxy models to the galaxies with overlapping isophotes. In this case, however, the marginalisation over amplitude and position could not be done in a single step, and the multiple model-fit would hence require longer computer processing time.

3.2.8 Shear and ellipticity

In the weak lensing regime, the shear γ is related to the average observed sheared ellipticity through

$$\gamma_i = \frac{\langle e_i \rangle}{2(1 - \sigma_e^2)}, \tag{3.60}$$

(equation 2.36) where $\sigma_e^2 = \langle e_1^2 \rangle = \langle e_2^2 \rangle$. Measurements of σ_e vary, for example Hudson et al. (1998) measure $\sigma_e = 0.23$ for galaxies in the Hubble deep field, Rhodes, Refregier & Groth (2000) measure $\sigma_e = 0.24$ for small galaxies and $\sigma_e = 0.34$ for large galaxies in HST images of the Groth strip, and Bernstein & Jarvis (2002) measure σ_e varying from 0.3 to 0.49 between the highest and lowest surface brightness bins in the CTIO survey, which they attribute to the difference between spheroid and disk dominated galaxies. In the magnitude range $20 < R < 21$ they find an average $\sigma_e = 0.38$.

In the presence of noise, shape measurements calculate $\hat{e}_i = e_i \pm \sigma$ where σ is the random shape measurement error, which for the model fitting technique is given by equation 3.58. A measure of σ_e from estimated shape measurements $\hat{e}_i$ will therefore include a systematic error as $\langle \hat{e_i}^2 \rangle = \langle e_1^2 \rangle + \sigma^2$, for constant σ. The effects of errors in different shape measurement techniques at faint surface brightnesses is therefore the most likely cause for the large variation in estimates of σ_e that is found in the literature.

An incorrect estimate of σ_e will introduce a calibration error in the weak lensing analysis of model fitted galaxies, and hence a good estimate of σ_e is vital. In practice the best estimate would come from a bright magnitude galaxy sample $R < 22$, preferably from space-based observations, if we can ignore the effects of changing galaxy morphology with redshift. Any cosmological parameter estimation would need to include the resulting calibration uncertainty and an additional error to take into account the uncertain effect of changes in typical galaxy morphology as a function of redshift.

3.2.9 Combining exposures

Typical survey strategy takes a series of three exposures per survey field, ideally offset by an integer number of pixels[7]. This effectively increases the exposure time without increasing saturation by bright stars and allows for cosmic ray removal. Weak lensing surveys are no different in their observation strategy, but how best to use these multiple exposures is debatable. In the case where the PSF and seeing is very stable, astrometric distortions are negligible, and exact integer pixel offsets have been achieved, the best method is to implement shape measurement techniques on the combined image, which will go fainter than the individual exposures. In the case of varying seeing, the use of a combined image will degrade the data to the worst seeing conditions of the three individual images, and with a varying PSF, a combined image can lead to a complicated co-added PSF which would fail KSB PSF correction (Kuijken 1999). Any slight mis-registration of the images, in the case where exact integer pixel offsets have not been achieved, will cause coherent elongations mimicking weak lensing shear. All these effects in theory are handled by an exact PSF correction scheme, but the alternative of using individual exposures may be preferable, especially in the case where one or two of the exposures have significantly worse seeing than the best seeing exposure. For the smallest objects one can do significantly better by upweighting the exposures with the best seeing. One can also get an estimate of the error on the shape measurement from the scatter between the results for the individual exposures.

Drawbacks to using individual exposures come from the increased requirements of data storage space and the fact that there will be many low surface brightness galaxies undetectable

[7] With space-based imaging, non-integer offsets may be preferable as the exposures can then be used to improve image sampling.

on the individual exposures. One compromise method is to therefore use to combined images to detect sources and determine their centre, and with this information measure shapes on the individual exposures. Note that astrometric distortions and non integer pixel offsets between exposures will introduce centroid bias when using galaxy positions as determined from a combined image. A solution to this problem is, on a galaxy by galaxy, exposure by exposure basis, to convolve each galaxy image on a fine grid with a Gaussian of width equivalent to the galaxy's measured FWHM (discussed further in section 3.3.1). The maximum in the convolved image will reveal the galaxy centre.

With the model fitting technique, centroiding bias is minimised as the positional uncertainty is marginalised over. Summing the likelihoods from each exposure will optimally combine the fitting results for each galaxy but will incur a slight increase in computer processing time. In the case of stable seeing and exact integer pixel offset exposures, where astrometric distortions are negligible, as a model fitting technique would be valid for any form of PSF including PSFs from combined exposures, it would be preferable to perform the model fitting on the combined image. This case is however rare, and it is more likely that model fitting would be applied to individual exposures.

3.3 Comparison of KSB+ and model fitting with COMBO-17

COMBO-17, the Classifying Objects by Medium-Band Observations spectrophotometric 17-filter survey (Wolf et al. 2003), is a deep multi-colour wide-field optical survey carried out with the Wide-field Imager (WFI) at the MPG/ESO 2.2m telescope that spans 1.25 square degrees to limiting magnitude $R = 25.5$ in five separate regions (Wolf et al. 2001). Multi-colour observations through a total of 17 filters, 5 broad-band ($UBVRI$) and 12 narrow band filters ranging from 420 to 914 nm, specifically chosen to facilitate accurate photometric redshift estimation (see section 4.1) with errors $\Delta_z \leq 0.05$ reliable to $R < 24$ currently span 1 square degree of the survey area. The WFI instrument consists of a 4×2 array of 2048×4096 CCDs with pixel scale $0.238''$. Weak lensing studies using the KSB+ shape measurement technique have been carried out on the deep R-band images with limiting magnitude $R = 25.5$, observed during the best seeing conditions (Brown et al. 2003), and it is the 0.27 square degree Chandra deep field south (CDFS) COMBO-17 R band image, observed in 0.81 arcsecond seeing conditions, that we will use in this section in order to compare KSB+ determined shape measurements with model fitted shape parameters. For further details on the observations and data reduction see Gray et al. (2002), and see Brown et al. (2003) for details on the creation of the KSB+ PSF and seeing corrected galaxy shape catalogues, selected with the *imcat hfindpeaks* software. For the KSB+ measurements, sky subtraction of the image was not performed. For model fitting zero sky gradients are important, and hence the CDFS images were sky subtracted with a method that will be described in section 4.2.1.

3.3.1 PSF selection

The anisotropic PSF can be determined from the shapes of stellar sources, which in the case of COMBO-17 have been classified using the stellar locus method discussed in section 4.2.2 and detailed with specific reference to COMBO-17 in Gray et al. (2002). For the KSB+ technique the resulting PSF pattern, shown in the central panel of figure 3.5, was modelled with a two-dimensional cubic to the measured ellipticities, iterating twice to remove outliers with large residuals. With the modelled stellar ellipticities the anisotropic PSF correction was made through equation 3.9, and the isotropic seeing correction was made through equation 3.20. For the model fitting stellar images extracted directly from the image are used to correct for the anisotropic PSF and seeing, a selection of which are shown in figure 3.5. To ensure that the stellar images are a good representation of the PSF at the CCD stellar position, the PSF selection was done by eye, rejecting saturated stars, stars with bad pixels, blended stars whose isophotes overlap and stars with nearby bright sources. There are cases shown in figure 3.5 (upper centre and upper right) where it is uncertain whether the stellar source is blended with a background object or whether it is a true representation of the PSF. In order to decide, the PSF pattern from neighbouring stellar sources must be consulted. For the stars shown in figure 3.5, only the upper left hand star is selected. Automation of this technique is feasible but can result in either over-zealous rejection or the inclusion of blended stellar sources in the model fitting correction. With a high density of stellar sources across the image neither of these outcomes are problematic, but for our comparison with KSB+ technique, PSF selection by eye was considered to be the most appropriate method. Note that in the case of space-based data where the PSF is fairly stable and sampled in time only

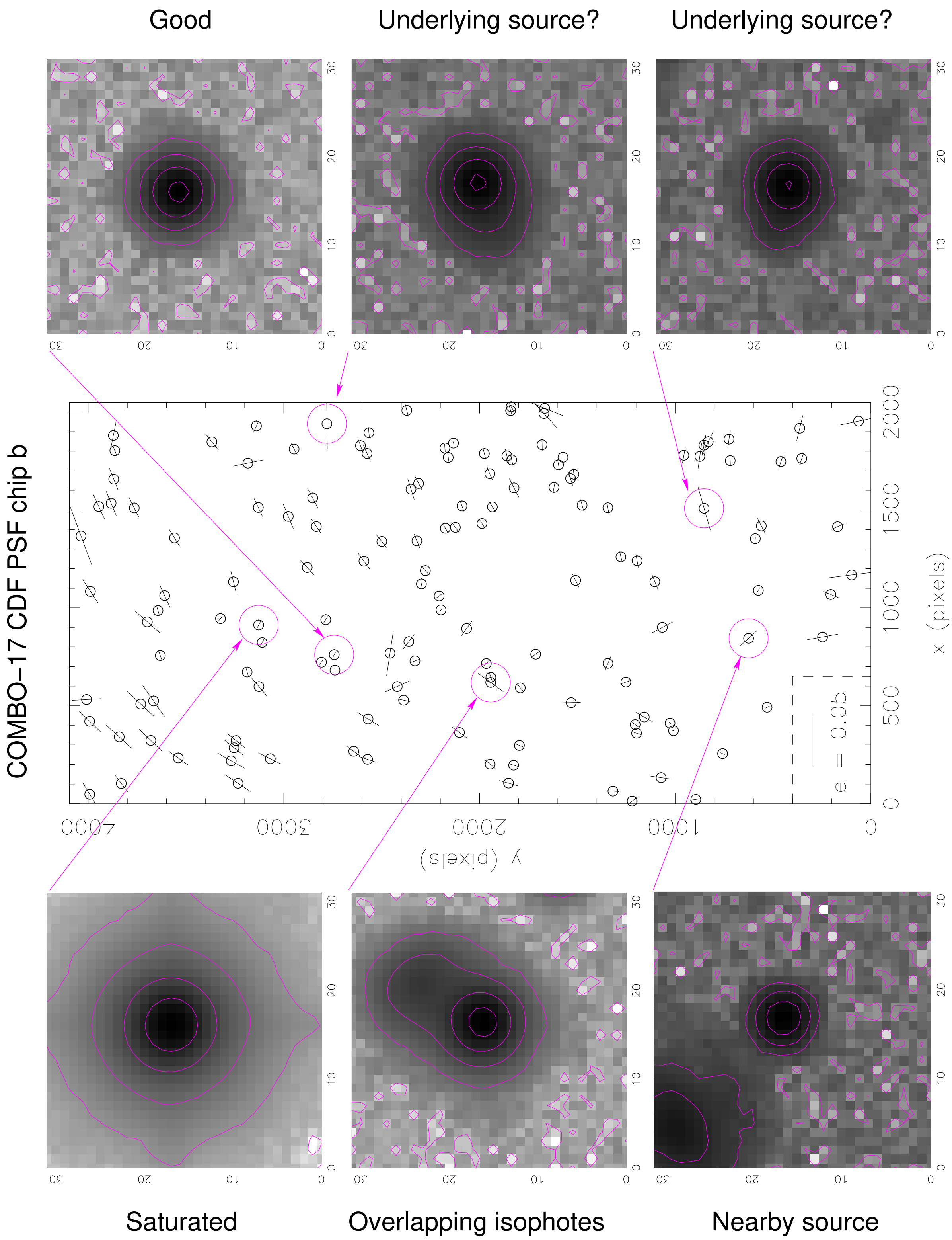

Figure 3.5: The COMBO-17 CDFS PSF chip b. Stars are individually examined to assess their suitability for model fitting. Saturated stars, stars with overlapping isophotes and stars with dominant nearby sources are rejected. For the stars shown, only the upper left hand star is selected.

occasionally through images of globular clusters (see for example Rhodes, Refregier & Groth (2000)), the application of PSF selection by eye will not be too arduous and hence would be the preferred technique. Out of the 960 stars ($\sim$ 0.9 stars per square arcminute), selected in the COMBO-17 CDFS for the KSB+ PSF correction, 738 stars ($\sim$ 0.7 stars per square arcminute) were selected for model fitting.

To increase the signal to noise of the PSF for the model fitting convolution, stellar sources are combined over an angular scale within which the PSF is considered to be fairly constant. Each selected star is cut from the image in a 32 pixel sized square, centred on the *hfindpeaks* centroid. Directly combining these pixelated stellar images would lead to a smearing of the resulting PSF image, as the true centre of each star would not be located in the centre of the *hfindpeaks* centroid pixel. The stellar image is therefore interpolated onto a fine 512 square grid of pixel scale 0.015 arcseconds, by convolving the sampled image with a Sinc function, which in Fourier space is a multiplication with a top-hat function. To interpolate the 32 pixel square image we therefore take its discrete Fourier transform, zero-pad it in Fourier space up to a 512 square grid, and take the inverse Fourier transform. The centroid is the maximum amplitude pixel in the convolution of this interpolated image with a Gaussian of width equivalent to the seeing size. Stars are combined lining up the centroid pixels, and the combined image is then sampled back down to the original image size. This is then cut down to six times the seeing size, a 20 pixel sized square, centred on the combined centroid, so as to fully sample the low surface brightness PSF wings without including contaminating light from neighbouring sources.

The drawback of combining stellar images over regions of the CCD image, is that very small scale PSF variations will effectively be averaged out, and therefore residual PSF systematics may exist below the angular scale Θ over which the stellar images are combined. For faint stars $R > 19$, at least two images are required for the PSF determination, and hence if too small an angular scale is chosen over which to combine the stellar sources, we are left with regions of the image where the PSF is undetermined and model fitting shape measurement is not possible. The solution to this problem comes from better sampling of the PSF across the chip, attainable in images where the number density of stellar objects is high. The potential contamination from residual PSF distortions below the angular scale Θ, means that the model fitting method is not well suited to weak lensing analysis with the shear variance statistic $\langle\gamma^2\rangle_\theta$ equation 2.100, which can be estimated by averaging the product of paired galaxy ellipticities for all pairs in a radial cell with radius θ equation 2.93, thereby including the PSF contamination that exists at small angular scales $\theta < \Theta$, in shear variance estimates at all angular scales θ. This is not just a problem for the model fitting technique, however, as most techniques will have some residual PSF distortions at small angular scales, due to higher order asymmetries in the PSF that are not removed using the standard second or third order two-dimensional polynomial model of the PSF variation across the image. The presence of small scale residual PSF distortions favours weak lensing analysis with the shear correlation statistic $\langle\gamma\gamma^*\rangle$ equation 2.79, and the mass aperture statistic $\langle \mathrm{M_{ap}}\rangle$ equation 2.105, estimated in terms of correlation functions (equation 2.113).

For COMBO-17 we choose to maximise the area over which model fitting is allowed by combining stellar sources over $\Theta = 3 \times 3$ arcminute regions where possible, corresponding to a 768×768 pixel boxes. The PSF is defined for the central 1 square arcminute region of each 3×3 arcminute combined region, such that the PSF for each 8×16 arcminute CCD chip is described by up to 128 combined stellar images which are Fourier transformed and stored for model fitting.

3.3.2 Ellipticity Distribution

As discussed in section 3.2, the model fitting technique requires some fine-tuning of a shape prior. One statistic which we can use to choose the shape prior is the ellipticity distribution which Bernstein & Jarvis (2002) have also shown can be used to derive an optimal weighting to reduce shot noise in the final weak lensing analysis. Figure 3.6 compares the differing probability distributions of galaxy ellipticities measured; in the APM bright galaxy survey, limited to $b_j < 16.5$ (Lambas, Maddox & Loveday 1992); in a 0.025 square degree ground-based observation of a blank field limited to $r < 26$ (Brainerd, Blandford & Smail 1996); in the HST Groth strip limited to $18 < I < 22$ (Ebbels 1998); and in the CTIO survey limited to $20 < R < 21$ (Berstein & Jarvis 2002). Some of the differences arise from the changing morphological mix in shallow and deep redshift surveys, for example the high e bump in the APM distribution comes from the high proportion of spiral galaxies in the low redshift APM

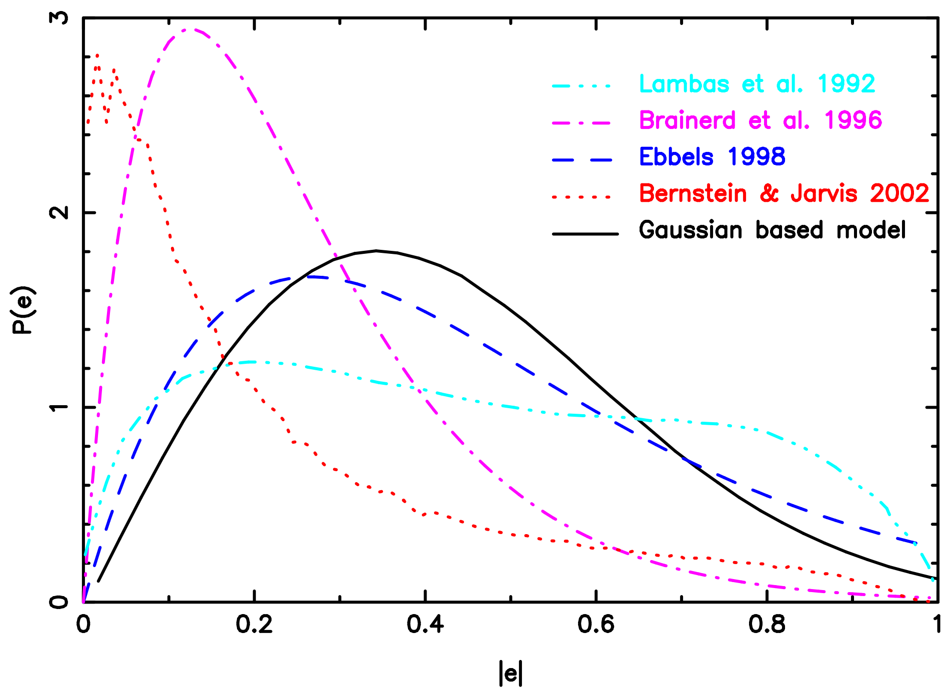

Figure 3.6: Probability distribution of ellipticities; Lambas et al. (1992) (light blue) APM bright galaxy survey $b_j < 16.5$; Brainerd et al. (1996) Palomar blank $r < 26$ (pink); Ebbels (1998) HST Groth strip $18 < I < 22$ (blue); Bernstein & Jarvis (2003) CTIO survey $20 < R < 21$ (red); Gaussian based model (black).

survey. The lower mean ellipticity in the Brainerd, Blandford & Smail (1996) distribution possibly arises from an incomplete seeing correction. Ebbels (1998) has measured the shapes of approximately 10,000 galaxies in a 108 square arcminute area of the HST Groth strip derived from second order moments using a top-hat weight function (equation 2.31). There has been no PSF or seeing correction but with HST imaging these corrections are deemed to be small. Bernstein & Jarvis (2002) have measured the shapes of 230,000 well resolved galaxies in the CTIO survey using their Gaussian decomposition technique, as described in section 3.1.5. They use this distribution as a representative measure of the real galaxy population, but comment that the distribution will vary substantially with magnitude. The variation with magnitude has been recorded by Bézecourt et al. (1999) who find a higher mean ellipticity of the Groth strip $18 < I < 25.5$ sample which they attribute to detection effects (Ebbels, Kneib & Ellis 1999), as the measured ellipticity distribution is actually a convolution of the true ellipticity distribution with measurement noise that increases for faint galaxy images. Hence the differences between the Ebbels (1998) and Bernstein & Jarvis (2002) measured ellipticity distributions is most likely a result of errors and biases in the different shape measurement

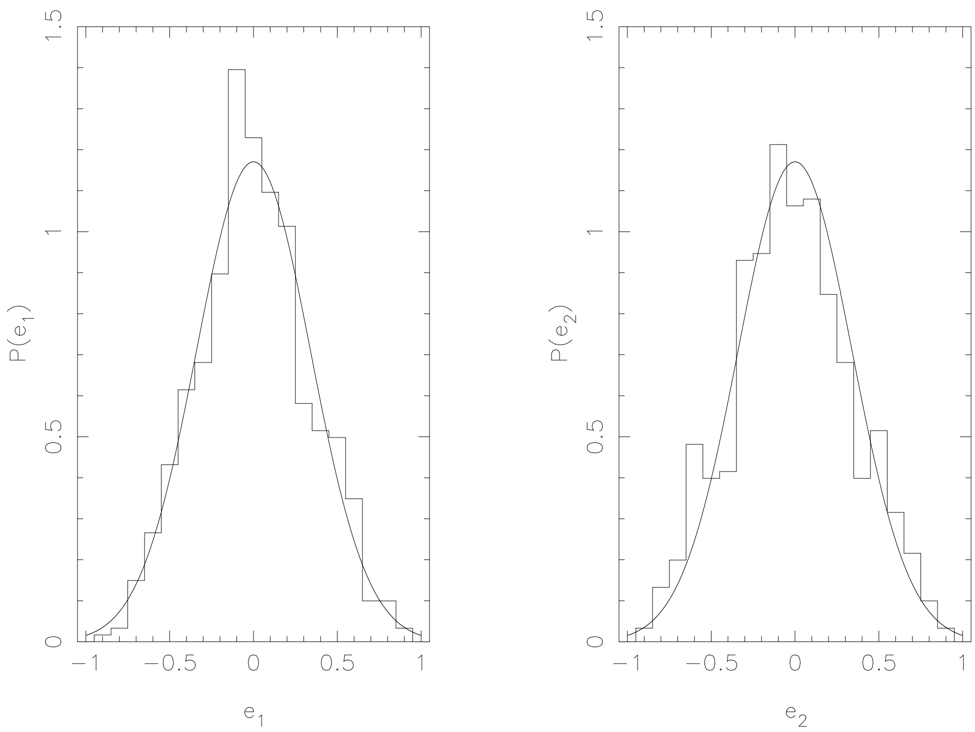

Figure 3.7: The probability distribution of model fitted ellipticity parameters determined with a weak prior with $e_p = 1.0$ from a bright galaxy sample of 602 galaxies in the CDFS with $20 < R < 22$. Over-plotted is the best fitting Gaussian, which has width $\sigma_e = 0.34$.

techniques, and only in part owing to any differences in galaxy morphology.

To simulate the effect of measurement error on the ellipticity distribution we will assume a simple model for the true distribution of galaxy shapes where e_1 and e_2 are distributed with a Gaussian probability distribution function with $\mu = 0$ and width $\sigma = \sigma_e$, where $\sigma_e^2 = \langle e_1^2 \rangle = \langle e_2^2 \rangle$, cut such that $|e| = \sqrt{e_1^2 + e_2^2} \leq 1$. We have measured σ_e from the 602 model fitted galaxies in the brightest magnitude range $20 < R < 22$ where random error measurements should be small. The bright magnitude distribution of ellipticity parameters determined with a weak prior with $e_p = 1.0$ is shown in figure 3.7 with the best fitting Gaussian, which has width $\sigma_e = 0.34$. For a range of shapes priors we find $\sigma_e = 0.34 \pm 0.01$ which agrees with the measurement of σ_e from large galaxies in the Groth strip (Rhodes, Refregier & Groth 2000). Note that from the COMBO-17 KSB+ measurements we find $\langle (\gamma_i^{\mathrm{KSB}})^2 \rangle = 0.16$ for the bright galaxies which from equation 2.36 corresponds to $\sigma_e = 0.3$. For $\sigma_e = 0.34$ the model-free ellipticity distribution $P(e)$, as shown in figure 3.6 (black), has been calculated from a sample of 10^6 mock galaxies with ellipticity parameters chosen at random from a Gaussian probability distribution with width σ_e, resulting in an ellipticity

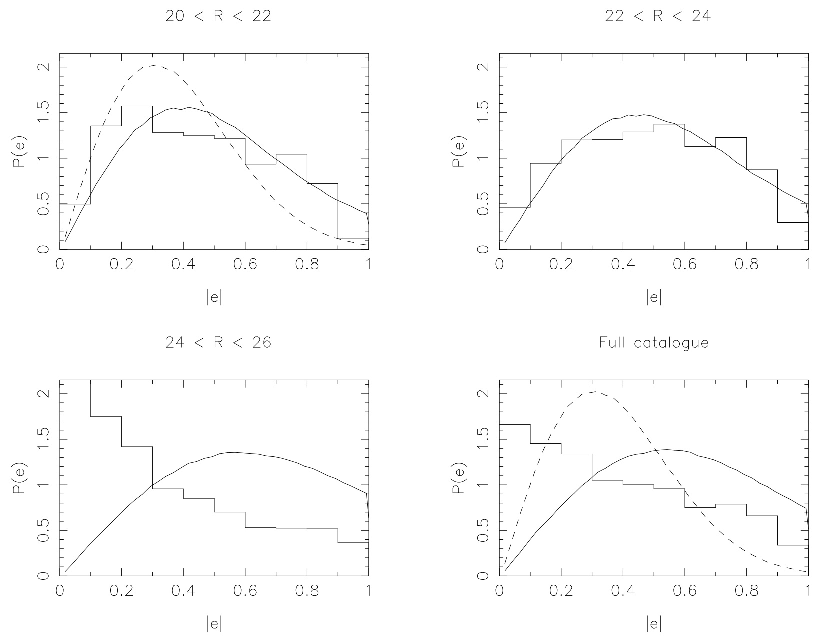

Figure 3.8: Ellipticity distribution of model fitted galaxies in the COMBO-17 in three magnitude bins determined with a strong shape prior $e_p = 0.3$. The lower right hand panel shows the distribution for the full catalogue. Over-plotted is the Gaussian based model for the true ellipticity distribution (dashed) and the error convolved model (solid). The strong prior dominates the model fitting likelihood analysis at faint magnitudes, falsely biasing the results to lower ellipticities.

distribution which is most similar to the Ebbels (1998) distribution.

We will now assume that our ellipticity parameter measurements $\hat{e}_i$ are distributed normally about the true observed ellipticity e_i with Gaussian widths given by Δe_i, where Δe_i is the average of the errors on $\hat{e}_i$, measured from equation 3.58, for the CDFS model fitted catalogue, calculated as a function of ellipticity and magnitude. We have set the unknown error in equation 3.58 to $\sigma_{\rm U} = 0.25$ which has been estimated from the unweighted scatter of the relationship between KSB+ determined shear estimators and model fitted shear estimators in section 3.3.4. We redistribute our sample of mock galaxies by these Gaussian error distributions, cut such that $|e| \leq 1$, and the resulting error convolved model ellipticity distributions for different magnitude bins can then be compared to the measured ellipticity distributions determined with different priors. Figure 3.8 shows the ellipticity distribution measured from the CDFS in different magnitude bins, with a strong prior from equation 3.59 with $e_p = 0.3$. This can be compared to figure 3.9 which shows the ellipticity distribution of the same data but this time measured with a weaker prior with $e_p = 1.0$. At bright magnitudes $20 < R < 22$

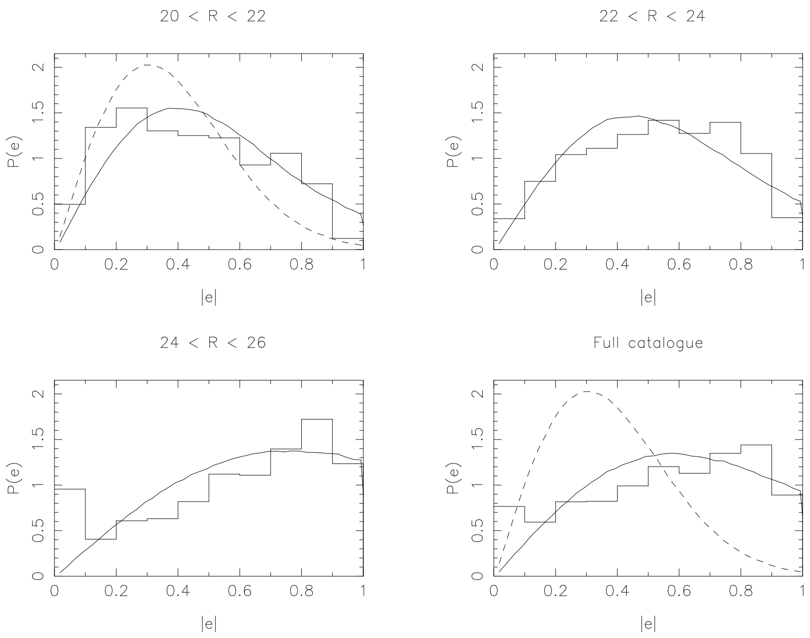

Figure 3.9: Ellipticity distribution of model fitted galaxies in the COMBO-17 in three magnitude bins determined with a weak shape prior $e_p = 1.0$. Over-plotted is the Gaussian based model for the true ellipticity distribution (dashed) and the error convolved model (solid). The weak prior produces ellipticity distributions which are consistent with the expected error convolved model distributions.

the ellipticity distributions agree, but as we go to fainter magnitudes, $24 < R < 26$, the strong prior shifts and biases the distribution to lower ellipticities. Note that this biased faint magnitude distribution is somewhat similar to the bright magnitude galaxy ellipticity distribution of Bernstein & Jarvis (2002) shown in figure 3.6, possibly hinting at a bias to circular ellipticities in their shape measurement technique, potentially arising from their initial process of PSF re-circularizing. The ellipticity distribution with a weak prior tends towards higher ellipticities as we go to fainter magnitudes in agreement with what is expected with the error convolved model distribution. The prior is strong enough however to prevent the existence of a dominant proportion of highly elliptical galaxies $e > 0.8$, which we find in the absence of any shape prior. Note that we find very little difference in the model fitted results when we also include a prior on galaxy size as discussed in section 3.2.7, implying that it is the ellipticity prior that is dominant.

The reader should now note that to implement weak lensing analysis from a model fitting technique, we have three parameters to set; the shape prior e_p in equation 3.59, the unknown shape measurement error σ_U in equation 3.58 and the ellipticity dispersion σ_e in equation 3.60.

In the simulations detailed above we have assumed $\sigma_e = 0.34$ and $\sigma_{\mathrm{U}} = 0.25$ which produces model error-convolved ellipticity distributions which are consistent with the measured ellipticity distributions in the bright magnitude bins for all tested priors. $\sigma_{\mathrm{U}} = 0.25$ has been assigned to all galaxies but for some blended objects with close neighbours that induce invalid model fits, shown in figure 3.4, $\sigma_U \gg 0.25$. It is likely that σ_U has a bi-modal distribution where $\sigma_{\mathrm{U}} \approx 0.25$ is the mean error. From figure 3.8 we can see that the use of a strong prior with $e_p = 0.3$ biases the shape measurement of faint objects towards smaller ellipticities. This would introduce a bias into weak lensing analysis, lowering the estimated value of the weak lensing shear. From figure 3.9 a weaker prior with $e_p = 1.0$ does not introduce such a strong bias whilst removing most of the erroneous high ellipticity model fits. At present we will therefore choose to use a weak shape prior with $e_p = 1.0$ placing a cut on the remaining highly elliptical objects $|e| < 0.8$. We will also use our proposed prior on galaxy size, in order to reduce the computer processing time.

With an good estimate for σ_e, our fine tuning parameters e_p, σ_U and the effects of a galaxy size prior, can be best tested with the application of the model fitting technique to simulated sheared sky images, such as those of Erben et al. (2001) Bacon et al. (2001) and Massey et al. (2003b). Testing with simulations will be important for the future use of model fitting in weak lensing analysis, and will be a key part of future work based on this chapter.

3.3.3 Object selection criteria

Objects were detected in the CDFS field with the *imcat hfindpeaks* software and selected if: the *hfindpeaks* measurement of galaxy size $r_g > 1.0$ pixel (see section 3.1.1); the *hfindpeaks* signal to noise based significance measurement $\nu > 5$; and the weighted quadrupole measurement of object ellipticity (equation 3.2), $\varepsilon < 0.5$. It should be noted that only 85% of the objects in the selected *hfindpeaks* catalogue were matched by sources in catalogues produced by the *SExtractor* source detection algorithm (Bertin & Arnouts 1996), from which aperture magnitude estimates were assigned. On application of the model fitting software to the selected *hfindpeaks* catalogue, the model fitting rejects 14.35% of the catalogue, where the best-fit galaxy model centroid is found to be more than three pixels away from the *hfindpeaks* centroid. Note that we have used a weak shape prior, equation 3.59, with $e_p = 1.0$ and our

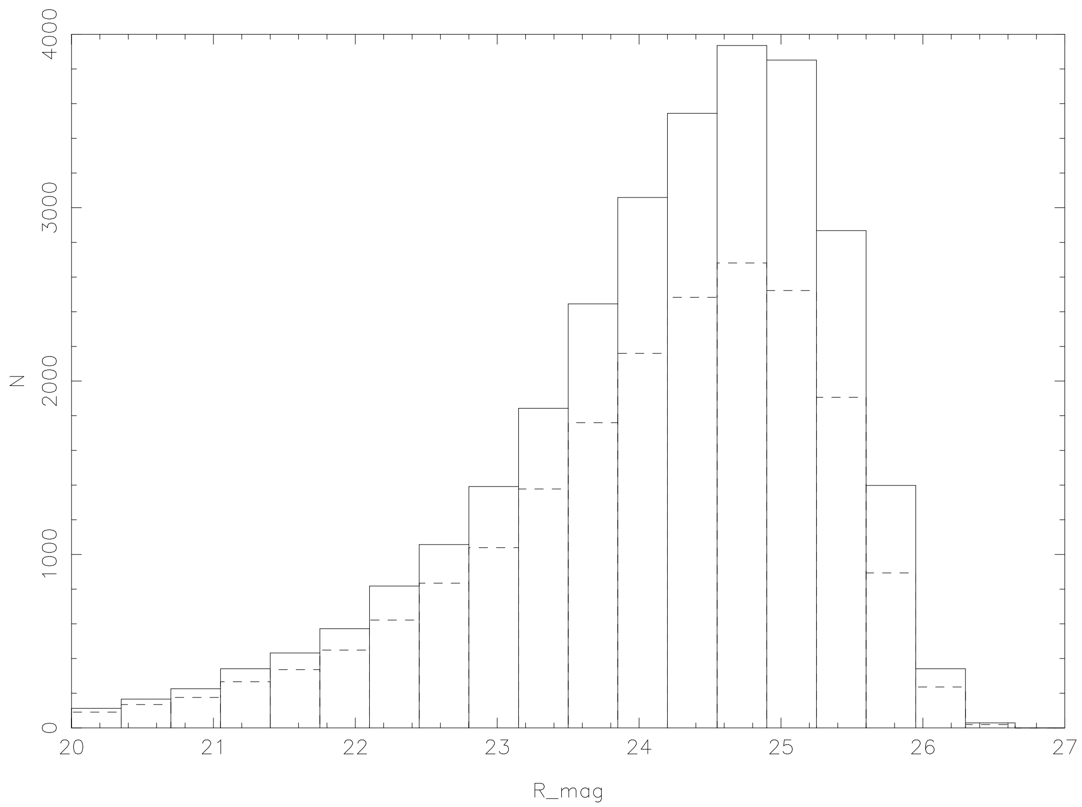

Figure 3.10: Magnitude distribution for the full COMBO-17 CDFS KSB+ shear catalogue (solid), and for the galaxies with fitted ellipticities (dashed).

proposed prior on galaxy size. Changes in the value of e_p cause only slight alteration to the percentage of rejected objects. Figure 3.10 shows the magnitude distribution of the selected *hfindpeaks* catalogue (solid) and the catalogue with model fits (dashed). The median magnitude of the full catalogue is $R = 24.35$, which decreases slightly to $R = 24.3$ for the catalogue of galaxies which have fitted parameters. This shows that the occasional rejection of objects in the model fitting technique is not caused by faint magnitudes and is most likely a result of close neighbour contamination as shown in figure 3.4, and the presence of spurious detections in the object catalogue. Note that there is no direct correlation between the rejected objects and objects which have not been detected by *SExtractor*, but the fact that at 5σ levels *hfindpeaks* extracts 15% different objects to *SExtractor*, and that *SExtractor*, will also extract sources that are undetected by *hfindpeaks*, suggests that there will be untrustworthy detections within both catalogues.

The KSB+ shear estimator produced by the *imcat* software is given by,

$$\gamma^{\mathrm{KSB+}} = \frac{\varepsilon^{\mathrm{cor}}}{P^{\gamma}}, \tag{3.61}$$

such that $\langle \gamma^{\mathrm{KSB+}} \rangle = \gamma$. It can therefore be related to the unweighted ellipticity of the observed galaxy through

$$e_i = g\gamma_i^{\mathrm{KSB+}} \tag{3.62}$$

where, from equation 3.60, $g = 2(1 - \sigma_e^2)$. Assuming that morphological differences in the full catalogue do not significantly change the ellipticity distribution measured in the bright magnitude bin where $\sigma_e = 0.34$, we can calculate an estimate of galaxy ellipticity from the KSB+ determined shear estimator by setting $g = 1.77$. in equation 3.62. In the KSB+ P^γ seeing correction equation 3.20, the PSF corrected ellipticity of galaxies $\varepsilon^{\mathrm{cor}}$ whose size is close to the seeing disc is greatly magnified such that in the COMBO-17 shear catalogue unphysical estimates of galaxy ellipticities are found, i.e $1.77\,|\gamma^{\mathrm{KSB+}}| > 1$. In order to compare KSB+ with the model fitting technique galaxies are selected from the COMBO-17 CDFS KSB+ shear catalogue if $|\gamma^{\mathrm{KSB+}}| \leq 0.56$ (17% rejection), where this cut reduces the median magnitude of the catalogue to $R = 24.15$, implying that KSB+ is failing to produce physical shape measurements mainly at the faint end. Note that for the 17% of the catalogue with unphysical KSB+ ellipticity estimates, 70% had model fit measurements. As discussed in section 3.3.1, two or more PSF selected stars are required to be within a square of 3 arcminutes from each galaxy, which yields a 2.5 % rejection rate from the galaxy catalogue. Overall the selection criteria results in model fits and physical KSB+ shear measurements for 71.25% of the catalogue, and it is this selected subset of the full CDFS COMBO-17 shear catalogue that we will use in all our tests.

3.3.4 Relationship between KSB+ shear and fitted shear

Model fitted ellipticity parameters are converted into shear estimators γ^{fit} through equation 3.60 where we will set $\sigma_e = 0.34$. With our object catalogues, where the selection criteria has been described above, we can now compare individual galaxy measurements of the KSB+ shear estimator $\gamma^{\mathrm{KSB+}}$ and the model fitted shear estimator γ^{fit}. Galaxies are binned as a function of their measured KSB+ shear estimator $\gamma_i^{\mathrm{KSB+}}$ and the weighted mean of their measured model fitted shear estimator γ^{fit} is calculated for each CCD chip with galaxy weights w_g, where

$$w_g^2 = \frac{1}{\sigma_M^2 + \sigma_s^2 + \sigma_{\mathrm{U}}^2}\,. \tag{3.63}$$

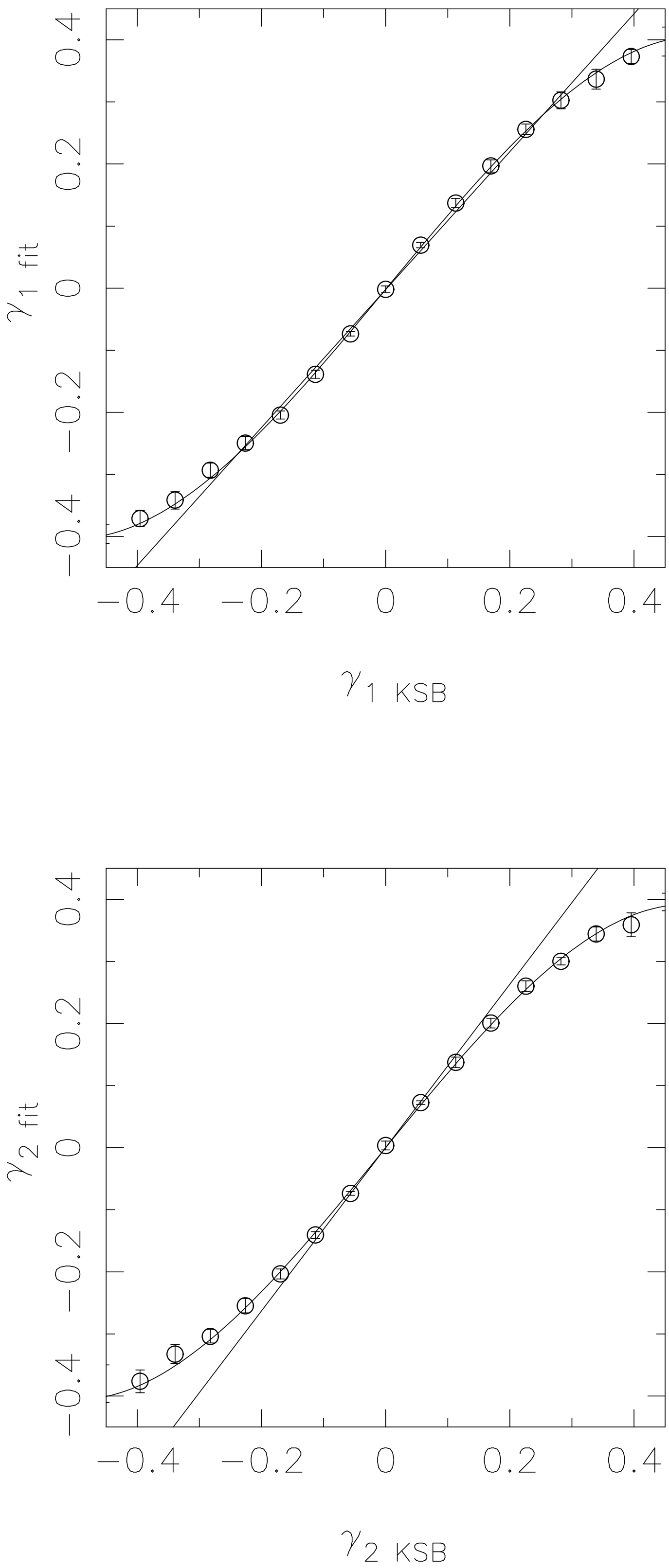

Figure 3.11: Relationship between KSB+ shear estimators and model fitted shear estimators for the CDFS selected object catalogue. Over-plotted is the Bacon et al. (2000) relationship from numerical simulations: $\gamma_1^{\rm fit} = \gamma_{1\rm KSB}/0.9$, $\gamma_2^{\rm fit} = \gamma_{2\rm KSB}/0.76$, and the best fit third order polynomial where the parameters are given in equation 3.64.

We set $\sigma_{\rm U} = 0.25$ which has been estimated from the unweighted scatter of the relationship between KSB+ shear and fitted shear and produced consistent results for our error convolved simulated ellipticity distributions discussed in section 3.3.2. Treating each CCD chip independently, the overall mean is then calculated from each chip with errors given by the empirical scatter between the chips. The resulting relationship is shown in figure 3.11 along with a linear relationship determined from sheared image simulations by Bacon et al. (2001) in the range $|\gamma_i| < 0.1$, where $\gamma_1^{\rm true} = 1.11\gamma_1^{\rm KSB}$ and $\gamma_2^{\rm true} = 1.32\gamma_2^{\rm KSB}$. We also plot the best χ^2 fit third order polynomial where

$$\begin{aligned} \gamma_1^{\rm fit} &= -1.37(\gamma_1^{\rm KSB})^3 - 0.017(\gamma_1^{\rm KSB})^2 + 1.26\gamma_1^{\rm KSB} - 0.0007 \\ \gamma_2^{\rm fit} &= -1.33(\gamma_2^{\rm KSB})^3 - 0.155(\gamma_2^{\rm KSB})^2 + 1.29\gamma_2^{\rm KSB} - 0.0013\,. \end{aligned} \tag{3.64}$$

A deviation from a linear relationship between KSB+ shear estimators and model fitted shear estimators persists in unweighted measurements, in the fitted measurements made in the absence of a shape prior, and at some degree at bright magnitudes, which can be seen in figure 3.12. It is therefore believed to be a real feature, but at this stage we would not recommend the correction to KSB+ measurements by equation 3.64, in a similar fashion to the linear correction recommended by Bacon et al. (2001) and implemented in weak lensing analysis of Bacon, Refregier & Ellis (2000); Bacon et al. (2003); Brown et al. (2003). This is because the relationship will be dependent on our choice of σ_e, and as can be seen from a comparison between figures 3.11 and 3.12, the relationship changes as a result of noise in both the KSB+ measurements and the model fitted measurements. To establish a robust correction function it will be necessary to compare KSB+ measurements and model fitted measurements in image simulations where galaxy source ellipticities and the external shear are known.

This comparison between KSB+ and model fitted shape measurements confirms the results from Bacon et al. (2001) supporting the use of a correction to KSB+ measurements in weak lensing analysis. How the need for a numerical correction factor arises in KSB+ shape determination is uncertain, possibly arising from a bias to lower ellipticities from the application of circular weighting (equation 3.3) in the measured weighted ellipticities ε equation 3.2. If it is real, which is supported by this work and the work of Bacon et al. (2001), the effect

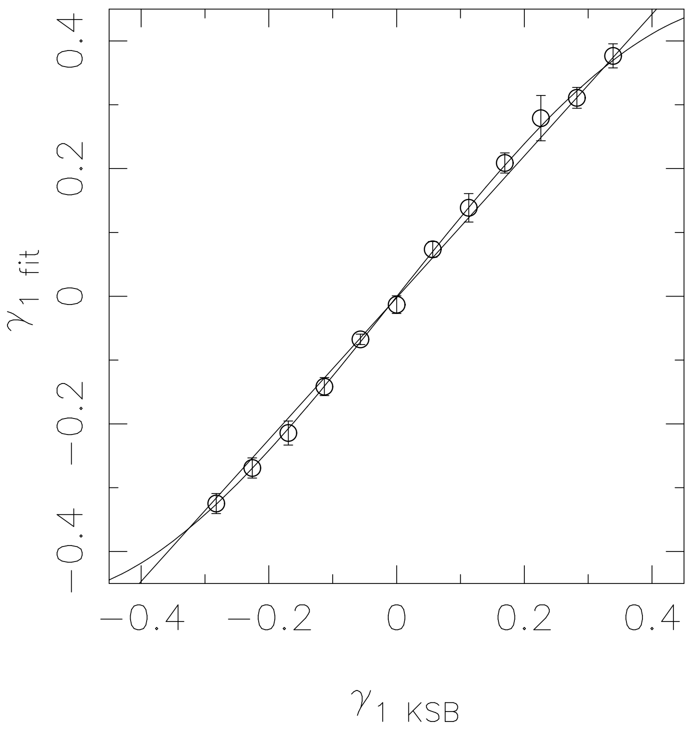

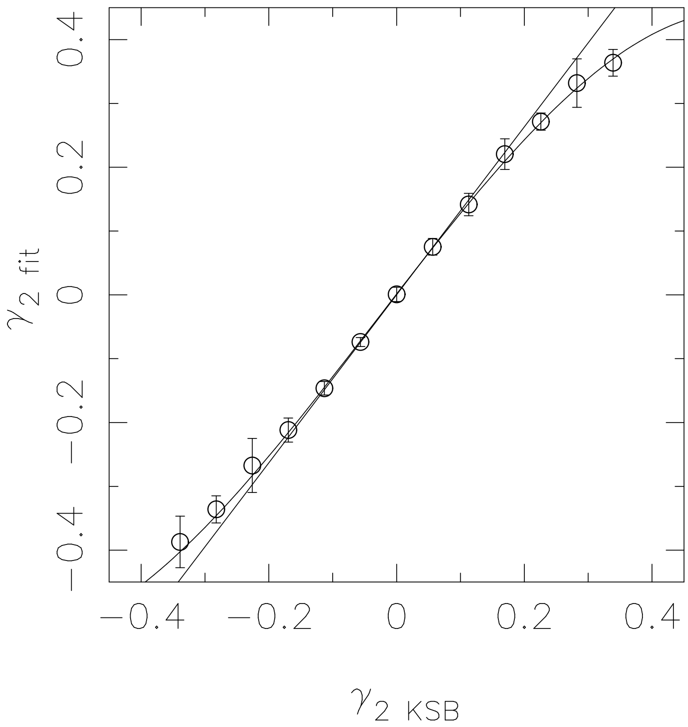

Figure 3.12: Relationship between KSB+ shear estimators and model fitted shear estimators for a bright sample of galaxies $20 < R < 22$. Over-plotted is the Bacon et al. (2000) relationship from numerical simulations: $\gamma_1^{\mathrm{fit}} = \gamma_{1\mathrm{KSB}}/0.9$, $\gamma_2^{\mathrm{fit}} = \gamma_{2\mathrm{KSB}}/0.76$, and the best fit third order polynomial.

of not including a correction would produce a calibration error in the final weak lensing analysis, resulting in the underestimation of σ_8 by $\sim 20\%$, assuming that $\langle\gamma\gamma^*\rangle \propto \sigma_8^2$, and that $\langle\gamma_{\rm true}\gamma^*_{\rm true}\rangle = k^2\langle\gamma_{\rm KSB}\gamma^*_{\rm KSB}\rangle$ where from the linear relationship of Bacon et al. (2001) $k = 1.2$.

3.3.5 Testing the success of PSF correction

A simple test for the presence of residual distortions remaining after PSF correction is to establish whether there is any correlation between the average cell measured shear $\langle\gamma_i\rangle = \Sigma w_g\gamma_i/\Sigma w_g$ with the average cell uncorrected PSF ellipticity $\langle {\rm e}_i^*\rangle$. Figure 3.13 shows the mean $\Sigma\langle\gamma_i\rangle/N_{\rm cells}$ as a function of cell PSF ellipticity $\langle {\rm e}_i^*\rangle$, where $\langle\gamma_i\rangle$ has been evaluated in square cells of side 2 arcminutes determined with KSB+ shear estimators (crosses) and model fitted shear estimators (circles). The uncertainty shown is the error on the mean. For the fitted shape parameters w_g is given by equation 3.63, and for the KSB+ shapes $w_g \equiv 1$. From figure 3.13 we see that after PSF correction the average galaxy shear estimator is bounded between ± 0.01, and that both shape measurement techniques produce results which are consistent with zero, although this test is dominated by the shot noise from the small 2 arcminute cells.

The effect of residual PSF distortions on the shear correlation estimator (equation 2.69) can be calculated by considering the measured shear γ_i' as the sum of the true shear γ_i with a small additional contribution from the PSF ellipticity,

$$\gamma_i' = \gamma_i + a_i e_i^* \tag{3.65}$$

An estimate of the shear correlation measures the true shear correlation plus a systematic PSF component,

$$\langle\gamma_i'\gamma_j'\rangle = \langle\gamma_i\gamma_j\rangle + a_i a_j\langle e_i^* e_j^*\rangle\,. \tag{3.66}$$

Noting that

$$\langle\gamma_i' e_j^*\rangle = a_i\langle e_i^* e_j^*\rangle\,, \tag{3.67}$$

as $\langle\gamma_i e_j^*\rangle = 0$, we find that uncorrected ellipticities add a component to the measured correlation function $c_k^{\rm sys}$ where

$$c_k^{\rm sys} = a_i a_j\langle e_i^* e_j^*\rangle = \frac{\langle\gamma_i' e_j^*\rangle\langle\gamma_j' e_i^*\rangle}{\langle e_i^* e_j^*\rangle}. \tag{3.68}$$

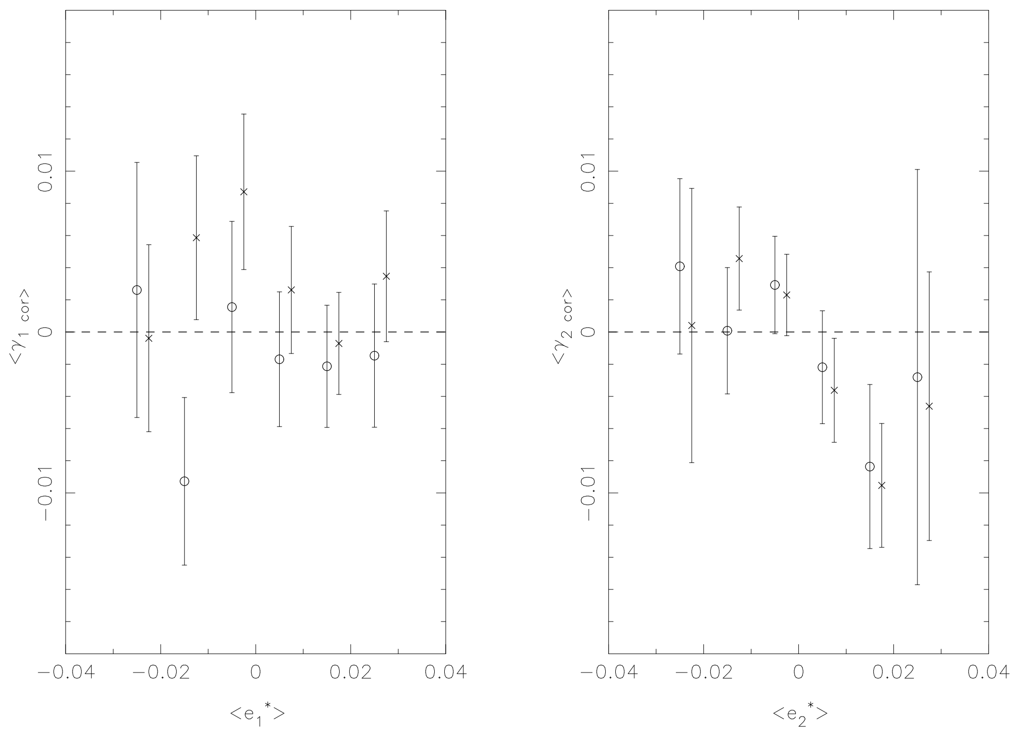

Figure 3.13: The average galaxy shear $\langle\gamma_i\rangle$ from KSB+ measurements (crosses), and from model fitting measurements (circles) measured in 2 arcminute cells with average stellar ellipticity e_i^*.

Assuming $a_i \approx a_j$ we can use equation 3.68 to calculate the residual systematics in the tangential (t) and radial (r) shear correlation estimators (equation 2.84), as the systematically induced cross-correlation between the galaxies corrected for PSF anisotropy and the uncorrected stars $c_k^{\rm sys}$ can be determined from the image for each CCD chip. The notation used is: when $i = j = {\rm t}$, $k = 1$, when $i = j = {\rm r}$, $k = 2$ and when $i = {\rm r}, j = {\rm t}$ and $k = 3$.

Figure 3.14 shows the resulting average star-galaxy cross-correlations for KSB+ shear estimators (crosses) and model fitted shear estimators (circles), where we have averaged over the 8 CCD chips in the CDFS in a similar fashion to the shear correlation estimator equation 2.69. Note that a weighted star-galaxy cross-correlation is given by $\langle\gamma_i' e_j^*\rangle = \Sigma(w_g \gamma_i' e_j^*)/\Sigma w_g$ where for the model fitted catalogue, w_g is given by equation 3.63, and for the KSB+ catalogues, $w_g \equiv 1$. We find that both shape measurement techniques fail to produce results that are consistent with zero finding $c_k^{\rm sys} \sim 2 \times 10^{-5}$. This is consistent with the published non-zero star-galaxy cross correlation of Bacon et al. (2003), but not with the zero star-galaxy cross correlation found in the full analysis of all five COMBO-17 deep R-band images (Brown et al. 2003). Interestingly the CDFS field contains a relatively low surface density of stars com-

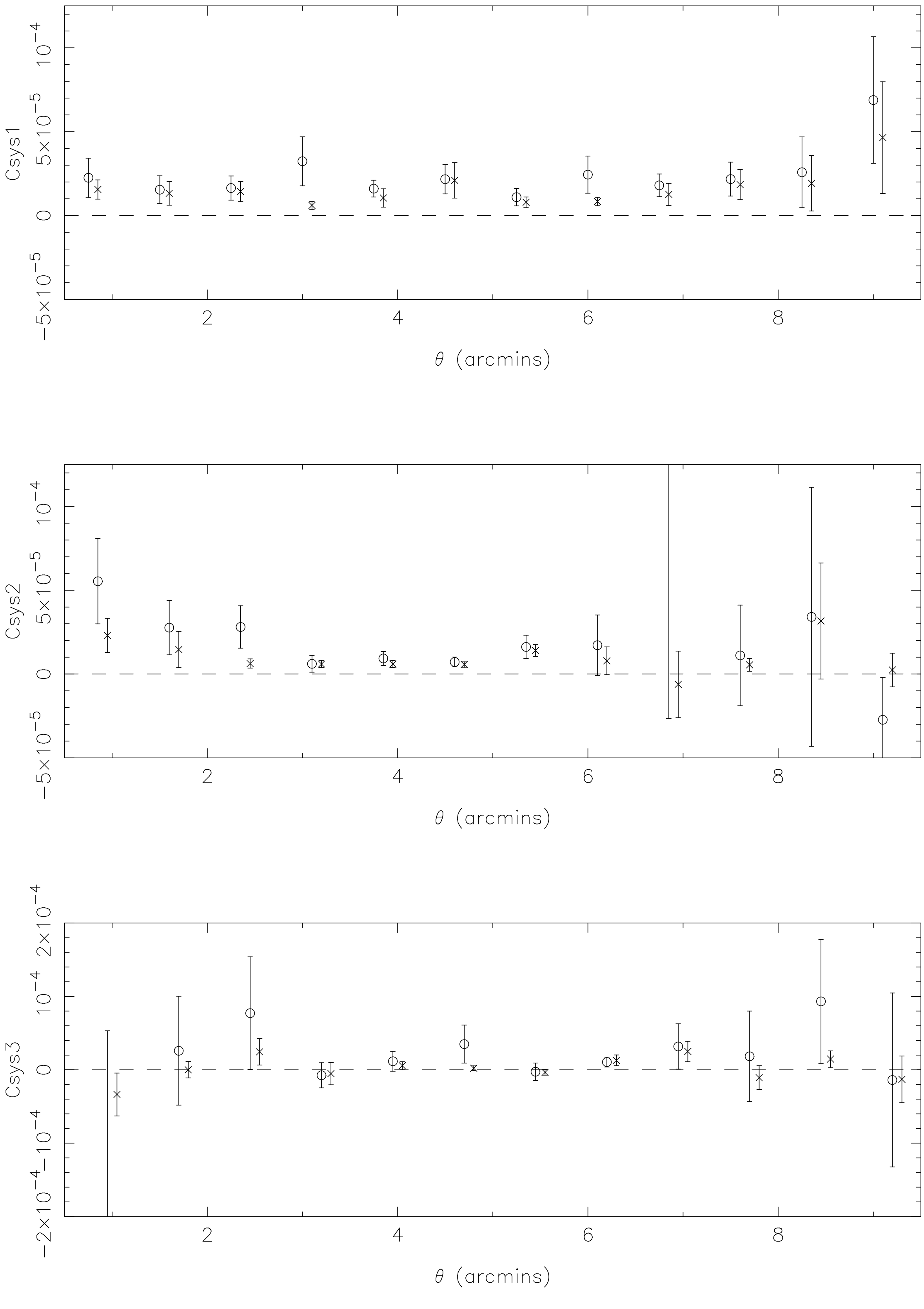

Figure 3.14: Star-galaxy cross correlation, defined in equation 3.68, using the KSB+ shear estimator (crosses) and weighted model fitted shear estimators (circles). Above 3 arcminutes the residual PSF contamination left by the KSB+ technique and the model fitting technique are similar, with the variation in the chip-to-chip residuals increasing at large angular scales $\theta > 7'$ owing to the fewer number of star-galaxy pairs.

pared to the other COMBO-17 fields analysed in the full COMBO-17 weak lensing survey. Hence, we can conclude that the residual PSF correction in both methods may arise from poor PSF sampling. For the model fitting technique small scale variations will be averaged out when stars are combined to produce PSF representations and this may produce residual PSF contamination at small scales $\theta < 3'$. At the edges of the chip $\theta > 7'$ where the PSF representations will be composed of small numbers of stars we can expect a poorer PSF correction. The larger variation between chips is an artifact of the shot noise from the smaller number of star-galaxy pairs at wide $\theta > 7'$ separations. For the KSB+ technique small scale variations will also be smoothed out by the polynomial PSF model, and at the edges of the chip where there are few stars to constrain the model the PSF correction will also be poor, accounting for the increased residual distortions at angular scales $\theta > 7'$. For the CDFS field the residual systematic errors measured are of the order 10% contamination to the expected weak lensing signal.

From the comparison of the residual PSF distortions left by both shape measurement techniques we find that the model fitting is not better than KSB+ at removing PSF distortions, but for angular scales above the PSF correction scales, which for the CDFS was set at 3 arcminutes, the model fitting is at least as good as KSB+, with the added advantage of error estimates determined for individual galaxy shape measurements. With a full analysis of the higher stellar density COMBO-17 fields, a better comparison will be attainable, where we expect PSF residuals in both methods to decrease.

3.3.6 COMBO-17 Shear Correlation

The benefit of using the model fitting technique is the ability to determine errors on the shape measurement, allowing for a signal-to-noise weighted lensing analysis. This will be carried out, in due course, on the full COMBO-17 1.25 square degrees of deep R-band data. For the purposes of this thesis, figure 3.15 shows the total galaxy-galaxy shear correlation measurement for the CDFS field, as defined in equation 2.69, where we have treated each CCD chip as an independent field, ($N_f = 8$). For the model-fitted parameters a noise weighting, given by equation 3.63, has been used for the shear correlation estimator (equation 2.68), and for the KSB+ measurements each galaxy pair weight has been set to unity. The measured

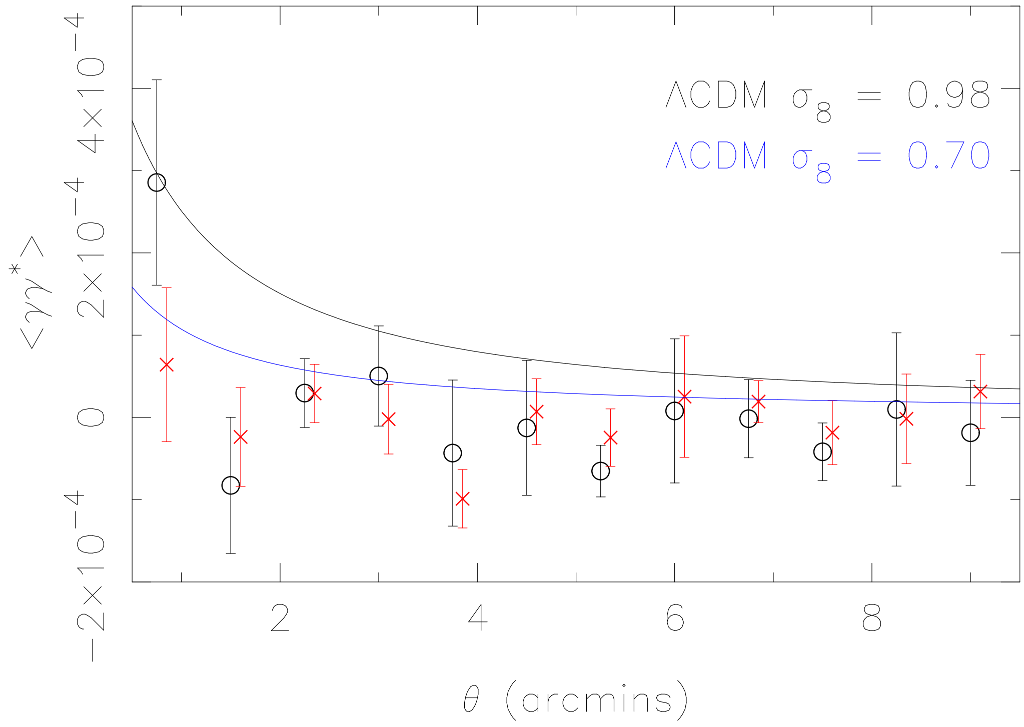

Figure 3.15: Galaxy-galaxy shear correlation $\langle\gamma\gamma^*\rangle$ using KSB+ shear estimators (crosses) and noise weighted model fitted shear estimators (circles), compared to the theoretical shear correlation derived for a $z_m = 0.85$ survey with a ΛCDM cosmology, normalised by $\sigma_8 = 0.98$ (black) and $\sigma_8 = 0.7$ (blue).

total correlation functions $\langle\gamma\gamma^*\rangle$ from both techniques shown in figure 3.15, are compared to a ΛCDM weak lensing signal calculated from a non-linear power spectrum normalised by $\sigma_8 = 0.98$ (black) and $\sigma_8 = 0.7$ (blue), calculated from equation 2.79 with $h = 0.7$, $\Gamma = 0.21$ and where we have assumed a smooth redshift distribution from equation 4.1 with $z_m = 0.85$. Both techniques favour the lower value for σ_8 but it should be noted that the points are strongly correlated. Note that the measured cross correlation $\langle\gamma_r\gamma_t\rangle$ is consistent with zero for both shape measurement techniques.

Future analysis will use a more preferable signal-to-noise weighting as a purely noise weighted sample will have a lower effective median redshift than the unweighted sample, as the faintest higher redshift galaxies tend to have the largest errors. Applying signal-to-noise weighting should produce a more accurate estimate of the weak lensing signal, although it will be important to quantify the effects of any weighting scheme on the theoretical expectation of the weak lensing signal, in a similar fashion to the derived galaxy-pair weighted lensing signal in appendix A.

In this section, promising results from a Bayesian approach for determining weak lensing shear have been presented. Provided one can arrive at a good estimate for the ellipticity dispersion σ_e in order to convert ellipticity measurements into shear estimators, the model fitting technique is an excellent alternative to the KSB+ technique which does not require the empirical correction proposed by Bacon et al. (2001), which is supported by the findings of this chapter. Future work will involve the fine-tuning of galaxy shape priors through the application of model fitting methods to sheared image simulations. Such work will also allow for the rigorous testing for any biases in the shape determination, yielding good prospects for future unbiased signal-to-noise optimised weak lensing measurements from the use of fast model-fitting techniques.

3.4 Selection Bias

To conclude this chapter we should note that even if a perfect deconvolution of PSF and seeing effects is feasible there are two important selection effects which will give rise to biased weak lensing measurements. Object selection bias is intimately linked to the selection criteria of source extraction algorithms. Consider identical galaxies A and B oriented perpendicularly on the sky such that $e_i^A > 0$ and $e_i^B < 0$. A PSF elongated in the same direction as galaxy A with $e_i^* > 0$, will increase the surface area of the convolved image of galaxy B compared to the surface area of the convolved image of galaxy A. This will lower the surface brightness of the observed galaxy B compared to the surface brightness of the observed galaxy A and as most detection algorithms involve some cut in surface brightness, at some magnitude only galaxy A will be selected. This means that the detected population will be biased towards those galaxies with $e_i > 0$ whose shape is similar to that of the PSF. This will bias the mean of the population such that $\langle e^s \rangle \neq 0$. One could imagine a circularizing procedure, which convolves the image with a re-circularizing PSF, oriented opposite to the original PSF, implementing source extraction algorithms on this new convolved image. This approach as proposed by Kaiser (2000), would also aid the PSF anisotropy correction, but introduces an analogous noise bias whereby the noise component in the original image becomes correlated in the convolution, with the re-circularizing PSF. With this scheme there is hence a tendency for convolved galaxies close to the detection threshold to be aligned opposite to the PSF. The solution to selection bias or noise bias, which has been estimated to produce a shear of around 1% in faint objects with a PSF asymmetry of $e \sim 0.3$ (Kaiser 2000), is to introduce a sensible limit on the significance of object detection. BJ02 propose that this significance threshold is determined in the re-circularized images, with shape measurement techniques implemented in the original image. This increased significance threshold has the effect of reducing the faint galaxy population in the sample, but as we have shown with our model fitting technique the information available from this faint population is minimal. Model-fitting allows for the correction of this bias exactly, as galaxy samples can be selected by the model-fitted flux, rather than the observed flux.

Hirata & Seljak (2003) have highlighted an additional shear selection bias which is perfectly anti-correlated with the shear signal, taking on the form of a final calibration error. This arises from the fact that object detection algorithms for low surface brightness objects may preferentially detect circular objects, which is likely to be the case for the *imcat* object detection software *hfindpeaks*. If galaxy A is aligned perpendicular to the shear field its image will become more circular, whereas galaxy B will be sheared to a higher ellipticity, but both will retain the same surface brightness. If at low surface brightnesses, the object detection algorithm favours more circular objects, only galaxy A will be detected. This only affects resolved galaxies and has been estimated to lead to underestimate of σ_8 by up to 8% (Hirata & Seljak 2003). Alternative detection algorithms such *SExtractor* are sufficiently 'black box' that it is unclear whether this effect is important or not. The only way to test and quantify such a bias is to use image simulations.

4

Cosmic shear and the Oxford Dartmouth Thirty degree survey

In this chapter a feasibility study of the Oxford Dartmouth Thirty degree survey (ODT) for use as a cosmic shear survey is undertaken. Observed with the 2.5m Isaac Newton Telescope in La Palma (INT) on the prime focus wide-field camera, the ODT currently spans twenty-five square degrees in BVRiz. Intended to reach limiting 5σ depths of $B = 26.0$, $V = 25.5$, $R = 25.25$, $i = 24.5$ and $z = 22.0$ with an additional two square degrees in U to a limiting depth of $U = 25.0$ and an additional 4 square degrees in K to a limiting depth of $K = 18.8$, the ODT could in principle be the widest deep, multi-colour survey presently available for weak lensing studies.

As the ODT, and in particular the wide-field camera, was not initially designed with weak lensing studies in mind, the imaging is subject to extensive sources of significant distortions which are typically minimised in surveys where weak lensing is the primary goal. The rationale for attempting such a study regardless, was the availability of deep and wide-field multi-colour data, which in principle would not only provide a good consistency check for the data analysis techniques, but more importantly provide vital photometric redshift information that is not often available for weak lensing studies as can be seen from the list of published weak lensing surveys in table 4.1.

ID	σ_8	Statistic	Survey	$\mathrm{m_{lim}}$	$\sim z_m$	Photo z's?	Shape	E/B mode?
Maoli	1.03 ± 0.05	$\langle\gamma^2\rangle$	VLT 8.2m	$I = 24.5$	1.1	$\times$	KSB+	$\times$
et al. 2001			$0.65\,\square^\circ$					
Rhodes	$0.91^{+0.25}_{-0.29}$	$\langle\gamma\gamma\rangle$	HST 2.4m	$I = 26.0$	0.9	$\times$	RRG00	$\times$
et al. 2001			$0.05\,\square^\circ$					
Van Waerbeke			CFHT 3.6m	$I = 24.0$	1.0	$\times$	KSB+	$\surd$
et al. 2001	0.88 ± 0.11	$\langle\gamma^2\rangle$, $\langle\gamma\gamma\rangle$, $\langle\mathrm{M}^2_{\mathrm{ap}}\rangle$	$8.0\,\square^\circ$					
et al. 2002	0.94 ± 0.12	$\langle\mathrm{M}^2_{\mathrm{ap}}\rangle$	$12.0\,\square^\circ$					
Hoekstra			CFHT+CTIO	$R = 24.0$	0.56	$\times$	KSB+	
et al. 2002 (a)	0.81 ± 0.08	$\langle\gamma^2\rangle$	$24.0\,\square^\circ$					$\times$
et al. 2002 (b)	$0.91^{+0.05}_{-0.12}$	$\langle\gamma^2\rangle$, $\langle\gamma\gamma\rangle$,$\langle\mathrm{M}^2_{\mathrm{ap}}\rangle$	$53.0\,\square^\circ$					$\surd$
Bacon	0.97 ± 0.13	$\langle\gamma\gamma\rangle$	WHT 4.2m +	$R = 25.0$	0.8	$\times$	KSB+	$\times$
et al. 2003			Keck 10m $1.6\,\square^\circ$					
Réfrégier	0.94 ± 0.17	$\langle\gamma^2\rangle$	HST 2.4m	$I = 23.5$	0.9	$\times$	RRG00	$\times$
et al. 2002			$0.36\,\square^\circ$					
Jarvis	$0.71^{+0.12}_{-0.16}$	$\langle\gamma^2\rangle$, $\langle\gamma\gamma\rangle$, $\langle\mathrm{M}^2_{\mathrm{ap}}\rangle$	CTIO 4m	$R = 23.0$	S/N weight	$\times$	BJ02	$\surd$
et al. 2003			$75\,\square^\circ$		0.66			
Brown	0.74 ± 0.09	$\langle\gamma^2\rangle$, $\langle\gamma\gamma\rangle$, $P_\kappa(k)$	ESO 2.2m	$R = 25.5$	0.85	$\surd$	KSB+	$\surd$
et al. 2003			$1.25\,\square^\circ$					
Hamana	$0.69^{+0.35}_{-0.25}$	$\langle\mathrm{M}^2_{\mathrm{ap}}\rangle$, $\langle\gamma\gamma\rangle$	Subaru 8m	$R = 26$	1.1	$\times$	KSB+	$\surd$
et al. 2003			$2.1\,\square^\circ$					

Table 4.1: Constraints on the power spectrum normalisation σ_8 for a flat Universe with $\Omega_m = 0.3$, obtained from a given 'Statistic'. 'E/B mode?' tells us whether or not a B mode decomposition has been performed. Those surveys which have performed such a decomposition have found a non-zero B mode and, with the exception of Van Waerbeke et al. (2001) and Brown et al. (2003), this B-mode has been used in the likelihood analysis. There are also cosmic shear detection results obtained by Wittman et al. (2000), Kaiser et al. (2000), Hämmerle et al. (2002) and Bacon et al. (2000) which have not been included in this table. Note that Maoli et al. (2001) include the results from different depth surveys; Van Waerbeke et al. (2000), Kaiser et al. (2000), Bacon et al. (2000) and Wittman et al. (2000) in the likelihood analysis for σ_8.

Deep wide-field lensing surveys with accompanying photometric redshift information do not currently exist mainly because of the extensive additional observing time required to gain the multi-colour information, although Heavens (2003) argues that for a set observing duration, the gain in information from photometric redshift estimates is approximately equal to the loss in information from the reduced survey area. The COMBO-17 survey is the only weak lensing survey to date with some photometric redshift information, where their observing strategy dictated that deep data was taken in R under good observing conditions, with additional multi-colour data taken to shallower depths in poorer seeing conditions (Wolf et al. 2003). This allows for photometric redshift estimation of the foreground structure which can be used in conjunction with model redshift distributions (equation 4.1) to provide a good estimate of the redshift distribution of the deeper lensing data (Brown et al. 2003). Even with this compromise measure however, the acquisition of photometric redshift estimates for deep wide-field surveys is very demanding on observing time. With this study we will therefore pose the question; do weak lensing surveys require highly competitive 3.6-metre-plus telescope time and/or space-based instrumentation, or can such surveys be carried out on the less competitive, possibly dedicated, smaller telescopes such as the INT?

4.1 Photometric Redshifts

The inclusion of redshift information in weak lensing surveys allows measurement of the true redshift distribution $\phi_z(z)$ that can often only be estimated from model redshift distributions where,

$$\phi_z(z) \propto z^2 \exp\left[-\left(\frac{z}{z_0}\right)^{1.5}\right], \tag{4.1}$$

(Baugh & Efstathiou 1994). For a survey with median redshift z_m, $z_0 \approx z_m/1.4$, where the median redshift can be estimated from the magnitude limit of the survey (Hoekstra et al. 2002; Brown et al. 2003). Knowledge of the true redshift distribution is vital for accurate cosmological parameter estimation from weak lensing studies. As the cosmic shear signal scales roughly with the square of the median redshift of the survey $\langle\gamma\gamma^*\rangle_\theta \propto z_m^2$ (Barber 2002), with a deeper survey we expect to see a higher cosmic shear signal. Assuming that a survey is shallower than it actually is would therefore result in an incorrect higher estimate of σ_8. In the absence of a measured redshift distribution the best solution is to use a model

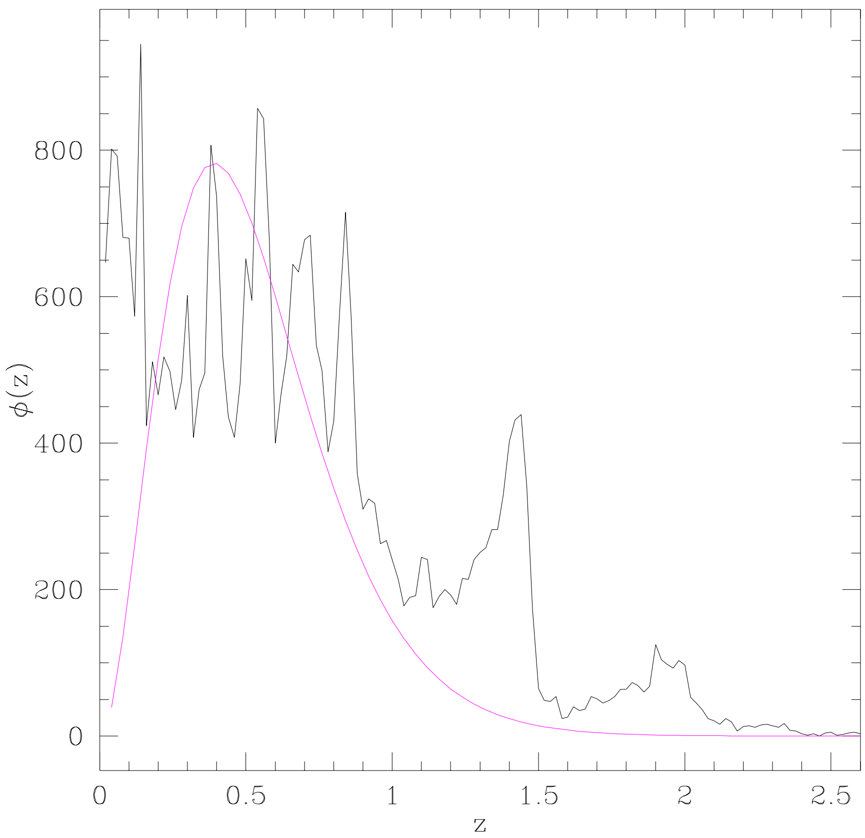

Figure 4.1: The COMBO-17 redshift distribution for 0.75 square degrees limited to $R = 24$, compared to the redshift distribution model equation 4.1, for a median redshift $z_m = 0.6$. Note that the normalisation of the model is arbitrary and that the peak at $z \sim 1.4$ is most likely a false artifact of the photometric redshift model fitting procedure.

distribution like equation 4.1, or assume that all galaxies lie in a plane at redshift $z_s = z_m$, and then marginalise over the uncertain median redshift of the survey in the likelihood analysis (Van Waerbeke et al. 2002). This solution however assumes that the chosen model redshift distribution is correct. As can be seen from the COMBO-17 photometric redshift distribution for 0.75 square degrees limited to $R = 24$ in figure 4.1, where from the limiting magnitude we would assume a median redshift of $z_m \sim 0.6$, for smaller area surveys, neither the plane assumption or the Baugh & Efstathiou (1994) model from equation 4.1 provide an adequate description of the true redshift distribution. It is important to be aware of any overdensities in the redshift distribution from galaxy clusters, as the mass of a cluster will increase the cosmic shear signal and, without knowledge of the true redshift distribution, this increase would affect the cosmological parameter estimation (Brown et al. 2003).

Redshift information also enables us to consider alternatives to the standard cosmic shear estimators detailed in section 2.5. For example, it allows the statistical properties of large scale structures to be determined tomographically by splitting a galaxy sample into redshift bins, lifting the degeneracies between the amplitude of the power spectrum σ_8 and the matter density parameter Ω_m which exist in current cosmological parameter estimation from two-point lensing statistics (Hu 1999; Refregier et al. 2003). Redshift estimates also allow the application of 3D lensing statistics (Heavens 2003).

Traditionally, redshift estimates have been determined spectroscopically, from the observed redshift of emission features in galaxy spectra, but as spectroscopy cannot probe as deep as photometry, and as for many studies, including weak lensing, the high accuracy acquired with spectroscopy is not strictly necessary, there has been an extensive development of a technique called photometric redshifts. With this technique evolutionary models for many different types of galaxy spectra are used to predict colours for different types of galaxies at varying redshifts. With a simple χ^2 analysis, equation 3.32, it is then possible to assign redshifts, with associated errors, to multi-colour galaxy data. If the models are a good description, then this technique can produce very sensible results. Software is now publicly available to calculate photometric redshifts from a catalogue of galaxy colours (Bolzonella, Miralles & Pello 2000), where the template models are typically taken from Bruzual & Charlot (1993) and Coleman, Wu & Weedman (1980). The uncertainty Δ_z, in the resulting redshift depends on the number of colours known for each object and the accuracy of the photometry, for example with $UBVRiJHK$ colours with photometry accurate to $\Delta m = 0.1$, $\Delta_z \approx 0.07$ to a limiting magnitude of $R < 22$, whereas with only $BVRi$, $\Delta_z \approx 0.2$. As the survey depth increases so also does the redshift uncertainty.

Alternatives to this photometric redshift model fitting technique have been proposed, for example using neural networks which have been trained with spectra from the Sloan digital sky survey (Tagliaferri et al. 2002; Firth, Lahav & Somerville 2003). For the Sloan filter set u' g' r' i' z', they find redshift uncertainties as small as $\Delta_z \approx 0.025$ for the low redshift Sloan photometric survey, on which the network was trained. This low uncertainty is reaching the theoretical minimum for photometric redshift accuracy from broad band filters, owing to the effective spectral resolution produced from the width of the broad-band filter transfer functions. This problem has been addressed by COMBO-17 whereby 5 broad-band ($UBVRI$) and 12 narrow band filters, ranging from 420 to 914 nm, have been used to facilitate redshift estimation for relatively faint galaxies with $R < 24$, with uncertainties as good as $\Delta_z \approx 0.03$ (Wolf et al. 2003). For weak lensing surveys an accuracy of $\Delta_z \sim 0.1$ is sufficient for most applications and hence a multi-colour survey with five or six broad-band filters is ideal.

4.2 The ODT: current status

The ODT INT data acquisition phase was completed in March 2003, after 63 nights observation spread over five years. The ODT spans twenty-five square degrees of multi-colour data in $BVRiz$ distributed across 4 distinct fields; Andromeda (0h), Lynx (9h), Virgo (13h) and Hercules (16h), (see Allen (2003) for details). Each ODT image or 'target field' is a series of three exposures with approximate 5 arcsecond offsets observed with the INT wide-field camera. The wide-field camera is a mosaic of four 2048×4096 CCDs with pixel scales of 0.333 arcseconds and a total field of view of approximately 0.27 square degrees. For our weak lensing feasibility study, ODT wide-field camera images are selected from the first 2.5 square degrees of reduced matched data in the Andromeda field, where sources have been extracted from the data using the *SExtractor* source detection algorithm (Bertin & Arnouts 1996). See Allen (2003) for the ODT data reduction and colour matching methods. As discussed in section 3.1.3 atmospheric turbulence blurs galaxy images, erasing any cosmic shear information from galaxies that are smaller than the seeing size. A selection criteria is therefore placed on the ODT images, such that stellar objects near the optic axis of the wide-field camera must have FWHM less than 1 arcsecond. This seeing selection criteria yields six ODT wide-field camera images, approximately 1.6 square degrees, for weak lensing analysis in the R band. PSF distortions across the image alter the average stellar FWHM such that, treating each wide-field CCD separately, the average stellar FWHM varies from $0.86 - 1.64$ arcseconds with a median average stellar FWHM of 1.15 arcseconds.

In the B and V band two images satisfy our seeing criteria, with only one image satisfying our seeing criteria in all three bands; B, V and R, unfortunately currently preventing multi-colour consistency checks of our data analysis techniques. In the i and z bands the fringing, discussed below, is too severe to consider performing a weak lensing analysis.

On proposal of an ODT weak lensing study, ODT observing strategy subsequently changed, with the best seeing observations reserved for the R band, increasing the coverage of the initial best seeing data. There has also been an effort to keep the best seeing multi-colour data in the same ODT target fields, allowing for future multi-colour consistency checks. The observing conditions over the duration of the ODT data acquisition period produced ≤ 1 arcsecond seeing in approximately 40% of the observing time and it is therefore estimated that approximately 10 square degrees of ODT data could be used for a full future weak lensing analysis in the R band, with additional good seeing multi-colour information in approximately 5 square degrees. For this feasibility study we will only use our selected 1.6 square degrees in the R band.

4.2.1 Sky and fringing subtraction

Initial ODT processing is applied to the data, as described in Allen (2003), producing exposures which have been de-biased, corrected for non-linearities and flat-fielded. It was found that standard packages for sky subtraction in *IRAF* and *SExtractor* failed with the wide-field camera imaging, leaving significant gradients in the number density of detected sources across some of the images. This is due to the severe nature of the observed large scale sky gradients across the images from scattered zodiacal light. With weak lensing studies sky gradients, varying even only slightly over the scale of the typical galaxy size, will bias galaxy shape determination, especially when using the quadrupole moment measurement of shape (equation 3.2). In response, modal filter software has been developed as an alternative to the standard packages using FITSIO routines[1], to remove sky gradients with a 20 arcsecond square modal filter. This method was found to be effective at removing the severe sky gradients, yielding a smooth distribution of extracted sources across the image.

Fringing has the appearance of a series of 'ripples' in the images and is caused by the multiple reflection and interference of the night-sky emission lines in the CCD substrate. It affects primarily the redder end of the spectrum and as, to first order, we can assume that it affects images identically, fringing can be removed from the images using a combined 'fringe frame' of all the sky subtracted exposures. By performing the data reduction steps in this order, the final fringe frame is not biased by sky gradients, and produces successfully

[1] *heasarc.gsfc.nasa.gov/docs/software/fitsio/fitsio.html*

de-fringed images in the R band. With the stronger fringing effects found in the i and z bands, the assumption of a static fringe pattern fails, leaving fringing distortions in the fringe subtracted image which have to be masked out. More recent ODT observation runs have made use of the new Sloan r' filter in the Virgo fields, as r' is less susceptible to fringing compared to R.

After sky and fringing subtraction, the individual exposures of the same target field are combined using integer pixel offsets to enable a higher signal to noise (SNR) source detection, and allow for cosmic ray removal. For weak lensing studies as discussed in section 3.2.9, each exposure is analysed individually, with the results optimally combined at the end of the analysis. This is particularly relevant to the weak lensing analysis of the ODT as even if we assume exact integer pixel offsets with zero rotation, the astrometric distortions described in section 3.1.4, will alone introduce shear of the order 4% at the chip edges when combining circles of typical seeing size. This effect will be enhanced with elliptical sources, particularly if the major axis points towards the optical axis.

4.2.2 Star-galaxy separation

In order to remove the effects of the PSF, stellar objects, which quantify the distortions, need to be selected. Stars are typically identified from their locus in the size-magnitude scatter plot, shown in figure 4.2, where the stellar arm located at the seeing size extends from bright magnitudes to faint magnitudes, into the main distribution of galaxies. The stellar arm is easy to identify by eye but significantly more difficult to identify automatically, especially when the stellar size varies across the chip, a result of varying PSF distortions. The *SExtractor* algorithm provides a star-galaxy classification *class*, based on a neural network classifier. For $class > 0.5$ the source is classified stellar, and for $class < 0.5$ the source is classified as a galaxy. Plotting the *SExtractor* classed stars in the size-magnitude scatter plot reveals some disagreement between the locus of stars and *SExtractor* classed stars, finding a better discriminant for stellar objects at $class > 0.9$.

With multi-colour data a possible alternative is to classify stellar objects from their colours, as shown by the 16 filter CADIS survey (Wolf, Meisenheimer & Röser 2001). The application of the CADIS multi-colour stellar classification technique to the $BVRiz$ ODT data has however

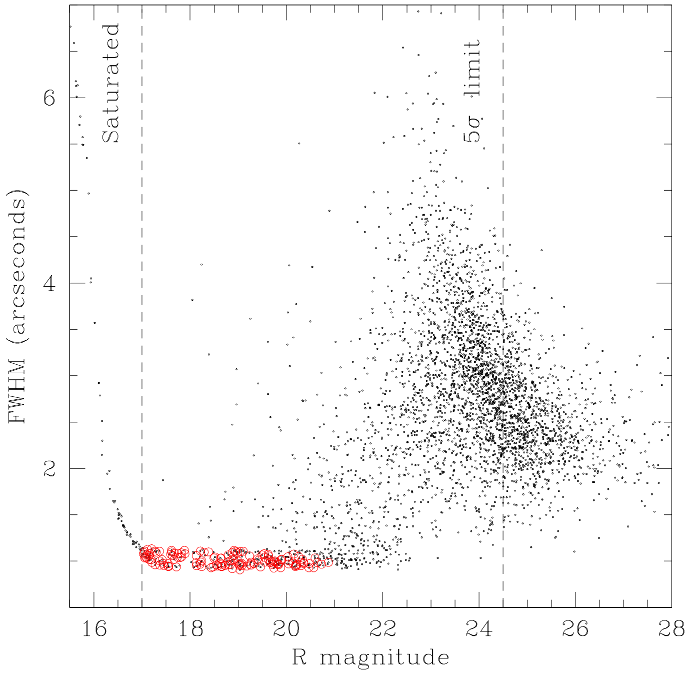

Figure 4.2: The distribution of aperture magnitude and FWHM for all *SExtractor* sources in ODT field I002R CCD2 with 1 arcsecond seeing. The stars shown by circles, form a locus in this plane at bright magnitudes and small sizes. The 5σ aperture magnitude limit $R \sim 24.5$, and saturation magnitude limit $R \sim 17.0$, are also shown.

produced inconsistent results when a comparison is made with the *SExtractor* classification. This suggests that the success of the CADIS stellar colour classification technique is dependent on the amount of multi-colour information available. A future straightforward improvement to the CADIS stellar colour classification technique would be to include some prior on object size.

Stellar contaminants in galaxy catalogues are a source of systematic error in, for example, galaxy clustering studies (McCracken et al. 2001), hence stellar classification schemes often aim to create a galaxy catalogue with very little stellar contamination at the expense of losing some galaxy sources. Our aim is, however, different as we require a catalogue of unblended stars with no galaxy contamination. Any small amount of residual stellar contamination in our galaxy catalogue will not affect any measured lensing signal. Our chosen star-galaxy separation technique, designed to reject all galaxies and blended stars with the potential loss of some stellar objects, uses the *SExtractor* classification as a guide and is detailed below.

1. Estimate average stellar size $\langle \mathrm{FWHM}^* \rangle$ from unsaturated sources with $18 < R < 21$, SNR > 30.0, FWHM $< 1.5'$ and $class > 0.98$.

2. Select stellar candidates from unsaturated sources with $|\mathrm{FWHM} - \langle \mathrm{FWHM}^* \rangle| < 0.5''$, $17 < R < 21$, SNR > 5.0, $class > 0.9$.

3. Reject stellar candidates if they have a SNR ≥ 5 neighbouring source closer than 2 arcminutes.

4. Measure shapes for stellar candidates from their weighted quadrupole moments (equation 3.2), using circular weighting (equation 3.3), with $\theta_g = \mathrm{FWHM}/2$.

5. Split each CCD image into 4 quadrants and calculate the mean and variance σ^2 of stellar shapes in each quadrant. Remove stellar objects with shape parameters $2\sigma+$ from the mean.

6. For model fitting shape measurement, the resulting stellar catalogue is then observed by eye as detailed in section 3.3.1.

4.2.3 The wide-field camera PSF

The wide-field camera PSF can be mapped from the measured ellipticities of stellar point sources across the image. The stellar ellipticity pattern for single exposures of the ODT fields I002R and I026R are shown in figure 4.3, where the star catalogues have been selected as described above, up to stage 5. Typically the PSF distortion is $\sim 10\%$ with significant spatial variation across all ODT images. The time variation is apparent from the significant differences between the I002R and I026R PSF patterns. Figure 4.4 shows the short time-scale PSF variation in the three individual 40 minutes exposures of ODT field I002R CCD 2. Each exposure was taken in series showing that even in this short time-scale we can see variation in the PSF across the chip. Time and spatial PSF instability results primarily from the response of the optics to the telescope orientation and the response of the optics to any temperature variation. As shown by figures 4.3 and 4.4, the INT wide-field camera PSF is significant, unstable and anisotropic, favouring the use of uncombined exposures for weak lensing analysis as discussed in section 3.2.9.

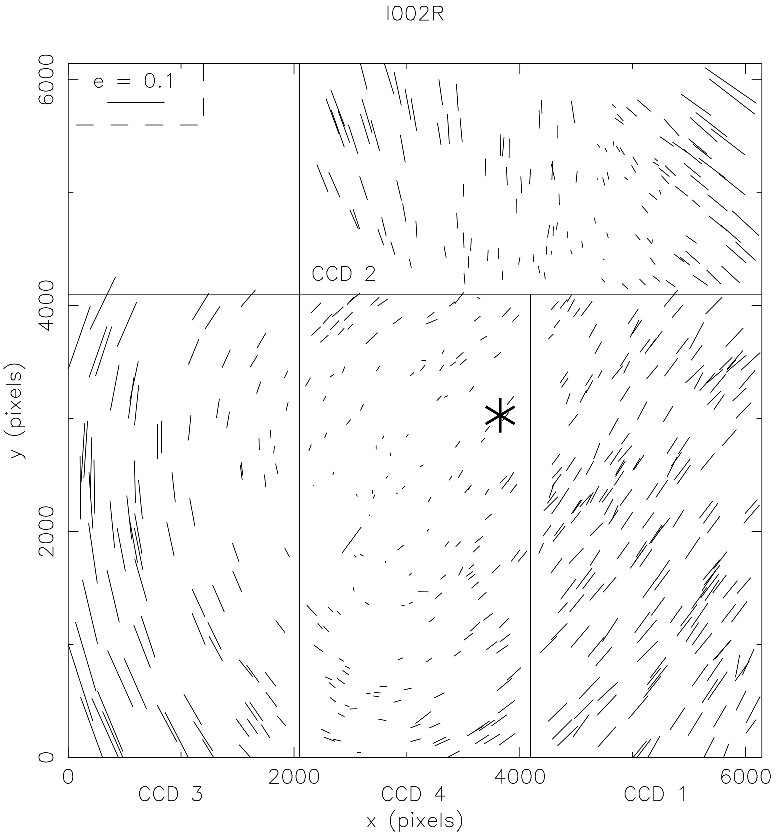

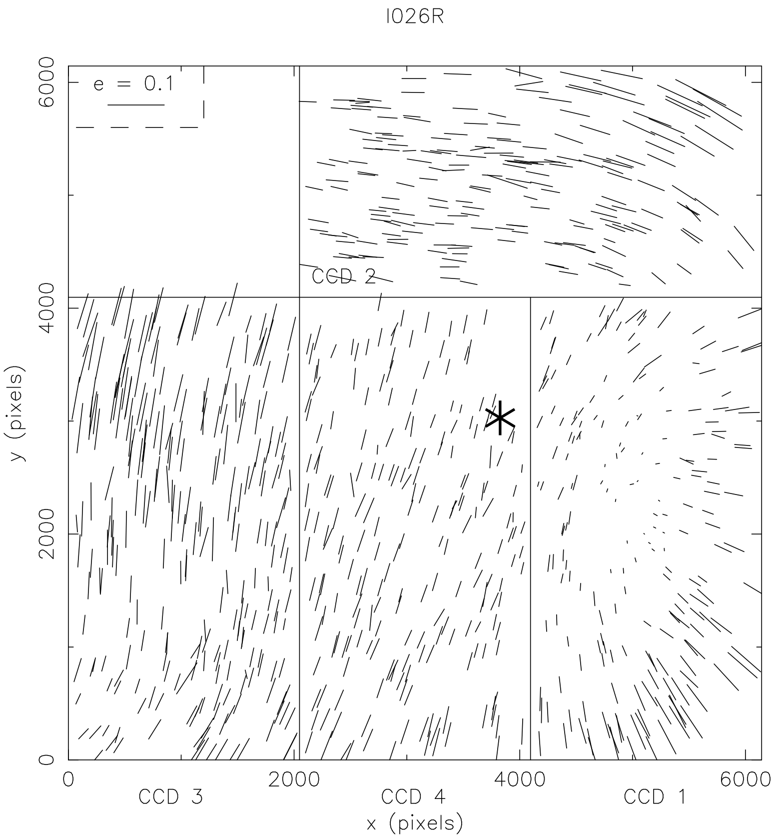

Figure 4.3: Stellar ellipticity pattern (PSF) across the four CCDs of ODT field I002R (upper) and ODT field I026R (lower), positioned in the same configuration as the wide-field camera. A 10% shear signal is shown in the upper left corner for comparison. The optic axis in CCD 4 is marked with a star.

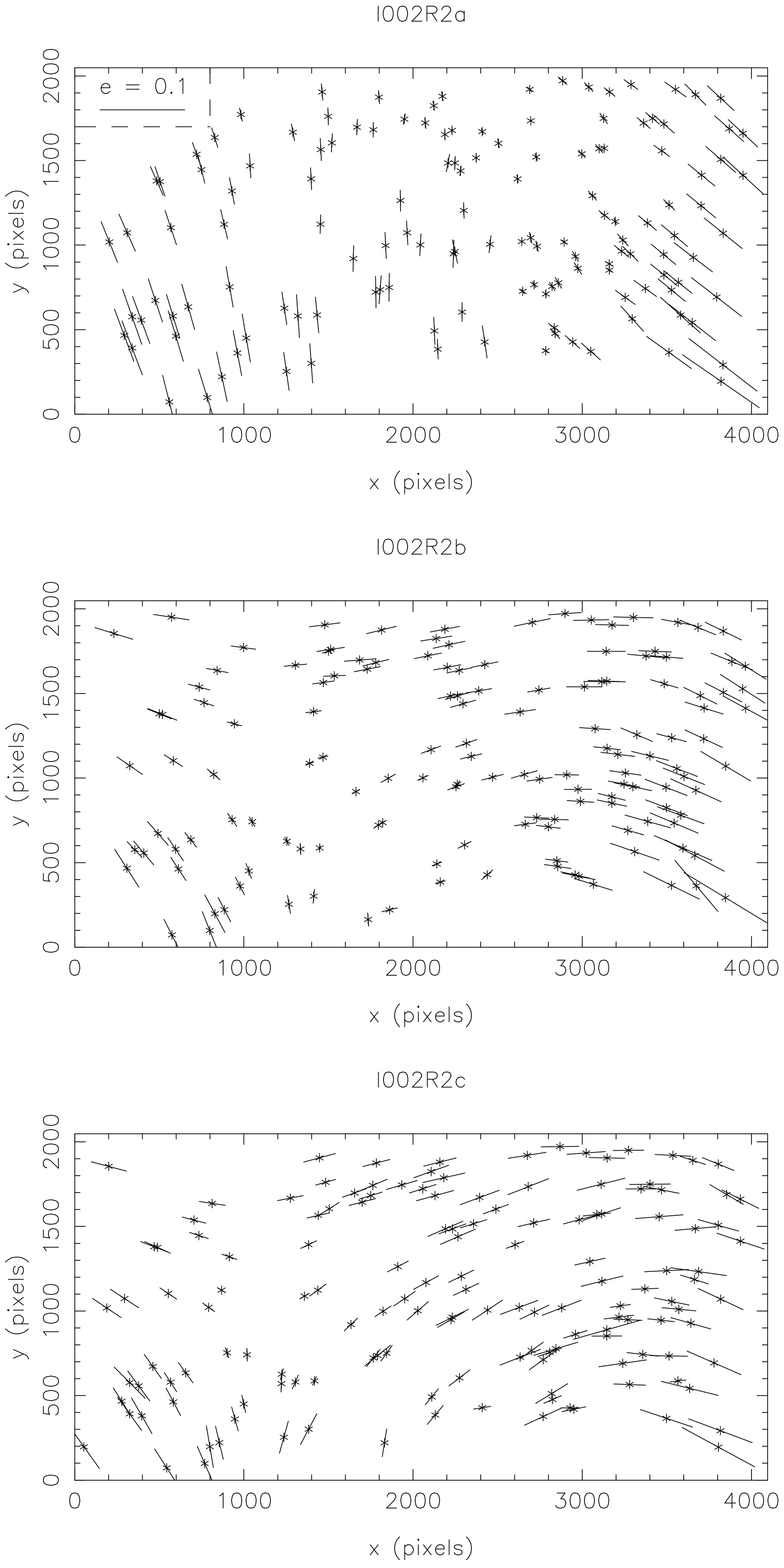

Figure 4.4: Stellar ellipticity pattern (PSF) across the three individual exposures of ODT field I002R CCD2 taken in sequence at 40 minute intervals. A 10% shear signal is shown in the upper left corner of exposure I002R2a for comparison.

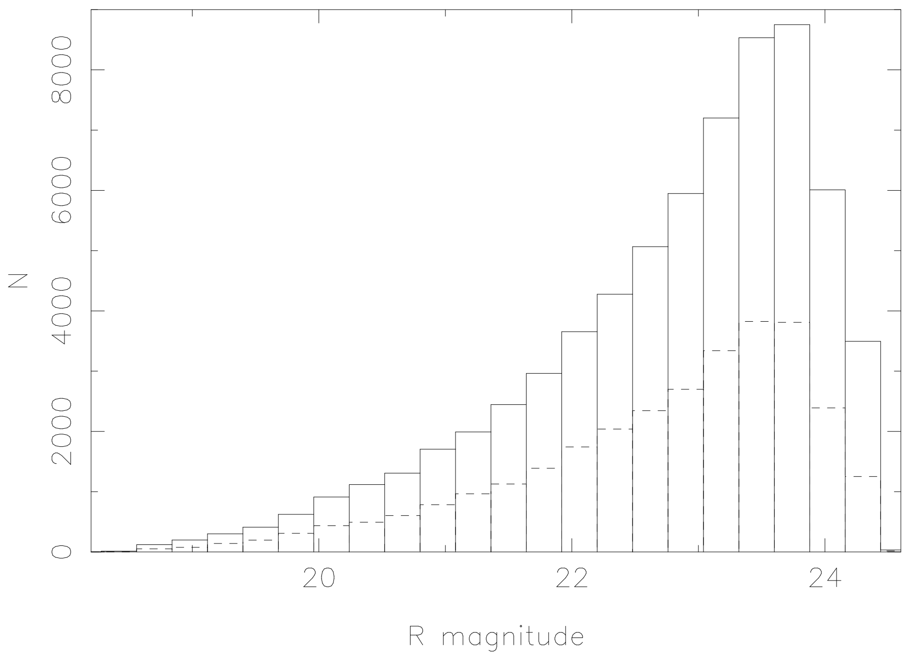

Figure 4.5: Aperture magnitude distribution for the 5σ limited ODT *SExtractor* catalogue (solid), and for the galaxies with fitted ellipticities and $e < 0.8$ (dashed).

4.2.4 Survey depth

During our weak lensing feasibility study it became apparent that the 5σ limiting survey depth of the ODT was significantly brighter than the originally proposed depth. For the ODT fields selected for this weak lensing study, the 5σ limiting aperture magnitude of the 2 hour R band imaging is actually only $R = 24.5$, with a median magnitude of $R = 23$ as shown in figure 4.5. Note that use of isophotal magnitudes would push the 5σ limiting depth to slightly fainter magnitudes, as aperture magnitudes can overestimate errors for small objects, but as for weak lensing we require good detections (compare to Bacon, Refregier & Ellis (2000) who use a signal to noise cut of 15), aperture magnitudes have been used to determine the limiting 5σ magnitude. The ODT survey is therefore of similar depth to the 53 square degree RCS survey (Hoekstra et al. 2002) and the 75 square degree CTIO survey (Jarvis et al. 2003). For our chosen 1.6 square degrees, 67078 sources are detected above the 5σ level, yielding approximately 12 galaxies per square arcminute. From the dependence of the median photometric redshift of the COMBO-17 galaxies on the median magnitude of the galaxies (Brown et al. 2003), the median redshift z_m of the ODT is estimated at $z_m \sim 0.65$. This estimate is consistent with a median redshift determined from the measured spectroscopic redshift distributions of Cohen et al. (2000) combined with photometric redshift distributions of Fernández-Soto, Lanzetta & Yahil (1999). On completion of the photometric redshift catalogues for the ODT survey a more robust estimate and a full redshift distribution will be available.

4.3 ODT cosmic shear detection

The goal of our feasibility study was to produce an estimate of the angular shear correlation function $\langle\gamma\gamma^*\rangle_\theta$ equation 2.79, from the ODT survey using the model fitting technique described in section 3.2. Stars representative of the PSF were chosen from stellar candidates by eye in each exposure, yielding approximately 0.6 stars per square arcminute which were then combined as described in section 3.3.1, over 2×2 arcminute regions where possible, corresponding to 384×384 pixel boxes. This is a smaller region than the region chosen for the COMBO-17 images owing to the strong anisotropy observed in the ODT images. PSFs are then defined for the central 45 square arcsecond region of each 2×2 arcminute combined region such that the PSF for each 11×22 arcminute CCD chip is described by up to 512 combined stellar images. These PSF images are Fourier transformed and stored for model fitting. Using 5σ limited *SExtractor* catalogues for the ODT images the model fitting technique was applied to the images using a weak shape prior with $e_p = 1.0$ in equation 3.59. From the ellipticity distribution of COMBO-17 shown in figure 3.9, we can see that there is a slight tendency with this weak prior for faint galaxies to be best fit by higher ellipticities, potentially caused by contamination from close neighbours, noise and possibly the presence of spurious and untrustworthy detections. A cut on object PSF and seeing corrected ellipticity is hence introduced such that $e < 0.8$, which is similar to the standard KSB+ cut on objects with a pre-seeing corrected weighted ellipticity of $\varepsilon > 0.5$ (Bacon, Refregier & Ellis 2000). Owing to the unstable PSF pattern and the varying seeing conditions, the model fitting technique is applied simultaneously to galaxy images in the three uncombined exposures, combining the likelihoods from each image to produce a final maximum likelihood estimate for (e_1, e_2, r_o). Ellipticity estimates are converted into a shear estimator from equation 3.62 with $\sigma_e = 0.34$, and the theoretical astrometric shear distortion for the wide-field camera is then subtracted as discussed in section 3.1.4.

Model fitted parameters were calculated for 55% of the data, where 29% of the objects were lost as two or more PSF selected stars were not within a square of 2 arcminutes, and 16% were rejected by the model fitting centroid criteria discussed in section 3.2.7. For the galaxies with model fitted parameters, 22% of the objects were rejected as $e > 0.8$. For the final model fitted galaxy catalogue the resulting mean shear is $\gamma_1 = -0.00015 \pm 0.00056$ and $\gamma_2 = -0.00008 \pm 0.00038$, which is consistent with zero offset as we would expect.

Figure 4.5 shows the magnitude distribution of the full 5σ limited *SExtractor* catalogue and the catalogue with model fits. The median magnitude of the full catalogue is $R = 23.05$, which decreases slightly to $R = 23.00$ for the catalogue of galaxies which have fitted parameters, agreeing with the results from the COMBO-17 CDF field, that the occasional rejection of objects by the model fitting centroid criteria is not caused by faint magnitudes.

4.3.1 Tests for residual systematics

We will now repeat the tests for residual systematic distortions described in section 3.3.5 on our model fitted PSF and seeing corrected catalogue of galaxy shapes for the ODT survey. Figure 4.6 shows, in the middle panel, the average ellipticity of PSF and seeing-corrected model-fitted galaxies in square cells of side 11 arcminutes with an average uncorrected PSF ellipticity $\langle e_i^* \rangle$. The stellar ellipticities have been determined from weighted quadrupole moments equation 3.2 with θ_g set equal to the seeing. The number of galaxies with a given value for the PSF ellipticity is shown in the lower panel. For comparison, the average ellipticity of galaxies which have not been corrected for PSF distortion is also shown in the upper panels, revealing a strong correlation which is not seen in the corrected ellipticities. Note that the uncorrected galaxy ellipticities have been determined from weighted quadrupole moments equation 3.2 with θ_g set equal to half the *SExtractor* FWHM. After PSF correction the average galaxy ellipticity is bounded between ± 0.01 in common with the published residuals from Van Waerbeke et al. (2001) and Hoekstra et al. (2002).

To calculate the contamination these residuals bring upon any estimate of the shear correlation function the star-galaxy cross correlation equation 3.68 is calculated, treating each ODT CCD chip as an individual field. At this stage it was found that each CCD chip 3 image, the CCD chip furthest from the optic axis and hence prone to the most significant astrometric

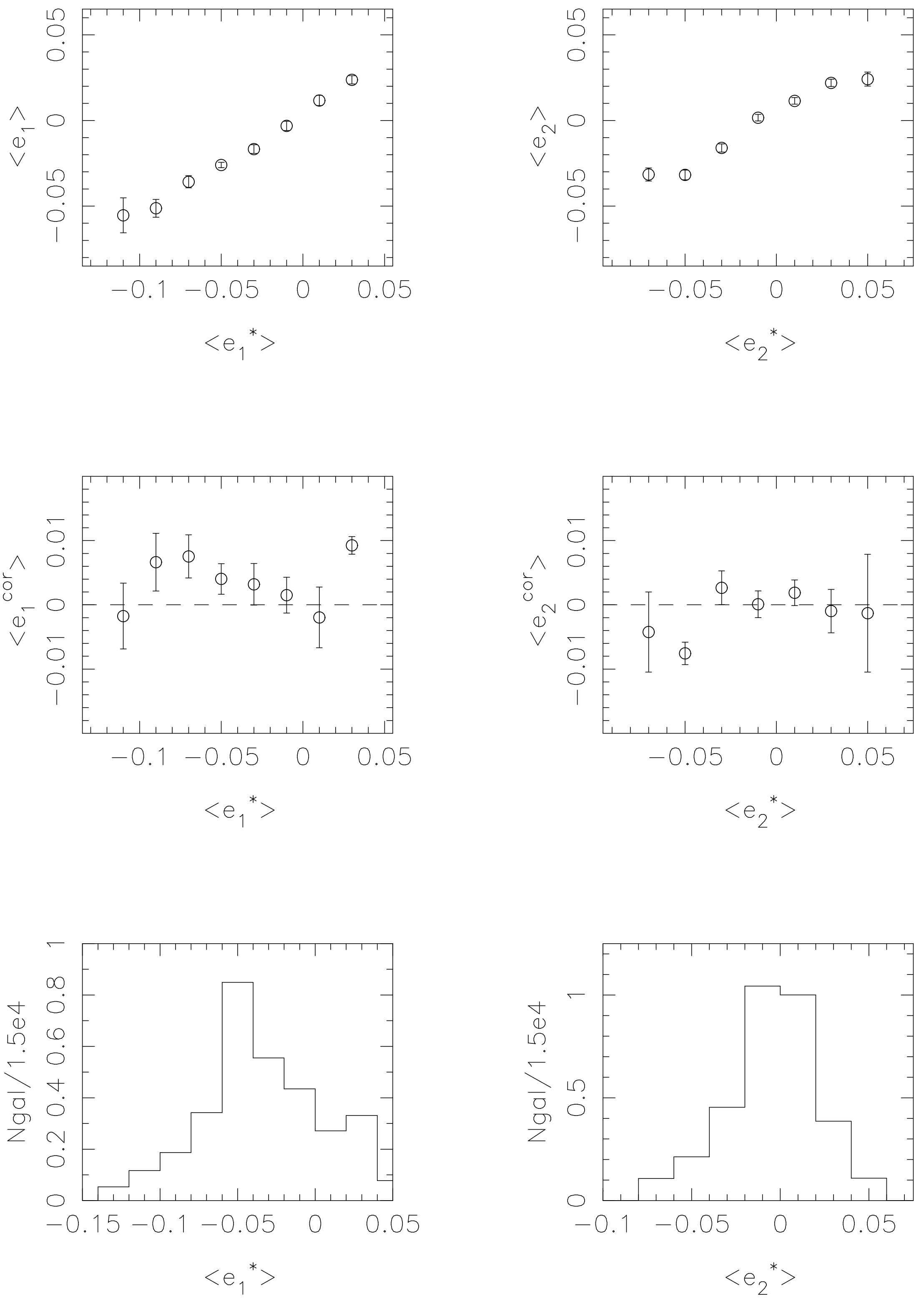

Figure 4.6: The mean ellipticities of galaxies $\langle e_1 \rangle$ (left) and $\langle e_2 \rangle$ (right) as a function of the value of the average ellipticity of the stars used to correct the galaxies. The upper panels show the correlation between the stellar ellipticities and the uncorrected weighted ellipticity measurements. The middle panel shows the mean PSF and seeing corrected model fitted ellipticities of the galaxies, note the change of scale. The number of galaxies with a given value for the PSF ellipticity is shown in the lower panels.

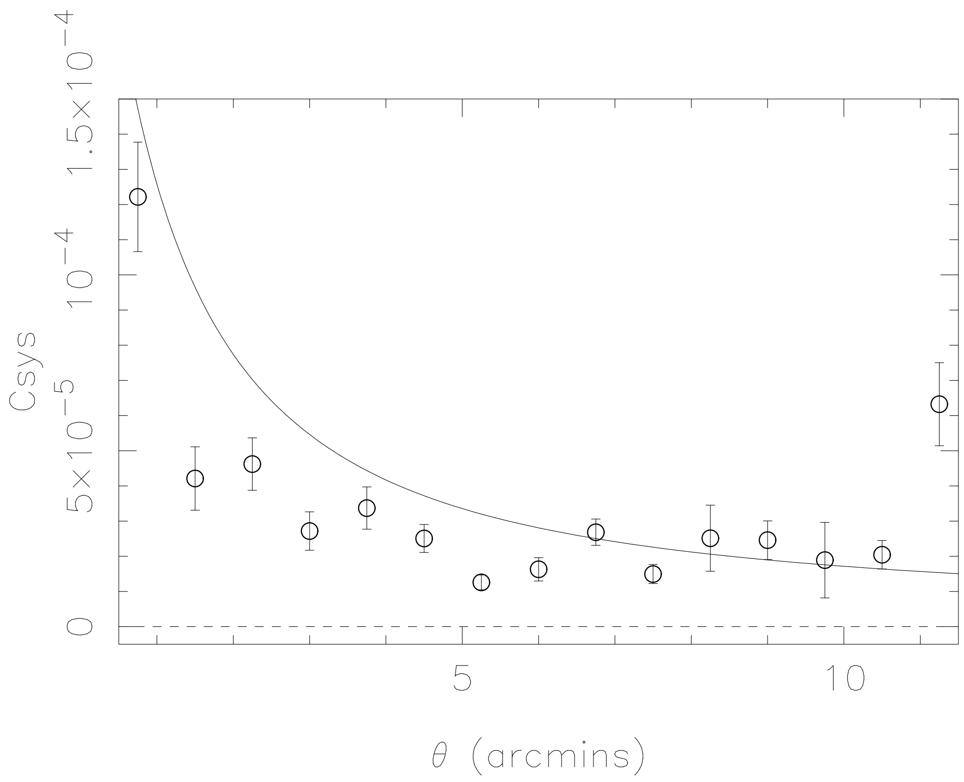

Figure 4.7: Total star-galaxy cross-correlation $\langle c_1^{\rm sys} + c_2^{\rm sys} \rangle_\theta$ for the ODT data compared to the $z_m = 0.65$ $\sigma_8 = 0.9$ ΛCDM shear correlation signal.

distortions, produced the most significant star-galaxy cross correlations, hinting that the theoretical description for the astrometric distortions in the wide-field camera was inadequate. We will therefore reject all CCD3 images from our analysis and at this stage remove our worst seeing image, which also produced higher than average star-galaxy cross correlations. In the remaining 15 CCD chips another 50% of the images were removed to minimise the average star-galaxy cross correlation leaving a final area of 0.7 square degrees. These rejected images; five CCD2 images and three CCD4 images, were found to be those with the most anisotropic PSF pattern. These higher than average star-galaxy cross correlations therefore hint that, in the case of highly anisotropic PSFs, 2 arcminute stellar combination representations of the PSF are inadequate.

Figure 4.8 shows the resulting star-galaxy cross correlations $\mathrm{Csys}_k(\theta) = \langle c_k^{sys} \rangle_\theta$ equation 3.68, which is of a similar level to the published non-zero star-galaxy correlation of Bacon et al. (2003) and the star-galaxy cross correlation shown for COMBO-17 in figure 3.14. Bacon et al. (2003) find that this small residual alignment of galaxy shear measurements to

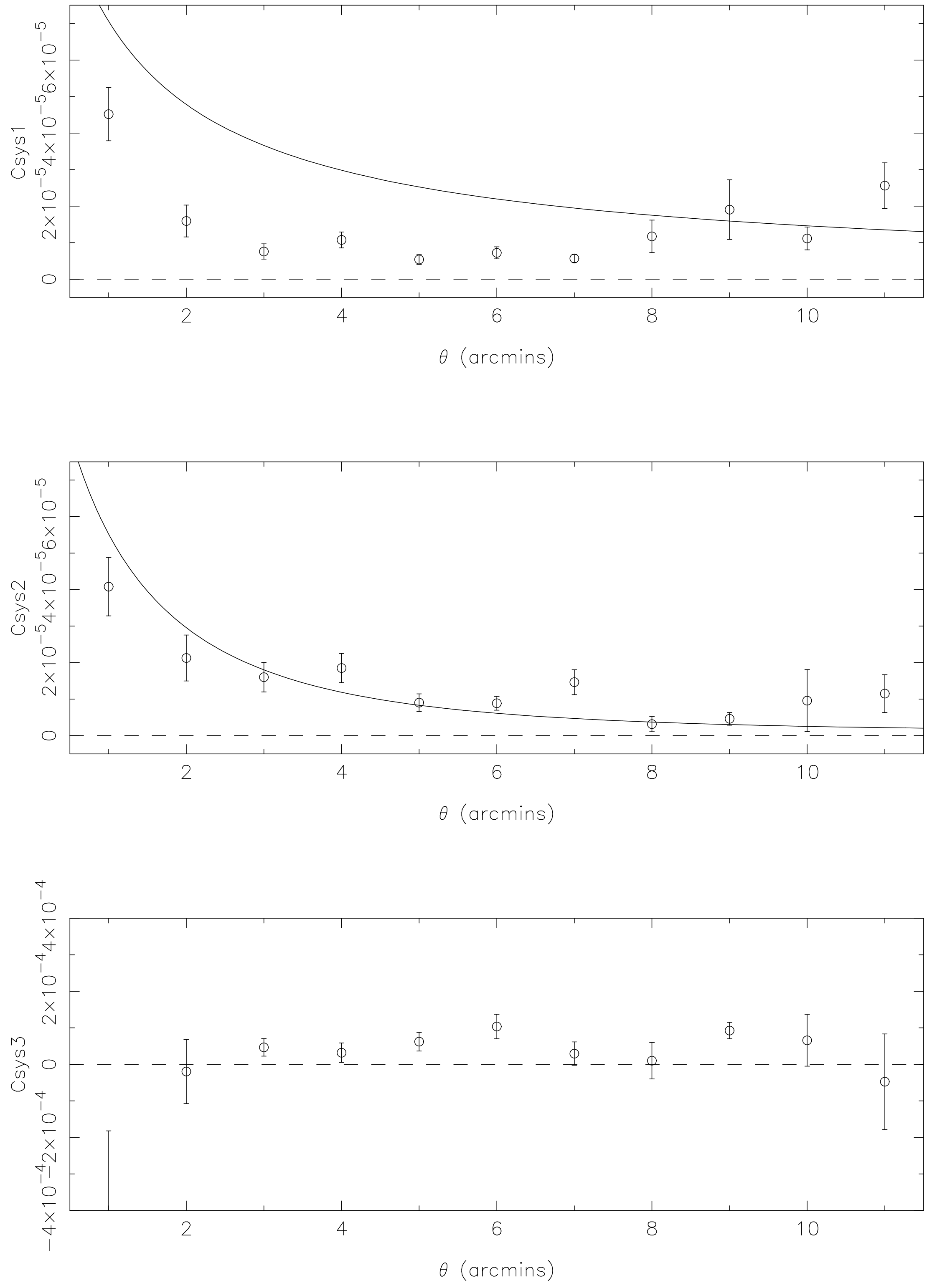

Figure 4.8: Star-galaxy cross-correlation for the ODT data, defined in equation 3.68. The residual correlations between galaxies and stars are comparable to the $z_m = 0.65$ tangential (upper) and radial (middle) ΛCDM $\sigma_8 = 0.9$ shear correlation signal that we are trying to measure.

the orientation of the original PSF is negligible to their measurement. Unfortunately the result of the shallower depth of the ODT sample is such that this residual alignment is actually comparable to the signal that we are trying to extract, which can be seen by comparing the measured star-galaxy correlation in figure 4.8 with $\langle\gamma_t\gamma_t\rangle_\theta$ (upper), and $\langle\gamma_r\gamma_r\rangle_\theta$ (middle) calculated from equation 2.92 with $z_m = 0.65$, $\sigma_8 = 0.9$ and a ΛCDM cosmology. Significant star-galaxy cross-correlations at $\theta < 2$ arcminutes can be attributed to the combination of stellar images to represent the PSF over this scale. The increased correlations on scales comparable to the size of the chip are potentially a result of a poorer PSF correction at the chip edges, as the chip edge PSF representations typically contain fewer stars. Provided, however, that we have a good estimate of the residual alignment of galaxy shear measurements to the orientation of the original PSF, following equation 3.66, we can simply subtract $\langle c_k^{sys}\rangle_\theta$ from our measurements of the shear correlation signal.

4.3.2 Results: Shear correlation

Figure 4.9 shows the galaxy-galaxy shear correlation $\langle\gamma\gamma^*\rangle_\theta$ equation 2.79, estimated for each CCD chip from equation 2.68 with weights given by equation 3.63, and averaged over all CCD chip images (equation 2.69), treating each CCD chip as an independent field. This approximation will be valid on scales which are small compared to the size of the chips ($= 11' \times 22'$), and will be discussed further in chapter 7. The total star-galaxy cross correlation $\langle c_1^{\rm sys} + c_2^{\rm sys}\rangle_\theta$, shown in figure 4.7, has been subtracted, where $c_k^{\rm sys}$ is given in equation 3.68. Note that the points are correlated. The errors are given by equation 2.70 summed in quadrature with the errors on the total star-galaxy cross correlation, where the dominant source comes from shot noise, $\sigma_{\rm SN}$ equation 6.3, introduced by the intrinsic ellipticity distribution of galaxies, which will reduce with the inclusion of more data.

The measured anti-correlations at $\theta > 9'$ are to be treated with caution as they will certainly be in part attributable to astrometric distortions which could introduce significant anti-correlations at these angular scales if the theoretical correction for radial astrometric distortions which has been applied was inadequate. Interestingly, the residual contamination for the radial cross correlation in figure 4.8 is more significant than the tangential cross correlation which hints that the theoretical correction for the radial astrometric distortions is

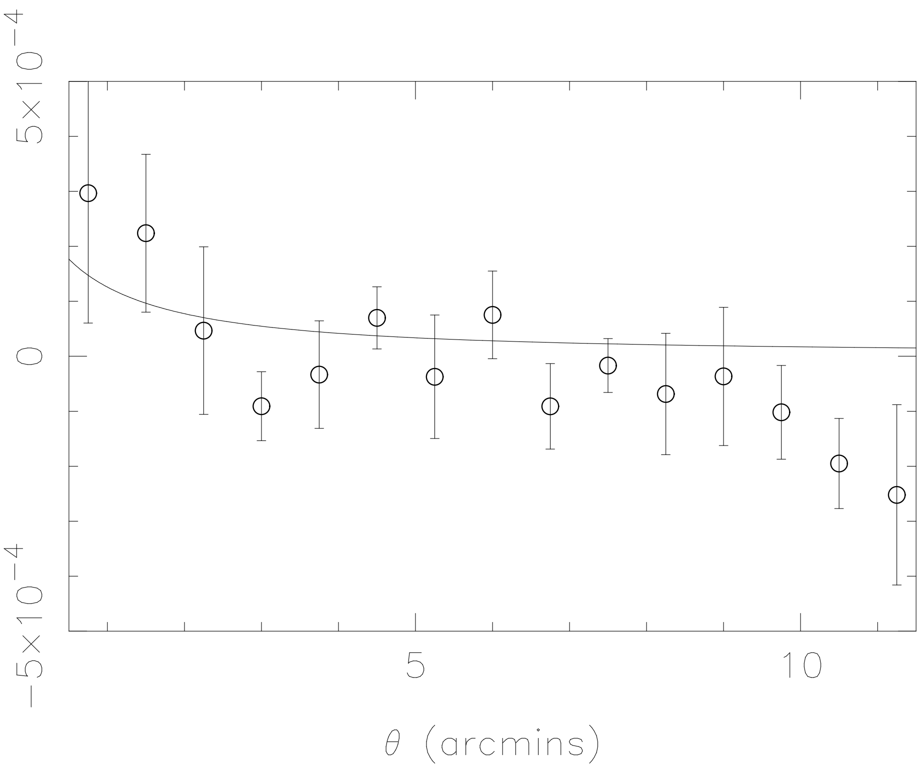

Figure 4.9: Measured angular shear correlation signal for the ODT data $\langle\gamma\gamma^*\rangle_\theta$ compared to the $z_m = 0.65$ $\sigma_8 = 0.9$ ΛCDM expected angular shear correlation signal.

not correct. The non-zero cross-correlations (lower) between tangential and radial components are an indication that the astrometric distortions may also have some tangential components. Note that the subtraction of $c_k^{\rm sys}$ from the weak lensing shear correlation signal will not correct for the astrometric distortions, as the astrometric shear is dependent on the size of the object and hence affects stellar objects and galaxies differently.

The astrometric distortion pattern can be measured from the astrometric shifts of objects observed in several frames, offset by known amounts (Bacon, Refregier & Ellis 2000), or alternatively can be estimated from the mean PSF and seeing corrected galaxy shear calculated as a function of chip position averaged over many wide-field camera images, which in the absence of astrometric distortions should sum to zero. A calculation of the true astrometric distortion pattern would be vital for any future weak lensing studies with the INT wide-field camera. For the current feasibility study however we will simply state that our correction for astrometric distortions could well be inadequate, possibly contributing to the non-zero star-galaxy cross correlations and the anti-correlations at large angular scales in the measured galaxy-galaxy shear correlation.

Considering angular scales between $2' < \theta < 9'$, above the PSF correction scale and below angular scales where astrometric distortions could become important, we see agreement with the expected shear correlation function for a median redshift survey $z_m = 0.65$ shown in figure 4.9 for a ΛCDM cosmology with $\sigma_8 = 0.9$. Note that changing the value of σ_8 from 0.7 to 1.0 makes very little difference to the expected shear correlation function on the scales shown in figure 4.9. We will not perform a cosmological parameter estimation analysis of this result primarily because of the very weak constraints any parameter estimation would yield in the presence of such high shot noise, but also because of the potential calibration errors from the conversion of ellipticity to shear, as discussed in section 3.2.8, and because of uncertainties in the true redshift distribution, which will be resolved with the completion of the photometric redshift ODT catalogue.

Our feasibility study has produced satisfactory results on angular scales between $2' < \theta < 9'$ from 0.7 square degrees allowing for a future weak lensing study of all the best seeing data in the ODT, provided astrometric distortions can be adequately corrected for. In light of the limiting 5σ depth of the ODT, $R = 24.5$, compared to existing wide-field cosmic shear surveys such as the 53 square degree RCS survey (Hoekstra, Yee & Gladders 2002) limited to $R = 24$, a depth where the redshift distribution is fairly well determined, any completion of an ODT weak lensing survey is, however, unlikely to be seen as competitive.

4.4 Cosmic shear survey design

The most significant factors in producing a successful weak lensing survey, listed in order of importance, are;

1. **Depth**: With an increase in survey depth comes an increase in the cosmic shear signal which scales approximately as $\langle\gamma\gamma^*\rangle_\theta \propto z_m^2$ (Barber 2002). The more significant the cosmic shear signal, the less problematic any small residual systematics from PSF distortions.

2. **Seeing**: Shear information from galaxies smaller than the seeing size is erased. Hence in poor seeing the depth of a weak lensing survey is not determined by the magnitude limit but by the angular size of typical galaxies as a function of redshift.

3. **Width**: Shot noise is a random error introduced in cosmic shear measurements by the intrinsic ellipticity distribution of galaxies, which tends to zero in the limit of an infinite number of sources. Cosmic variance offers an additional source of error which for small contiguous area surveys can dominate on scales larger than a few arcminutes (Schneider et al. 2002). This can be reduced to negligible levels by sampling different areas of the sky and combining to produce a wide-field survey.

4. **Multi-colour data**: Weak lensing analysis requires knowledge of the redshift distribution which can be estimated photometrically with multi-colour information. In addition multi-colour data allows for consistency checks in shape measurement techniques and allows for 3D lensing studies (Heavens 2003). In chapter 6 we will see that with photometric redshift estimates it is also possible to remove a potentially significant contaminant to weak lensing analysis from intrinsic galaxy alignments.

5. **PSF**: In $\sim 50\%$ of ODT good seeing images, the INT wide-field camera PSF can be removed on angular scales $\theta > 2'$ leaving residuals $\sim 2\times10^{-5}$ which for a median redshift survey $z_m \sim 1.0$ is only $\sim 10\%$ contamination. Provided there is adequate sampling of the PSF distortion, i.e a high density of stellar objects across the field of view, using a model fitting technique can in principle remove any form of PSF distortion. The minimisation of PSF distortions in instrumentation design such as the relatively stable PSF in the wide-field imager at the ESO 2.2m telescope, will however be important for future weak lensing surveys.

6. **Astrometric Distortions**: All wide-field cameras will have some level of astrometric distortions and it is this additional source of shear which has produced some limitation to our ODT weak lensing study. Provided the distortion pattern is stable however it is possible to remove. Tests to quantify the success of the removal of astrometric distortions are difficult to determine as the shear distortion is dependent on source size, hence the minimisation of astrometric distortions in instrumentation design will be important with new square degree field of view cameras such as MegaCam[2] on the Canada-France-Hawaii Telescope (CFHT) and OmegaCam[3] on the VLT Survey Telescope.

[2] *www.cfht.hawaii.edu/Instruments/Imaging/MegacamNew/home.html*
[3] *www.astro.rug.nl/~omegacam*

We originally asked whether weak lensing surveys require highly competitive 3.6 metre plus telescope time and/or space-based instrumentation, or whether weak lensing surveys could be carried out on the less competitive possibly dedicated smaller telescopes such as the INT. With smaller telescopes, longer exposures are required to gain the same depth as that attainable in shorter periods of time on larger telescopes and with these longer exposures the seeing conditions can vary significantly. With dedicated survey telescopes wide-area multi-colour surveys should be easily attainable but without regularly good and stable observing conditions only a small percentage of the data will be useful for weak lensing analysis, as shown in this chapter with the ODT data. The INT 2.5m telescope in La Palma with the wide-field camera combines the need for long exposures to gain depth with strong unstable PSF distortions, and it is therefore not appropriate for any future weak lensing cosmic shear studies. COMBO-17 have used the ESO 2.2m telescope in Chile with the wide-field imager designed such that the PSF distortions are minimised. Observing deep R-band weak lensing data in the best seeing conditions the COMBO-17 survey has achieved excellent success over 1.75 square degrees. An extension of this survey for weak lensing with only five or six broad band colours would increase the survey area whilst retaining the best asset of photometric redshift estimates, albeit with slightly less accuracy.

In 2007 the complete CFHT Legacy wide survey (CFHTLS) is intended to cover 172 square degrees in the Sloan filter set $u'g'r'i'z'$ down to $i' = 24.5$, which is equivalent to a median redshift $z_m \sim 1.0$. With a galaxy density of 35 galaxies per square arcminute on average, the CFHTLS will achieve accurate cosmological parameter estimation, but will have reached the limitation of a ground based weak lensing survey because of the effects of atmospheric seeing. To obtain a higher surface density of resolved sources, probing more distant galaxies, it will be necessary to use space-based instrumentation such as the proposed SuperNova/Acceleration Probe (SNAP) which is due for launch in 2008. In 10 months of observation a wide weak lensing survey on SNAP could cover 300 square degrees to an equivalent median redshift of $z_m = 1.23$ with a galaxy density of 120 galaxies per square arcminute in 6 wide-band optical filters and 3 near infra-red filters, allowing for photometric redshift accuracy of $\Delta_z = 0.02$ (Rhodes et al. 2003). The high density of galaxy images is made feasible as SNAP 'seeing' has a FWHM $= 0.12 - 0.16$ arcseconds. The PSF has been designed to have stable PSF distortions at maximum 5% with a maximum variation of $\pm 0.5\%$. Calibration of the PSF will be made every month with observations of a globular cluster, providing the high number density of stellar sources required for any model fitting technique where PSFs are taken directly from the data.

In conclusion, although in this chapter we have shown that in principle the INT could be used for a weak lensing survey, with the current expectation for high precision cosmological parameter estimation, most easily attainable with deeper weak lensing surveys, space-based instrumentation would be the choice of most ambitious future weak lensing survey designs.

5

Weak gravitational lensing or intrinsic galaxy alignments?

A key assumption for all weak lensing studies to date is that galaxy ellipticities are randomly oriented on the sky, and therefore any degree of alignment that we see between nearby galaxies is induced purely by weak gravitational lensing. This assumption, however, neglects the fact that gravitational interactions during galaxy formation could in fact produce intrinsic shape correlations between nearby galaxies mimicking to an extent weak lensing shear correlations.

In the cluster weak lensing regime, where the shearing of background galaxy images induced by the mass of the cluster is of the order 10%, this has not been an unreasonable assumption to make (Gray et al. 2002). We expect to see intrinsic signals only from galaxy pairs that are close in real space, and as galaxy shear measurements are averaged over a wide redshift distribution of background galaxies, we would not expect intrinsic alignments to be this significant. In the search for large scale structure, however, where the detection involves the measurement of lensing shear correlation signals that are typically of the order $\langle\gamma\gamma^*\rangle \sim 10^{-4}$, it is not clear that intrinsic contributions are small enough to neglect in this fashion.

In this Chapter we will discuss potential origins for the intrinsic alignment of nearby galaxies and the implication of a non-zero intrinsic alignment measurement for weak lensing analysis. We will review theoretical methods employed to determine the degree of ellipticity correlations between nearby galaxies, and their inferred contribution to weak lensing measurements, focusing on a necessary modification to previous intrinsic alignment analysis of numerical simulations. Introducing four different models for intrinsic galaxy alignments that

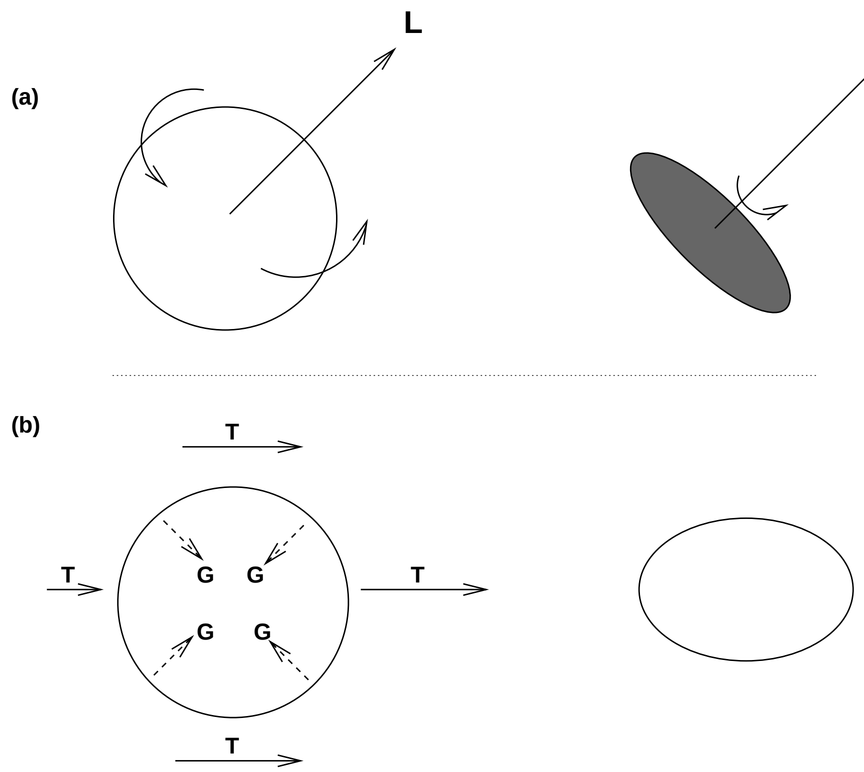

Figure 5.1: Different theories for the origin of galaxy ellipticity give rise to alignments between nearby galaxies. Panel (a) pictures the tidal torque theory, where the galaxy forms a thin disk perpendicular to its angular momentum, **L**, whose direction will be correlated with the local tidal field. If **L**, was directed towards our line of sight, we would see a circular galaxy with ellipticity $e = 0$. With **L** at ninety degrees to our line of sight, the galaxy would have ellipticity $e = 1$. Panel (b) pictures the theory of a halo collapsing under its own gravity G, in a constant gravitational field T, the source of which would be to the right of the picture. This eventually will form an oblate halo.

will be referred to in future chapters, we will calculate the intrinsic alignment contamination to various weak lensing surveys.

5.1 The potential origin of intrinsic galaxy alignments

A natural consequence from traditional theories of galaxy formation, is a net alignment of nearby galaxies that arises from the origin of their shape. Hoyle (1949), was the first to suggest that in the formation of a protogalaxy, the galaxy would acquire angular momentum due to gravitational coupling with the surrounding matter. Peebles (1969) and Heavens & Peacock (1988) developed this idea, showing that it fitted well with the gravitational instability picture for the formation of galaxies and the predictions of this now widely accepted theory of 'tidal torques' agrees on the whole with N-body simulations (White 1984).

A very simple picture for the formation of disk galaxies starts with a gravitationally collapsing baryonic cloud of gas, dust and dark matter. Angular momentum can be transfered to this system from gravitational interactions with the tidal field of neighbouring proto-galaxies. As the collapse becomes non-linear, angular momentum gain is suppressed as the newly formed dark matter halo shrinks. Pressure within the halo can no longer support the collapsing cloud and we see the formation of a thin rotationally supported disk, perpendicular to the axis of its angular momentum (Heavens, Refregier & Heymans 2000), see figure 5.1a. The disk orientation and hence the galaxy ellipticity is therefore correlated with the local tidal field.

An alternative picture proposes that galaxy ellipticity is determined by the shape of the dark matter halo in which it forms, (Heavens, Refregier & Heymans 2000; Croft & Metzler 2000; Catelan, Kamionkowski & Blandford 2001). If this is the case, we could picture a spherical halo, experiencing gravitational collapse in a constant tidal field. This halo will experience different gravitational forces on each side, resulting not in a spherically symmetric collapse, but instead forming an oblate halo, see figure 5.1b. Galaxies forming within halos experiencing the same tidal field will therefore show some net elongation.

What we can conclude from both of these simple pictures, is that if several galaxies form in the same tidal field they will, to some degree, become aligned with one another. Effects such as gas dynamics, merger events and satellite accretion, (Vitvitska et al. 2002), complicate this simple picture, but it is clear to say that we should expect to find some level of intrinsic alignment between neighbouring galaxy pairs.

5.2 Implications for weak lensing measurements

The aim for weak lensing surveys to date has been to go as deep and as wide as possible in order to maximise the weak lensing signal whilst also minimising the unknown potential contamination from intrinsic galaxy alignments. The decrease of angular intrinsic alignment correlations with survey depth arises from purely geometrical reasons; for a higher redshift population, there is a lower proportion of nearby galaxy pairs at a given angular separation θ.

To calculate the contamination to weak lensing measurements by intrinsic galaxy alignments, we require an estimate of the angular intrinsic correlation function $C_I(\theta)$, to directly compare with the expected angular shear correlation lensing signal $\langle\gamma\gamma^*\rangle_\theta$, equation 2.79. $C_I(\theta)$ can either be measured from low redshift surveys such as the SuperCOSMOS survey (Brown et al. 2002) and the Tully catalogue (Pen, Lee & Seljak 2002), or can be calculated from theoretical estimates of the three dimensional intrinsic ellipticity correlations between galaxies $\eta(r)$ where

$$\eta(r) =< e(\mathbf{x})e^*(\mathbf{x}+r) >, \tag{5.1}$$

r is the comoving distance between galaxy pairs, and e is the ellipticity of a galaxy approximated as an ellipse, defined by its ellipticity parameters, equation 2.32, such that $e = e_1 + ie_2$. Consider the following:

An observer has two lines of sight, separated by angle θ on the sky. Each line of sight is effectively a cone of solid angle $d\Omega$. If $\rho(w)$ is the mean number density of galaxies at a comoving radial geodesic distance w, then in a small volume element of cone A, there will be $\rho(w_a)w_a^2 dw_a d\Omega_a$ galaxies. Picking a small volume element in cone B separated from our volume element in cone A by a distance $r_{ab} = |\mathbf{w_a} - \mathbf{w_b}|$, we can see that the number of galaxy pairs in this small subset that contribute to the observed angular ellipticity correlations will be proportional to $\rho(w_a)w_a^2 dw_a d\Omega_a\, \rho(w_b)w_b^2 dw_b d\Omega_b\, \eta(r_{ab})$.

Before we continue any further we must consider the effects of galaxy clustering, as use of only the mean number density of galaxies $\rho(w)$ will not take into account the fact that at small separations galaxies tend to cluster, increasing the expected number of galaxy pairs at small separations. To quantify this effect we will include the clustering two-point correlation function $\xi_{gg}(r_{ab})$. This is defined as the ratio of the number of neighbours, separated by distance r_{ab}, that are in excess of the number expected by random, compared to the number of neighbours expected from a normal distribution. For an object chosen at random from our observers galaxy sample, the probability of finding that it has a neighbour at distance r_{ab} in volume $w^2 dw d\Omega$, is given by $dP = \rho(w)w^2 dw d\Omega[1 + \xi_{gg}(r_{ab})]$. Therefore the ellipticity correlations that our observer will measure from our small galaxy subset is proportional to $\rho(w_a)w_a^2 dw_a d\Omega_a \rho(w_b)w_b^2 dw_b d\Omega_b[1 + \xi_{gg}(r_{ab})]\eta(r_{ab})$.

As $\eta(r)$ and $\xi_{gg}(r)$ are rotationally invariant we can now compute the total angular ellipticity correlation $C_I(\theta)$, by integrating along our observers line of sight and across the sky. Dividing by the total number of galaxy pairs to get an average, we find, writing in terms of redshift,

$$C_I(\theta) = \frac{\int dz_a dz_b \phi_z(z_a)\phi_z(z_b)\left[1+\xi_{gg}(r_{ab},z)\right]\eta_I(r_{ab})}{\int dz_a dz_b \phi_z(z_a)\phi_z(z_b)\left[1+\xi_{gg}(r_{ab},z)\right]}, \tag{5.2}$$

where $\phi_z(z)$ is the redshift distribution such that $\phi_z(z)dz = 4\pi\rho(w)w^2dw$, where $\phi_z(z)$ is either known or can be approximated by equation 4.1. Most studies have found $\eta(r_{ab})$ is significant only for galaxies closer than a few tens of Mpc, such that the comoving separation, r_{ab} is given by

$$r_{ab}^2 \simeq (w_a - w_b)^2 + \left[f_K\left(\frac{w_a+w_b}{2}\right)\right]^2\theta^2, \tag{5.3}$$

where $f_K(w)$ is the comoving angular diameter distance out to a comoving radial geodesic distance w, given in equation 1.2. For the present we will assume, as do most intrinsic alignment studies, that

$$\xi_{gg}(r,z) = (r/5\mathrm{h}^{-1}\mathrm{Mpc})^{-1.8}, \tag{5.4}$$

thereby ignoring any redshift dependence in view of the weak evolution seen by Cole et al. (1994); Giavalisco et al. (1998); Adelberger et al. (1998). In chapter 7, however, due to differing observational evidence for the evolution of galaxy clustering (Le Fevre et al. 1996; Postman et al. 1998; Baugh et al. 1999; Carlberg et al. 2000; Firth et al. 2002; Wilson 2003), we will also investigate the effects for intrinsic alignment studies of including a redshift dependent galaxy clustering model;

$$\xi_{gg}(r,z) = \left(\frac{r}{r_o}\right)^{\gamma}(1+z)^{-(3+\epsilon)}. \tag{5.5}$$

With an estimate for the 3D intrinsic ellipticity correlations $\eta(r)$ and a model for $\xi_{gg}(r,z)$, we can calculate the angular intrinsic ellipticity correlation function $C_I(\theta)$ from equation 5.2 which can then be converted into an intrinsic angular 'shear' correlation function $\langle\gamma\gamma^*\rangle_I = \frac{1}{4}C_I(\theta)$. Note that the factor $\frac{1}{4}$ comes from the conversion from ellipticity to shear, equation 2.37. $\langle\gamma\gamma^*\rangle_I$ can be directly compared to the theoretical weak lensing shear correlation function $\langle\gamma\gamma^*\rangle$ equation 2.79 in order to calculate the contamination to weak lensing measurements by intrinsic galaxy alignments.

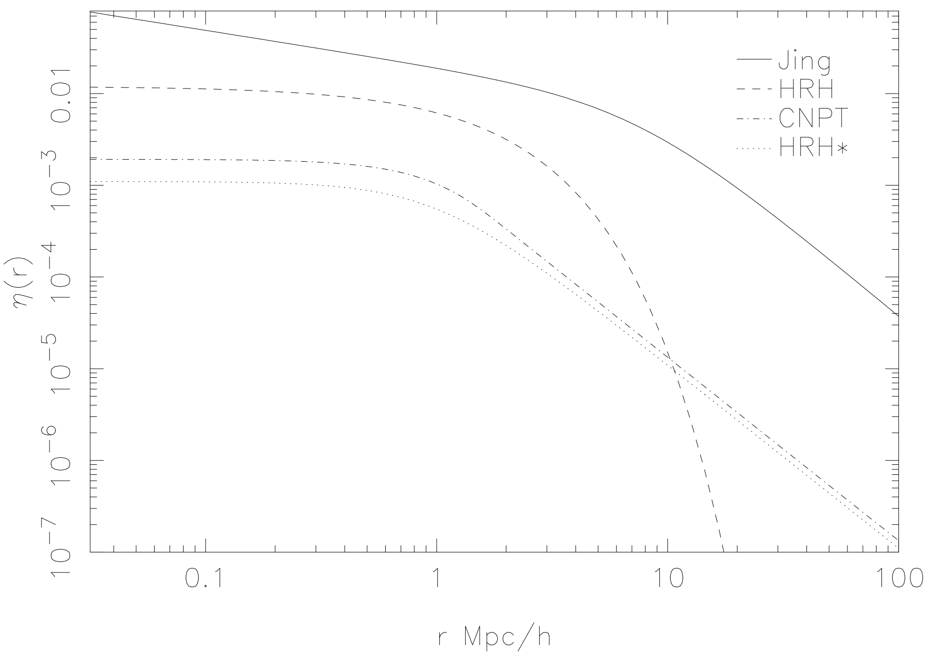

Figure 5.2: Intrinsic ellipticity correlation models. Comparison of different functional fits to three intrinsic alignment studies, Jing (solid) (Jing 2002), HRH (dashed) (Heavens, Refregier & Heymans 2000) and CNPT (dot dash) (Crittenden et al. 2001) and the modified HRH model, HRH* (dotted) (Heymans et al. 2003)

5.3 Theoretical estimates for 3D intrinsic ellipticity correlations: $\eta(r)$

Several independent groups have theoretically investigated the three dimensional intrinsic ellipticity correlations between galaxies $\eta(r)$, and have found strong evidence for a non-zero intrinsic alignment contribution to weak gravitational lensing measurements (Heavens, Refregier & Heymans 2000; Catelan, Kamionkowski & Blandford 2001; Crittenden et al. 2001; Croft & Metzler 2000; Hui & Zhang 2002; Lee & Pen 2001; Jing 2002; Mackey, White & Kamionkowski 2002; Porciani, Dekel & Hoffman 2002). The existing methods used to determine $\eta(r)$ can be broadly split into two approaches. The first employs numerical simulations assuming that luminous galaxies have similar properties to their dark matter halo counterparts thereby relating galaxy shape to dark matter halo shape. The second uses analytic techniques, relating ellipticity correlations to initial linear tidal shear field correlations. Bearing in mind the very different simplifying assumptions that are incorporated into all these studies, it is very gratifying to know that there is broad agreement in the results. Figure 5.2 shows $\eta(r)$ for the four intrinsic alignment models that we will focus on in this and in future chapters, showing that in the finer details however, these models can differ by up to an order of magnitude, or more.

5.3.1 Numerical Simulations

Assuming that luminous matter forms galaxies in all dark matter halos above some minimum mass limit, M_h, it is possible to acquire a three dimensional catalogue of galaxy shapes from a large N-body dark matter numerical simulation. This requires educated guesses for the relationship between luminous galaxies and their parent dark matter halos, following the two different pictures for the origin of galaxy ellipticity, as discussed in section 5.1.

Elliptical Galaxy Models

Heavens, Refregier & Heymans (2000), Croft & Metzler (2000) and Jing (2002), hereafter HRH, CM and Jing, use an elliptical-type galaxy model where the shape of the luminous galaxy is identical to that of its dark matter halo. Dark matter halos are identified using a friends-of-friends algorithm (Davis et al. 1985), and chosen to be above a minimum halo mass, which relates to a minimum number of occupying dark matter particles. With dark matter particles positioned at $\boldsymbol{\xi}_i = (x_i, y_i, z_i)$ the density profile $\rho(\boldsymbol{\xi})$, can be modelled as a sum of delta functions,

$$\rho(\boldsymbol{\xi}) = \Sigma_i \delta(\boldsymbol{\xi} - \boldsymbol{\xi}_i) = \Sigma_i \delta(x - x_i)\delta(y - y_i)\delta(z - z_i). \tag{5.6}$$

The galaxy ellipticity e can then be calculated from the quadrupole moments of the projected halo density Q_{ij} (equation 2.30) through equation 2.31. The result should be independent of which reference frame we project, acting as a good consistency check. Here we project in the xy plane.

$$Q_{xy} = \int d^3\boldsymbol{\xi}\; xy\, \Sigma_i \delta(x - x_i)\delta(y - y_i)\delta(z - z_i) = \Sigma_i x_i y_i \tag{5.7}$$

Similarly $Q_{xx} = \Sigma_i x_i^2$, and $Q_{yy} = \Sigma_i y_i^2$. With this simple model it is possible to obtain a catalogue of galaxy shapes from which the 3D intrinsic ellipticity correlation function $\eta(r)$ can be measured.

In order to get the large number of halos required in order to detect correlations in halo shape and/or halo 'orientation' it was necessary for both HRH and CM to use halos with as few as 10 (HRH) and 20 (CM) occupying particles, below which the shape was not well determined. This provided a minimum halo mass limit $M_h = 6.9 \times 10^{11} M_\odot$. Jing used a new state-of-the-art cosmological N-body simulation with 512^3 particles. He investigated the effect of simulation resolution and the dependence of the intrinsic alignment signal on the minimum allowed halo mass, finding that a minimum halo occupation number of 160 particles was necessary to get accurate shape measurements. Using the same minimum halo mass, HRH, CM and Jing find good agreement in their results for $\eta(r)$, with better resolution simulations increasing $\eta(r)$ by a factor of around two. This result alone shows that in numerical simulations there is a preferred angular momentum direction for nearby dark matter halos. Jing notes a dramatic increase of the halo ellipticity correlation signal with increasing minimum halo mass, which is most likely due to the fact that larger halos have stronger gravitational effects on each other, and therefore experience a larger degree of alignment. Including the lower halo masses, which do not have such strong tidal effects, will lower the average signal but provide a more representative halo sample. The minimum halo mass should really be chosen by consideration of which halos are unlikely to form galaxies, but this is a very difficult figure to set.

Jing quotes a fitting formula to his results for the three dimensional ellipticity correlations $\eta(r)$, with r in h^{-1}Mpc, with a best fitting functional form defined for $\langle e_1 e_1 \rangle$.

$$\eta_{\mathrm{Jing}}(r) \approx 2\langle e_1 e_1 \rangle = 2\,\frac{3.6 \times 10^{-2}\left(\frac{M_h}{10^{10} h^{-1} Mpc}\right)^{0.5}}{r^{0.4}(7.5^{1.7} + r^{1.7})} \tag{5.8}$$

Spiral Galaxy Models

HRH also uses a spiral-type galaxy model where the luminous matter is modelled as a thin disk, oriented perpendicular to its angular momentum vector $\mathbf{L} = (\sin\mu\cos\nu, \sin\mu\sin\nu, \cos\mu)$, where μ and ν are the polar and azimuthal angles in the reference frame of the simulation box. The ellipticity of such a galaxy is easily calculated, see figure 5.3. First consider an observer in the xy plane who will see a circular galaxy of radius r when $\mathbf{L}$ is directed along the line of sight z. A polar rotation of μ about the x axis will produce an observed ellipse oriented with its major axis of length r along the x axis and its minor axis reduced to $r\cos\mu$. The ellipticity of this galaxy is $|e| = \sin^2\mu/(1+\cos^2\mu)$. An azimuthal rotation of ν about the z axis gives us an ellipse with position angle $\phi = \nu + \pi/2$, when ϕ is measured counter clockwise from the x axis. Re-writing the ellipticity and position angle in terms of the angular

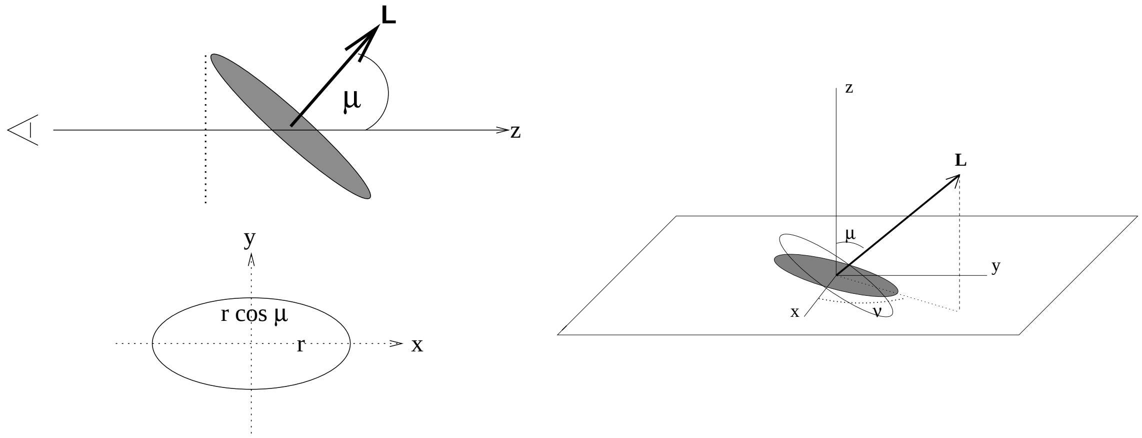

Figure 5.3: Simple model of a spiral galaxy which is taken to be a thin disc perpendicular to its angular momentum vector $\mathbf{L}$. The diagrams on the left show the effect of the initial polar rotation by μ in the yz plane (upper) and then in the observers xy plane (lower). The diagram on the right shows the disk galaxy after the azimuthal rotation ν as the open ellipse, and its projection on the sky as the filled ellipse.

momentum we find

$$|e(L_z)_{\rm HRH}| = \frac{1-L_z^2}{1+L_z^2}, \tag{5.9}$$

$$\phi(L_x, L_y) = \tan^{-1}\left(\frac{L_y}{L_x}\right) + \frac{\pi}{2}. \tag{5.10}$$

Assuming that the angular momentum distribution of the luminous galaxy is identical to the angular momentum distribution of its parent dark matter halo (Fall & Efstathiou 1980), it is again possible to produce a catalogue of galaxy shapes from an N-body simulation. As with the elliptical galaxy model, dark matter halos were identified using a friends-of-friends algorithm and chosen above a minimum halo mass, $M_h = 6.9 \times 10^{11} M_\odot$ such that the angular momentum was well defined. The resulting ellipticity correlation function is fitted with an exponential such that

$$\eta_{\rm HRH}(r) = 0.012 \exp\left(-\frac{r}{1.5h^{-1}Mpc}\right). \tag{5.11}$$

Fitting an exponential model could underestimate $\eta_{\rm HRH}(r)$ on large scales $r > 10\rm h^{-1}Mpc$, where the signal-to-noise is low. This would then lead to an underestimation of the intrinsic signal on angular scales $\theta \geq 10'$. Due to the lack of detection of an aperture mass B mode signal on these scales however (Hoekstra, Yee & Gladders 2002), an intrinsic correlation that was significantly higher would then be inconsistent, where the B mode is treated as a diagnostic of intrinsic alignment contamination and is discussed further in chapter 7.

5.3.2 Analytical Techniques

If we state that galaxy ellipticity should be determined, at least in part, by the tidal gravitational field in which the galaxy forms, we can use analytic theory to derive a model for galaxy ellipticity correlations. These models are really only educated guesses as to the origin and relationship between galaxy ellipticity and tidal fields, and are often chosen in part because of their mathematical simplicity. They do however provide valuable models for the shape and amplitude of these long range correlations, and we will see later in chapter 7, that these models are well matched to observational constraints.

The most simple form for an analytical model comes from Catelan, Kamionkowski & Blandford (2001), where it is assumed that galaxy ellipticity is proportional to the tidal shear from a cold dark matter primordial Gaussian density field. The long-range correlations calculated in the gravitational field are propagated through to long-range correlations in galaxy ellipticities. Catelan, Kamionkowski & Blandford (2001) also outline an alternative analytic model, from tidal torque theory, discussed more fully by Crittenden et al. (2001), hereafter CNPT, and Mackey, White & Kamionkowski (2002), where galaxy ellipticity is determined by its angular momentum.

CNPT consider galaxy shape to be uncorrelated with its neighbours. Its orientation however, which is determined by its angular momentum, is considered to be correlated with its neighbours due to tidal interactions during galaxy formation. Using a realistic distribution of galaxy shapes taken from the APM catalogue (Lambas, Maddox & Loveday 1992), CNPT relate an average galaxy ellipticity to its angular momentum through

$$\langle|e(L_z)|\rangle = \beta\left(\frac{1-L_z^2}{1+L_z^2}\right) = \beta|e(L_z)_{\rm HRH}| \tag{5.12}$$

where β accounts for galaxy thickness; $\beta = 1$ corresponds to a thin disc approximation, $\beta = 0$ corresponds to a spherical galaxy. CNPT find that for spirals $\beta \approx 0.85$ ranging down to $\beta \approx 0.5$ for spheroids and ellipticals. Following CNPT we will use $\beta = 0.73$, which is the value determined from the observed distribution of ellipticities measured for lensing studies (Ebbels 1998), and the mean β value of the APM.

The angular momentum of a protogalaxy depends on the tidal field within which it collapses and its moment of inertia, i.e. how easy it is to start it turning. The moment of inertia of the gas clump could also be correlated with the shear field however and the degree of correlation is very uncertain. CNPT quantify this uncertainty with a parameter Υ. When $\Upsilon = 0$, the moment of inertia is correlated with the tidal shear field. The stronger the shear field, the larger the moment of inertia and the harder it is to effect the protogalaxies angular momentum, leaving it random and uncorrelated with the shear field. With $\Upsilon = 1$ the moment of inertia is uncorrelated with the shear field, increasing the correlation between a galaxy's angular momentum and its local shear field. CNPT use $\Upsilon = 0.55$, which is inferred from numerical simulation results (Heavens, Refregier & Heymans 2000). Assuming that the density field has a Gaussian distribution, CNPT find that the ellipticity correlation is well approximated at large $r > 3\mathrm{h}^{-1}$Mpc by

$$\eta_{\mathrm{CNPT}}(r) = \frac{\Upsilon^2\beta^2}{84}\frac{\varepsilon^2(r)}{\varepsilon^2(0)}, \tag{5.13}$$

where $\varepsilon(r)$ is the density correlation function,

$$\varepsilon(r) = \int_0^\infty dk\, k^2 J_0(kr) P_\delta(k)\,, \tag{5.14}$$

$J_0(kr)$ is the first order Bessel function and $P_\delta(k)$ is the non-linear matter power spectra. To produce a simple model for $\eta_{\mathrm{CNPT}}(r)$, we will use the following analytic solution to equation 5.14 for the model proposed in CNPT, who took $P_\delta(k) \propto k^{-2}$, assuming top-hat smoothing on $r_s = 1h^{-1}$Mpc scales, such that

$$\begin{aligned}
\varepsilon(r < 2r_s) &= -\frac{\pi(r^5 - 30r^3r_s^2 + 80r^2r_s^3 - 192r_s^5)}{2880r_s^6}, \\
\varepsilon(r > 2r_s) &= \frac{\pi}{18r}.
\end{aligned} \tag{5.15}$$

Hui & Zhang (2002) repeat this method finding a non-negligible addition from non-Gaussian fluctuations in the density field. Mackey, White & Kamionkowski (2002) also revisit this idea in Fourier space, obtaining very similar results to CNPT.

5.4 Modification to the HRH spiral model

To produce the HRH spiral model it was assumed that the angular momentum vector of the gas disc was directly aligned with its parents dark matter halo angular momentum vector. It is however plausible that the gas and dark matter do not in fact have the same angular

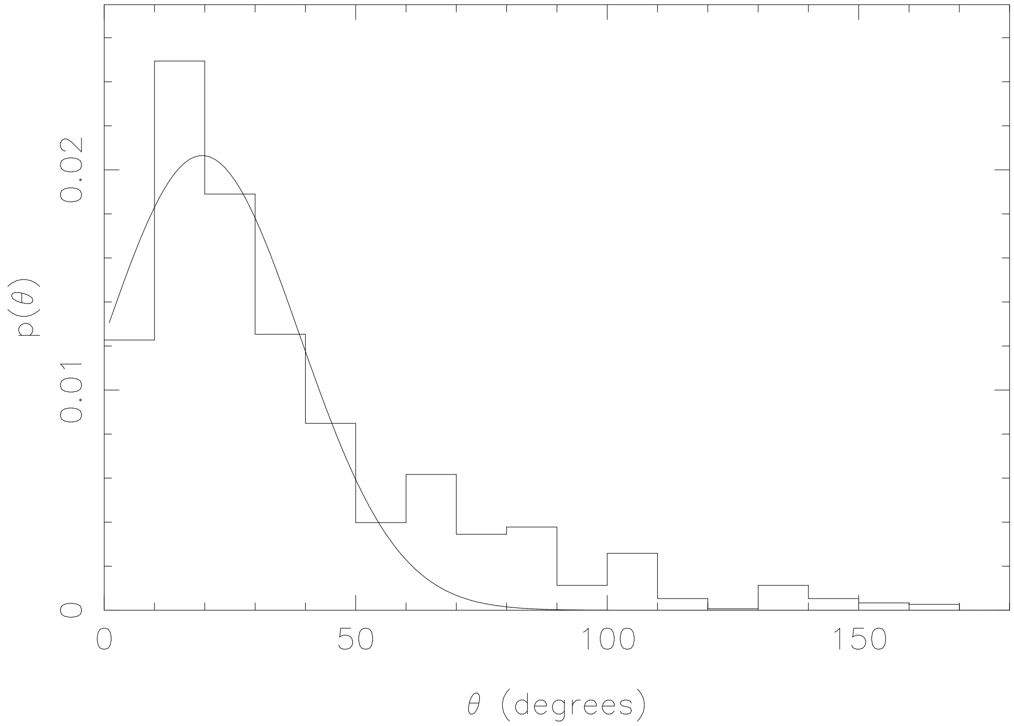

Figure 5.4: Distribution of the misalignment angle between the total angular momentum vectors of the dark matter and gas, as found by Van Den Bosch et al. (2002). Overplotted is the best fit Gaussian model with mean $\mu = 20°$ and width $\sigma = 20°$..

momentum distribution as they experience different relaxation mechanisms during gravitational collapse. Dark matter undergoes collisionless virialization and gas achieves hydrostatic equilibrium through shocks which in principle could cause the redistribution of its angular momentum. This theory has been tested through numerical simulations of structure formation which contain equal numbers of dark matter and nonradiative gas particles. The comparison of the resulting angular momentum distributions of the gas and parent dark matter halo particles in a large sample of cold dark matter haloes for a concordance cosmology, has shown that the gas and dark matter total angular momentum vectors are in fact poorly aligned with a median misalignment angle of $\sim 30°$ (van den Bosch et al. 2002). Observational support for some misalignment, albeit smaller, comes from strong lensing considerations in the CASTLES survey (Keeton, Kochanek & Falco 1998). Figure 5.4 shows the probability distribution of the polar misalignment angle θ' as found by van den Bosch et al. (2002) and the best fit Gaussian model. van den Bosch et al. (2002) note that higher resolution simulations are required to reduce the possible impact of discreteness effects on this probability distribution, but they do conclude that there is a true misalignment that is significantly different from zero.

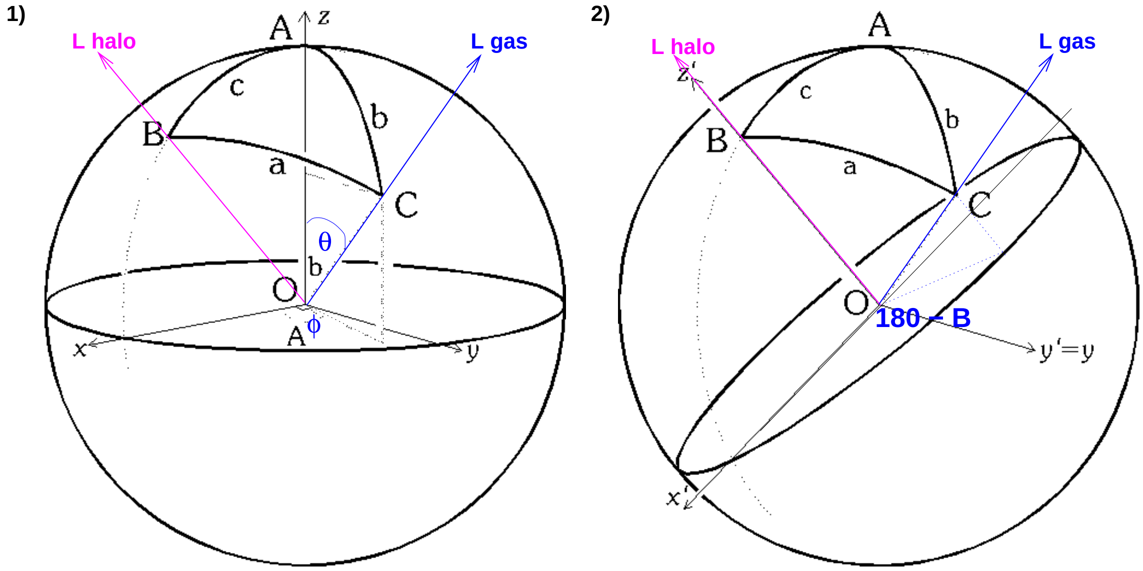

Figure 5.5: Spherical trigonometry to calculate the angular momentum of a misaligned gas disc. Right hand figure pictures the reference frame of the simulation box. A simple rotation keeping the y axis fixed, places the left hand figure in the reference frame of the angular momentum of the dark matter halo. Underlying figures from F. Vincent[2].

In light of these new results we repeat the analysis of HRH for the N-body simulation developed by the Virgo Consortium (Jenkins et al. 1998), for a ΛCDM cosmological model, ($\Omega_m = 0.3$, $\Omega_\Lambda = 0.7$, $\sigma_8 = 0.9$, $\Gamma = 0.2$). Instead of assuming perfect alignment between the angular momentum of the dark matter halo $\mathbf{L}_{\rm halo}$ and the angular momentum of the gas disc $\mathbf{L}_{\rm gas}$, we will now assume that $\mathbf{L}_{\rm gas}$ is misaligned with $\mathbf{L}_{\rm halo}$ by polar angle θ' and by an azimuthal angle ϕ', when $\mathbf{L}_{\rm halo}$ is oriented along the z axis. θ' is given by the probability distribution shown in figure 5.4 as found by van den Bosch et al. (2002) which we will approximate as a Gaussian with mean $\mu = 20°$ and width $\sigma = 20°$ which is truncated at zero misalignment. ϕ' is random, chosen from a uniform distribution such that $0 < \phi' < 2\pi$.

Figure 5.5 pictures how we can derive polar and azimuthal position angles θ and ϕ for $\mathbf{L}_{\rm gas}$ in the reference frame of the simulation box, in terms of θ', ϕ' and the polar and azimuthal position angles, μ and ν for $\mathbf{L}_{\rm halo}$.

$$\mathbf{L}_{\rm halo} = (\sin\mu\cos\nu, \sin\mu\sin\nu, \cos\mu). \quad (5.16)$$

$$\mathbf{L}_{\rm gas} = (\sin\theta\cos\phi, \sin\theta\sin\phi, \cos\theta). \quad (5.17)$$

Figure 5.5.1 pictures $\mathbf{L}_{\rm halo}$ and $\mathbf{L}_{\rm gas}$ in the reference frame of the simulation box. For the

[2] *star-www.st-and.ac.uk/~fv/webnotes/chapter2.htm*

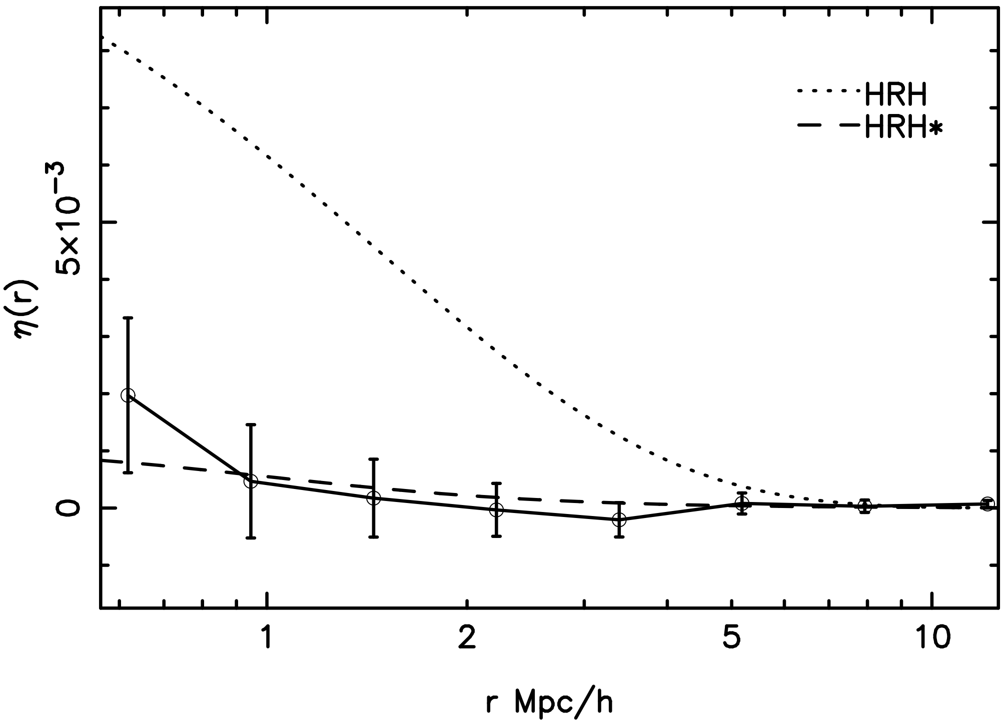

Figure 5.6: 3D ellipticity correlation function estimated from the ΛCDM Virgo simulation, assuming that the gas disc and dark matter halo are misaligned. Over-plotted is the HRH model $\eta_{\rm HRH}(r)$ (dotted) and the best fit HRH modified model $\eta_{\rm HRH*}(r)$ (dashed).

present we will assume that $\nu = 0$ and then reintroduce $\nu \neq 0$ at the end. μ is represented in figure 5.5 by angle c. We require the position angles of $\mathbf{L}_{\rm gas}$, θ and ϕ, which are represented in this figure by b and A respectively. Figure 5.5.2 rotates the reference frame such that $\mathbf{L}_{\rm halo}$ lies along the z' axis. In this reference frame we can see that a is our known polar misalignment angle θ', and that $(180° - B)$ is our known azimuthal misalignment angle ϕ'. Once these angles have been identified we can use the transposed cosine rule $\cos b = \cos a \cos c + \sin a \sin c \cos B$, to get θ in terms of θ', μ and ϕ' such that

$$\theta = \cos^{-1}[\cos\theta' \cos\mu - \sin\theta' \sin\mu \cos\phi']. \tag{5.18}$$

Using the sine rule, $\sin a / \sin A = \sin b / \sin B$, and including a non zero ν, which we can simply add on, we find

$$\phi = \nu + \sin^{-1}\left[\frac{\sin\theta' \sin\phi'}{\sin\theta}\right]. \tag{5.19}$$

The ellipticity and position angle of the resulting galaxy is then easily calculated from equations 5.12 and 5.10, where we will now also account for galaxy thickness, following CNPT by taking $\beta = 0.73$.

Figure 5.6 compares the resulting 3D ellipticity correlation function from the Virgo simulation with the HRH model, equation 5.11, (dotted). This shows that with the inclusion of baryon halo angular momentum misalignment, the amplitude of the galaxy alignments predicted from numerical simulations is significantly reduced. We will fit a simple function to these results such that

$$\eta(r) = \frac{A}{1 + (r/B)^2}, \tag{5.20}$$

where we fix $B = 1h^{-1}$ Mpc, which is similar to the CNPT choice of a smoothing length of $1h^{-1}$Mpc, constraining $\eta(r) \to A$ at small r instead of allowing $\eta(r) \to \infty$. If this was allowed, this exponential upturn in the model would dominate the intrinsic alignment predictions and it would neglect the fact that for galaxy pairs at smaller separations than 1 Mpc, effects from gravitational interactions become important. The likelihood L of this simple two-power law model has been calculated from

$$\ln L = -\frac{1}{2}\chi^2 = -\frac{1}{2}\Sigma_i \left(\frac{d(r_i) - m(r_i)}{\sigma(r_i)}\right)^2, \tag{5.21}$$

where $d(r_i)$ is the measured $\eta(r_i)$ with associated error $\sigma(r_i)$, and $m(r_i)$ is the value of the model $\eta_{\mathrm{HRH*}}(r_i)$ with A allowed to vary. The relative likelihood $\ln(L) - \ln(L_{\max})$ is shown dot-dashed in figure 7.7 showing that a small positive value for A is preferred. It should also be noted from figure 7.7 that the reduced signal from the misalignment means the data is actually consistent with zero. The best fit, with $\chi^2 = 3.14$ for 7 degrees of freedom, is

$$\eta_{\mathrm{HRH*}}(r) = \frac{0.0011}{1 + r^2}, \tag{5.22}$$

with r in h^{-1} Mpc, which is consistent with the CNPT analytical model.

It should be noted that this new model fit lies above the old HRH model at large scales $r > 10h^{-1}$ Mpc, which should not be taken to imply that misalignment increases the correlations. Rather, it reflects the fact that the old exponential fit of HRH underestimated the (noisy) correlations on large scales as discussed in section 5.3.1.

Comparing the HRH* model with the ellipticity variance measured in the low redshift $z_m \sim 0.1$ SuperCOSMOS survey (Brown et al. 2002), we see in figure 5.7, excellent agreement on scales $\theta > 35'$, where an HRH* angular intrinsic ellipticity correlation function has been calculated from equation 5.2 with a median redshift $z_m = 0.1$, and related to the ellipticity

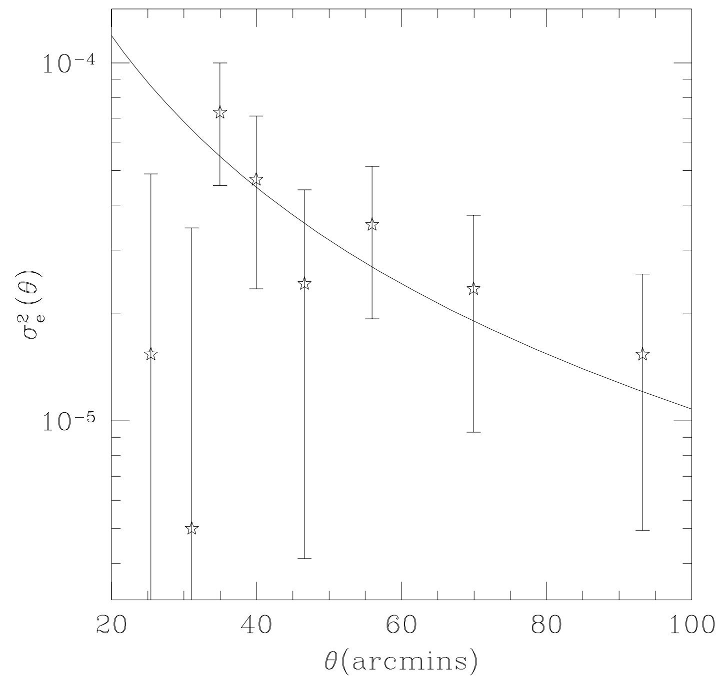

Figure 5.7: Comparison of the measured ellipticity variance in the $z_m \sim 0.1$ SuperCOSMOS survey, see Brown et al. (2002) for details, compared to the ellipticity variance expected at this redshift from the modified HRH* model.

variance following Bacon et al. (2003)

$$\sigma_e^2(\theta)_\square = \frac{2\sqrt{\pi}}{\theta^2}\int_0^\theta d\theta'\,\theta' C_I(\theta')\,. \tag{5.23}$$

Note that the factor $\sqrt{\pi}$ is a good approximation to use in order to scale the ellipticity variance measured in circular apertures of radius θ to the ellipticity variance as measured in SuperCOSMOS, in square cells of length θ (Bacon, Refregier & Ellis 2000). The relative likelihood $\ln(L) - \ln(L_{\rm max})$ of the HRH* model compared to the SuperCOSMOS results on scales $\theta > 20'$ is shown dotted in figure 7.7 where the amplitude A is allowed to vary. Below this angular scale the SuperCOSMOS results are extremely noisy and could well suffer contamination from residual PSF anisotropy distortions as in SuperCOSMOS, PSF distortions have only been corrected on $\theta > 10'$ scales. There will therefore be a non-negligible PSF distortion contribution to the ellipticity variance up angular scales $\theta \approx 20'$ scales. The small angular scale results are therefore omitted from the likelihood fitting procedure, finding the best fit amplitude with $\chi^2 = 7.4$ for 8 degrees of freedom, with $A = 0.0009 \pm 0.0005$, (95% confidence limits).

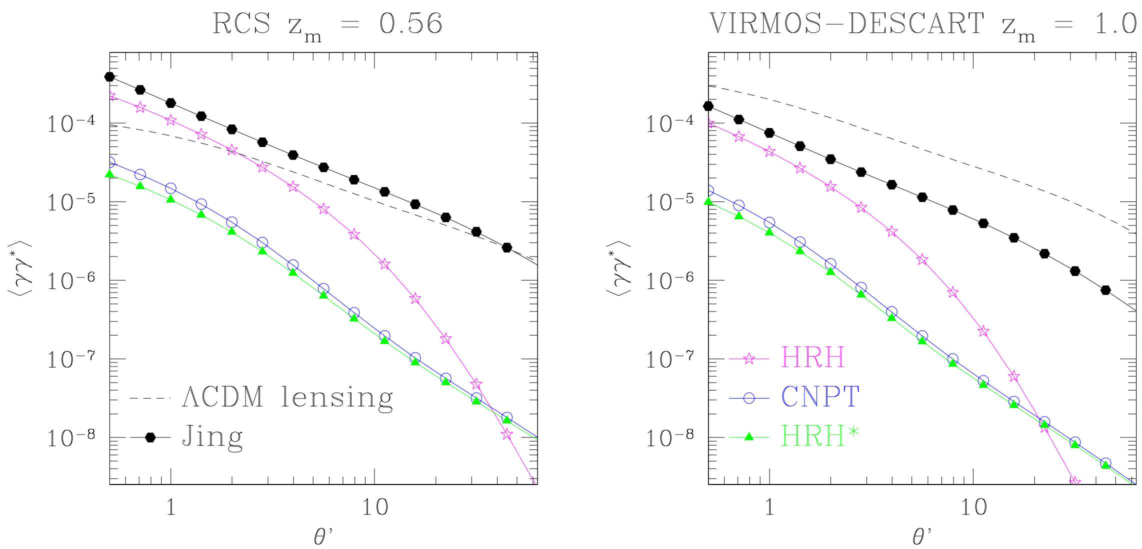

Figure 5.8: Predicted intrinsic alignment angular shear correlation functions, Jing (filled), HRH (stars), CNPT (circles) and HRH* (triangles). The intrinsic alignment contributions are compared to the angular shear correlations from ΛCDM weak gravitational lensing, normalised to $\sigma_8 = 0.8$, (dashed), for the RCS with depth $z_m = 0.56$, (left) and for the VIRMOS-DESCART survey with depth $z_m = 1.0$, (right).

5.5 Intrinsic alignment contamination to weak lensing measurements

With theoretical models for $\eta(r)$ it is possible to estimate the contamination to weak lensing measurements from equation 5.2. Figure 5.8 shows the intrinsic angular shear correlations $\langle\gamma\gamma^*\rangle_I = \frac{1}{4}C_I(\theta)$, for two different depth weak lensing surveys, the Red sequence Cluster Survey (RCS) with a median redshift $z_m \approx 0.56$ (Hoekstra et al. 2002), and the VIRMOS-DESCART survey with $z_m \approx 1.0$ (Van Waerbeke et al. 2002), for different $\eta(r)$ models. Also plotted for comparison are the shear correlations expected from weak gravitational lensing, for an $\Omega_m = 0.3$, $\Omega_\Lambda = 0.7$ cosmology with a $\Gamma = 0.2$, $\sigma_8 = 0.8$, nonlinear CDM matter power spectrum, P_δ calculated using the fitting formula from Smith et al. (2003). For the medium RCS depth survey we see significant contamination from the HRH and Jing model at angular scales $\theta < 10'$. The CNPT and HRH* models predict contamination at the 10% level. For the deeper VIRMOS-DESCART survey, with the exception of the Jing model, the intrinsic contribution for $\theta > 2'$ is less than 10% of the expected shear correlation function which is in agreement with other intrinsic alignment studies (Catelan, Kamionkowski & Blandford 2001; Croft & Metzler 2000; Hui & Zhang 2002; Mackey, White & Kamionkowski 2002; Porciani, Dekel & Hoffman 2002). Note that the new modification HRH* model and the CNPT model yield expected intrinsic contributions for a survey with $z_{\rm m} = 1$ at less than 2%.

For figure 5.8 we have used a Jing model with the HRH chosen minimum halo mass $M_h = 6.9 \times 10^{11} M_{\odot}$. Varying the halo mass dependent function, equation 5.8, produces contributions of up to 60% of the expected shear correlation function for a $z_m \sim 1$ survey, depending on the choice of halo mass. This result from Jing would imply a very low value of σ_8 from weak lensing observations (Van Waerbeke & Mellier 2003), and is incompatible with the measurement of $\sigma_8 \sim 0.9$ by both Hoekstra, Yee & Gladders (2002) at $z_m \sim 0.6$ and Van Waerbeke et al. (2002) at $z_m \sim 1.0$. The redshift dependence of intrinsic alignments would, in the case of the Jings conclusions, predict a significantly higher value from the shallower RCS, in comparison with the value from the deeper VIRMOS-DESCART. It is important however not to automatically reject his results, as they disagree with data known to be plagued by systematics.

For low redshift surveys with $z_{\rm m} < 0.2$, such as the Sloan Digital all Sky Survey (SDSS), all models concur that any correlation signal measured is not induced primarily by weak gravitational lensing but is instead the more dominant intrinsic correlation signal, for example see figure 6.3.

We will discuss the implications for weak gravitational lensing in more depth in the next two chapters, showing that with photometric redshift information it is possible to eliminate the contaminating intrinsic signal. But for the moment we will say that although it is true that the presence of intrinsic galaxy alignments is an annoyance to weak lensing teams, it is an interesting topic in its own right as it has the potential to shed new light on the origin of angular momentum in galaxies which is intimately linked to the understanding of structure and the formation of disk galaxies.

6

Removing the contamination to weak lensing measurements from intrinsic galaxy alignments

If an accurate estimate of the angular intrinsic ellipticity correlation strength $C_I(\theta)$ existed, then it would be possible to subtract it from shear correlation measurements leaving correlations induced purely by weak gravitational lensing. As detailed in chapter 5 though, intrinsic galaxy alignment studies are far from converging on an agreed model. This uncertainty is further compounded by the unestablished nature of the evolution of galaxy clustering, an important factor in converting theoretical estimates of the 3D intrinsic ellipticity correlation, $\eta(r)$, into an angular correlation function $C_I(\theta)$, see equation 5.2. As we are absent of a good estimate for the intrinsic correlation, we can make significant improvements on a straightforward weak lensing analysis by simply downweighting galaxy pairs that are close enough in three dimensions to contribute to any intrinsic contaminating signal. This however is done at the expense of increasing the random shot noise contribution from individual galaxy ellipticities. In this chapter we will derive an optimal weighting scheme for an arbitrary weak lensing survey with accurate information about the galaxy distances and propose a semi-optimised procedure for multi-colour surveys with photometric redshift information. We will detail how these methods would apply to different spectroscopic and multi-colour surveys, using as an example the HRH intrinsic galaxy alignment model equation 5.11. We will find that by using a galaxy-pair weighting scheme, intrinsic alignment contamination can be reduced by several orders of magnitude.

6.1 Optimal Pair Weighting for Spectroscopic Surveys

The shear correlation function $\langle\gamma\gamma^*\rangle_\theta$, for galaxy pairs separated by an angle θ can be estimated from a catalogue of galaxy shapes, equation 2.68, as in the weak lensing regime the observed complex ellipticity e is related to the source ellipticity e^s and the complex shear γ by $e \simeq e^s + 2\gamma$. (See equation 2.36 for exact relationship). To estimate the shear correlation observationally includes an uncertain contribution from intrinsic correlations between the ellipticities of nearby galaxy pairs $I_{ab} \equiv e^s_a e^{s*}_b$ if, when averaging over many galaxy pairs, $\langle I_{ab}\rangle \neq 0$. The true estimate of the lensing shear correlation function $E[\gamma\gamma^*;\theta]$ is therefore

$$E[\gamma\gamma^*;\theta] = \frac{1}{4}\frac{\sum_{ab} W_{ab}\,(e_a e^*_b - I_{ab})}{\sum_{ab} W_{ab}}. \tag{6.1}$$

The error in this estimator, σ_L, has two main sources: uncertainty in the intrinsic correction σ_{IA}, and shot noise from the intrinsic ellipticity distribution $\sigma_{\rm SN}$. To quantify our uncertainty on the intrinsic correlations, we assume the intrinsic alignment model has a fractional error f and a variance

$$\sigma^2_{IA} = f^2\langle I_{ab}\rangle^2, \tag{6.2}$$

where $\langle I_{ab}\rangle$ is a weighted average over many galaxy pairs. We will conservatively take $f \simeq 1$ in what follows, assuming that our chosen intrinsic alignment model $\eta(r)$ is the highest amplitude model that is compatible with weak lensing measurements. If the variance of Real$(e_a e^*_b)$ is $\sigma^2_{\rm pair}$, then the shot noise error is

$$\sigma^2_{\rm SN} = \frac{\sum_{ab} W^2_{ab}\sigma^2_{\rm pair}}{\left(\sum_{ab} W_{ab}\right)^2}, \tag{6.3}$$

which, in the limit of an infinite number of galaxies, tends to zero, (note for $W_{ab} \equiv 1$, $\sigma^2_{\rm SN} = \sigma^2_{\rm pair}/N_{\rm pairs}$). Considering the shot noise error and intrinsic alignment error only, the total error on the lensing correlation function is then given by

$$\begin{aligned}\sigma^2_{\rm L} &= \sigma^2_{IA} + \sigma^2_{\rm SN} \\ &= \frac{\sum_{ab} W^2_{ab}\sigma^2_{\rm pair} + \left(\sum_{ab} W_{ab} f I_{ab}\right)^2}{\left(\sum_{ab} W_{ab}\right)^2}.\end{aligned} \tag{6.4}$$

We will minimise this variance subject to a constraint $\psi = \sum_{ab} W_{ab} - K = 0$, where K is a constant. Choosing λ', a Lagrange multiplier, such that it satisfies

$$\frac{\partial(\sigma^2_L)}{\partial W_{ab}} - \lambda'\frac{\partial\psi}{\partial W_{ab}} = 0, \tag{6.5}$$

we find that the weights for a galaxy pair $p = \{a, b\}$ then satisfy

$$W_p \sigma_{\rm pair}^2 + f^2 I_p \sum_q W_q I_q = \frac{\lambda'}{2}. \tag{6.6}$$

If we define a matrix

$$M_{pq} \equiv J_p J_q, \tag{6.7}$$

where,

$$J_p \equiv \frac{f I_p}{\sigma_{\rm pair}}, \tag{6.8}$$

then W_p satisfies

$$W_p + M_{pq} W_q = \lambda U_p, \tag{6.9}$$

where λ is an constant that now includes a factor of $\sigma_{\rm pair}$ but is unimportant. U_p is a unit vector consisting entirely of ones. The solution for $\mathbf{W}$ is then given by

$$\mathbf{W} = \lambda (\mathbf{I} + \mathbf{M})^{-1} \mathbf{U}. \tag{6.10}$$

The inverse can be computed, by expanding $(\mathbf{I} + \mathbf{M})^{-1} = \mathbf{I} - \mathbf{M} + \mathbf{M}^2 - \ldots$, with elements $[(\mathbf{I} + \mathbf{M})^{-1}]_{pq} = \delta_{pq} + J_p J_q(-1 + \Lambda_2 - \Lambda_2^2 + \ldots)$, where

$$\Lambda_2 \equiv \sum_r J_r^2. \tag{6.11}$$

Hence, reducing the expansion of $(1 + \Lambda_2)^{-1}$, we find

$$[(\mathbf{I} + \mathbf{M})^{-1}]_{pq} = \delta_{pq} - \frac{J_p J_q}{1 + \Lambda_2}. \tag{6.12}$$

The weight is then obtained from equation (6.10), equivalent to summing (6.12) over pairs q:

$$W_p = \left(1 - \frac{J_p \Lambda_1}{1 + \Lambda_2}\right) \lambda, \tag{6.13}$$

where $\Lambda_1 \equiv \sum_r J_r$. For uncorrelated galaxy pairs, $I_p = 0$, and we will choose the weight to be equal to one by setting $\lambda = 1$. This is the optimal weighting scheme if distances to the galaxies are accurately known.

6.1.1 Reduction in variance

The variance in the lensing signal, given by equation (6.4), can be written in terms of J_p,

$$\sigma_L^2 = \sigma_{\rm pair}^2 \frac{\left[\sum_p W_p^2 + \left(\sum_p W_p J_p\right)^2\right]}{\left(\sum_p W_p\right)^2}. \tag{6.14}$$

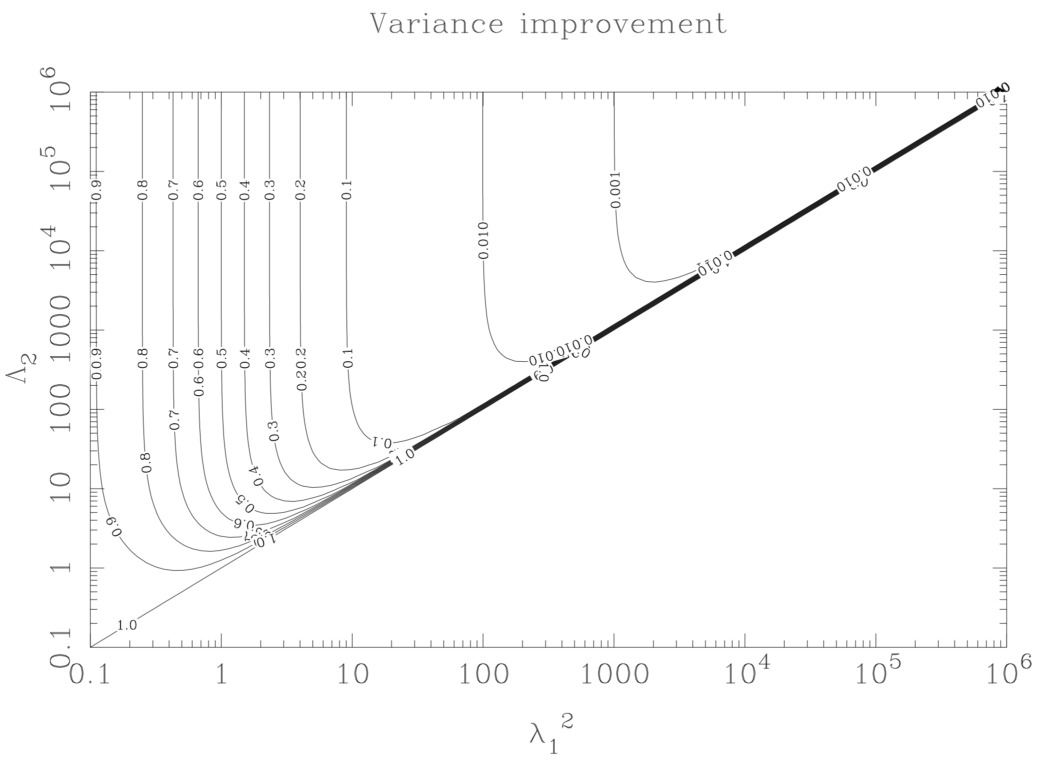

Figure 6.1: Ratio of optimal variance to the equal weighting variance.

With equal weighting of N galaxy pairs, the variance is

$$\sigma_L^2 = \frac{\sigma_{\rm pair}^2}{N^2}\left(N + \Lambda_1^2\right). \tag{6.15}$$

For optimal weighting,

$$\sigma_L^2 = \sigma_{\rm pair}^2 \frac{(1+\Lambda_2)}{N\,(1+\Lambda_2) - \Lambda_1^2}. \tag{6.16}$$

The ratio of the optimal variance to the equal weighting variance is therefore given by

$$\text{Ratio} = \frac{(1+\Lambda_2)}{(1+\lambda_1^2)(1+\Lambda_2-\lambda_1^2)}. \tag{6.17}$$

as shown in figure 6.1 as a function of $\lambda_1 \equiv \Lambda_1/\sqrt{N}$ and Λ_2. This shows that for large N, small λ_1, for example in a wide-field, deep weak lensing survey, the reduction in the error on the lensing signal can be very impressive. Note that $\lambda_1^2 \leq \Lambda_2$, i.e. above the 1:1 line in figure 6.1, which can be shown by considering $\sum_p (J_p - \langle J_p\rangle)^2 = \sum_p J_p^2 - N\langle J_p\rangle^2 > 0$.

6.1.2 Calculating optimal galaxy-pair weights

To calculate the weight for a galaxy pair ab for a particular survey we can calculate Λ_1 and Λ_2, estimated from integrals over the mean number density of the survey.

$$\begin{aligned}\Lambda_n &= \left(\frac{f}{\sigma_{\text{pair}}}\right)^n \sum_{a,b}\langle I_{ab}\rangle \\ &\simeq 2\pi\theta\Delta\theta\Delta\Omega\left(\frac{f}{\sigma_{\text{pair}}}\right)^n \int dz_a dz_b \eta^n(r_{ab})\phi_z(z_a)\phi_z(z_b)\left[1+\xi_{gg}(r_{ab})\right] \end{aligned} \tag{6.18}$$

where the redshift selection function $\phi_z(z)$ is the number of objects at redshift z included in the survey. This is given by either the true redshift distribution of the survey $n(z)$, or approximated by equation 4.1, which is normalised by $\int dz\, \phi_z(z) = n_{\text{str}}$, where n_{str} is the number of galaxies per steradian in the survey. ξ_{gg} is the galaxy two-point correlation function which we will assume is independent of redshift and is given by equation 5.4, and r_{ab} is the comoving separation of the galaxy pair as given by equation 5.3.

For $n = 0$, the integral gives the number of galaxy pairs per steradian at separation $\theta \to \theta + \Delta\theta$, see section 5.2 for derivation. Multiplying by $2\pi\theta\Delta\theta\Delta\Omega$ where $\Delta\Omega$ is the total solid angle of the survey on the sky, calculates N, the total expected number of pairs at separation between θ and $\theta + \Delta\theta$. For σ_{pair}, we will assume that the dispersion in ellipticity is given by $\sigma_e \sim 0.2$, as reported by Hudson et al. (1998), giving $\sigma_{\text{pair}} \sim 0.04$. Note that as discussed in section 3.2.8 measurements of σ_e in the literature vary which would slightly modify our estimates for the shot noise error equation 6.3.

Typically, for angular scales less than $\theta \simeq 15$ arcminutes, $\lambda_1^2 \ll \Lambda_2$ and the ratio, equation 6.17, is simply λ_1^{-2}. The optimally-weighted error is therefore almost pure shot-noise $\sigma_L^2 \approx \sigma_{\text{pair}}^2/N$. Changing $\Delta\theta$ predominantly alters N and hence the amplitude of the shot noise component.

Figure 6.2 shows the calculated optimal weights for a galaxy pair at different angular scales θ in the Sloan spectroscopic sample, see next section, with $z_b = 0.025$ and z_a varying. At small angular scales, $\theta < 2'$, N is small, hence the shot noise is large. The optimal weighting is therefore only to downweight the very closest pairs. As θ increases, N increases, and so it is feasible to strongly downweight more of the close galaxy pairs which contribute to the contaminating intrinsic signal without significantly increasing the shot noise error. As θ increases still further, $\theta > 150'$, the actual number of pairs close enough to contribute to

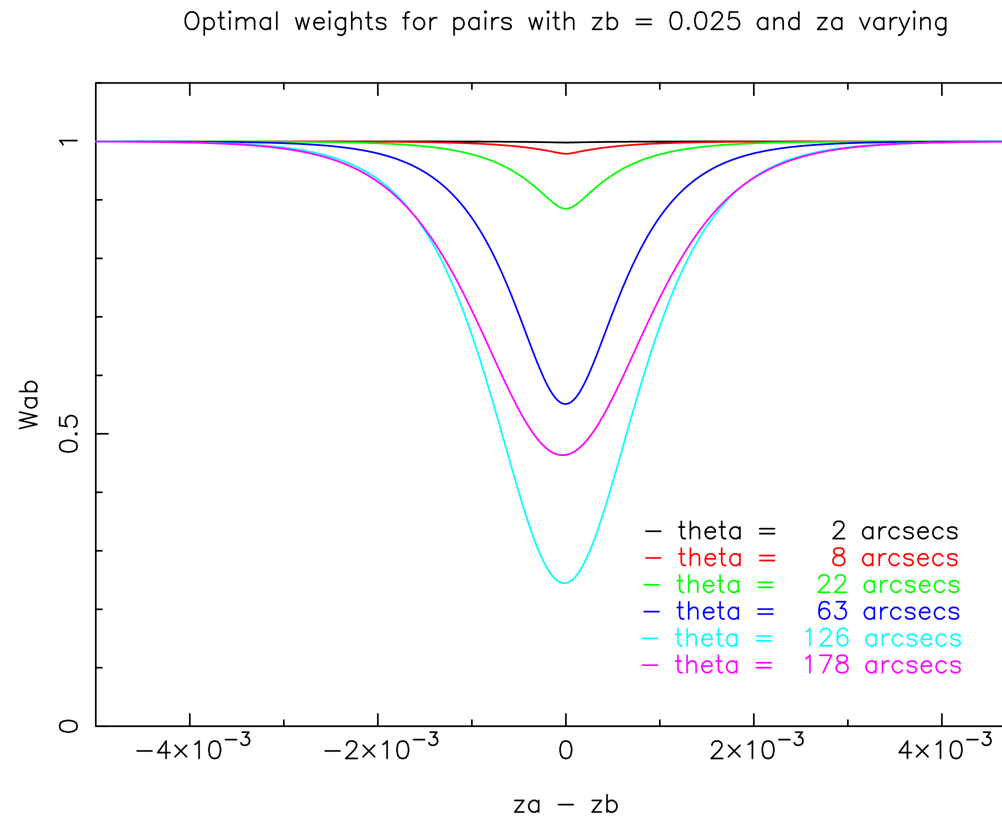

Figure 6.2: Optimal galaxy pair weighting for a pair of galaxies separated by angle θ in the Sloan Spectroscopic sample, where $z_b = 0.025$ and z_a is varying.

a contaminating intrinsic signal is very small, and so the optimal weighting tends back to $W_{ab} \equiv 1$. Note that the weights are not constrained to be positive and in extreme cases, if J_p is large, can be negative. The reason for this is that the contribution to the error from intrinsic alignments is assumed to be proportional to the intrinsic alignment signal itself. If this is the dominant error term, it is possible that one can have a net gain by reducing this term through giving some pairs negative weight. This behaviour is, however, rare.

6.1.3 Results for the Sloan Spectroscopic Sample

Covering π steradian, the Sloan Digital Sky Survey, SDSS, is a wide, shallow survey. The spectroscopic galaxy sample has a median redshift of 0.1 with redshift measurements known to an accuracy of $\Delta z = 0.0001$ (Stoughton & SSDS Team 2002). Peculiar velocity distortions will lead to additional errors of the order $\Delta z = 0.001$, but for the purpose of testing the application of this weighting scheme we will ignore these small uncertainties, assuming that the galaxy distances are essentially known. In section 6.2 we will show how this weighting

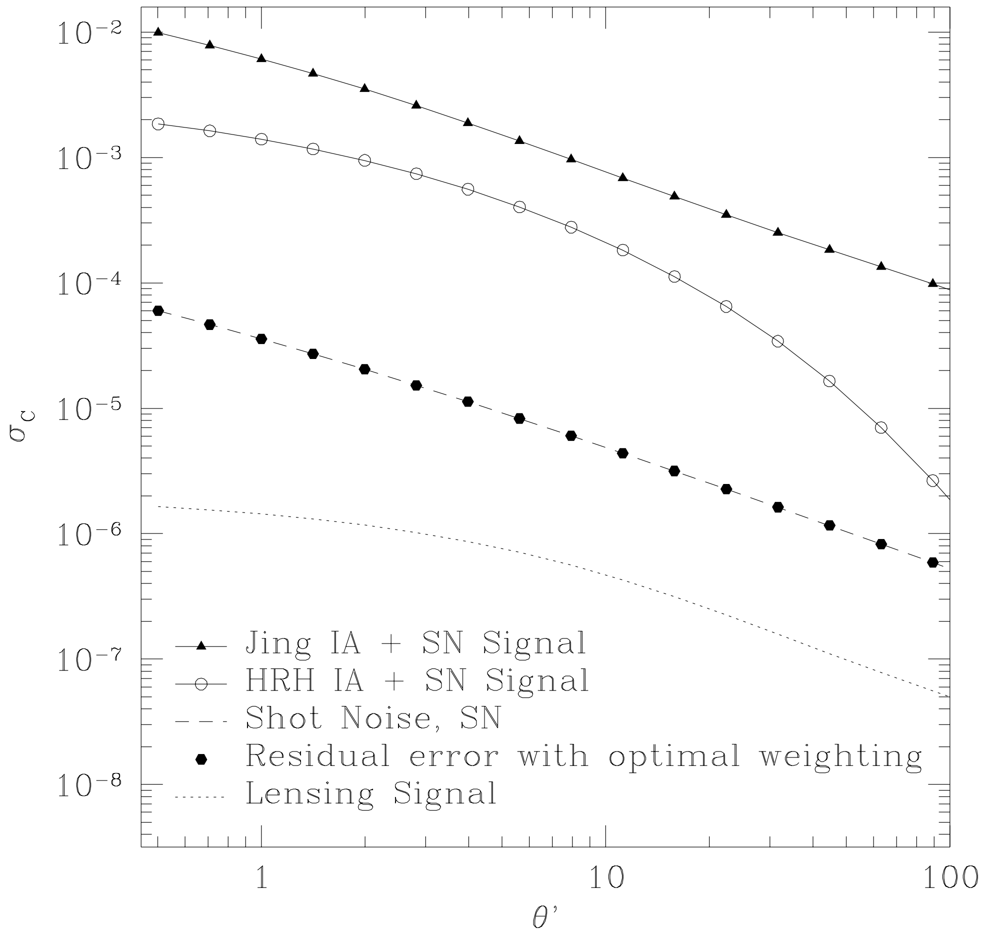

Figure 6.3: Reduction in the error from intrinsic alignments and shot noise for the Sloan spectroscopic sample. The upper curves show the total error in the shear correlation function for two intrinsic alignment models, assuming all galaxy pairs are weighted equally. Note that these curves essentially combine a random statistical error (shot noise) with a systematic contamination (intrinsic alignments), $\sigma_c = \sqrt{\sigma_{IA}^2 + \sigma_{SN}^2}$. Triangles show the Jing model and circles HRH's spiral model. The error with optimal weighting is shown as filled circles, and has reduced both intrinsic alignment model signals close to shot noise (shown dashed). Note that the increase in shot noise is negligible due to the small proportion of downweighted pairs in the optimal weighting scheme. The expected weak gravitational lensing correlation function for a ΛCDM model normalised to $\sigma_8 = 0.9$, (dotted), is still dominated by shot noise for this shallow $z_m = 0.1$ sample.

scheme applies when their are redshift uncertainties.

Figure 6.3 shows the reduced intrinsic alignment error calculated using the optimal weighting scheme, (filled), compared to the error introduced to the lensing signal $C_I(\theta)$ equation 5.2, by an unweighted HRH intrinsic alignment signal, equation 5.11, (circles), and an unweighted Jing intrinsic alignment signal, equation 5.8, (triangles), at a median redshift of $z_m = 0.1$. The minimised signal for both intrinsic alignment models is close to pure shot noise, (dashed), with residuals of less than 1%. As the Sloan spectroscopic sample is so shallow, the expected lensing signal, (shown dotted), is negligible preventing this spectroscopic sample from being used as a weak lensing data set. It is however an interesting test of the method showing that the optimal weighting scheme will almost completely remove both the HRH and the stronger Jing model for intrinsic alignments. We will therefore only proceed with the HRH model for intrinsic alignments, as the method has been shown to remove successfully any amplitude of intrinsic alignment provided the signal is significant only for galaxy pairs closer than a few tens of Mpc.

6.2 Using Photometric Redshifts

The method detailed in section 6.1 is only feasible for spectroscopic surveys with known galaxy distances. More typically we will have good estimates of galaxy distances from photometric redshifts with associated root mean square errors Δ_z, see section 4.1. These errors are much larger than the scale over which the intrinsic alignments are correlated and so we must define a new weighting scheme for galaxy pairs dependent on their estimated redshifts alone, using the minimum lensing error derived in section 6.1 as a benchmark. We will propose that for a pair of galaxies with estimated redshift $\hat{z}_a$ and $\hat{z}_b$, a zero weight is assigned if $|\hat{z}_a - \hat{z}_b| < \alpha\Delta_z$ and a weight of one is assigned otherwise, where α is chosen to minimise the total error on the shear correlation function. This simple approach when applied to the Sloan spectroscopic sample, with $\Delta_z = 0.001$, comes very close to reproducing the previously derived minimum and therefore, in the limit of very accurate photometric redshift information, this proposed method is close to the optimal result.

In order to calculate the best α values, the galaxy pair weighting defined in terms of estimated redshifts $(\hat{z}_a, \hat{z}_b)$, needs to be transformed into an average weight, $\langle W_{ab}\rangle$, assigned to a pair at true redshifts (z_a, z_b). This is because intrinsic correlations from very close pairs of galaxies in the true redshift distribution are 'washed out' when considering galaxy pairs in the smoothed estimated redshift space. Hence the intrinsic alignment contamination can be defined only in terms of the true redshift distribution.

Assuming that the estimated redshifts are distributed normally about the true redshifts with Gaussian widths given by Δ_z, we find that the average weight for a galaxy pair at true redshifts z_a and z_b is derived as follows.

$$\langle W_{ab}\rangle = \langle W(\hat{z}_a, \hat{z}_b | z_a, z_b)\rangle = \int d\hat{z}_a\, d\hat{z}_b\, p(\hat{z}_a|z_a) p(\hat{z}_b|z_b)\, W(\hat{z}_a, \hat{z}_b|z_a, z_b), \tag{6.19}$$

where $W(\hat{z}_a, \hat{z}_b|z_a, z_b) = 1$, if $|\hat{z}_a - \hat{z}_b| < \alpha\Delta_z$ and zero otherwise, and

$$p(\hat{z}|z) = \frac{\exp^{(\hat{z}-z)^2/2\Delta_z^2}}{\sqrt{2\pi\Delta_z^2}}. \tag{6.20}$$

Noting that $\int d\hat{z}_a\, d\hat{z}_b p(\hat{z}_a|z_a) p(\hat{z}_b|z_b) = 1$, we find

$$\begin{aligned}
\langle W_{ab}\rangle &= 1 - \int d\hat{z}_a\, d\hat{z}_b\, p(\hat{z}_a|z_a)\, p(\hat{z}_b|z_b)\, (1 - W_{ab}) \\
&= 1 - \int d\hat{z}_a\, p(\hat{z}_a|z_a) \int_{\max[\hat{z}_a - \alpha\Delta_z, 0]}^{\hat{z}_a + \alpha\Delta_z} d\hat{z}_b\; p(\hat{z}_b|z_b) \\
&= 1 - \frac{1}{2\sqrt{\pi}} \int_{-\infty}^{\infty} dx\, \exp^{-x^2} \left[\mathrm{erf}(y + x) - \mathrm{erf}(v + x)\right],
\end{aligned} \tag{6.21}$$

where,

$$x \equiv \frac{\hat{z}_a - z_a}{\sqrt{2}\,\Delta_z} \quad y \equiv \frac{z_a - z_b + \alpha\Delta_z}{\sqrt{2}\,\Delta_z} \quad v \equiv \frac{z_a - z_b - \alpha\Delta_z}{\sqrt{2}\,\Delta_z}, \tag{6.22}$$

and the error function is defined as,

$$\mathrm{erf}(x) = \frac{2}{\pi} \int_0^x \exp^{-u^2} du. \tag{6.23}$$

The optimum values of α are dependent on survey size, depth, photometric redshift accuracy and the choice of $\eta(r)$, and is formally set by minimising the total error contribution from the intrinsic alignments, σ_{IA} and the shot noise, σ_{SN}.

$$\sigma_{IA} = \frac{f \int dz_a dz_b \phi_z(z_a)\phi_z(z_b) \left[1 + \xi_{gg}(r_{ab})\right] \langle W_{ab}\rangle \eta(r_{ab})}{\int dz_a dz_b \phi_z(z_a)\phi_z(z_b) \left[1 + \xi_{gg}(r_{ab})\right] \langle W_{ab}\rangle}, \tag{6.24}$$

$$\sigma_{SN} = \sigma_{\mathrm{pair}} \left(\int dz_a dz_b \phi_z(z_a)\phi_z(z_b) \left[1 + \xi_{gg}(r_{ab})\right] \langle W_{ab}\rangle \right)^{-1}. \tag{6.25}$$

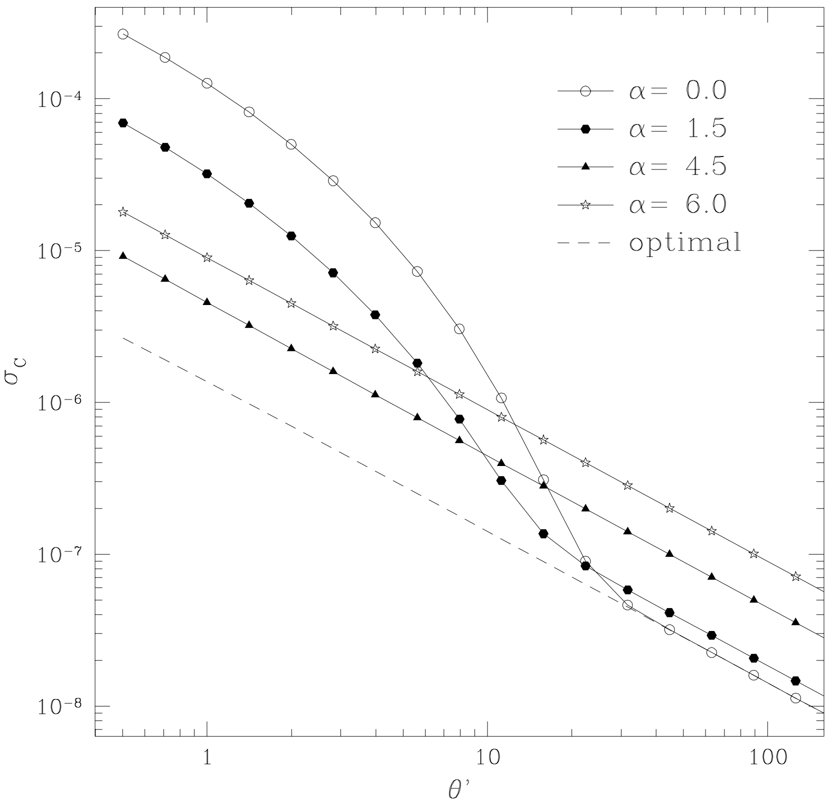

Figure 6.4: Residual error expected after removing pairs within $\alpha\Delta_z$ of each other for the ODT survey, for $\Delta_z = 0.2$.

Figure 6.4 shows $\sigma_c = \sqrt{\sigma_{IA}^2 + \sigma_{SN}^2}$ for different values of α for a low accuracy photometric redshift survey with $\Delta_z = 0.2$, for example the ODT. As α increases the probability of removing all close galaxy pairs increases and the intrinsic contribution decreases to zero, the total galaxy count however decreases, increasing the shot noise. We can therefore find an optimum value of $\alpha(\theta)$ from the lowest value of $\sigma_c(\theta)$. As θ increases, the intrinsic alignment signal decreases and a progressively lower value of α is favoured.

Figure 6.5 shows an example of the average weight, derived for a galaxy pair in the COMBO-17 survey at true redshift $z_b = 0.2$ with z_a varying. The weights $\langle W_{ab} \rangle$, derived from $\alpha(\theta)$ for the COMBO-17 survey, are Gaussian with a width dependent on the survey redshift accuracy Δ_z which is set to 0.03 in figure 6.5. The more severe the galaxy rejection criteria is, i.e. the higher the value of α, the stronger the downweighting in terms of true redshifts. For comparison, over-plotted is the optimal weighting for the same θ values. With known galaxy distances, significantly less galaxy pairs are downweighted, but we can note that

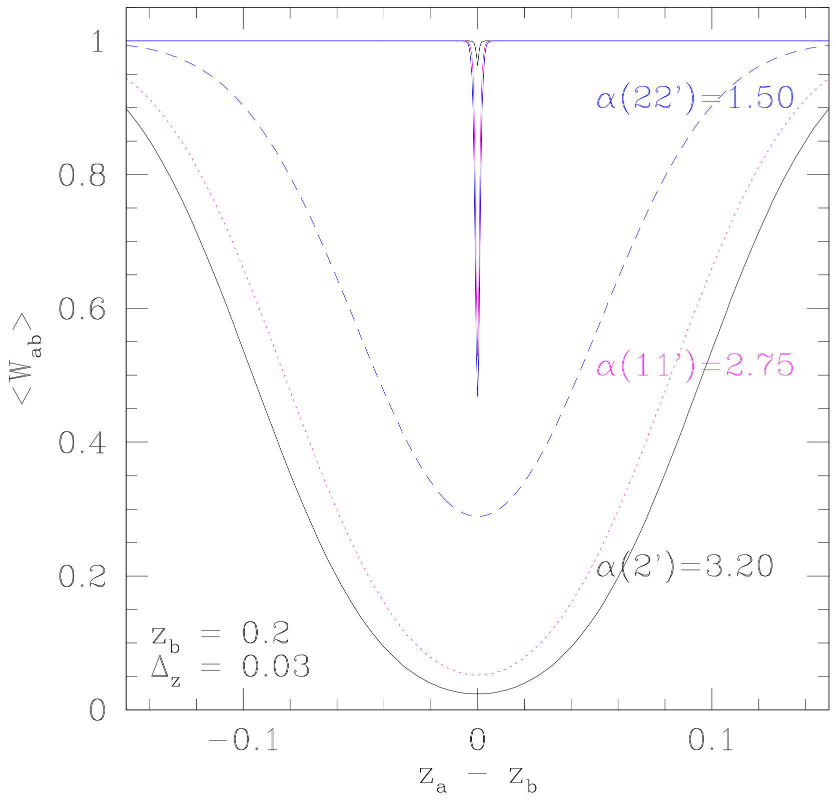

Figure 6.5: The average weight for a galaxy pair in the COMBO-17 survey, at true redshift $z_b = 0.2$ with z_a varying, for a survey with redshift accuracy $\Delta_z = 0.03$, given different weighting parameters, $\alpha(\theta = 2') = 1.5$ (solid), $\alpha(\theta = 11') = 2.75$ (dotted), $\alpha(\theta = 22') = 3.2$ (dashed).

the semi-optimal weighting is similar to the optimal weighting convolved with a Gaussian of width $\sim \Delta_z$.

6.3 Application of semi-optimised weighting scheme to multi-colour survey designs

We will now consider the application of this technique to four multi-colour surveys with varying depth, angular size and photometric redshift accuracy: the Sloan photometric survey (SDSS) with $z_m \sim 0.2$, and three deeper surveys, the Red-sequence Cluster Survey (RCS) with $z_m \sim 0.56$, (Hoekstra et al. 2002), a sample of the COMBO-17 survey with $z_m \sim 0.6$, (Wolf et al. 2001) and a deep multi-colour weak lensing survey, like the ODT, with $z_m \sim 1.0$. Table 6.1 details the relevant survey parameters that we will use. For photometric redshift errors for SDSS we will assume use of a neural-network-based photometric redshift estimator

Survey	size str	z_m	Δ_z
Sloan spectroscopic sample	π	0.1	0.0001
SDSS photometric	π	0.2	0.025
COMBO-17	0.0005	0.6	0.03
RCS *BVRz'*	0.015	0.56	0.3
Deep ODT *UBVRIz'*	0.005	1.0	0.2

Table 6.1: Survey parameters for SDSS, COMBO-17, RCS and intended deep ODT

(Tagliaferri et al. 2002; Firth, Lahav & Somerville 2003). For the RCS and a deep survey like the originally intended ODT we will assume the use of hyper-z (Bolzonella, Miralles & Pello 2000). The COMBO-17 survey has colour information in 17 bands producing very accurate photometric redshift estimates down to a limiting magnitude of $R \sim 24$. It is this magnitude-limited sample of the full COMBO-17 weak lensing survey that we will consider.

Figure 6.6 shows the application of the weighting scheme producing very encouraging results. The best reduction that can be achieved with this method (filled), with photometric redshift information at the accuracy assumed for each survey, is significantly less that the correlation signal we expect to find from HRH-derived intrinsic alignments (circles). The weighted correlation functions have been calculated using the values of $\alpha(\theta)$ shown in figure 6.7. The dashed line in Figure 6.6 shows the optimal improvement in the error obtainable using the method detailed in section 6.1 if accurate distances were known,. This acts as a useful benchmark to see how close the semi-optimal method for multi-colour surveys gets to the ideal. The intrinsic alignment signals can be compared to the expected weighted lensing signal for each survey, derived in appendix A, equation A.9. This is calculated for a nonlinear CDM mass power spectrum with $\Omega_m = 0.3$, $\Omega_\Lambda = 0.7$, $\Gamma = 0.21$, $\sigma_8 = 0.9$, calculated using the 'halomodel' fitting formula (equation 1.41) (Smith et al. 2003). For the pair weighting proposed, this signal is slightly lower than the unweighted lensing signal (equation 2.79). Galaxy pairs that are close enough to contribute to intrinsic alignments, will have light paths that travel through almost the same intervening large scale structure, experiencing the same shearing effect, producing stronger lensing correlations compared to distant galaxy pairs at the same angular separation. In the absence of these close galaxy pairs in the weighted analysis, the overall signal will therefore decrease somewhat.

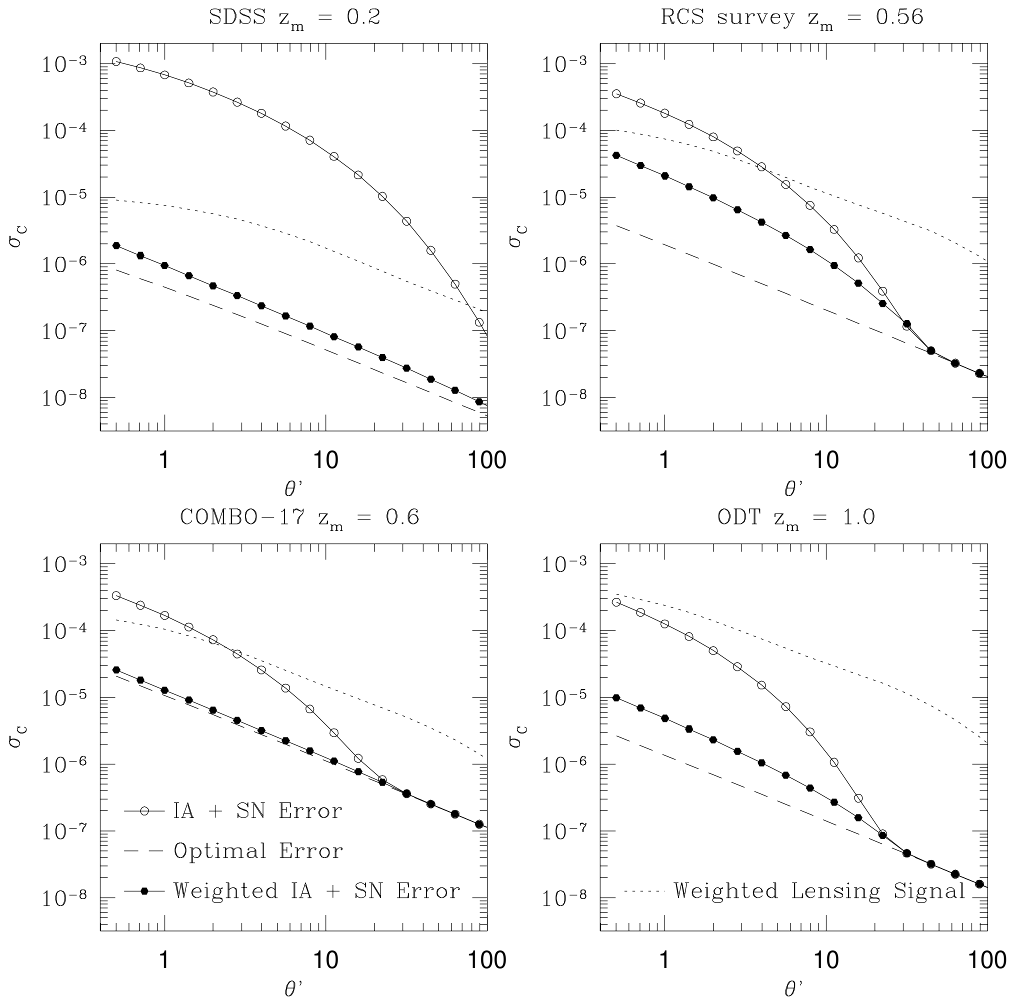

Figure 6.6: Reduction in the error from intrinsic alignments and shot noise for photometric SDSS, RCS, COMBO-17 and a deep ODT. The semi-optimal weighting, (filled circles), has reduced the unweighted HRH intrinsic alignment error plus shot noise (circles) to well below the expected amplitude of the weighted weak lensing shear signal, (dotted). The effect of semi-optimal weighting can be compared to the optimally weighted error, (dashed), attainable with accurate spectroscopic redshifts.

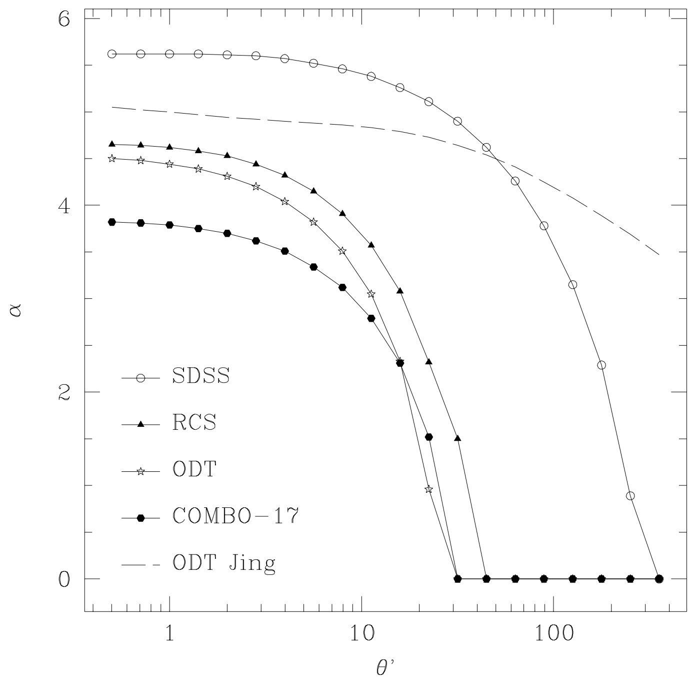

Figure 6.7: Optimum values of α for the four different surveys, assuming the HRH spiral model for intrinsic alignments equation 5.11. The dashed line shows the optimal values of α for the intended deep ODT survey, assuming the higher intrinsic signal found by Jing (2002). At the expense of marginally-higher residual shot noise, this conservative pruning of the pairs virtually guarantees almost complete removal of the intrinsic alignment contamination.

For an HRH model for intrinsic alignments we find the most startling results for the SDSS where the intrinsic alignment signal is expected to dominate completely the weak lensing shear signal. Due to the wide sky coverage and accurate photometric redshift information it is possible, with judicious removal of pairs within ~ 0.14 in estimated redshift, to reduce the intrinsic alignment signal from well above, to well below the expected lensing signal, opening up the possibility of using the SDSS for future cosmic shear studies. With the deeper surveys, such as the RCS, COMBO-17 and the ODT survey, intrinsic alignments in the weak lensing shear signal are significantly reduced. With the highly accurate photometric redshifts of COMBO-17, the reduction is close to optimal, reducing the largely systematic $\sim 220\%$ error at small angular scales to a much smaller and largely statistical error of $\sim 17\%$ of the expected lensing shear correlation. This limiting error is predominantly shot noise which will decrease as the survey size grows. The ODT and RCS have less accurate distance estimates but even with current photometric redshift estimates, which undoubtedly will improve with time, the reduction is quite significant. For deep multi-colour surveys such as the intended $z_m \sim 1$ depth

ODT survey, the intrinsic alignment signal is almost completely removed, leaving noise at a level of $\leq 2\%$ of the lensing signal. For the wide RCS, the strong contamination at angular scales less than 10 arcminutes, as high as 130% contamination at angular scales $\theta \sim 2'$, is reduced to an error $\sim 20\%$.

All of these results have assumed an HRH model for intrinsic galaxy alignment. The true amplitude of the intrinsic alignment signal however is rather uncertain; the correlation signal from intrinsic alignments could move up, as argued by Jing (2002), or down, as argued by Crittenden et al. (2001) and found when disc-halo angular momentum misalignments are included in the numerical analysis, see section 5.4. Figure 6.7 also shows the optimum $\alpha(\theta)$ if the intrinsic alignment signal is as high as found by Jing (2002), for the intended deep ODT survey. Due to the presence of Jing intrinsic correlations at larger galaxy pair spatial separations, see figure 5.2, it is necessary with this model to remove more pairs at larger angular scales. At the expense of a higher residual shot noise, this more-or-less guarantees removal of any plausible intrinsic alignment signal, leaving errors at less than 3% of a weighted weak lensing signal from a survey with median redshift $z_m \sim 1$.

It should be noted that similar conclusions to those presented in this chapter were independently drawn by King & Schneider (2002) who simultaneously proposed a weighting scheme based on photometric redshifts. The technique discussed in this chapter is however more precise as it uses a model for the intrinsic alignments and provided one is conservative, assuming the largest feasible model, it can be fairly certain that this weighting scheme will reduce the true intrinsic alignment contamination to lensing correlation signals to a negligible level. One purpose of the next chapter will be to observationally constrain models of intrinsic galaxy alignments for use with this weighting scheme, such that the conservative use of potentially invalid high amplitude intrinsic galaxy alignment models, that could produce a needlessly high residual shot noise error in a galaxy-pair weighted weak lensing analysis, is not always required.

7

Separating intrinsic galaxy alignments from weak lensing correlations in the COMBO-17 survey

As discussed in chapter 5, there is a potentially significant error to weak lensing measurements arising from the possible presence of intrinsic galaxy alignments. This error can be suppressed in weak lensing analysis by downweighting galaxy pairs which are physically close, and in this chapter we will apply the galaxy-pair weighting scheme derived in chapter 6, to a weak lensing analysis of the photometric redshift sample of the COMBO-17 survey. This can be done optimally without significantly increasing the shot noise in the final weak lensing analysis, if we have a good estimate of the level of contamination. Obtaining an observationally constrained estimate is therefore also one of the purposes of this chapter, using published results from the Red-sequence Cluster Survey (RCS; Hoekstra et al. 2002) and the VIRMOS-DESCART survey (Van Waerbeke et al. 2002), and the analysis of ellipticity correlations between close galaxy pairs in the COMBO-17 survey. With these observational constraints, the COMBO-17 weak lensing constraints in the $\Omega_m - \sigma_8$ plane are updated, taking into account the intrinsic alignment signal. We will then consider the impact of intrinsic alignments on two future deep wide-field multi-colour surveys: the Canada-France-Hawaii Telescope Legacy Survey (CFHTLS), and the space-based SuperNova/Acceleration Probe (SNAP).

7.1 Upper limits on the intrinsic alignment signal: Aperture mass B modes

A good diagnostic for determining the level of systematic errors present in weak lensing measurements, is to decompose the shear correlation signal into E and B modes. This was first proposed by Crittenden et al. (2002), and is now a standard statistical test for the presence of non-lensing contributions to weak lensing measurements. See section 2.5.5 for a detailed theoretical description of E and B modes in weak gravitational lensing which produces pure curl-free distortions (E-type), and contributes only to the B-type distortions at small angular scales $\theta < 1'$, due to source redshift clustering (Schneider, Van Waerbeke & Mellier 2002). A significant detection of a B-type signal in weak lensing surveys is therefore an indication that ellipticity correlations exist either from residual systematics within the data and/or from intrinsic galaxy alignments, as most models for intrinsic galaxy alignments predict B modes. Note that there are alternatives, such as the model proposed by Catelan, Kamionkowski & Blandford (2001), that produce pure E-mode.

The decomposition has previously been carried out using the aperture mass statistic, $M_{\rm ap}$, equation 2.105, (Hoekstra, Yee & Gladders 2002; Van Waerbeke et al. 2002; Hamana et al. 2003; Jarvis et al. 2003), or by determining the B mode shear power spectrum, $P_B(k)$, equation 2.122, (Brown et al. 2003; Pen, Van Waerbeke & Mellier 2002). In this section we will focus on the B mode of the aperture mass statistic $M_\perp$, which can be directly calculated from angular ellipticity correlation functions as given by equation 2.124. In the absence of contaminating non-lensing sources we expect $M_\perp \approx 0$, but this is found not to be the case in all the weak lensing surveys that have measured this diagnostic statistic. Known data systematics introduce positive correlations and therefore we can use observations of $M_\perp$ from the RCS and VIRMOS-DESCART survey as upper limits for the intrinsic alignment B mode contamination within these surveys. This is probably a valid assumption on small scales over which the distorting PSF is relatively constant, provided a consistent subtraction method for the PSF has been applied. Highly anisotropic PSF distortions which vary from $e_i^* \rightarrow -e_i^*$ across the image could introduce a negative aperture mass B mode on large scales. On inspection of the published RCS PSF pattern, this effect is not seen in the CTIO camera PSF pattern, but is seen in 2/12 CCD chips on the CFHT camera which could, in principle, introduce a data systematic source of negative aperture mass B modes at large scales $\theta \sim 10$ arcminutes, preventing the use of B modes as an upper limit for intrinsic alignment contamination above these scales.

The contribution to the aperture mass B mode from the four intrinsic alignment models: Jing, HRH, CNPT, HRH* as defined in chapter 5, is calculated from the intrinsic angular shear correlations, $\langle \gamma\gamma^* \rangle_I = \frac{1}{4} C_I(\theta)$, shown in figure 5.8, for the two different depth weak lensing surveys: the RCS with a median redshift $z_m \approx 0.56$, and the VIRMOS-DESCART survey with $z_m \approx 1.0$. The aperture mass B mode contributions from the shear correlation functions shown in figure 7.1, can be calculated through equation 2.124, provided we make the simplifying assumption that for intrinsic galaxy alignments there is no preferred tangential or radial alignment. This is a valid assumption to make as CNPT find that $\langle e_t e_t \rangle \approx \langle e_r e_r \rangle$ at small angular scales, deviating at separations $\theta > 3'$, which is also consistent with the results from HRH. Hence $\xi_- \simeq \frac{1}{4}(\langle e_t e_t \rangle - \langle e_r e_r \rangle) = 0$ and

$$\langle M^2_{\perp\,(\mathrm{IA})} \rangle = \frac{1}{2} \int_0^\infty \frac{d\vartheta\, \vartheta}{\theta^2} \left[\xi_+(\vartheta) T_+ \left(\frac{\vartheta}{\theta} \right) \right], \tag{7.1}$$

where $\xi_+(\theta) = \frac{1}{4} C_I(\theta)$, and T_+ is given in equation 2.115. Figure 7.1 shows the aperture mass B mode measurements reported by the RCS, (Hoekstra, Yee & Gladders 2002), (upper panel), and VIRMOS-DESCART survey, (Van Waerbeke et al. 2002), (lower panel), compared to the contributions from the four different intrinsic alignment models. With no evolution in galaxy clustering, considering the observed B modes as upper limits, we can see that the Jing and HRH models are strongly rejected by the RCS results and that the CNPT and HRH* models are favoured by both the VIRMOS-DESCART at angular scales $\theta < 10'$, and the RCS. Note that none of the intrinsic alignment models can account for the significant B mode at large angular scales $\theta > 15'$ found in the VIRMOS-DESCART data, which may be caused by other PSF related data systematics (Hoekstra 2003).

7.2 Estimation and removal of the intrinsic alignment signal

Decomposing cosmic shear correlation measurements into E and B modes provides an estimate of the intrinsic alignment contamination in weak lensing measurements. However it is not clear how to correct the E mode given a measured non-zero B mode. To date the practice has been to add in quadrature the B mode to the E mode error (Hoekstra, Yee & Gladders 2002). An

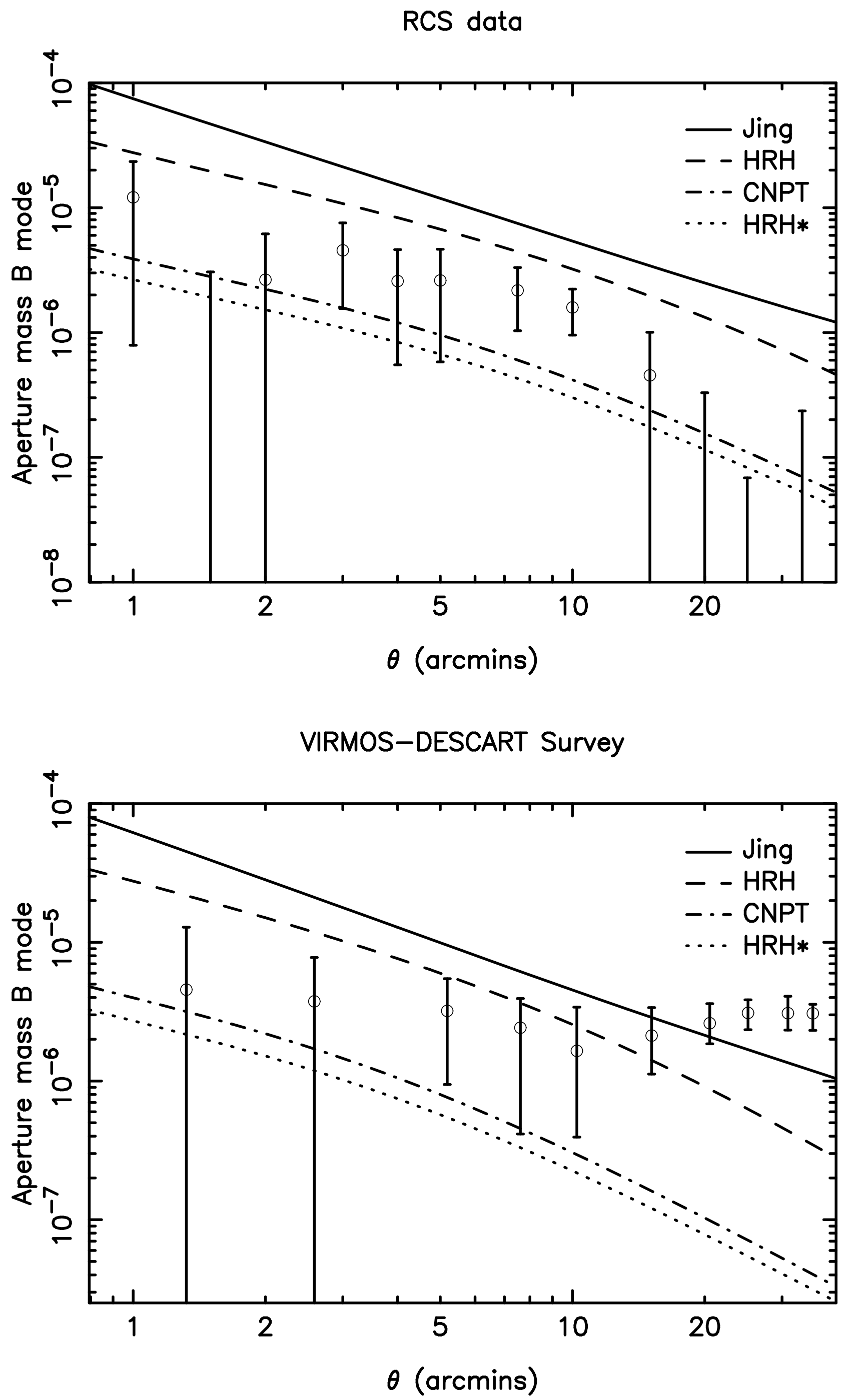

Figure 7.1: Intrinsic alignment contributions to the aperture mass B mode $\langle M_\perp^2 \rangle$; Jing(solid), HRH (dashed), CNPT(dot dash) and HRH* (dotted). The upper panel compares intrinsic alignment predictions for the RCS survey with their measured B mode. The lower panel compares intrinsic alignment predictions for the VIRMOS-DESCART with their measured B mode.

alternative technique, detailed in chapter 6, that is applicable to weak lensing surveys with photometric redshift estimates, is to remove, essentially completely, the intrinsic alignment signal by downweighting pairs of galaxies which are likely to be physically close. King & Schneider (2003) have also proposed separating cosmic shear from intrinsic galaxy alignments using correlation function tomography. In this section, we will extend the method of chapter 6, to determine the intrinsic alignment signal, as well as to remove it from the shear correlation function in the COMBO-17 data set.

7.2.1 Constraining intrinsic galaxy alignments with COMBO-17: Method

Weak lensing studies have been carried out on the deep R-band COMBO-17 images observed during the best seeing conditions (Brown et al. 2003), and it is a subset of this R-band selected galaxy sample with a median redshift $z_m \sim 0.6$, limited to $R < 24$ to allow for photometric redshifts estimates, that will be used in this section. The selected survey area totals 0.75 square degrees from the Abell 901/902 supercluster field, A901, the Chandra deep field south, CDFS, and the 11 hour survey field, S11, yielding a catalogue of 3.55×10^4 galaxies with KSB+ shape measurements and photometric redshifts accurate to $\Delta_z = 0.042$. For a detailed description of the photometric methods used to assign redshifts to the galaxies, see Wolf et al. (2003).

The total observed shear correlation function in the COMBO-17 dataset can be expressed as

$$C(\theta) = C_{\text{lens}}(\theta) + C_{\text{I}}(\theta) + C_{\text{sys}}(\theta), \tag{7.2}$$

where $C_{\text{lens}}(\theta)$ is the cosmic shear weak lensing signal $\langle\gamma\gamma^*\rangle$ equation 2.79, and $C_{\text{I}}(\theta)$ is the signal due to the intrinsic alignment of galaxy shapes equation 5.2. $C_{\text{sys}}(\theta)$ is the correlation function due to any observational systematic effects which may be present in the dataset, which can be estimated from equation 3.68. $C_{\text{I}}(\theta)$ can effectively be eliminated by excluding galaxy pairs which are closer than $\alpha(\theta)\Delta_z$ in redshift, where $\Delta_z = 0.042$ is the typical redshift error for the COMBO-17 galaxies and $\alpha(\theta)$ is optimised to minimise the total error from intrinsic alignments and shot noise (see chapter 6.2). By measuring the shear correlation function for pairs of galaxies which are sufficiently distant from each other, intrinsic alignments are excluded. Furthermore, if the shear correlation for only the close galaxy pairs which have

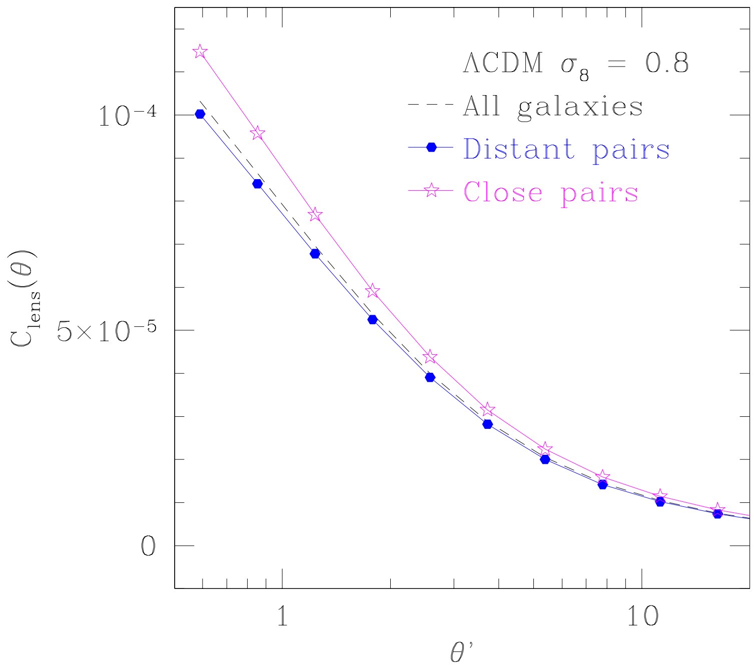

Figure 7.2: Predictions for the weak lensing shear correlation functions for the distant pairs and for the close pairs as described in the text. The difference in amplitude between the predicted signals is $\Delta C_{\rm lens}(\theta) \leq 1.5 \times 10^{-5}$ at all measured scales.

been excluded from the analysis is also measured, we will have two independent correlation functions from which we can estimate the intrinsic alignment signal from the close galaxy pairs:

$$C_{\rm IA}(\theta) = C_{\rm close}(\theta) - C_{\rm distant}(\theta) - \Delta C_{\rm lens}(\theta), \tag{7.3}$$

where $C_{\rm close}(\theta)$ is the correlation function measured from the close pairs, $C_{\rm distant}(\theta)$ is the correlation function for the distant pairs and $\Delta C_{\rm lens}(\theta)$ is the difference in the correlations caused by weak gravitational lensing for the distant and close pairs. Equation 7.3 assumes that in the distant data set the intrinsic alignment signal is zero and that $C_{\rm sys}(\theta)$ is the same as for the close pairs. To ensure all possible intrinsic alignment contamination has been removed from the distant dataset, we will choose the most conservative estimate of $\eta_{\rm Jing}(r)$ (equation 5.8) to derive the α weighting scheme as described in section 6.2. The assumption for $C_{\rm sys}(\theta)$ is reasonable since there is no reason to believe that systematic effects would depend on the redshift separation of galaxy pairs. To calculate $\Delta C_{\rm lens}(\theta)$, in figure 7.2 the expected lensing signal for a median redshift $z_m = 0.6$ ΛCDM model, normalised to $\sigma_8 = 0.8$

is plotted, for both the distant-pair dataset and for the close pairs, according to equation A.9. Although the difference is small, at the 10^{-5} level, and could be ignored, it is included in the analysis, assuming that $\Delta C_{\rm lens}(\theta)$ is approximately the same for each field. The underlying weak lensing signal $C_{\rm lens}(\theta)$ will however differ significantly between the three fields; A901, CDFS and S11, due to the significant mass concentrations in two of the fields. The S11 field contains a fairly large cluster (Abell 1364) at a redshift of $z = 0.11$ while the A901 field includes a supercluster system (Abell 901/902) at $z = 0.16$. In the following analysis, equation 7.3 has been applied to the three fields individually and the three resulting measurements of $C_{\rm IA}(\theta)$ have been combined with minimum variance weighting, where the weight w_i for each measurement with associated error σ_i is given by $w_i = 1/\sigma_i^2$. This ensures that $C_{\rm lens}(\theta)$ is eliminated in the subtraction. Note also that, for the various $C(\theta)$ calculations, cluster member galaxies have been removed from the A901 and S11 fields to eliminate contamination of the field intrinsic alignment signal by intra-cluster galaxy alignments, (Plionis et al. 2003). To estimate $C_{\rm close}(\theta)$ and $C_{\rm distant}(\theta)$ for the three fields, each field is split into eight chip-sized sections and the relevant correlation function $c_{i,s}$ for each section is calculated,

$$c_{\rm i,s}(\theta) = \frac{\sum_{\rm ab} W_{\rm ab}\,\gamma(\boldsymbol{\theta}_a)\,\gamma^*(\boldsymbol{\theta}_b)}{\sum_{\rm ab} W_{\rm ab}}, \tag{7.4}$$

where $W_{\rm ab}$ is the weight for the galaxy pair ab. For the distant-pair data set $i =$ 'distant', $W_{\rm ab} = 0$ if $|\hat{z}_a - \hat{z}_b| < \alpha\Delta_z$ and $W_{\rm ab} = 1$ otherwise, where the derived values of $\alpha(\theta)$ are shown in figure 7.3 (circles). For the close pairs $i =$ 'close' the weighting is simply reversed. Following equation 2.69, the final estimate of the correlation function for the intrinsic galaxy alignments for the entire field, is the average difference,

$$C_{\rm IA}(\theta) = \frac{1}{N_s}\sum_{s=1}^{N_s} c_{{\rm close},s}(\theta) - c_{{\rm distant},s}(\theta) - \Delta C_{\rm lens}(\theta), \tag{7.5}$$

where N_s is the number of sections in a field, making the approximation that sections of the same field are uncorrelated. The uncertainty on the estimate is then given by the error on the mean (equation 2.70). Neighbouring sections of the same field are, in fact, correlated but this approximation appears to be valid on scales which are small compared to the size of the sections ($= 8' \times 16'$), as the results from the use of $16' \times 16'$ size sections are unchanged. Also note the results from the maximum likelihood power spectrum analysis of Brown et al. (2003), conducted on the full COMBO-17 fields, were found to be in excellent agreement with the results from their correlation function analysis, which also used this approximation.

With estimates of the intrinsic correlation function $c_s(\theta)$ from each section, where

$$c_s(\theta) = c_{\mathrm{close},s}(\theta) - c_{\mathrm{distant},s}(\theta) - \Delta C_{\mathrm{lens}}(\theta)\,, \tag{7.6}$$

the covariance is given by

$$\mathrm{cov}[c_s(\theta_i), c_s(\theta_j)] = \langle\, [c_s(\theta_i) - C_{\mathrm{true}}(\theta_i)]\, [c_s(\theta_j) - C_{\mathrm{true}}(\theta_j)]\,\rangle\,, \tag{7.7}$$

where $C_{\mathrm{true}(\theta)}$ is the unknown true intrinsic alignment correlation function. Making the assumption that the CCD sections are independent, $C_{\mathrm{IA}}(\theta) \approx C_{\mathrm{true}}(\theta)$, and the covariance of the individual estimates $c_s(\theta)$ is then given by

$$\mathrm{cov}[c_s(\theta_i), c_s(\theta_j)] = \frac{1}{N_s}\sum_{s=1}^{N_s} [c_s(\theta_i) - C_{\mathrm{IA}}(\theta)]\, [c_s(\theta_j) - C_{\mathrm{IA}}(\theta_j)]\ . \tag{7.8}$$

An estimate of the covariance matrix of the $C_{\mathrm{IA}}(\theta)$ measurements is therefore given by

$$\mathrm{cov}[C_{\mathrm{IA}}(\theta_i) C_{\mathrm{IA}}(\theta_j)] \simeq \frac{1}{N_s^2}\sum_{s=1}^{N_s} [c_s(\theta_i) - C_{\mathrm{IA}}(\theta_i)][c_s(\theta_j) - C_{\mathrm{IA}}(\theta_j)]\,. \tag{7.9}$$

7.2.2 An observationally constrained intrinsic alignment model

Equations 7.3, 7.5 and 7.9 were applied to the three fields, A901, CDFS and S11, with α weighting based on a Jing model for intrinsic galaxy alignments, as shown in figure 7.3 (circles). The α values depend on angular separation θ, the COMBO-17 redshift distribution, $\phi_z(z)$, shown solid in figure 7.4, the median photometric redshift accuracy, $\Delta_z = 0.042$, and the shot noise error, which comes from the COMBO-17 intrinsic distribution of galaxy ellipticities[1] with $\sigma_e = 0.67$.

The resulting measurements from the A901, CDFS and S11 fields were combined with minimum variance weighting, yielding a final measurement of the intrinsic alignment signal for the close pairs in the COMBO-17 dataset, shown in figure 7.5 along with the predicted intrinsic alignment signal for the close pairs as given by,

$$C_{IA}(\theta) = \frac{\int dz_a dz_b \phi_z(z_a)\phi_z(z_b)\,[1+\xi_{gg}]\,(1-\langle W_{ab}\rangle)\eta(r_{ab})}{\int dz_a dz_b \phi_z(z_a)\phi_z(z_b)\,[1+\xi_{gg}]\,(1-\langle W_{ab}\rangle)} \tag{7.10}$$

[1]The reader should compare this value with other estimates of σ_e in section 3.2.8 and the measurement of $\sigma_e = 0.3$ for bright objects in the CDFS field in section 3.3.2 where objects were rejected if they had 'unphysical' ellipticities. The effect of including these objects and the fainter galaxy sample dramatically increases the measured value of σ_e.

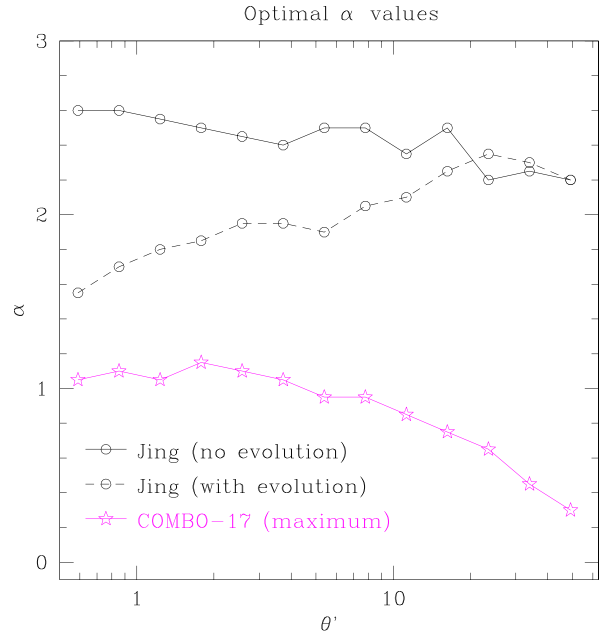

Figure 7.3: Optimal α values for the COMBO-17 redshift distribution for the Jing intrinsic alignment model $\eta_{\rm Jing}$ (circles), and the upper limit from the COMBO-17 constrained model $\eta_{\rm C17}$ (stars). For the Jing model the optimal α values considering two different galaxy clustering models are shown: zero evolution (solid) and stable clustering (dashed). Spikes in the COMBO-17 redshift distribution, shown in figure 7.4, mean that $\alpha(\theta)$ is not as smooth a function as the $\alpha(\theta)$ shown in figure 6.7.

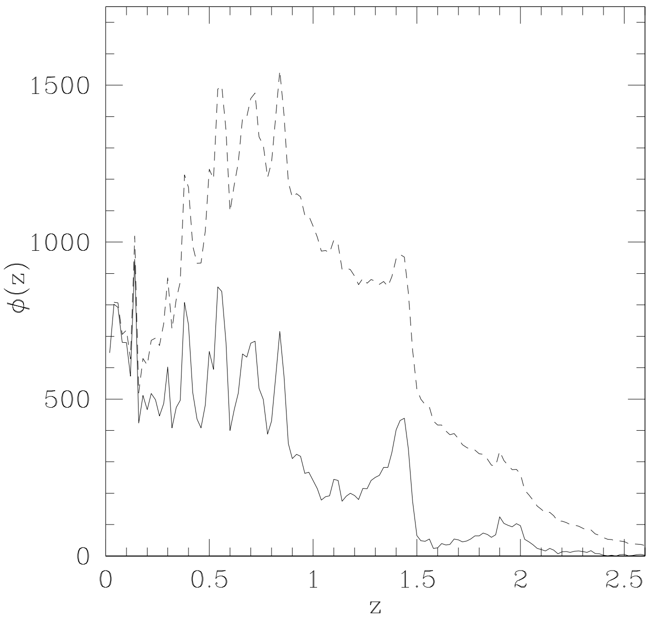

Figure 7.4: COMBO-17 total redshift distribution for the A901, CDFS and S11 fields, limited to $R < 24$, with known galaxy cluster members removed (solid). For the deep $R < 25.5$ COMBO-17 survey an estimated redshift distribution is used for making model predictions (dashed), which is composed of the measured n(z) distribution (solid) and a parameterised model as given by equation 4.1 with $z_m = 0.85$.

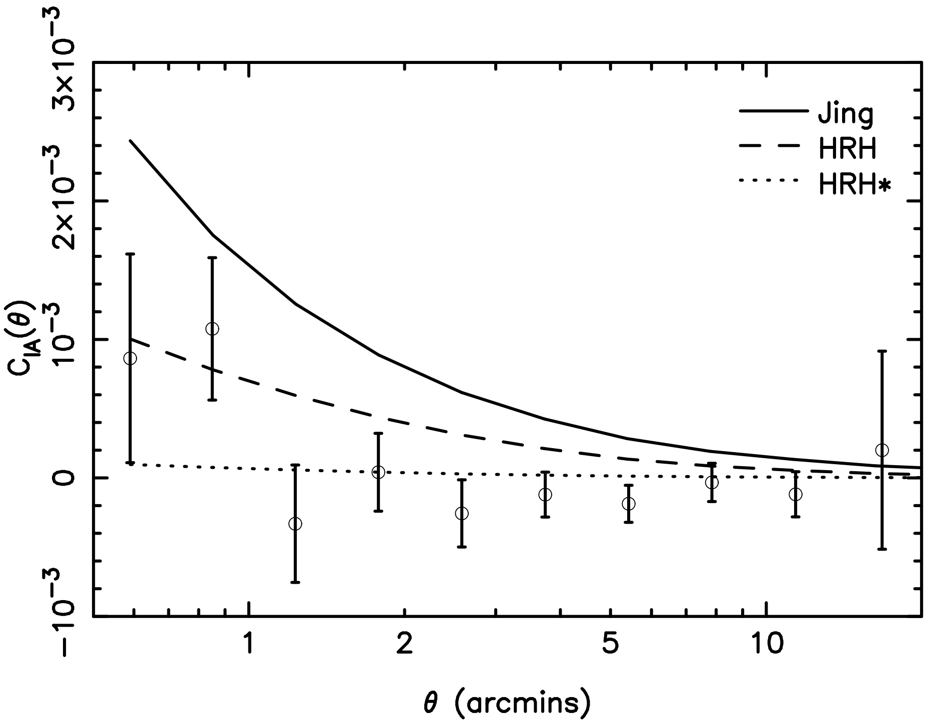

Figure 7.5: The intrinsic shear correlation functions from close galaxy pairs in the COMBO-17 survey, compared to predictions from Jing (solid), HRH (dashed) and HRH* (dotted). The CNPT prediction lies slightly above the HRH* prediction but on this scaling is indistinguishable and is therefore not plotted.

where $\langle W_{ab} \rangle$ is given by equation 6.21, and three different models for the intrinsic alignment $\eta(r_{ab})$ have been tested: Jing, HRH, and HRH*. Figure 7.6 shows the correlation matrix of the $C_{\rm IA}(\theta)$ measurements, defined by

$$\mathrm{cor}(\theta, \theta') = \frac{\mathrm{cov}(\theta, \theta')}{\sqrt{\mathrm{cov}(\theta, \theta)\mathrm{cov}(\theta', \theta')}}, \tag{7.11}$$

where $\mathrm{cov}(\theta, \theta') = \mathrm{cov}[C_{\rm IA}(\theta), C_{\rm IA}(\theta')]$ is the covariance matrix of the $C_{\rm IA}(\theta)$ measurements, which have been estimated from the data using equations 7.9 and 7.3. One can immediately see from figure 7.5, in agreement with the aperture mass B mode analysis in section 7.1, that the measured COMBO-17 $C_{\rm IA}(\theta)$ strongly rejects the Jing model for the intrinsic alignment signal while the HRH model is also highly inconsistent with the data. The modified HRH model, HRH*, introduced in section 5.4, and therefore also the CNPT model, are much better fits to the data. Note also that the $C_{\rm IA}(\theta)$ measurements are consistent with a null result on scales $> 1'$ although, from figure 7.6 it is clear that there are some (anti-) correlations between the correlation function measurements at different scales.

Figure 7.7 shows the relative likelihood $\ln(\mathcal{L}) - \ln(\mathcal{L}_{\rm max})$, for values of the amplitude A of

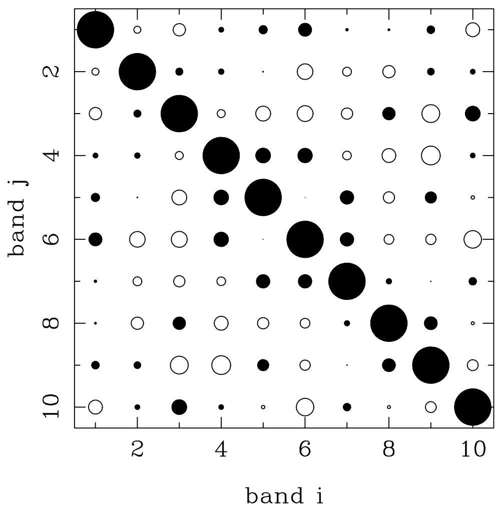

Figure 7.6: Correlation matrix of the optimally combined $C_{\rm IA}(\theta)$ measurements plotted in figure 7.5. The area of each circle is proportional to the degree of correlation between points i and j. Filled circles denote that the points are correlated whereas unfilled circles denote an anti-correlation between the points. The points are the same as those plotted in figure 7.5, numbered 1 to 10, in order from left to right.

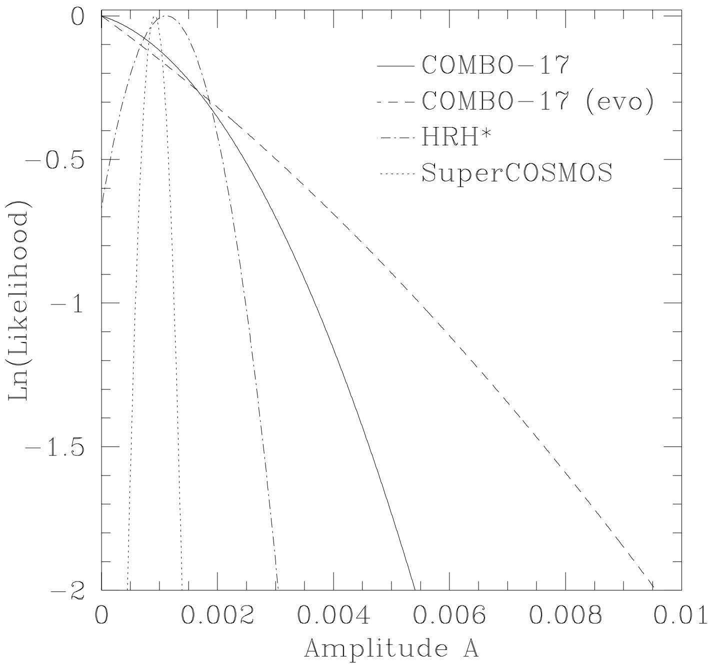

Figure 7.7: The likelihood of the amplitude A of the two-power law HRH* intrinsic galaxy alignment correlation function $\eta_{\rm HRH*}(r)$ (equation 5.20), as determined from the COMBO-17 photometric redshift dataset assuming no evolution galaxy clustering, (solid), and assuming stable galaxy clustering, (dashed), see section 7.3.2. Over-plotted is the likelihood of the amplitude from the modified HRH* results from the Virgo ΛCDM simulation, (dot dash), and the likelihood of the amplitude from the SuperCOSMOS ellipticity variance measurements, (dotted), as detailed in section 5.4.

the HRH* two power-law model, $\eta_{\mathrm{HRH}*}(r) = A(1+r^2)^{-1}$, as calculated from the COMBO-17 results.

$$\ln \mathcal{L} = -\frac{1}{2}\chi^2 = -\frac{1}{2}\Sigma_{i,j}[d(\theta_i) - m(\theta_i)]\,\mathrm{cov}_{ij}^{-1}\,[d(\theta_j) - m(\theta_j)]\,, \tag{7.12}$$

where $d(\theta_i)$ is the measured shear correlation function at θ_i with covariance matrix cov_{ij} as given by equation 7.9, and $m(\theta_i)$ is the value of the model $C_{IA}(\theta_i)$ as given by equation 7.10. We can see that the best fit is at zero amplitude with $\chi^2 = 11.34$ for 9 degrees of freedom. An HRH* model with an amplitude greater than $A = 0.0054$ can be rejected with 95% confidence and hence we have an observationally constrained maximum amplitude intrinsic alignment model such that:

$$\eta_{\mathrm{C17}}(r) < \frac{0.0054}{1+r^2} \qquad 95\%\ \text{confidence.} \tag{7.13}$$

7.2.3 Removal of intrinsic alignment contamination to COMBO-17

With the constraints on the amplitude of the intrinsic alignment signal from the previous section, we can now apply the weighting scheme, described in chapter 6.2, to the COMBO-17 data with α weighting based on the upper limit of the $\eta_{\mathrm{C17}}(r)$ model, thereby removing no more galaxy pairs than is strictly necessary. In order to compare with the expected ΛCDM weak lensing shear signal, we will apply the weighting scheme to the CDFS and S11 fields only, in order to avoid the much larger shear signal seen in the A901 field due to the presence of the supercluster (Gray et al. 2002). With values for $\alpha(\theta)$, as shown in figure 7.3, (stars), derived for the COMBO-17 redshift distribution of the CDFS and S11 fields only, the total and distant galaxy-pair correlation functions given by equations 7.4 and 7.5, have been calculated, with the results shown in figure 7.8. The total $C(\theta)$ (circles) will include intrinsic alignment contamination, whereas the distant-pair signal (triangles) excludes virtually all intrinsic alignment at the expense of a small increase in the shot noise. Over-plotted is the cosmic shear prediction for a ΛCDM model, equation 2.79, normalised to $\sigma_8 = 0.8$, where the COMBO-17 photometric redshift distribution for the CDFS and S11 fields has been used for this calculation. Note that for the weighting scheme derived for this survey, the weighted lensing signal, (from distant galaxy pairs), is not significantly different from the unweighted lensing signal, (from all galaxy pairs), see figure 7.2, but in the case of precise cosmological parameter estimation from measurements of weighted shear correlations, it should be taken

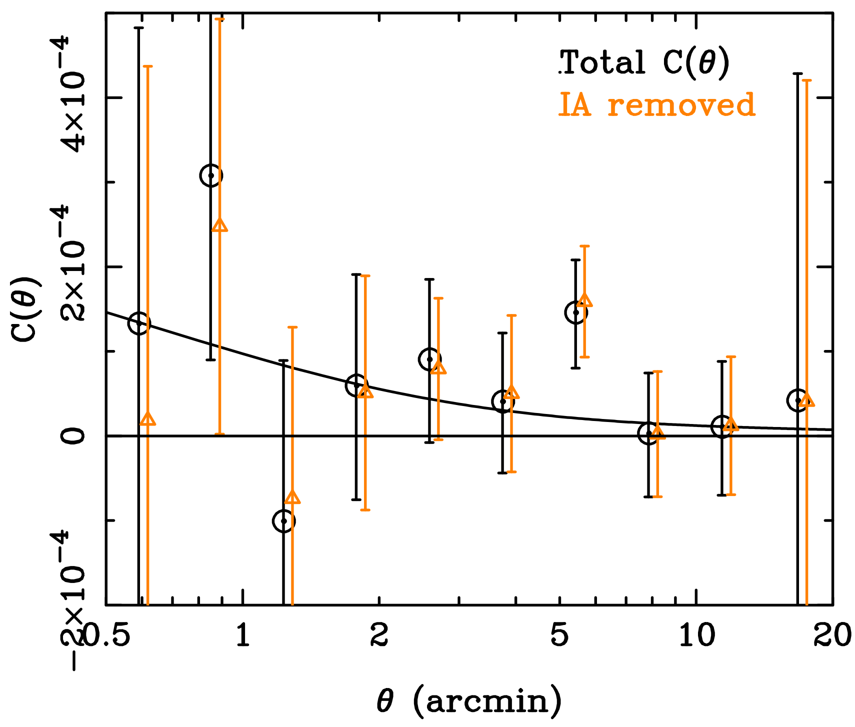

Figure 7.8: Application of the intrinsic alignment suppression weighting scheme as described in the text. The circles are the total correlation function $C(\theta)$ measurements from all galaxy pairs whereas the triangles are the $C(\theta)$ measurements from just the distant galaxy pairs. The curve plotted is the expected weak lensing signal for a ΛCDM model normalised to $\sigma_8 = 0.8$.

into account.

This result is a good example of the application of the α weighting to a weak lensing data set, effectively removing the systematic error from intrinsic galaxy alignments whilst producing only a small increase in the shot noise. Due to the fact that only a small subset of the COMBO-17 data set has been used, 0.5 square degrees limited to magnitude $R < 24$, we will be unable to use this noisy result directly to investigate the effect on cosmological parameter estimation.

7.3 Effect of galaxy clustering evolution

All previous studies of intrinsic galaxy alignment have assumed weak evolution in galaxy clustering which becomes important when converting measured 3D intrinsic ellipticity correlations $\eta(r)$, into angular correlation functions $C_I(\theta)$, see equation 5.2, as it partly determines how many pairs of galaxies which are close on the sky are actually physically close together, and susceptible to physical interactions which could lead to intrinsic alignments. If there is evolution in galaxy clustering such that at high redshift there are proportionally less nearby galaxy pairs than at low redshifts, this will lower predictions of $C_I(\theta)$. The clustering evolution of galaxies has often been quantified, although without strong theoretical motivation, by a redshift-dependent two point correlation function of the form (Groth & Peebles 1997)

$$\xi_{gg}(r,z) = \left(\frac{r}{r_0}\right)^{\gamma}(1+z)^{-(3+\epsilon)}. \tag{7.14}$$

Observational studies have found that this simple redshift-dependent model provides a poor fit to data (Wilson 2003; McCracken et al. 2001), which is most likely due to the fact that different populations of galaxies have different intrinsic clustering. Parameters for equation 7.14 are therefore observationally challenging to determine and as yet fairly uncertain. Wilson (2003) investigates the redshift evolution for a single population of galaxies in the UH8K weak lensing fields, and it is these results that we will use for illustration in order to investigate the effects of galaxy clustering evolution in intrinsic alignment studies such that $\gamma = -1.8$, $r_0 = 5.25h^{-1}$Mpc and $\epsilon = 0$. For $\epsilon = 0$, the evolution is of stable clustering, where the galaxies are dynamically bound and stable at small scales. The clustering amplitude grows with time as the background density of galaxies is diluted by the expansion of the Universe, hence the voids are effectively growing, increasing the relative galaxy clustering.

Figure 7.9 shows the predicted angular shear correlation function, $\langle\gamma\gamma^*\rangle_I = \frac{1}{4}C_I(\theta)$ calculated including galaxy clustering evolution for each intrinsic alignment model for the RCS and VIRMOS-DESCART surveys. For comparison the shear correlations expected from weak gravitational lensing, equation 2.79 are also plotted (dashed). Comparing this with figure 5.8 we can see that by assuming stable clustering evolution, the intrinsic alignment contribution at small angular scales is significantly reduced compared to the previous results. This is due to the fact that it is at small angular scales that high redshift galaxy pairs are close enough to contribute to any intrinsic correlations. If galaxies are less strongly clustered at high redshift then there will be fewer high-redshift close pairs and hence the angular intrinsic correlation function is reduced.

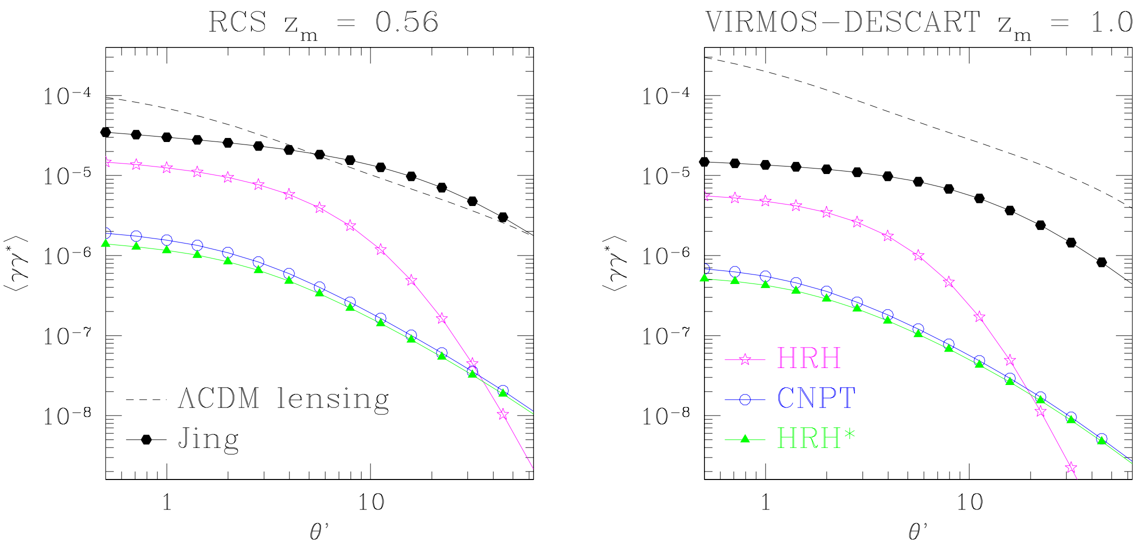

Figure 7.9: Predicted intrinsic alignment angular shear correlation functions including stable galaxy clustering evolution, Jing (filled), HRH (stars), CNPT (circles) and HRH* (triangles). The intrinsic alignment contributions are compared to the angular shear correlations from ΛCDM weak gravitational lensing, normalised to $\sigma_8 = 0.8$, (dashed), for the RCS with depth $z_m = 0.56$, (left) and for the VIRMOS-DESCART survey with depth $z_m = 1.0$, (right).

7.3.1 Aperture mass B modes

The analysis of section 7.1 has been repeated with the intrinsic alignment correlation functions now calculated including galaxy clustering evolution, as shown in figure 7.9. Figure 7.10 shows these results, comparing the aperture mass B mode measurements reported by the RCS, (upper panel), and VIRMOS-DESCART survey, (lower panel), and the four different intrinsic alignment B modes. Unlike the clear result from Section 7.1 the inclusion of stable galaxy clustering reduces the expected B mode contribution from intrinsic galaxy alignments, permitting all intrinsic alignment models where the observed B modes are considered as upper limits.

7.3.2 COMBO-17 Correlation Analysis

The effect of including galaxy evolution in the intrinsic alignment models for the COMBO-17 correlation analysis has also been investigated. The $C_{\rm IA}(\theta)$ measurements were calculated with α weighting now based on a stable galaxy clustering Jing model, as shown in figure 7.3 (filled). Note that as the predicted angular correlation signal from intrinsic galaxy alignments is much less with the inclusion of galaxy clustering evolution, the optimal α values are less.

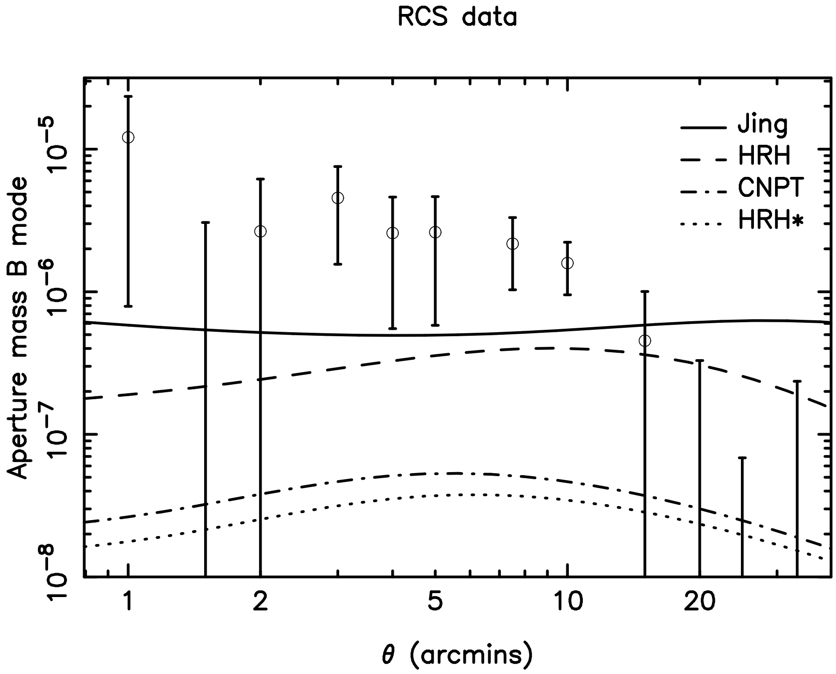

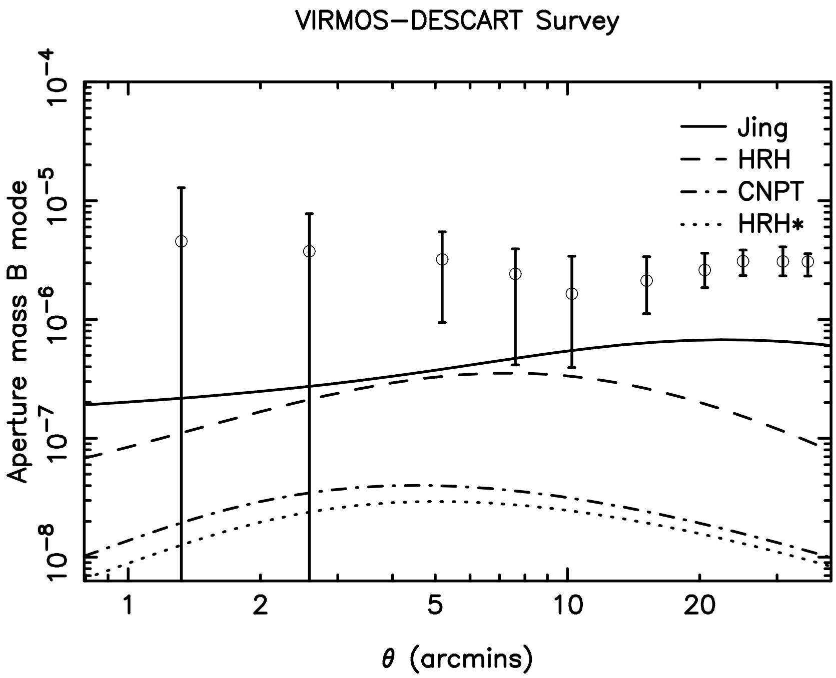

Figure 7.10: Intrinsic alignment contributions to the aperture mass B mode $\langle M_{\perp}^2 \rangle$ assuming evolution in galaxy clustering; Jing(solid), HRH (dashed) and CNPT(dot dash). The upper panel compares stable clustering intrinsic alignment predictions for the RCS survey with their measured B mode. The lower panel compares stable clustering intrinsic alignment predictions for the VIRMOS-DESCART with their measured B mode.

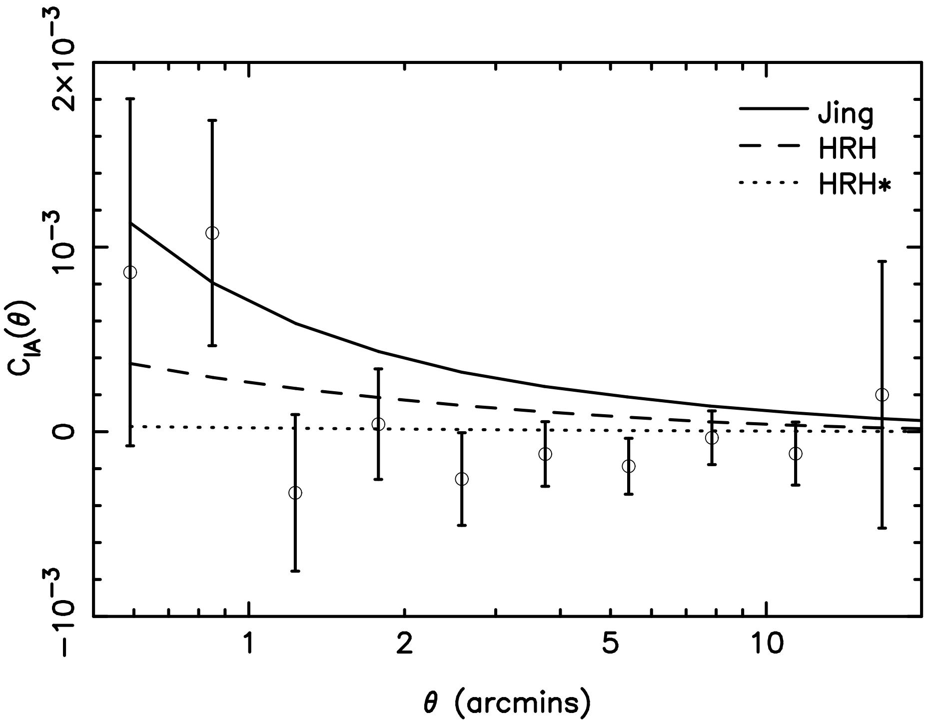

Figure 7.11: The intrinsic shear correlation function from close galaxy pairs in the COMBO-17 survey, compared to predictions from Jing (solid), HRH (dashed) and HRH* (dotted) for stable clustering galaxy evolution.

The predicted intrinsic alignment ellipticity correlation signal with stable clustering, is fairly constant for angular scales $\theta < 10'$ and this is reflected in the optimal α values. As the shot noise decreases with increasing θ, the optimal α can increase to remove more of the intrinsic alignment signal without increasing the total error.

The results of the correlation analysis are shown in figure 7.11 along with the predictions for the Jing, HRH and HRH* intrinsic alignment models where stable clustering galaxy evolution has been included. Here, we can see that, although not as clear a result as found in section 7.2, we can still exclude the Jing model and, once again, the HRH* model is favoured. The relative likelihood of the HRH* model which includes clustering evolution, has been calculated allowing the amplitude A to vary, according to equation 7.12, see figure 7.7, (dashed). The best fit is again at zero amplitude with $\chi^2 = 14.1$ for 9 degrees of freedom. An HRH* model which includes galaxy clustering evolution with an amplitude greater than $A = 0.0096$ can be rejected with 95% confidence

7.4 Implications for COMBO-17 cosmological parameter constraints

We will now turn to the implications of our intrinsic alignment amplitude constraints for cosmological parameter estimation. Measurements of the two correlation functions, $C_1(\theta) = E[\gamma_t\gamma_t : \theta]$ and $C_2(\theta) = E[\gamma_r\gamma_r : \theta]$ from equation 7.5, with $W_{ab} = 1$ for all galaxy pairs, are taken from the deep $R < 25.5$ COMBO-17 data in order to obtain a joint measurement of the normalisation of the matter power spectrum σ_8, and the matter density Ω_m. χ^2 fitting is performed on the correlation function measurements ordered in a data vector $\mathbf{d} = \{C_1(\theta_1), ..., C_1(\theta_n), C_2(\theta_1), ..., C_1(\theta_n)\}$, for a set of theoretical parameters, (σ_8, Ω_m, A), where A is the amplitude of the intrinsic alignment signal in equation 5.20, by calculating

$$\chi^2 = [\mathbf{d} - \mathbf{x}(\sigma_8, \Omega_m, A)]^T \; \mathbf{V}^{-1} \; [\mathbf{d} - \mathbf{x}(\sigma_8, \Omega_m, A)] \,, \tag{7.15}$$

where $\mathbf{x}(\sigma_8, \Omega_m, A)$ is a theory vector containing the $C_1(\theta)$ and $C_2(\theta)$ correlation functions calculated for the cosmological model. We will assume a flat cosmology $\Omega_m + \Omega_\Lambda = 1.0$ and marginalise over the Hubble constant H_0 with a Gaussian prior $p(H_0)$ set by the WMAP results with $H_0 = 72 \pm 5\,\mathrm{km\,s^{-1}\,Mpc^{-1}}$ (Spergel et al. 2003). The nonlinear CDM matter power spectrum, P_δ is calculated using the fitting formula from Smith et al. (2003) with the transfer function of Eisenstein & Hu (1999) where $\Gamma = H_0\Omega_m/100$, and the initial slope of the power spectrum $n = 1$. $\mathbf{V} = \langle \mathbf{d}\mathbf{d}^T \rangle$ is the covariance matrix of the data measurements which can be estimated, assuming that sections of the same field are uncorrelated, by

$$\mathrm{cov}[C_i(\theta) C_j(\theta')] \simeq \frac{1}{N_s^2} \sum_{s=1}^{N_s} [c_{i,s}(\theta) - C_i(\theta)][c_{j,s}(\theta') - C_j(\theta')] \,, \tag{7.16}$$

where $c_{i,s}(\theta)$ is $E[\gamma_i\gamma_i : \theta]$ in section s.

χ^2 (equation 7.15), is calculated for values of σ_8 ranging from 0.3 to 1.5 and values of Ω_m ranging from 0.1 to 1.0, on a grid with 0.01 spacing in both these parameters, for two cases (a) the case where we will ignore any effect of intrinsic alignments setting $A = 0$ and (b) the case where we will also vary values of A from 0.0 to 0.01 in steps of 0.0005 and then marginalise over the intrinsic alignment amplitude. For the marginalisation we use the probability distribution for the intrinsic alignment amplitude $p(A)$ obtained from COMBO-17 and shown in Fig. 7.7 such that

$$p(\sigma_8, \Omega_m) = \int dA \int dH_0 \, p(\sigma_8, \Omega_m, H_0, A) p(H_0) p(A) dA, \tag{7.17}$$

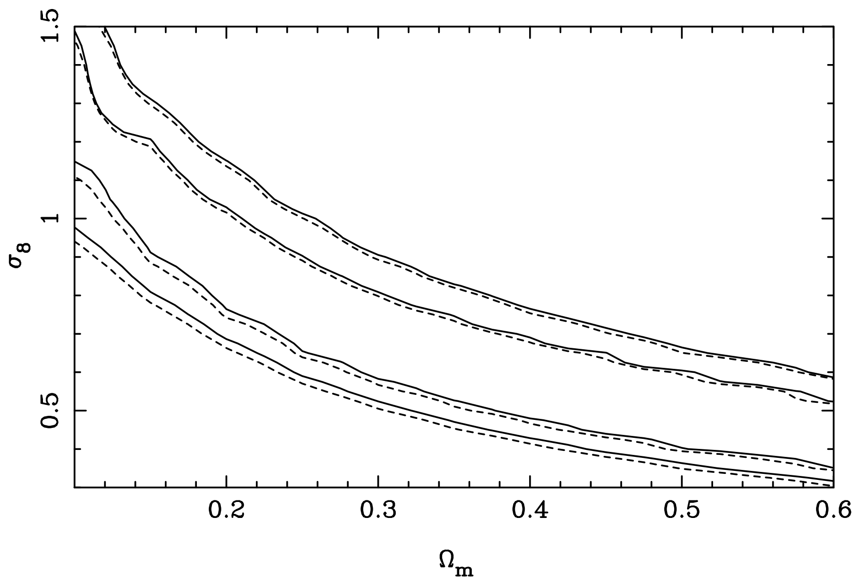

Figure 7.12: The likelihood surface of σ_8 and Ω_m from COMBO-17 as calculated using the shear correlation function measurements $C_1(\theta)$ and $C_2(\theta)$ in combination, where the intrinsic alignment signal is assumed to be zero (light solid contours) and where the amplitude of the intrinsic alignment signal has been marginalised over (heavy dashed contours). The inner and outer contours in each case enclose the 68% and 95% confidence regions respectively.

where $p \propto \exp(\chi^2/2)$. As in section 7.1, we will assume that intrinsic galaxy alignments have no preferred tangential or radial alignment, and that $C_{\rm I}(\theta)_{tt} \approx C_{\rm I}(\theta)_{rr} \approx \frac{1}{2}C_{\rm I}(\theta)$, where $C_{\rm I}(\theta)$ is calculated for the deep $R < 25.5$ COMBO-17 redshift distribution shown dashed in figure 7.4.

The resulting constraints in the $\sigma_8 - \Omega_m$ plane are shown in figure 7.12. Assuming no intrinsic alignment signal, the best fit measurement for the normalisation of the power spectrum of is found to be

$$\sigma_8(\Omega_m/0.27)^{0.6} = 0.74 \pm 0.11, \tag{7.18}$$

while for the case where the intrinsic alignment amplitude is marginalised over, derived assuming no clustering evolution, the estimate is found to drops to

$$\sigma_8(\Omega_m/0.27)^{0.6} = 0.71 \pm 0.11. \tag{7.19}$$

giving a best-fitting value of $\sigma_8 = 0.71$ for the value from WMAP of $\Omega_m = 0.27$ (Spergel et al. 2003). The errors are larger than quoted in Brown et al. (2003) because H_0 has been marginalised over rather than fixing it at 68 $\mathrm{km\,s^{-1}Mpc^{-1}}$. They remain relatively small in comparison to other surveys, bearing in mind the COMBO-17 survey area. This is a result of the good determination of source redshifts in the COMBO-17 survey, and the relatively high

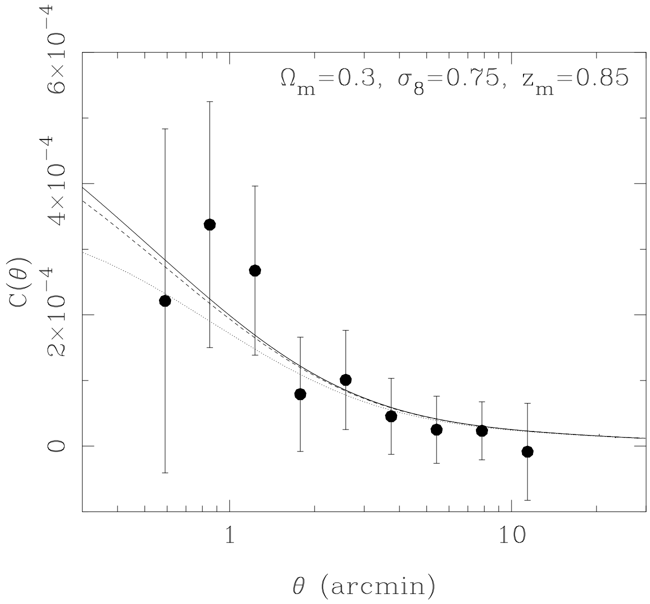

Figure 7.13: The total shear correlation function for the deep COMBO-17 survey, along with the best fit ΛCDM weak lensing correlation function assuming no intrinsic alignments (solid). Subtracting off the the best-fitting intrinsic alignment model (HRH*) decreases the lensing correlation function to the dashed line, and with the 95% upper limit (obtained from the shallower survey with photometric redshifts) the lensing correlation function decreases to the dotted line.

number density of resolved background sources used in this analysis. If we marginalise over the H_0 distribution obtained from CMB and 2dF with $H_0 = 68 \pm 5\,\mathrm{km\,s^{-1}\,Mpc^{-1}}$ (Efstathiou et al. 2002; Percival et al. 2002), these numbers change to $\sigma_8(\Omega_m/0.27)^{0.6} = 0.78$ and 0.77, with an error of 0.12. Note that all these error bars include a small error added in quadrature from the imperfect estimation of the covariance matrix in section 7.2.1.

If the alternative measurement of the total correlation function $C(\theta) = C_1(\theta) + C_2(\theta)$ is used, the same reduction of 0.02 in our estimates of σ_8 is seen. This reduction is halved if the intrinsic alignment constraints from the SuperCOSMOS survey are used. Figure 7.13 shows the effect on the lensing correlation function with the intrinsic alignment signal subtracted, along with the COMBO-17 measured total shear correlation function, which includes intrinsic alignment contamination.

For the case of stable clustering galaxy evolution, the resulting angular intrinsic alignment contamination significantly decreases, such that the constraints in the $\sigma_8 - \Omega_m$ plane are unchanged after marginalising over the intrinsic alignment signal, derived assuming stable clustering galaxy evolution.

7.5 Implications for future weak lensing surveys : CFHTLS and SNAP

The implications for weak lensing surveys is obviously dependent, as shown in section 7.3, on our understanding of galaxy clustering evolution. Until agreement is reached upon the true redshift dependence of galaxy clustering we will only consider the contamination to weak lensing measurements derived assuming no evolution in galaxy clustering, which should be considered as upper limits as redshift evolution will dilute the signal. For the modified HRH model $\eta_{\mathrm{HRH}*}(r)$,

$$\begin{aligned}\frac{C_I}{4\langle\gamma\gamma^*\rangle}(\theta=1') &= 0.02 \text{ (CFHTLS)},\\ &= 0.01 \text{ (SNAP)},\end{aligned} \tag{7.20}$$

where $C_I(\theta)$ has been calculated from equation 5.2 with $\phi_z(z)$ as given in equation 4.1, with $z_m = 1.0$ for the CFHTLS wide survey, and $z_m = 1.23$ for the SNAP wide survey. $\langle\gamma\gamma^*\rangle$ has been calculated from equation 2.79 with $\Omega_m = 0.3$, $\Omega_\Lambda = 0.7$, $\sigma_8 = 0.8$ and $\Gamma = 0.2$. The contamination of weak lensing measurements at angular scales $\theta > 1'$ is therefore less than 2% for CFHTLS, and less than 1% for SNAP. Using the 95% upper limit for the intrinsic alignment amplitude $\eta_{\mathrm{C17}}(r)$, obtained from the COMBO-17 data, these estimates are multiplied by approximately 5, giving 95% upper limits on any possible intrinsic alignment contamination at 10% and 5% respectively. For comparison, with stable clustering evolution, contamination for both surveys is practically negligible, less that 0.2% for CFHTLS, and less that 0.1% for SNAP.

Refregier et al. (2003) have shown that for SNAP, the application of redshift tomography as proposed by Hu (1999), increases the accuracy of cosmological parameter estimates by a factor of about 2. This method involves splitting the galaxy sample into two or three redshift slices, enabling measurements of the evolution of the power spectrum and hence a more accurate determination of the underlying cosmology. The thin widths of the redshift bins however increase the proportion of close galaxy pairs making the lensing tomography result more susceptible to higher levels of intrinsic alignment contamination, (Croft & Metzler 2000). Using the redshift slice distributions as proposed by Refregier et al. (2003) the intrinsic alignment contamination for the best-fit HRH* model has been calculated. The tomographic

z bin	z_m	z_0	α	β	z_+	z_-	ζ
1/3	0.81	1.13	1.95	5.55	1.11	0.00	0.031
2/3	1.31	0.80	20.07	3.45	1.11	1.59	1.515
3/3	1.93	1.57	1.50	2.48	5.00	1.59	0.042

Table 7.1: Proposed tomographic redshift distributions for the SNAP survey.

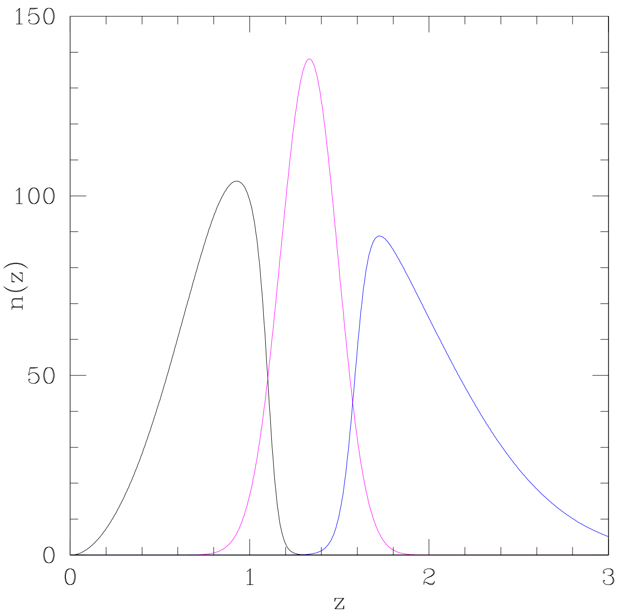

Figure 7.14: The proposed tomographic redshift distributions for the SNAP wide survey, where the normalisation is arbitrary.

redshift slices, shown figure 7.14, are defined by

$$n(z) \propto f_-(z)\phi(z)f_+(z), \tag{7.21}$$

with $\phi(z)$ given by equation 4.1 and the high and low redshift filter functions $f_+(z)$ given by

$$f_\pm(z) = \left[1 + e^{\pm(z_\pm - z)/\zeta_\pm}\right]^{-1}, \tag{7.22}$$

where the parameters are detailed in table 7.1. For the three SNAP redshift slices $z_{(1/3)}$, $z_{(2/3)}$ and $z_{(3/3)}$, the contamination at angular scales $\theta > 1'$ is found to be, 7.0%, 2.5% and 0.7% respectively. For the two lowest redshift bins, this level of contamination is significant, especially if we consider instead the 95% upper limit from our COMBO-17 constraint, which increases the contamination by a factor of approximately 5. When considering stable galaxy clustering evolution the contamination is 1% for the lowest redshift bin.

With current surveys these levels of contamination are small enough to be neglected, but they will be significant in the error budget of future high-precision weak lensing surveys, especially in the case of lensing tomography. Since SNAP and CFHTLS will have photometric redshift information, it will therefore be vital to remove the intrinsic alignment signal using the exclusion of nearby galaxy pairs as described in chapter 6.2.

8

Conclusions

Weak gravitational lensing in principle gives an unbiased picture of the matter distribution in the Universe, as it can detect mass independently of its state or nature. It does however suffer from many practical difficulties, some technical and some more fundamental, which this thesis has highlighted, and in most cases sought to resolve, by covering the following topics: an improved method for the measurement of galaxy ellipticities; an investigation into the effectiveness of the Oxford Dartmouth Thirty degree survey for gravitational lensing studies; a method for removing the contaminating effects from intrinsic correlations of galaxy ellipticities; revised theoretical modelling of intrinsic galaxy alignments with new observational constraints; the impact of intrinsic galaxy alignments on cosmological parameter estimation in the COMBO-17 survey, and the inferred implications for the next generation of cosmic shear surveys.

In this final chapter, the exciting prospects for cosmic shear studies will be reviewed, reiterating the importance of placing significant effort into overcoming the practical limitations of cosmic shear studies now, such that the future scientific goals of the weak lensing community can be achieved. The main conclusions of this thesis are also summarised.

8.1 Future prospects for cosmic shear studies

In this thesis we have focused on two-point statistics for cosmic shear analysis, which have been shown, in chapter 7, to produce good joint constraints on the matter density parameter Ω_m, and the amplitude of the matter power spectrum σ_8. For the next generation of cosmic shear surveys, higher-order statistics will become important, in order to break the degeneracies that exist in the current cosmological parameter estimation from two-point lensing statistics

(Bernardeau, Van Waerbeke & Mellier 1997; Jain & Seljak 1997). An example is the skewness of the convergence, defined as

$$S_3(\kappa) = \frac{\langle \kappa^3 \rangle}{\langle \kappa^2 \rangle^2} \approx 40\, \Omega_m^{-0.8} z_m^{-1.35}\,, \tag{8.1}$$

such that the ratio makes this third order statistic fairly insensitive to the normalisation σ_8, and shape Γ, of the power spectrum. The skewness statistic can therefore provide a direct test for the matter density parameter Ω_m, as shown in the approximate Ω_m solution (which should be noted is not valid for a non-linear power spectrum). To measure $S_3(\kappa)$ one needs to reconstruct the convergence κ from the shear γ (equation 2.117), which is unfortunately sensitive to the survey geometry and hence has so far produced fairly noisy results (Bernardeau, Mellier & Van Waerbeke 2002; Pen, Van Waerbeke & Mellier 2002; Jarvis, Bernstein & Jain 2003). With larger data sets, such as the CFHT Legacy survey, better results will be attainable.

Cosmic shear studies to date have only analysed the two-dimensional projection of the weak lensing signal, but with additional redshift information it will be possible to analyse the 3D matter distribution, investigating the evolution of the power spectrum with redshift (Hu 1999; Heavens 2003), thereby allowing for tests of cosmological models beyond the standard model that has been considered in this thesis (Benabed & Bernardeau 2001). Future scientific goals of weak lensing will also include 3D dark matter mapping, potentially feasible with deep multi-colour space-based data (Bacon & Taylor 2003).

In order for cosmic shear studies to achieve their ambitious goals and become a tool for high precision cosmology, all sources of systematic error need to be identified, and either be removed or be accounted for correctly in the lensing analysis.

8.2 Approximations and limitations

In chapter 2 we outlined gravitational lens theory and its application to weak gravitational lensing by large scale structure, showing that the theoretical predictions of weak gravitational lensing are robust, relying on results from General Relativity and one assumption in section 2.1.1: the Born approximation, which has been shown to be valid to better than 2% (Bernardeau, Van Waerbeke & Mellier 1997). Cosmological parameter estimation is sensitive to the accuracy of the non-linear correction to the power spectrum, where current correction schemes (Peacock & Dodds 1996; Smith et al. 2003), result in cosmology dependent errors up to $\sim 10\%$ for second order statistics and up to $\sim 20 - 30\%$ for the skewness (Van Waerbeke & Mellier 2003). As discussed in section 1.2.2 this sort of fundamental limitation may change the role of weak lensing from a precision cosmological parameter tool, to a probe of the non-linear end of the power spectrum. Aside from these limitations in the theoretical aspects of cosmic shear analysis, there are: limitations from systematic errors associated with measuring cosmic shear, as discussed in chapter 3; practical limitations from the choice of technology, as discussed in chapter 4; and potential contamination to weak lensing results from the intrinsic alignment of nearby galaxy pairs, as discussed in chapter 5.

8.2.1 Data systematics

In chapter 3, a review of the most often used method to measure cosmic shear (Kaiser, Squires & Broadhurst (1995) with the additional improvements of Luppino & Kaiser (1997) and Hoekstra et al. (1998)), termed KSB+, discussed why this technique is far from desirable, owing to, amongst other reasons, the potential for calibration bias in the Luppino & Kaiser (1997) seeing correction. Dissatisfaction with the KSB+ analysis has prompted many to produce alternatives, one of which is the development of a new and fast model-fitting technique in section 3.2. Observed galaxy images are compared to PSF convolved galaxy models, producing maximum likelihood estimates for PSF and seeing corrected ellipticity parameters e_i, with 1σ errors. In the weak lensing regime, galaxy ellipticity is a good estimator for the weak lensing shear, and hence the use of a model-fitting technique allows for a signal-to-noise optimised weak lensing analysis. Initial testing of the technique with the COMBO-17 observations of the Chandra deep field have shown promising results, with the model-fitting method fairing at least as well as the KSB+ method in tests for residual PSF distortions. A comparison of individual galaxy shape measurements from the KSB+ method and the model-fitting method has found a non-linear relationship, best fitted by a third-order polynomial, where, for low ellipticity objects $|e| < 0.5$, KSB+ measured lower shear estimates, compared to estimates found with the model-fitting technique. This result is in good agreement with the results of Bacon et al. (2001) who found biased underestimation of shear values with the KSB+ method.

There are current limitations to the model-fitting technique presented in chapter 3, with the most important arising from the relationship between ellipticity e_i and shear γ_i, equation 2.36. This relies on a conversion factor which is dependent on the ellipticity dispersion of galaxies $\sigma_e^2 = \langle e_i^2 \rangle$. Random errors in the measurement of e_i become systematic errors in the measurement of σ_e, resulting in calibration errors in any model-fitted weak lensing analysis. A good estimate of σ_e will be vital for future use of the model-fitting technique, and may well be attainable from deep, relatively wide-field, space-based observations such as the GEMS survey[1] observed with the Hubble Space Telescope Advanced Camera for Surveys. Limitations also arise when the density of stellar objects across the CCD image is not sufficient to produce good representations of the anisotropic PSF. We should note that this is also a limitation, however, for the KSB+ analysis and can be resolved, in the case of stable PSFs, by regular imaging of globular clusters.

The model-fitting technique requires future testing with sheared image simulations, in order to ensure that the priors on ellipticity and galaxy size, introduced in the likelihood analysis, do not introduce bias into the shear measurements. Once this is established, model fitting will offer what should be an unbiased measurement of galaxy ellipticity with error estimates that, with a high enough density of stellar objects, has rigorously corrected for the PSF distortion and seeing smear, providing an excellent alternative to KSB+.

In chapter 4 we asked whether the choice of instrumentation was of vital importance, launching a feasibility study of the Oxford Dartmouth Thirty degree survey (ODT) for use as a cosmic shear survey. Whilst the Isaac Newton Telescope and the wide-field camera are not ideal for weak lensing studies, it was found possible to extract a cosmic shear signal, albeit one contaminated by astrometric distortion induced shear at large angular scales. Provided the astrometric distortion is stable it could be removed in the future with an analysis of the CCD positional shear, averaged over many wide-field camera images.

The accuracy of the ODT determined signal was limited by shot noise from the small numbers of galaxies used in the analysis, 0.7 square degrees, and the 1:1 ratio of residual PSF distortions $\sim 10^{-5}$ to the expected weak lensing signal $\sim 10^{-5}$, for the relatively shallow ODT survey, with median redshift $z_m \sim 0.65$. The shot noise would significantly decrease with an analysis of the best seeing images from the full thirty degree survey, but the depth, shallower than the initially proposed depth, is fixed, and hence any future cosmic shear analysis of the

[1] Galaxy Evolution from Morphology and SEDs, *www.mpia.de/homes/rix/GEMS/GEMS.htm*

full ODT survey is unlikely.

With the current expectation for high precision cosmology, the choice of instrumentation is important in order to initially minimise the instrumentation-based sources of systematic error, such that their ultimate removal has a better chance of 100% success. As deeper weak lensing surveys yield higher cosmic shear signals, the choice of most ambitious future weak lensing surveys will involve space-based technology.

8.2.2 The intrinsic correlations of close galaxy pairs

In weak lensing analysis, it is necessary to make the assumption that galaxy ellipticities are intrinsically uncorrelated, such that any observed correlation can be attributed solely to weak gravitational lensing. Chapter 5 however, discussed the strong theoretical evidence for the existence of intrinsic galaxy ellipticity correlations between galaxy pairs separated by less than a few tens of Mpc. These theoretical findings are supported by observations of relatively significant galaxy ellipticity correlations in the low redshift SuperCOSMOS survey (Brown et al. 2002), which mimic cosmic shear in a survey that is far too shallow to detect the lensing phenomenon.

In chapter 6, it was found that with distance information, the level of intrinsic ellipticity correlation in the shear correlation function can be reduced by up to several orders of magnitude, by down-weighting appropriately the contribution from pairs of galaxies which are likely to be close in three dimensions. For spectroscopic surveys, optimal galaxy-pair weights were derived, which reduce the contamination to a negligible component, leaving almost pure shot noise.

For multi-colour surveys with photometric redshift estimates, a partially-optimised method was proposed, which removed pairs with close photometric redshifts from the computation of the shear correlation function. With accurate photometric redshifts this simple method has been shown to be almost as effective as the fully optimised method, and that even with relatively crude photometric redshift estimates, the contamination by intrinsic alignments can be significantly reduced. Provided weak lensing surveys have some multi-colour information, assuming the highest feasible model for intrinsic galaxy alignment contamination, one can be fairly certain that this galaxy-pair weighting scheme will reduce the true intrinsic alignment contamination of lensing correlation signals to a negligible level, at the expense of a small increase in shot-noise. This method has been applied to the photometric redshift sample ($R < 24$) of the COMBO-17 survey in chapter 7, and should be applied to any future multi-colour weak lensing surveys, in particular any lensing study that analyses the survey in a series of redshift bins, in order to ensure that the contamination to weak gravitational lensing measurement from the intrinsic alignment of nearby galaxies is removed.

8.3 Intrinsic galaxy alignments

Owing to the wide range of theoretical predictions for the intrinsic alignment of nearby galaxies, and the need for a good intrinsic alignment model in order to derive optimal galaxy-pair weights, observational constraints were sought, in chapter 7, for models of intrinsic galaxy alignments. With an analysis of the aperture mass B mode in the RCS and VIRMOS-DESCART surveys, and an analysis of the photometric redshift sample of the COMBO-17 survey, where the shear correlation function from distant galaxy pairs, uncontaminated by intrinsic galaxy alignments, was compared with that of close galaxy pairs, a consistent picture was found, where the intrinsic alignment signal was significantly lower than that expected from analysis of numerical simulations (Heavens, Refregier & Heymans 2000; Jing 2002).

In chapter 5 the numerical simulations of Heavens, Refregier & Heymans (2000) were reanalysed, including two effects which were originally ignored. These were a misalignment between the angular momentum of the baryons and the halo (van den Bosch et al. 2002), and the finite thickness of disk galaxies (Crittenden et al. 2002). Both these effects reduce the intrinsic galaxy ellipticity correlation function to a level similar to that found analytically by Crittenden et al. (2002), and consistent with the level determined observationally in this thesis and the level measured in the SuperCOSMOS survey (Brown et al. 2002).

Having estimated the contribution of intrinsic alignments to the brighter part of the COMBO-17 data, the likelihood for the contamination of the whole COMBO-17 sample, which extends to $R < 25.5$, has been computed. Marginalising over the amplitude of the contamination, the value of σ_8, the normalisation of the matter power spectrum, is found to reduce by about 0.02 to $\sigma_8(\Omega_m/0.3)^{0.55} = 0.73 \pm 0.08$, where Ω_m is the matter density parameter.

Interest in the intrinsic alignment of nearby galaxy pairs initially arose from concern about the potential contamination of weak lensing measurements, but in this thesis we have learned that it is an interesting topic, which is intimately linked to the understanding of galaxy structure and the formation of disk galaxies. With our COMBO-17 intrinsic alignment constraint and the SuperCOSMOS results favouring an intrinsic alignment model which includes misalignments between baryon and halo angular momentum, there is now observational evidence indirectly supporting the finding by van den Bosch et al. (2002). An interesting by-product of a galaxy-pair weighted weak lensing analysis of a large area photometric redshift survey, would be the ability to determine the strengths of intrinsic galaxy alignments as a function of redshift, which throughout this thesis has been assumed constant. This could then lead to new information for galaxy formation and galaxy evolution studies, leading to the conclusion that although, for studies of weak gravitational lensing, the presence of intrinsic galaxy alignments is an inconvenience, they are an interesting topic in their own right.

References

Adelberger K., Steidel C. G., Giavalisco M., Dickinson M., Pettini M., Kellogg M., 1998. ApJ, 505, 18.

Alcock C., Allsman R. A., Alves D. R., Axelrod T. S., Becker A. C., Bennett D. P., Cook K. H., Dalal N., Drake A. J., Freeman K. C., Geha M., Griest K., Lehner M. J., Marshall S. L., Minniti D., Nelson C. A., Peterson B. A., Popowski P., Pratt M. R., Quinn P. J., Stubbs C. W., Sutherland W., Tomaney A. B., Vandehei T., Welch D., 2000. ApJ, 542, 281.

Allen P., 2003. PhD thesis, Oxford University, .

Athreya R. M., Mellier Y., Van Waerbeke L., Pelló R., Fort B., Dantel-Fort M., 2002. A& AS, 384, 743.

Bézecourt J., Kneib J. P., Soucail G., Ebbels T. M. D., 1999. A& A, 347, 21.

Bacon D., Taylor A., 2003. MNRAS, 344, 1307.

Bacon D. J., Refregier A., Clowe D., Ellis R. S., 2001. MNRAS, 325, 1065.

Bacon D., Massey R., Refregier A., Ellis R., 2003. MNRAS, 344, 673.

Bacon D., Refregier A., Ellis R., 2000. MNRAS, 318, 625.

Barber A. J., 2002. MNRAS, 335, 909.

Bardeen J. M., Bond J. R., Kaiser N., Szalay A. S., 1986. ApJ, 304, 15.

Bardeen J. M., 1980. Phys. Rev. D, 22, 1882.

Bartelmann M., Schneider P., 2001. Physics Reports, 340, 291.

Baugh C. M., Efstathiou G., 1994. MNRAS, 267, 323.

Baugh C., Benson A., Cole S., Frenk C., Lacey C., 1999. MNRAS, 305, L21.

Benabed K., Bernardeau F., 2001. Phys. Rev. D, 64, 83501.

Benabed K., Van Waerbeke L., 2003. Phys. Rev. D, submitted, astroph/0306033, .

Bernardeau F., Mellier Y., Van Waerbeke L., 2002. A& A, 389, L28.

Bernardeau F., Van Waerbeke L., Mellier Y., 1997. A& A, 322, 1.

Bernstein G. M., Jarvis M., 2002. AJ, 123, 583.

Berstein G., Jarvis M., 2002. AJ, 123, 583.

Bertin E., Arnouts S., 1996. A& AS, 117, 393.

Blandford R. D., Narayan R., 1992. ARAA, 30, 311.

Bolzonella M., Miralles J., Pello R., 2000. A& A, 363, 476.

Bond J. R., Efstathiou G., 1984. ApJ(Lett), 285, L45.

Brainerd T. G., Blandford R. D., Smail I., 1996. ApJ, 466, 623.

Brand K., Rawlings S., Hill G., Lacy M., Mitchell E., Tufts J., 2003. MNRAS, 344, 283.

Brown M., Taylor A., Hambly N., Dye S., 2002. MNRAS, 333, 501.

Brown M., Taylor A., Bacon D., Gray M., Dye S., Meisenheimer K., Wolf C., 2003. MNRAS, 341, 100.

Bruzual A. G., Charlot S., 1993. ApJ, 405, 538.

Calchi Novati S., Iovane G., Marino A. A., Aurière M., Baillon P., Bouquet A., Bozza V., Capaccioli M., Capozziello S., Cardone V., Covone G., De Paolis F., de Ritis R., Giraud-Héraud, Y. andGould A., Ingrosso G., Jetzer P., Kaplan, J. andLambiase G., Le Du Y., Mancini L., Piedipalumbo E., Re V., Roncadelli M., Rubano C., Scarpetta G., Scudellaro P., Sereno M., Strafella F., 2002. A& AS, 381, 848.

Caldwell R. R., Dave R., Steinhardt P. J., 1998. Physical Review Letters, 80, 1582.

Carlberg R. G., Yee H. K. C., Morris S. L., Lin H., Hall P. B., Patton D., Sawicki M., Shepherd C. W., 2000. ApJ, 542, 57.

Carroll S. M., Press W. H., Turner E. L., 1992. ARAA, 30, 499.

Carter D., Clegg R., 1994. *ING Observers Guide*, Isacc Newton Group.

Catelan P., Kamionkowski M., Blandford R. D., 2001. MNRAS, 320, L7.

Clowe D., Schneider P., 2002. A& AS, 395, 385.

Cohen J. G., Hogg D. W., Blandford R., Cowie L. L., Hu E., Songaila A., Shopbell P., Richberg K., 2000. ApJ, 538, 29.

Cole S., Ellis R., Broadhurst T., Colless M., 1994. MNRAS, 267, 541.

Coleman G. D., Wu C.-C., Weedman D. W., 1980. ApJ Suppl., 43, 393.

Contaldi C., Hoekstra H., Lewis A., 2003. Phys. Rev. Lett., 90, 303.

Courbin F., 2003. In: *"Gravitational Lensing: a unique tool for cosmology "*, astroph/0304497, eds Kneib J., Valls-Gabaud D.

Crittenden R., Natarajan R., Pen U., Theuns T., 2001. ApJ, 559, 552.

Crittenden R., Natarajan R., Pen U., Theuns T., 2002. ApJ, 568, 20.

Croft R. A. C., Metzler C. A., 2000. ApJ, 545, 561.

Davis M., Efstathiou G., Frenk C. S., White S. D. M., 1985. ApJ, 292, 371.

de Vaucouleurs G., Capaccioli M., 1979. ApJ Suppl., 40, 699.

Ebbels T., Kneib J. P., Ellis R., 1999. In: *IAU Symp. 183: Cosmological Parameters and the Evolution of the Universe*, p. 247, ed. Sato K.

Ebbels T., 1998. PhD thesis, Cambridge University, .

Efstathiou G., Moody S., Peacock J. A., Percival W. J., Baugh C., Bland-Hawthorn J., Bridges T., Cannon R., Cole S., Colless M., Collins C., Couch, W. andDalton G., de Propris R., Driver S. P., Ellis R. S., Frenk C. S., Glazebrook K., Jackson C., Lahav, O. andLewis I., Lumsden S., Maddox S., Norberg P., Peterson B. A., Sutherland W., Taylor K., 2002. MNRAS, 330, L29.

Eisenstein D. J., Hu W., 1999. ApJ, 511, 5.

Erben T., Van Waerbeke L., Bertin E., Mellier Y., Schneider P., 2001. A& A, 366, 717.

Fall S. M., Efstathiou G., 1980. MNRAS, 193, 189.

Fan X., Strauss M. A., Schneider D. P., Becker R. H., White R. L., Haiman Z., Gregg M., Pentericci L., Grebel E. K., Narayanan V. K., Loh Y., Richards G. T., Gunn J. E., Lupton R. H., Knapp G. R., Ivezić Ž., Brandt W. N., Collinge M., Hao L., Harbeck, D. andPrada F., Schaye J., Strateva I., Zakamska N., Anderson S., Brinkmann J., Bahcall N. A., Lamb D. Q., Okamura S., Szalay A., York D. G., 2003. AJ, 125, 1649.

Fernández-Soto A., Lanzetta K. M., Yahil A., 1999. ApJ, 513, 34.

Firth A., Somerville R., McMahon R., Lahav O., Ellis R., Sabbey C., McCarthy P., Chen H., Marzke R., Wilson J., Abraham R., Beckett M., Carlberg R., Lewis J., Mackay C., Murphy D., Oemler A., Persson S., 2002. MNRAS, 332, 617.

Firth A., Lahav O., Somerville R., 2003. MNRAS, 339, 1195.

Freedman W. L., Madore B. F., Gibson B. K., Ferrarese L., Kelson D. D., Sakai S., Mould J. R., Kennicutt R. C., Ford H. C., Graham J. A., Huchra J. P., Hughes S. M. G., Illingworth G. D., Macri L. M., Stetson P. B., 2001. ApJ, 553, 47.

Freeman K. C., 1970. ApJ, 160, 811.

Gaztanaga E., 2003. ApJ, 589, 82.

Giavalisco M., Steidel C., Adelberge K., Dickinson M., Pettini M., Kellogg M., 1998. ApJ, 503, 543.

Gray M., Taylor A., Meisenheimer K., Dye S., Wolf C., Thommes E., 2002. ApJ, 568, 141.

Groth E., Peebles J., 1997. ApJ, 217, 385.

Hamana T., Miyazaki S., Shimasaku K., Furusawa H., Doi M., Hamabe M., Imi K., Kimura M., Komiyama Y., Nakata F., Okada N., Okamura S., Ouchi M., Sekiguchi M., Yagi M., Yasuda N., 2003. ApJ, 597, 98.

Harrison E. R., 1970. Phys. Rev. D, 1, 2726.

Heavens A., Peacock J., 1988. MNRAS, 232, 339.

Heavens A., Refregier A., Heymans C., 2000. MNRAS, 319, 649.

Heavens A., 2003. MNRAS, 343, 1327.

Heymans C., Heavens A., 2003a. In: *"Gravitational Lensing: a unique tool for cosmology "*, astroph/0310495, eds Kneib J., Valls-Gabaud D.

Heymans C., Heavens A., 2003. MNRAS, 339, 711.

Heymans C., Brown M., Heavens A., Meisenheimer K., Taylor A., Wolf C., 2004. MNRAS, 347, 895.

Hinshaw G., Spergel D. N., Verde L., WMAP Collaboration, 2003. ApJS, 148, 135.

Hirata C., Seljak U., 2003. MNRAS, 343, 459.

Hoekstra H., Franx M., Kuijken K., Squires G., 1998. ApJ, 504, 636.

Hoekstra H., Yee H., Gladders M., Barrientos L. F., Hall P., Infante L., 2002. ApJ, 572, 55.

Hoekstra H., Franx M., Kuijken K., 2000. ApJ, 532, 88.

Hoekstra H., Yee H., Gladders M., 2001. ApJ, 558, L11.

Hoekstra H., Yee H., Gladders M., 2002. ApJ, 577, 595.

Hoekstra H., 2003. MNRAS, submitted, astroph/0306097, .

Hoyle F., 1949. Problems of Cosmical Aerodynamics, , 195.

Hu W., Keeton C., 2002. Phys. Rev. D, 66, 3506.

Hu W., Spergel D. N., White M., 1997. Phys. Rev. D, 55, 3288.

Hu W., 1999. ApJ, 552, L21.

Hubble E., 1929. Proceedings of the National Academy of Science, 15, 168.

Hudson M., Gwyn S., Dahle H., Kaiser N., 1998. ApJ, 501, 531.

Hui L., Zhang J., 2002. ApJ, submitted, astroph/0205512, .

Jain B., Seljak U., 1997. ApJ, 484, 560.

Jain B., Taylor A., 2003. Phys. Rev. Lett., 91, 1302.

Jarvis M., Bernstein G., Jain B., 2003. MNRAS submitted, astroph/0307393, .

Jarvis M., Bernstein G., Jain B., Fischer P., Smith D., Tyson J., Wittman D., 2003. ApJ, 125, 1014.

Jenkins A., Frenk C., Thomas P., Colberg J., White S., Couchman H., Peacock J., Efstathiou G., Nelson A., 1998. ApJ, 499, 20.

Jing Y. P., 2002. MNRAS, 335, L89.

Kaiser N., Squires G., Fahlman G., Woods D., 1994. Clusters of Galaxies, Editions Frontieres. Gif-sur-Yvette, , 269.

Kaiser N., Squires G., Broadhurst T., 1995. ApJ, 449, 460.

Kaiser N., 2000. ApJ, 537, 555.

Keeton C. R., Kochanek C. S., Falco E. E., 1998. ApJ, 509, 561.

King L., Schneider P., 2002. A&A, 396, 411.

King L., Schneider P., 2003. A&A, 398, 23.

Komatsu E., Kogut A., Nolta M., Bennett C. L., Halpern M., Hinshaw G., Jarosik N., Limon M., Meyer S. S., Page L., Spergel D. N., Tucker G. S., Verde L., Wollack E., Wright E. L., 2003. ApJS, 148, 119.

Kristian J., Sachs R., 1966. ApJ, 143, 379.

Kuijken K., 1999. A& A, 352, 355.

Lambas D. G., Maddox S. J., Loveday J., 1992. MNRAS, 258, 404.

Lasserre T., The EROS collaboration, 2000. A& AS, 355, L39.

Le Fevre O., Hudon D., Lilly S., Crampton D., Hammer F., Tresse L., 1996. ApJ, 461, 534.

Lee J., Pen U., 2001. ApJ, 555, 106.

Lombardi M., Rosati P., Nonino M., Girardi M., Borgani S., Squires G., 2000. A& AS, 363, 401.

Luppino G. A., Kaiser N., 1997. ApJ, 475, 20.

Mackey J., White M., Kamionkowski M., 2002. MNRAS, 332, 788.

Massey R., Rhodes J., Refregier A., Albert J., Bacon D., Bernstein G., Ellis R., Jain B., McKay T., Perlmutter S., Taylor A., 2003a. ApJ submitted, astroph/0304418, .

Massey R. J., Refregier A. R., Conselice C. J., Bacon D. J., 2003b. MNRAS submitted, astroph/0301449, .

McCracken H. J., Le Fevre O., Brodwin M., Foucard S., S L., Crampton D., Mellier Y., 2001. A& A, 376, 756.

Peacock J., Dodds S., 1996. MNRAS, 280, 19.

Peacock J. A., 1999. *Cosmological Physics*, Cambridge University Press.

Peebles P. J., Ratra B., 2003. Reviews of Modern Physics, 75, 559.

Peebles J., 1969. ApJ, 155, 393.

Pen U., Lu T., Van Waerbeke L., Mellier Y., 2003. MNRAS, 346, 994.

Pen U., Lee J., Seljak U., 2002. ApJ, 543, L107.

Pen U.-L., Van Waerbeke L., Mellier Y., 2002. ApJ, 567, 31.

Penzias A. A., Wilson R. W., 1965. ApJ, 142, 419.

Percival W. J., Sutherland W., Peacock, J. A. andBaugh C. M., Bland-Hawthorn J., Bridges T., Cannon R., Cole S., Colless M., Collins C., Couch W., Dalton G., De Propris R., Driver S. P., Efstathiou G., Ellis R. S., Frenk C. S., Glazebrook K., Jackson C., Lahav O., Lewis I., Lumsden S., Maddox S., Moody S., Norberg P., Peterson B. A., Taylor K., 2002. MNRAS, 337, 1068.

Plionis M., Benoist C., Maurogordato S., Ferrari C., Basilakos S., 2003. ApJ, 594, 144.

Porciani C., Dekel A., Hoffman Y., 2002. MNRAS, 332, 325.

Postman M., Lauer T., Szapudi I., Oegerle W., 1998. ApJ, 506, 33.

Press W., Teukolsky S., Vetterling W., Flannery B., 1986. *Numerical recipes*, Cambridge University Press.

Refregier A., Bacon D., 2003. MNRAS, 338, 48.

Refregier A., Massey R., Rhodes J., Ellis R., Albert J., Bacon D., Bernstein G., McKay T., Perlmutter S., 2003. ApJ submitted, astroph/0304419, .

Rhodes J., Refregier A., Massey R., Albert J., Bacon D., Bernstein G., Ellis R., McKay T., Akerlof C., Aldering G., Amanullah R., Astier P., Barrelet E., SNAP Collaboration, 2003. ApJ submitted, astroph/0304417, .

Rhodes J., Refregier A., Groth E. J., 2000. ApJ, 536, 79.

Rhodes J., Refregier A., Groth E., 2001. ApJ(Lett), 552, 85.

R.Maoli, Van Waerbeke L., Mellier Y., Schneider P., Jain B., Bernardeau F., Erben T., 2001.

A& A, 368, 766.

Sackett P. D., 2000. In: *From Extrasolar Planets to Cosmology: The VLT Opening Symposium, Proceedings of the ESO Symposium held at Antofagasta, Chile, 1-4 March 1999. Edited by Jacqueline Bergeron and Alvio Renzini. Berlin: Springer-Verlag, 2000. p. 436.*, p. 436, eds Bergeron J., Renzini A.

Schneider P., Seitz C., 1995. A& A, 294, 411.

Schneider P., Van Waerbeke L., Jain B., Kruse G., 1998. MNRAS, 296, 873.

Schneider P., Van Waerbeke L., Kilbinger M., Mellier Y., 2002. A&A, 369, 1.

Schneider P., Van Waerbeke L., Mellier Y., 2002. A& A, 389, 741.

Seitz C., Kneib J.-P., Schneider P., Seitz S., 1996. A& AS, 314, 707.

Seljak U., 2002. MNRAS, 337, 7695.

Sivia D. S., 1996. *Data analysis; A Baysian tutorial*, Oxford Science publications.

Smith R., Peacock J., Jenkins A., White S., Frenk C., Pearce F., Thomas P., Efstathiou G., Couchman. H., 2003. MNRAS, 341, 1311.

Spergel D., Verde L., Peiris H., WMAP Collaboration, 2003. ApJS, 148, 175.

Stoughton C., SSDS Team, 2002. AJ, 123, 485.

Tagliaferri R., Longo G., Andreon S., Capozziello S., Donalek C., Giordano G., 2002. astroph/0203445, .

Taylor A., 2001. Phys. Rev. Lett, submitted, astroph/0111605, .

Tegmark M., Zaldarriaga M., 2002. Phys. Rev. D, 66, 103508.

Tyson J. A., Wenk R. A., Valdes F., 1990. ApJ(Lett), 349, L1.

van den Bosch F. C., Abel T., Croft R. A. C., Hernquist L., White S. D. M., 2002. ApJ, 576, 21.

Van Waerbeke L., Mellier Y., 2003. In: *"Gravitational Lensing: a unique tool for cosmology "*, astroph/0305089, eds Kneib J., Valls-Gabaud D.

Van Waerbeke L., Mellier Y., Erben T., Cuillandre J. C., Bernardeau F., Maoli R., Bertin E., Mc Cracken H. J., Le Fèvre O., Fort B., Dantel-Fort M., Jain B., Schneider P., 2000. A& A, 358, 30.

Van Waerbeke L., Mellier Y., Radovich M., Bertin E., Dantel-Fort M., McCracken H., Fevre O. L., Foucaud S., Cuillandre J., Erben T., Jain B., Schneider P., Bernardeau F., Fort

B., 2001. A& A, 374, 757.

Van Waerbeke L., Mellier Y., Pello R., Pen U.-L., McCracken H., Jain B., 2002. A& A, 393, 369.

Verde L., Heavens A. F., Percival W. J., Matarrese S., Baugh C. M., Bland-Hawthorn J., Bridges T., Cannon R., Cole S., Colless M., Collins C., Couch W., Dalton G., De Propris R., Driver S. P., Efstathiou G., Ellis R. S., Frenk C. S., Glazebrook K., Jackson C., Lahav O., Lewis I., Lumsden S., Maddox S., Madgwick D., Norberg P., Peacock J. A., Peterson B. A., Sutherland W., Taylor K., 2002. MNRAS, 335, 432.

Vitvitska M., Klypin A., Kravtsov A., Wechsler R., Primack J., Bullock J., 2002. ApJ, 381, 799.

Wang L., Caldwell R. R., Ostriker J. P., Steinhardt P. J., 2000. ApJ, 530, 17.

White S. D. M., Davis M., Frenk C. S., 1984. MNRAS, 209, 27.

White S., 1984. ApJ, 286, 38.

Wilson G., 2003. ApJ, 585, 191.

Wolf C., Dye S., Kleinheinrich M., Rix H., Meisenheimer K., Wisotzki L., 2001. A& A, 377, 442.

Wolf C., Meisenheimer K., Rix H., Borch A., Dye S., Kleinheinrich M., 2003. A& A, 401, 73.

Wolf C., Meisenheimer K., Röser H., 2001. A& A, 365, 660.

Zebrun K., Soszynski I., Wozniak P. R., Udalski A., Kubiak M., Szymanski M., Pietrzynski G., Szewczyk O., Wyrzykowski L., 2001. Acta Astronomica, 51, 317.

Zeldovich Y. B., 1972. MNRAS, 160, 1.

Zwicky F., 1933. Helv. Phys. Acta, 6, 110.

Appendix A

Theoretical Lensing Signal for Weighted Ellipticities

In chapter 6 a weighting scheme was derived to effectively remove the contamination to weak lensing measurements from intrinsic galaxy alignments. This involved removing nearby galaxy pairs from the weak lensing analysis. In this appendix we will derive the theoretical lensing signal for weighted galaxy pairs to establish how this weighting will alter the measured shear correlation function in a weighted lensing analysis.

The weighting scheme depends on the 3D position of the galaxies and we will therefore the weight the 3D convergence which is projected along the line of sight to give the effective 2D convergence as given in equation 2.58. For the weight function $H(w, w', |\boldsymbol{\theta}|)$, the weighted convergence correlation function is given by

$$\begin{aligned}\langle \bar{\kappa}_{\rm eff}(\boldsymbol{\theta})\bar{\kappa}^*_{\rm eff}(\boldsymbol{\theta}')\rangle &= \frac{1}{Q}\int_0^\infty dw \int_0^\infty dw'\, H(w,w',|\boldsymbol{\theta}-\boldsymbol{\theta}'|)\langle \kappa_{\rm eff}(\boldsymbol{\theta},w)\kappa^*_{\rm eff}(\boldsymbol{\theta}',w')\rangle \phi(w)\phi(w') \\ &= B\int_0^\infty dw \int_0^\infty dw'\, \phi(w)\phi(w')H(w,w',|\boldsymbol{\theta}-\boldsymbol{\theta}'|) \\ &\quad \int_0^w dw_1 \frac{f_K(w_1)f_K(w-w_1)}{f_K(w)a(w_1)} \int_0^{w'} dw_2 \frac{f_K(w_2)f_K(w'-w_2)}{f_K(w')a(w_2)} \\ &\quad \langle \delta(f_K(w_1)\boldsymbol{\theta},w_1)\delta^*(f_K(w_2)\boldsymbol{\theta}',w_2)\rangle \end{aligned} \quad (A.1)$$

where

$$Q \equiv \int_0^\infty \int_0^\infty dw dw'\, H(w,w',\theta)\phi(w)\phi(w') \quad (A.2)$$

and

$$B \equiv \frac{1}{Q}\left(\frac{3H_0^2\Omega_m}{2c^2}\right)^2. \quad (A.3)$$

Following the same method as detailed in appendix 2.4.4,

$$\langle \bar{\kappa}_{\rm eff}(\boldsymbol{\theta})\bar{\kappa}^*_{\rm eff}(\boldsymbol{\theta}')\rangle = B\int_0^\infty dw \int_0^\infty dw'\, \phi(w)\phi(w')H(w,w',|\boldsymbol{\theta}-\boldsymbol{\theta}'|)$$

$$\int_0^w dw_1 \int_0^{w'} dw_2 F(w, w_1) F(w', w_2)$$
$$\int \frac{d^3\mathbf{k}}{(2\pi)^3} \exp[-i\mathbf{k}_\perp \cdot (f_K(w_1)\boldsymbol{\theta} - f_K(w_2)\boldsymbol{\theta}')]$$
$$\exp[ik_z(w_1 - w_2)] P(k, w_1) \tag{A.4}$$

where $\mathbf{k} = (\mathbf{k}_\perp, k_z)$ and

$$F(w, w') \equiv \frac{f_K(w') f_K(w - w')}{f_K(w) a(w')} \tag{A.5}$$

Again assuming that the correlation function of δ is non-zero only if w_1 and w_2 are almost equal we can set $f_K(w_1) = f_K(w_2)$ in the first exponential, and also approximate $F(w', w_2) \simeq F(w', w_1)$. The w_2 integral then simplifies using equation 2.43 and we are left with

$$\begin{aligned}\langle \bar{\kappa}_{\rm eff}(\boldsymbol{\theta}) \bar{\kappa}^*_{\rm eff}(\boldsymbol{\theta}') \rangle &= B \int_0^\infty dw \int_0^\infty dw' \, \phi(w)\phi(w') H(w, w', |\boldsymbol{\theta} - \boldsymbol{\theta}'|) \int_0^w dw_1 F(w, w_1) F(w', w_1) \\ & \int \frac{d^3\mathbf{k}_\perp}{(2\pi)^2} \exp[-i\mathbf{k}_\perp \cdot f_K(w_1)(\boldsymbol{\theta} - \boldsymbol{\theta}'))] \exp[ik_z w_1] P(|\mathbf{k}_\perp|, w_1). \end{aligned} \tag{A.6}$$

An angle integration of P gives

$$\int \frac{d^3\mathbf{k}_\perp}{(2\pi)^2} \exp[-i\mathbf{k}_\perp \cdot f_K(w_1)(\boldsymbol{\theta} - \boldsymbol{\theta}'))] P(|\mathbf{k}_\perp|) = \int_0^\infty \frac{kdk}{2\pi} P(k, w_1) J_0[k f_K(w_1)|\boldsymbol{\theta} - \boldsymbol{\theta}'|] \tag{A.7}$$

where J_0 is the zeroth Bessel function of the first order. Hence we can write the correlation function as

$$\begin{aligned}\langle \bar{\kappa}_{\rm eff}(\boldsymbol{\theta}) \bar{\kappa}^*_{\rm eff}(\boldsymbol{\theta}') \rangle &= B \int_0^\infty dw \int_0^\infty dw' \, \phi(w)\phi(w') H(w, w', |\boldsymbol{\theta} - \boldsymbol{\theta}'|) \int_0^w dw_1 F(w, w_1) F(w', w_1) \\ & \int_0^\infty \frac{kdk}{2\pi} P(k, w_1) J_0[k f_K(w_1)|\boldsymbol{\theta} - \boldsymbol{\theta}'|]. \end{aligned} \tag{A.8}$$

Writing this in a form as close to equation 2.79 as possible, by reversing the order of integration, and remembering that in the weak lensing limit shear and convergence have the same statistical properties as shown by equation 2.82.

$$\langle \gamma(\boldsymbol{\theta}) \gamma(\boldsymbol{\theta}')^* \rangle = B \int_0^\infty dw_1 X(w_1, |\boldsymbol{\theta} - \boldsymbol{\theta}'|) \int_0^\infty \frac{kdk}{2\pi} P(k, w_1) J_0[k f_K(w_1)|\boldsymbol{\theta} - \boldsymbol{\theta}'|]. \tag{A.9}$$

where

$$X(w_1, \theta) \equiv \int_{w_1}^\infty dw \int_{w_1}^\infty dw' \phi(w)\phi(w') F(w, w_1) F(w', w_1) H(w, w', \theta). \tag{A.10}$$

In the equal-weighted case, $H = 1$, and $X(w, \phi)$ simplifies to the product of two equal integrals, each independent of ϕ and equal to $g(w) f_K(w)/a(w)$.

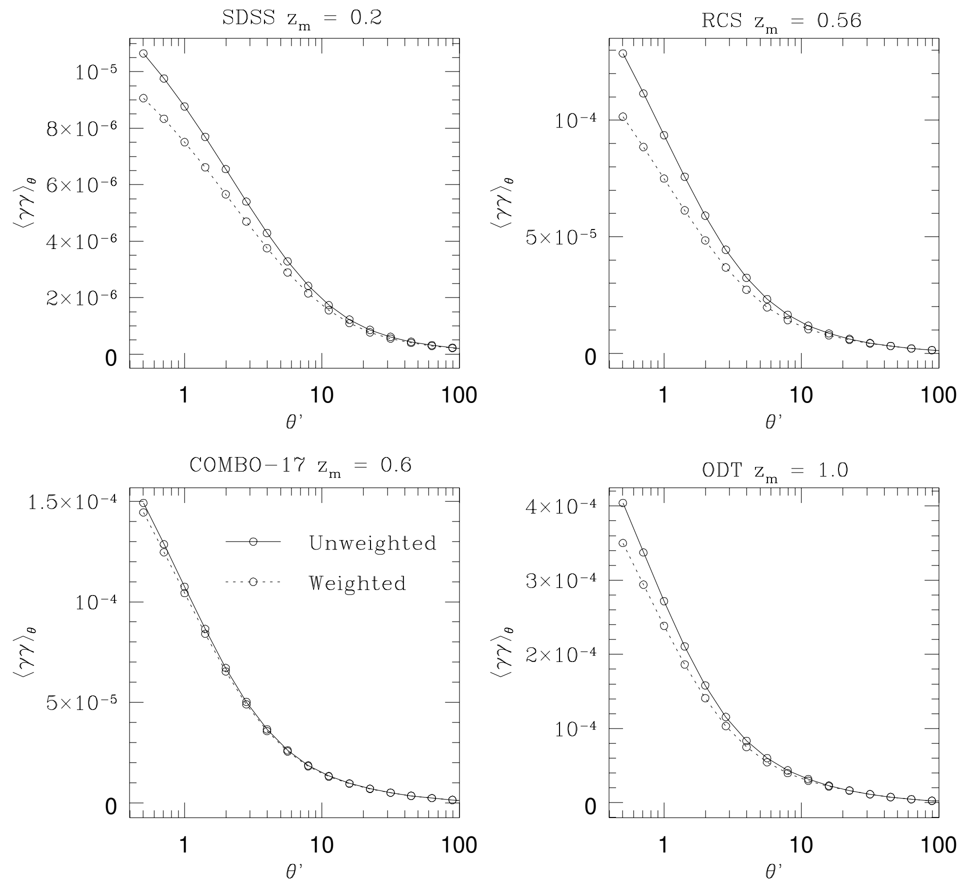

Figure A.1: Expected weak lensing signal for a ΛCDM model with $\sigma_8 = 0.9$, for the surveys listed in Table 6.1. . The solid line shows equal weighting of galaxies; the dotted line shows the effect of employing the multi-colour survey weighting scheme proposed in chapter 6.

The effect of the weighting is shown in Fig. A.1. For surveys such as COMBO-17 with accurate photometric redshifts, the lensing signal changes by up to $\sim$ 3%. For the Sloan photometric survey, the effect is $\sim$ 10%; the greatest effect is for RCS, which has the least accurate photometric redshifts.